Pollutant prediction in numerical simulations of laminar and turbulent flames using virtual chemistry

Giampaolo Maio

Giampaolo Maio. Pollutant prediction in numerical simulations of laminar and turbulent flames using virtual chemistry. Chemical and Process Engineering. Université Paris-Saclay; Politecnico di Milano, 2020. English. NNT : 2020UPASC003 . tel-02893174

HAL Id: tel-02893174
https://theses.hal.science/tel-02893174v1

Submitted on 8 Jul 2020

Pollutant prediction in numerical simulations of laminar and turbulent flames using virtual chemistry

Thèse de doctorat de l'Université Paris-Saclay

École doctorale n° 579, Sciences mécaniques et énergétiques, matériaux et géosciences (SMEMAG).
Spécialité de doctorat: Combustion.
Unité de recherche: Université Paris-Saclay, CNRS, CentraleSupélec, Laboratoire EM2C, 91190, Gif-sur-Yvette, France.
Référent: : CentraleSupélec.

Thèse présentée et soutenue à Gif-sur-Yvette, le 17/01/2020, par

Giampaolo MAIO

Composition du jury:

Alessandro Parente Professeur, Université Libre de Bruxelles	Président
Bart Merci Professeur, Ghent University	Rapporteur
Dominique Thévenin Professeur, Otto von Guericke University de Magdebourg	Rapporteur
Prof. Gaetano Continillo Professeur, University of Sannio	Examinateur
Karine Truffin Docteur, IFP Energies nouvelles	Examinatrice
Mélody Cailler Docteur, Safran Tech	Examinatrice
Benoît Fiorina Professeur, CentraleSupélec	Directeur
Alberto Cuoci Professeur, Politecnico di Milano	Codirecteur

Thèse de doctorat

NNT: 2020UPASC003

Acknowledgements

First of all, I would like to acknowledge all the the members of the jury for accepting to evaluate my work and for the interesting comments raised. I would like to thank also all the people that attended my public thesis discussion. I would like also to express my gratitude to both my supervisors, Benoît and Alberto, who guided me during my Phd giving me sound advice and contributing to my professional growth with their different scientific sensibilities. I would also thank Melody who put together the basis *virtual chemistry* and for the great help she gave me, above all during my first PhD year. A special acknowledgement also to Prof. Nasser Darabiha for the useful discussions and for helping me to set-up the REGATH simulations. Thank you to the YALES2 team, Vincent, Ghislain and Pierre for sharing the solver and for giving me all the technical support.

This PhD was part of the Clean-Gas project that was financed by the European Union Horizon 2020 research and innovation programme under Marie Sklodowska-Curie grant agreement N^{o}643134. For the great opportunity they offered me, I want to acknowledge all the members of the Clean-Gas project: the professors who organized it, Isabella who coordinates everything, the other PhD students for the exchange of knowledge, the friendship and the good time that we shared together during summer schools. I had a really good time both at EM2C and at Politecnico during my "foreign period" in Milano. For this reason, I wuold like to thank all the people I met in the two institutions.

During my years in Paris I encountered a lot of wonderful friends who have really supported me and who have contributed to make my experience abroad enjoyable and memorable. In particular, I want to thank my Spanish/South American friends Jan and Abi and my Italian friends Lorella, Nicola, Giunio, Alfredo and Stefano; he has also given me technical support for my OpenFOAM simulations. "Last but not least" I would like to thank all my family for the support and for coming from Italy for my public discussion and especially Jenine who uniquely and lovely supported me during the entire PhD period.

Abstract

CFD is nowadays used by research engineers as a numerical tool to design and optimize advanced combustion devices that are employed in energy conversion systems. In the development of advanced numerical CFD tools, one of the main research challenges is the identification of a reduced combustion chemistry model able to find a compromise between accurate reproduction of the flame structure and pollutants formation with an affordable CPU cost. In particular, pollutants formation prediction is a difficult task when complex flame environments are encountered: flame characterized by mixture stratification, heat loss and burnt gas recirculation. The present research work focuses on the modeling of CO and NOx formation in complex flame conditions using a reduced finite rate chemistry approach. CO and NOx reduced chemistry models are here developed using the recent *virtual chemistry* model; it consists in designing reduced mechanisms made of a network of an optimized number of virtual species interacting through virtual optimized reactions. In the first step, the virtual chemistry mechanisms are developed and validated in 1-D flames comparing the results with detailed chemistry. In a second step, they are employed to compute several 2-D laminar and 3-D turbulent flame configurations which include different combustion regimes: premixed, non-premixed, partially-premixed and non-adiabatic conditions. The obtained results are validated either with experimental data or with detailed chemistry computations.

Keywords: Combustion model, Reduced mechanism, Pollutants formation, Complex flame structures, Mixture stratification, Flame heat loss.

Résumé

La CFD est aujourd'hui utilisée par les ingénieurs de recherche comme un outil numérique pour concevoir et optimiser les dispositifs de combustion avancés qui sont utilisés dans les systèmes de conversion d'énergie. L'un des principaux objectifs de la recherche, dans le développement d'outils numériques avancés pour la CFD, est l'identification d'un modéle réduite de cinitique chimique de la combustion qui reproduit la structure de la flamme et la formation de polluants avec un coût de calcul abordable. En particulier, la prédiction de la formation de polluants est une tâche difficile lorsque des flammes complexes sont rencontrées: stratification du mélange, pertes de chaleur et recirculation des gaz brûlés. Le travail de recherche mené dans cette these se concentre sur la modélisation de la formation monoxyde de carbone (CO) et des oxydes d'azote (NOx) dans des conditions de flamme complexes en utilisant une methode récemment développée et appelée chimie virtuelle: celle-ci consiste à concevoir des mécanismes réduits constitués d'un réseau d'un nombre optimisé d'espèces virtuelles interagissant via des réactions virtuelles optimisées. Dans une première étape, les mécanismes virtuels sont développés et validés dans des configurations de flammes 1-D. Dans un deuxième temps, ceux-ci sont utilisés pour calculer plusieurs configurations de flammes 2-D laminaires et 3-D turbulentes sur une large gamme de régimes de combustion: prémélangé, non prémélangé, partiellement prémélangé et non adiabatique. Les résultats obtenus sont validés avec des données expérimentales et avec des calculs incluant une cinetique chimique détaillée.

Mots-clés: Modéle de combustion, Mècanisme réduit, Formation de polluants, Structures complexes de flamme, Stratification du mélange, Pertes thermique de la flamme.

Contents

Introduction

This thesis is part of the CLEAN-Gas project (Combustion for Low Emission Applications of Natural Gas)(`http://www.clean-gas.polimi.it`.) CLEAN-Gas project is funded by the European Community through the Horizon 2020 Actions. CLEAN-Gas Project, coordinated by Politecnico di Milano, started January 1st, 2015; it involves 4 partners from the Academia (Politecnico di Milano, Centrale Supélec, Technische Universität Darmstadt and Université Libre de Bruxelles), 3 industrial partners (Ansaldo Energia, Rolls-Royce Deutschland and Numeca) and T.I.M.E. Association.

The CLEAN-Gas scientific goal is to develop new experimental and numerical tools for improving natural gas combustion in innovative burners.

One of the main key points of the project was the mobility of the Phd canditates among the institutions involved in the program, creating the opportunity to strengthen research collaborations and connections.

In line with the spirit of the mobility program, the present work of thesis was conducted in collaboration with the Department of Chemistry, Materials, and Chemical Engineering at Politecnico di Milano.

Combustion science in the energy scenario

In 2016, the global energy demand measured in TPES (Total Primary Energy Supply) was about 13800 Mtoe.[1]

Figure 1 (International Energy Agency 2018) shows a comparison between the Total Primary Energy Supply (TPES), globally demanded respectively in 1971 and 2016, divided by energy sources. Although the amount of TPES has largely increased through the years (of about 2.5 times), the repartition has just slightly changed among the primary sources. It is clear that the role of the fossil fuels still remains predominant. Hence, combustion energy technologies, that convert chemical potential energy of fossil fuels into thermal power, are largely the most used in the energy scenario.

Furthermore, combustion technologies are also used for energy valorization of wastes and bio-fuels that also play a significant role in the TPES repartition (about 10%).

---

[1] 1 Tonne of Oil Equivalent $\sim$ 42GJ

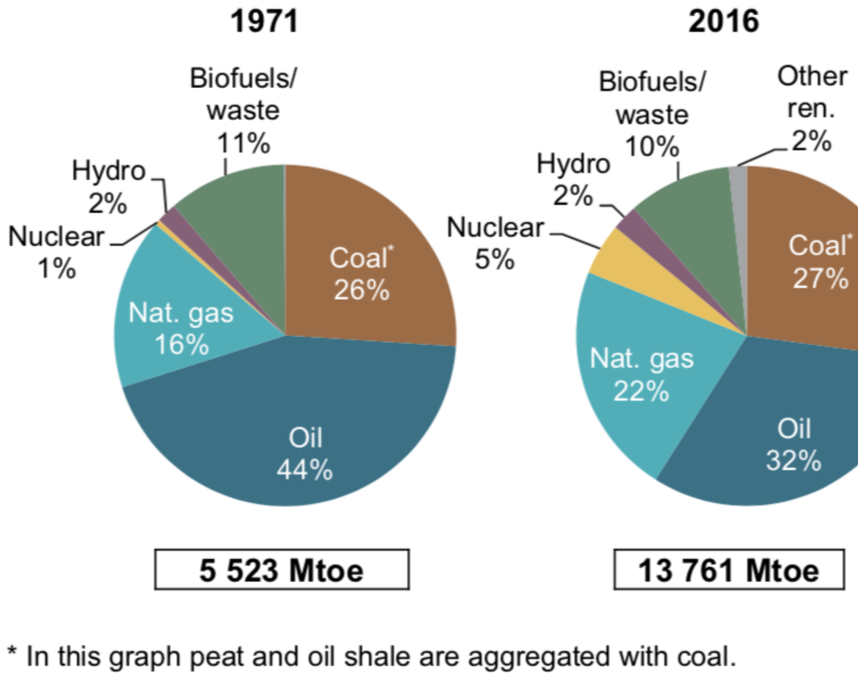

Figure 1: *Total Primary Energy Supply (TPES) divided by fuel. Data from International Energy Agency: World energy balance 2018 overview (`https://www.iea.org/`).*

In the World Energy Outlook 2017 of the International Energy Agency (International Energy Agency 2017), keeping into account the rise of final energy demand through future years, two possible energy scenarios have been projected until 2040, in terms of TPED, characterized by energy sources:

- The NPS (New Policies Scenario), presented in Fig. 2, is evaluated considering the existing energetic policies and the ones announced by the various countries.
- The SDS (Sustainable Development Scenario), presented in Fig. 3, outlines an integrated approach to achieve internationally agreed objectives on climate change, air quality and universal access to modern energy in accordance with the recent Paris Agreement COP21[2].

Observing at the NPS, in 2040, the global energy demand is expected to grow by 30%. Despite the development, deployment and falling costs of renewable energy technologies it is expected that they will cover only 40 % of this growth. Consequently, although the transformation in energy conversion technologies

---

[2] The result of the United Nations Framework Convention on Climate Change (UNFCCC) Conference of the Parties 21st (COP21) meeting in December 2015

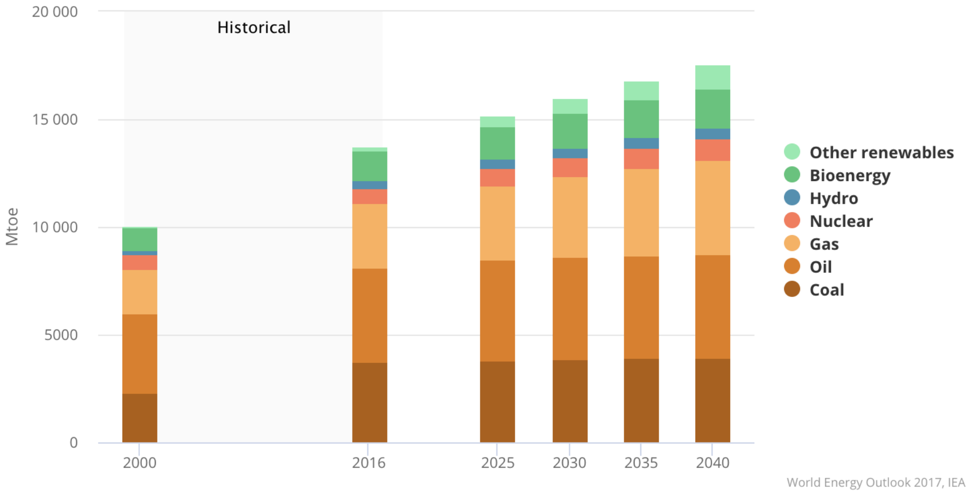

Figure 2: *Primary energy demand in the* ***New Policies Scenario****. Data from International Energy Agency: World Energy Outlook 2017 (`https://www.iea.org/`).*

is continuing to meet the energy demand, combustion energy conversion technologies will still play a major role. However, it can be observed a stagnation in oil and coal usage; on the contrary the natural gas demand is expected to grow accounting for a quarter of global energy demand.

Analysing the SDS scenario, it can be observed that: besides the increase of renewable energy technologies contribution the most important role is played by the increase of the energy conversion efficiency and by the substitution of oil and coal by natural gas.

It clearly appears that to follow the NPS and to gear it toward the SDS, in order to deal with global warming and air pollution, two main routes must be followed:

- Invest in low-carbon technologies diversifying energy sources.
- Improve the efficiency of energy conversion devices that are based largely on combustion technologies.

The focus of the research activity conducted in this thesis is on the second route and in particular on combustion processes.

The two main drawbacks of combustion processes are: their contribution to global warming and to the pollution of industrial and urban areas. The energy sector, production, transformation and the use of energy, is central for the climate change challenge. It accounts for around two-thirds of global Green House Gases (GHG) emissions and about 90% of carbon dioxide (CO_2) emissions, most prevalent GHG.

The CO_2 emissions are directly related to the efficiency of the combustion

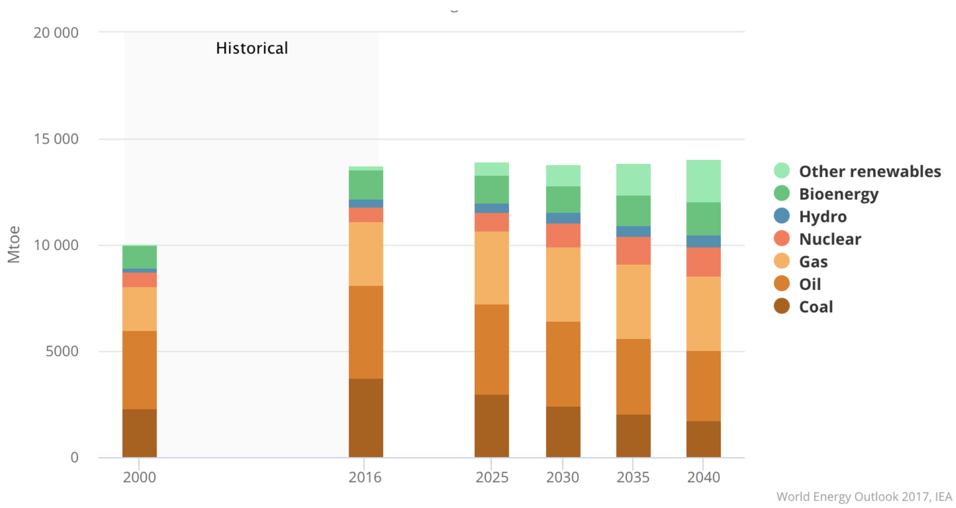

Figure 3: *Primary energy demand in the* ***Sustainable Development Scenario****. Data from International Energy Agency: World Energy Outlook 2017 (* `https://www.iea.org/` *)*

devices and to the type of fuel that is used in the combustion process. Hence, improving the efficiency of the combustion devices and looking for cleaner fuel such as natural gas are the main objectives to pursue.

Instead, to improve the local air quality (especially in the urban and industrial areas) the reduction of pollutant emissions from combustion processes is of paramount importance.

Policy attention to air quality is rising because its impacts on human health is causing great concern. Making reference to the New Policies Scenario, world-wide premature deaths from outdoor air pollution, from 3 million today, will have rise to more than 4 million by 2040. Fuel combustion in the energy sector is the main origin of air pollutants: for example 85% of particulate matter and almost all of the sulfur oxides and nitrogen oxides (International Energy Agency 2016). Therefore it is important to invest in research solutions to tackle this issue, reconciling it with the world's energy requirement.

Numerical simulation tools for flame modeling

Combustion engineers use numerical simulation to design and optimize combustion devices. This is an alternative and sometimes cheaper solution to large scale experiments. Furthermore, numerical simulation allows to access to flame quantities that cannot be reached with experimental studies. Numerical tools can reproduce the entire combustion device or a single part of it or only one particular phenomenon involved in the process.

However, the transfer of engineering tools from the academia to industry requires the research of numerical models that are reliable and at the same time relatively cheap in terms of computational cost.

CFD (Computational Fluid Dynamics) simulation, applied to the solution of complex combustion processes, has made significant efforts in recent years, allowing the simulation of real-scale combustion chambers such as industrial and power generation furnaces (Vascellari et al. 2014; Galletti et al. 2013), gas turbine combustors (Boileau et al. 2008; Philip et al. 2015; Esclapez et al. 2017) and piston engines (Hasse et al. 2010; Vermorel et al. 2009). With the increase of available CPU power, LES models replace RANS models more and more, even for industrial scale burner simulations. LES allows to solve the large-scale turbulent eddies in time and space giving finer information about the non-stationary phenomenon affecting the flame (Poinsot and Veynante 2018).

Despite the recent important research achievements, developing numerical models for combustion applications, that are suitable for LES, still constitute a challenge for the research community.

The accurate reproduction of pollutant formation (CO, NOx, unburnt hydrocarbons, etc...) and inner flame structure prediction in turbulent flame simulations, at an affordable CPU cost, is still a research topic of interest and that needs to be fully addressed and better understood.

Pollutant formation prediction is even a more challenging task when complex phenomena (such as mixture stratification, heat transfer, burnt gases recirculation, etc...) affect the flame.

Indeed, industrial combustion devices operate in complex flame conditions: air and fuel are often injected separately in the combustor or they are partially premixed before entering the chamber to improve flame stability. Consequently, coexistence of premixed and non-premixed flame structures is encountered. Furthermore, in enclosed flames, the non-adiabaticity of the chamber walls lowers the flame enthalpy affecting pollutant formation and it is at the origin of strain and extinction phenomena. Model pollutant formation in such complex operating conditions, at an affordable CPU cost, is indeed a challenging task.

Pollutant prediction at low-CPU cost

Pollutant formation modeling (CO, NO$_x$ and polycyclic aromatic hydrocarbons (PAHs)), requires the accurate reproduction of the inner flame structure. This is achieved through the inclusion of complex detailed chemistry at one stage of the modeling process: either detailed chemistry is directly included in the computation or it is used as reference to derive a reduced combustion chemistry model.

For hydrocarbon fuels, detailed chemistry schemes include hundreds of species and thousands of reactions and the size of the scheme scales with the complexity of the fuel (Lu and Law 2009). The size of the chemical mechanism employed in the numerical simulation directly affects its CPU cost (Lu et al. 2009). Furthermore, the direct inclusion of complex chemistry in large scale CFD simulations is a complex task: the time and spatial resolution scales, required by some detailed chemistry species, are smaller than the flow ones by several orders of magnitude.

The above motivations make detailed chemistry not suitable for multidimensional CFD computations. But, 0-D reactors and 1D-flame computations are easily carried out employing detailed chemistry.

Several reduced order chemistry models are currently employed (Fiorina et al. 2015) in multi-dimensional CFD computations to limit the simulation CPU demand:

- Global or semi-global reduced mechanisms (Westbrook and Dryer 1981; Jones and Lindstedt 1988; Franzelli et al. 2010).
- Tabulated chemistry (Peters 1984; Gicquel et al. 2000; Van Oijen et al. 2001; Pierce and Moin 2004).
- Systematically reduced mechanisms. (Lu and Law 2008a; Pepiot-Desjardins and Pitsch 2008; Felden 2016).

All these reduced chemistry strategies use detailed chemistry information, coming from 0-D and/or 1-D computations, in the preprocessing phase, to build up the model and to tune its parameters.

Semi-global kinetic schemes, generally made of 1 up to 4 global reactions, are not suitable for pollutant prediction. Pollutants species are not often included in the mechanism. If CO is included, only its final equilibrium concentration is correctly retrieved but the CO along the inner flame structure is not accurate (Franzelli et al. 2013).

Tabulated chemistry methods, in the original formulation, allow to reproduce CO when the flame regime is apriori identified and the local flame structure stays close to the tabulated archetype. In the tabulated chemistry formalism, when the flame regime is apriori identified, NO prediction need further modeling assumptions (Nafe and Maas 2002). Additional coordinates have to be added to the chemtable (Pecquery et al. 2014) and additional scalars have to be transported in the flow solver (Ihme and Pitsch 2008; Ketelheun et al. 2011; Godel et al. 2009).

The capability of analytically reduced chemistry to predict CO and NO_x has been recently demonstrated in laboratory scale jet flame (Jaravel et al. 2018) and in aeronautical burners (Jaravel et al. 2017). However, the computational cost associated with this methodology still remains very high making its applicability restrictive. The CPU cost increases rapidly with the number of transported species and numerical difficulties arise because a wide range of chemical time scales have to be considered (Lu et al. 2009).

Cailler (2018) has recently developed an alternative methodology called *Virtual chemistry* to face the above limitations. Virtual chemistry aims at combining low CPU cost with accurate flame structure prediction, including pollutant species. Cailler (2018) have demonstrated the applicability of the methodology to multi-modal flame (premixed and non premixed) conditions for the scope of temperature, heat release and CO prediction.

Thesis scope and contributions

In line with the combustion modeling challenges described above, the present research work focuses on the prediction of CO and NO_x formation in complex flame conditions at reduced CPU cost. Multi-modal flame regimes and flame heat losses are considered. Here, the words multi-modal or multi-regime stand equivalently for coexistence of premixed and non-premixed flame structures.

In this thesis, CO and NO_x reduced chemistry models are developed using the recent *virtual chemistry* approach (Cailler 2018).

Once the mechanisms are developed and validated in 1-D laminar flame archetypes, their applicability to multidimensional laminar and turbulent CFD computations is shown, demonstrating the value of the approach. The multidimensional CFD results are either validated versus experimental data for the turbulent test cases or compared to fully detailed chemistry computations for laminar configurations.

The validity domain of the virtual chemistry approach is further broadened with respect to Cailler (2018) thesis work. The virtual chemistry applicability to multi-dimentional CFD computations (turbulent LES and laminar) at reduced CPU cost, is further demonstrated.

In particular, virtual chemistry is challenged and validated in the LES context in two turbulent flame configurations:

1. **Sydney inhomogeneous piloted burner** (Meares and Masri 2014; Barlow et al. 2015) representative of multi-modal turbulent flame conditions.
2. **Preccinsta burner** (Meier et al. 2007) which is a confined flame impacted by wall heat losses.

NO virtual chemistry prediction is validated in 2-D laminar premixed, non-premixed and partially premixed configurations.

A schematic and brief overview over the thesis research scopes and achievements is presented in Fig. 4. CO and NO_x emissions are modelled in CFD computations. CO is reproduced in 3-D turbulent conditions in the Sydney inhomogeneous piloted burner and in Preccinsta burner. Instead, NO is reproduced in 2-D multi-modal laminar flame benchmarks and directly compared to detailed reference chemistry.

Thesis outline

The present thesis work is divided in 3 parts:

1. The first thesis part includes the first three chapters. Chapter 1 deals

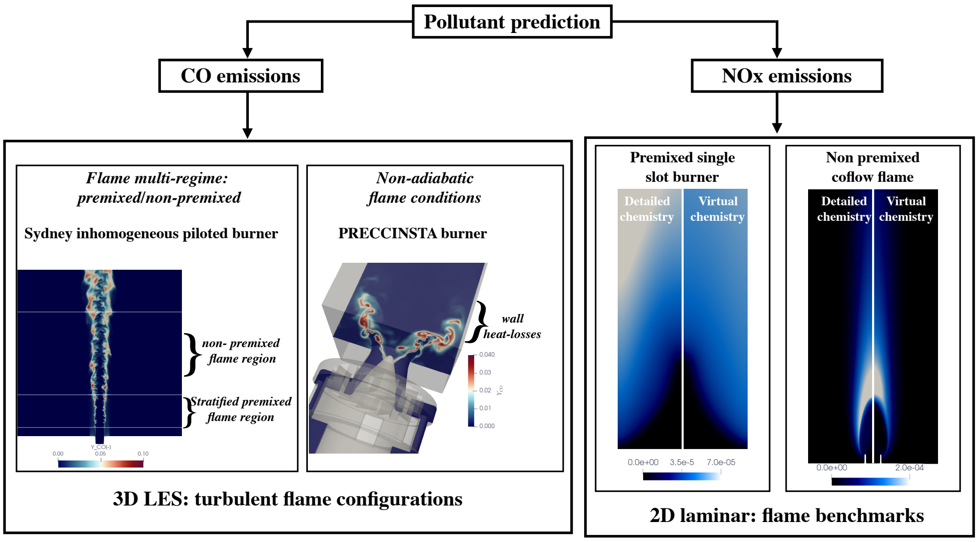

Figure 4: *Overview on the thesis scope and achievements*

with basis of the thermal and kinetic theory valid for reactive ideal gases including the 3-D governing equations. The equations are also presented in the LES formalism, describing the possible modeling strategies for the unclosed terms. Chapter 2 presents the challenges related to combustion chemistry description and the most used literature strategies to describe combustion chemistry at reduced CPU cost. Chapter 3 introduces and describes the recent *virtual chemistry* methodology in the original formulation proposed by Cailler (2018). Finally the research challenges addressed by this work are briefly reminded.

2. The second part presents the virtual chemistry developments conducted in this research work. Virtual chemistry is before enlarged to non-adiabatic flame conditions in Chapter 4: the non adiabatic virtual chemistry model is developed and validated in 1-D non adiabatic flame conditions. In Chapter 5, an NO virtual chemistry mechanism is designed and validate in 1-D laminar premixed and non premixed flame conditions. The developed NO reduced mechanism is employed to carry out a premixed, a non-premixed and a partially premixed 2-D laminar flame computations and compared to detailed reference chemistry simulations.
3. The third part is dedicated to the 3-D turbulent flame computations. Chapter 6 focuses on the LES modeling of the new Sydney inhomogeneous piloted burner (Meares and Masri 2014). Here, LES-virtual chemistry results are compared with an LES-tabulated chemistry reference solution and to experiments. In Chapter 7, LES of the Preccinsta burner is carried out, prescribing non adiabatic boundary conditions along the chamber walls. Eventually, LES-virtual chemistry results are compared to

experiments and to a literature recent LES-analytic chemistry reference solution.

Part I

Combustion chemistry modeling

Chapter 1

Combustion theoretical basis

Contents

The present chapter gives the basis of the thermal and kinetic theory for reactive ideal gases. This theory is usually employed in the generation of thermo-chemical databases dedicated to hydrocarbon fuels oxydation. Furthermore, laminar and turbulent flame simulation requires the coupling of the thermo-chemistry with 3-D fluid transport equations (mass, momentum, energy and species) which are also briefly introduced in the chapter. In addition, the 3-D transport governing equations are presented in the LES formalism to address turbulent flows description. The combustion modeling challenges introduced by the closure of the LES filtered scalars source term are finally discussed.

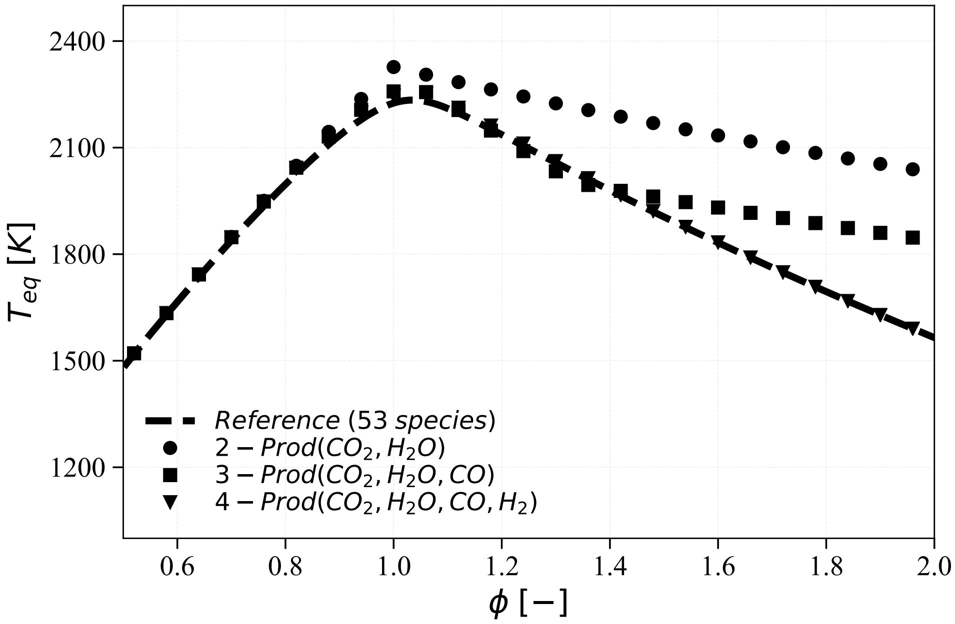

Figure 1.1: *Equilibrium adiabatic flame temperature versus equivalence ratio for CH_4/air combustion. The calculation are at atmospheric pressure and considering a fresh mixture temperature of 300K. The reference solution (53 species) is compared with solutions obtained with a simplified set of products.*

1.1 Thermo-chemical equilibrium and detailed kinetic

A combustion process, involving a hydrocarbon fuel, does not occur in a single global reaction, but it involves a huge number of reaction steps, involving multiple species and radicals. These steps depend from the nature of the fuel and on the operating conditions. Starting from pure fuel and oxidizer, it takes a certain number or chemical pathways to reach combustion products and hence chemical equilibrium conditions.

The equilibrium state can be determined through the knowledge of thermodynamic properties of the mixture. The inclusion of a sufficient number of species in the mixture is the controlling parameter to retrieve accurately the equilibrium conditions. For example, starting from a methane-air atmospheric mixture, considering a constant pressure flame, the adiabatic equilibrium temperature and composition depend from the number of species included in the model.

Figure 1.1 shows the evolution of the adiabatic equilibrium temperature across the whole flammability limit, comparing the reference solution versus simplified ones (Franzelli et al. 2010). The reference mixture includes 53 species, as in the GRI.3.0 detailed mechanism (Smith et al. 2011), while the simplified ones include an increasing number of product species in the mixture: from 2 products (CO_2, H_2O) to 4 products (CO_2, H_2O, CO, H_2). At least 4 products, in addition to the fresh species, are necessary to capture the proper equilibrium temperature over the whole flammability limit.

Instead, the analysis of the chemical pathways that describe the transition from fresh gases to burnt equilibrium conditions is given by chemical kinetic.

The correct description of chemical kinetic is of paramount importance in combustion processes because the operating conditions and the short residence time lead to a departure from thermo-chemical equilibrium state.

The knowledge of the detailed oxidation process of an hydrocarbons fuel is a complex task. It involves a huge number of intermediate species, radicals and intermediate reactions.

Detailed thermo-chemical databases are retained in this thesis as reference to develop reduced-order chemistry models which are more suitable for multidimensional simulations.

Hydrocarbons oxidation: the example of CH_4/Air system To show the complexity of the detailed kinetic description of an oxidation process, here, the example for the CH_4/Air system is presented. The oxidation process of methane involves a large number of chemical reaction steps. A "schematic" interaction model is presented in Fig. 1.2, as proposed by Ranzi et al. (1994) and recently revised by Curran (2018).

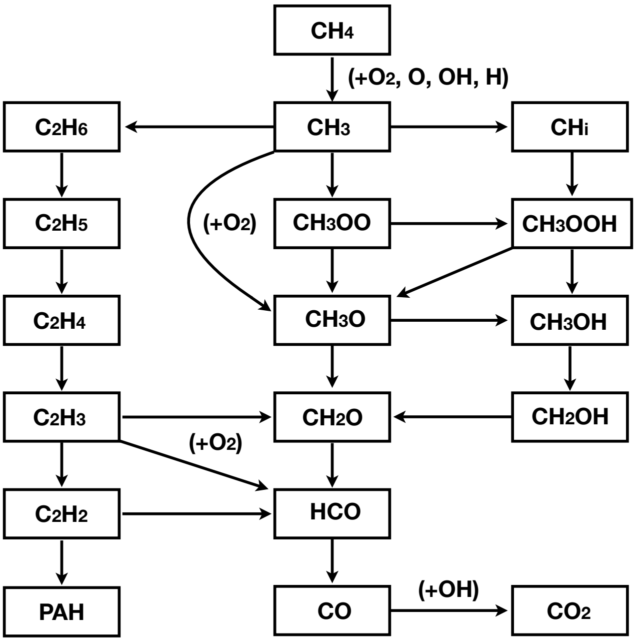

Figure 1.2: *Simplified scheme of methane and oxygen interaction.*

Figure 1.2 shows a linear progression from CH_4 to CO_2 including several pathways originating from methyl (CH_3) radical. The mechanism starts with an attack to the CH_4 molecule by oxygen and/or hydrogen radicals (O, H, OH) to produce the methyl radical. From methyl radical different paths can be covered to reach the complete or incomplete oxidation:

- High temperature oxidation: formation of methoxy radicals (CH_3O) and successive formation of formaldehyde (CH_2O).
- Low temperature oxidation: alternative routes are pursued to form CH_3O and CH_2O through the intermediate production of methanol (CH_3OH) and other radicals.
- Pyrolysis reactions: ethane (C_2H_6) is formed as results of recombination process. Subsequently, pyrolysis reactions take place including the possible PAH (poly-aromatic hydrocarbons) formation.

At high temperature, CH_3, may also form CH_i radicals that are precursors of prompt NO formation.

The competition among the various oxidation paths strongly depends from the operating conditions of the system such as temperature, pressure and local equivalence ratio.

1.2 Thermo-chemistry combustion modeling

Along a combustion process, the local state of a reactive ideal gas mixture is uniquely defined by the knowledge of ρ, T, Y_k for k=1,...,N_s. Where ρ is the gas density, T the gas temperature and Y_k is the mass fraction of the N_s species present in the system. The pressure is uniquely relate to the above quantities through the equation of state (EOS).

Considering an ideal gas mixture, at local thermal equilibrium, the EOS reads:

$$P = \sum_{k=1}^{N_s} [X_k]\, RT = \frac{\rho RT}{\overline{W}} \tag{1.1}$$

Where R[1] is the universal gas constant, $[X_k]$ is the species molar concentration equal to $\rho Y_k / W_k$. W_k is the species molecular weight and $\overline{W}$ is the mixture mean molecular weight.

$\overline{W}$ is computed from the knowledge of either the species mole fractions or the species mass fractions, respectively as:

$$\overline{W} = \sum_{k=1}^{N_s} W_k X_k; \qquad \overline{W} = \frac{1}{\sum_{k=1}^{N_s} Y_k / W_k} \tag{1.2}$$

---

[1] R = 8.3143 J/(mol.K) in the S.I

1.2.1 Thermodynamic

Each species of the gas-phase mixture is characterized by own thermodynamic properties. In the "thermally perfect gas" hypothesis the thermodynamic properties of the species are functions of the temperature only (independent on pressure), following an n-order polynomial fit function. The polynomial function are usually expressed in accordance with the NASA formulation for gas-phase kinetic (McBride et al. 1993). For each species, seven coefficients are needed for each of the two temperature ranges: for temperature lower and greater than 1000 K (Burcat et al. 2005). These coefficients allow to generate the thermodynamic functions: heat capacity, enthalpy and entropy. The molar heat capacity is calculated as a $4th$-order temperature polynomial function :

$$\frac{C_{pk}}{R} = a_{1k} + a_{2k}T + a_{3k}T^2 + a_{4k}T^3 + a_{5k}T^4 \tag{1.3}$$

The species molar enthalpy H_k is given as the molar heat capacity integral, as follows:

$$H_k = \int_0^T C_{pk}dT + H_k(0) \tag{1.4}$$

The first contribution is the sensible enthalpy while the second one in the standard enthalpy of formation evaluated at the reference temperature T_0, known also as $\Delta H^0_{f,k}$. The reference temperature T_0 is a usually chosen equal to 0 K or 298 K. According to the NASA polynomial functions (McBride et al. 1993), the molar enthalpy H_k is equal to:

$$\frac{H_k}{RT} = a_{1k} + \frac{a_{2k}}{2}T + \frac{a_{3k}}{3}T^2 + \frac{a_{4k}}{4}T^3 + \frac{a_{5k}}{5}T^4 + \frac{a_{6k}}{T} \tag{1.5}$$

The molar entropy is calculated as:

$$S_k = \int_0^T \frac{C_{pk}}{T}dT + S_k(0) \tag{1.6}$$

and using the NASA-polynomial formulation (McBride et al. 1993), it is equal to:

$$\frac{S_k}{R} = a_{1k}\, lnT + a_{2k}T + \frac{a_{3k}}{2}T^2 + \frac{a_{4k}}{3}T^3 + \frac{a_{5k}}{4}T^4 + a_{7k} \tag{1.7}$$

Each of the three above molar properties are generically identified with a capital letter Ψ_k that can be also expressed in mass units ψ_k by dividing Ψ_k by the species molecular weight W_k.

1.2.2 Kinetic and chemical-equilibrium theory

A chemical reactive system can be formalized by the following set of stoichiometric equations:

$$\sum_{k=1}^{N_s} \alpha_{ki}^{'}\chi_k \leftrightarrow \sum_{k=1}^{N_s} \alpha_{ki}^{''}\chi_k \quad (i = 1, ..., N_r) \tag{1.8}$$

where N_r is the number of reversible or irreversible reactions and N_s the number of chemical species present in the system.
$\alpha_{ki}^{'}$ and $\alpha_{ki}^{''}$ are respectively the forward and backward stoichiometric coefficients of the kth species χ_k involved in the i^{th} reaction.
The net kth species molar production rate results from a summation of individual rates q_{ki} over all the reactions:

$$\dot{\omega}_k = \sum_{i=1}^{N_r} q_{ki} \tag{1.9}$$

The reaction progress q_{ki} of k^{th} species in the i^{th} reaction is expressed as the temporal variation of $[X_k]$ in the reaction i:

$$q_{ki} = \left.\frac{d\left[X_k\right]}{dt}\right|_i = \alpha_{ki}q_i \tag{1.10}$$

where $\alpha_{ki} = \alpha_{ki}^{''} - \alpha_{ki}^{'}$ is the net species stoichiometric coefficient and q_i the net reaction rate for reaction i that is expressed as:

$$q_i = k_{fi} \prod_{k=1}^{N_s} \left[X_k\right]^{\alpha_{ki}^{'}} - k_{bi} \prod_{k=1}^{N_s} \left[X_k\right]^{\alpha_{ki}^{''}} \tag{1.11}$$

where k_{fi} and k_{bi} are the forward and backward rate for the reaction i.
Eq. 1.10 is valid under the hypothesis of mass-action kinetic and when the mechanism is written in term of elementary reactions.
The forward rate constant k_{fi} is usually expressed as a temperature-depended modified Arrhenius function:

$$k_{fi} = A_i T^{\beta_i} \exp\left(\frac{-E_a^i}{RT}\right) \tag{1.12}$$

where A_i is the pre-exponential factor, E_a^i is the activation energy and in the modified Arrhenius law a temperature exponent β_i is added. The term AT^{β} is the frequency factor and it accounts for the effect of the molecules size while

the exponential part specifies the fraction of collision that have energy level greater than the threshold activation energy E_a.
For a given chemical reaction, the Arrhenius parameters are neither functions of the concentrations nor functions of temperature (Kuo 2005).
For the ith reaction, the equilibrium constant relates k_{bi} to k_{fi} as:

$$k_{bi} = \frac{k_{fi}}{K_{eq,i}} \tag{1.13}$$

The equilibrium constant is calculated from the knowledge of species thermodynamic properties defined in Sec. 1.2.1, as follows:

$$K_{eq,i} = K_{pi} \left(\frac{P_{atm}}{RT} \right)^{\sum_{k=1}^{N_s} \alpha_{ki}} \qquad with \quad K_{pi} = \exp\left(\frac{\Delta S_i}{R} - \frac{\Delta H_i}{RT} \right) \tag{1.14}$$

Δ refers to the change in standard thermodynamic properties along the reaction i.
In elementary kinetic, species concentration reaction orders are assumed equal to the species stoichiometric coefficients ($\alpha^{'}_{ki}$ and $\alpha^{''}_{ki}$). Arbitrary reaction orders are sometimes specified, to represent global reactions. In this case, the species concentration proportionality follows an arbitrary reaction order concentration and q_i is rewritten as:

$$q_i = k_{fi} \prod_{k=1}^{N_s} [X_k]^{F_k^i} - k_{bi} \prod_{k=1}^{N_s} [X_k]^{R_k^i} \tag{1.15}$$

Using arbitrary reaction orders, a constraints between the forward F_k^i and the backward R_k^i coefficients must be fulfilled to ensure that equilibrium elementary kinetic is not modified. In fact, at equilibrium, according to elementary kinetic the condition $q_i = 0$ have to be fulfilled. This condition is ensures only if:

$$\frac{k_{bi}}{k_{fi}} = \prod_{k=1}^{N_s} [X_k]^{\alpha^{'}_{ki} - \alpha^{''}_{ki}} = \prod_{k=1}^{N_s} [X_k]^{F_k^i - R_k^i} \tag{1.16}$$

As consequence, in the case of arbitrary defined reaction order are used, the proper equilibrium behaviour is retrieve, if:

$$F_k^i - R_k^i = \alpha^{'}_{ki} - \alpha^{''}_{ki} \quad for \quad (k = 1, ..., N_s) \tag{1.17}$$

In an hydrocarbon oxidation process, some reactions require a third body to proceed. In this case, the third body concentration explicitly appears in the expression of the rate-of-progress q_i (Kee et al. 1989).

Some reactions exhibit dependency from pressure. In this case, the reaction rate is increased (unimolecular/recombination fall-off reactions) or decreased (chemically activated bimolecular reactions) with increasing pressure (Kee et al. 1989).
The reaction rate parameters detailed above along with species themodynamic properties, presented in Sec. 1.2.1 are used for the generation of detailed thermo-kinetic databases (Kee et al. 1989).

1.3 Governing transport equations

In addition to thermodynamic species properties and chemical kinetics, the solution of a combustion process, involves the knowledge of the flow conditions. For that purpose, the interaction between the flow governing equations and combustion chemistry must be described.
For a reactive gas, the derivation of the conservation equations must consider the presence of N_s species that can be transformed each other releasing heat.
The governing equations for continuity, momentum and energy, classically used in fluid mechanics, must be coupled to transport equations for scalars that track the reactivity of the system.
The transported scalars usually coincide with all the species involved in the chemistry mechanism plus the energy. Then, the number of scalar transport equations in the flow solver is equal to $N_s + 5$ (3 for momentum, 1 for mass and 1 for energy).
The general governing equations are presented in the following sections, using Einstein notation.

1.3.1 Mass

The continuity or mass equation is:

$$\frac{\partial \rho}{\partial t} + \frac{\partial}{\partial x_i}(\rho u_i) = 0 \tag{1.18}$$

u_i is the the ith velocity component and ρ is the mixture density. In a combustion process, the density is not constant and it is related to temperature pressure and composition through the EOS that for ideal gases has the formulation expressed in 1.1.

1.3.2 Momentum

The flow field, through the velocity components u_i, is the solution of the momentum equation:

$$\frac{\partial \rho u_i}{\partial t} + \frac{\partial}{\partial x_i}(\rho u_i u_j) = -\frac{\partial p}{\partial x_i} + \frac{\partial \tau_{ij}}{\partial x_i} + F_i \tag{1.19}$$

p is the static pressure, F_i represents the body forces and τ_{ij} is the viscous stress tensor:

$$\tau_{ij} = \mu \left(\frac{\partial u_i}{\partial x_j} + \frac{\partial u_j}{\partial x_i} - \frac{2}{3}\delta_{ij}\frac{\partial u_k}{\partial x_k} \right) \tag{1.20}$$

μ is the dynamic viscosity and δij is Kronecker symbol[2].

1.3.3 Energy

The energy balance equation can be expressed by using multiple formulations, as detailed in Poinsot and Veynante (2005). In the present thesis work, the balance equation for total enthalpy h (chemical plus sensible), as defined in Eq.1.4, is detailed. In all the multi-species computations that are performed in the following chapters, the total enthalpy balance equation (or equivalently the sensible enthalpy) is considered.
The balance equation for enthalpy h is written as:

$$\frac{\partial}{\partial t}(\rho h) + \frac{\partial}{\partial x_i}(\rho u_i h) = -\frac{\partial f_i}{\partial x_i} + \tau_{ij}\frac{\partial u_i}{\partial x_j} \tag{1.21}$$

and it can be rewritten in term of sensible enthalpy h_s as:

$$\frac{\partial}{\partial t}(\rho h_s) + \frac{\partial}{\partial x_i}(\rho u_i h_s) = -\frac{\partial f_i}{\partial x_i} + \tau_{ij}\frac{\partial u_i}{\partial x_j} + \dot{\omega}_T \tag{1.22}$$

The diffusive heat fluxes f_i include the following terms:

$$q_i = -\lambda\frac{\partial T}{\partial x} + \rho\sum_{k=1}^{N_s} h_k Y_k V_{k,i} \tag{1.23}$$

The first term is the heat diffusion expressed through the Fourier's Law, while the second is the heat transfer associated with diffusion of species.
$\dot{\omega}_T$ is the heat released from the combustion proces:

$$\omega_T = \sum_{k=1}^{N_s} \Delta h^0_{f,k}\dot{\omega}_k \tag{1.24}$$

The term $\tau_{ij}\partial u_i/\partial x_j$ describes frictional heating. It is usually neglected in combustion application at low speed (low-Mach flames).

---

[2] δ_{ij}=1 if $i = j$ and 0 otherwise.

1.3.4 Species

A balance equations for the mass fraction of each species k, involved in the combustion process, is written:

$$\frac{\partial}{\partial t}\left(\rho Y_k\right) + \frac{\partial}{\partial x_i}\left(\rho u_i Y_k\right) = -\frac{\partial}{\partial x_i}\left(\rho V_{k,i} Y_k\right) + \dot{\omega}_k \tag{1.25}$$

$V_{k,i}$ is the diffusion velocities of the species k in the i^{th} direction and $\dot{\omega}_k$ is the chemical source term, computed as in Eq. 1.9.
By definition:

$$\sum_{k=1}^{N_s} Y_k V_{k,i} = 0 \quad and \quad \sum_{k=1}^{N_s} \dot{\omega}_k = 0 \tag{1.26}$$

The molecular transport process that causes the diffusive species fluxes is a complex phenomenon that involves the kinetic theory of gases for the computation of binary diffusion coefficients D_{kj}.
A full description of the complex species diffusion, can be found in Williams (1985) and in Ern and Giovangigli (1994).
In CFD codes the diffusion velocities is usually closed using an equivalent diffusion coefficient D_k for each species describing the diffusion of the species k in the rest of the mixture. One possibility is to use the Hirschfelder and Curtiss approximation (Hirschfelder et al. 1954) in which the diffusion velocity is expressed using the following formulation:

$$V_{k,i} = -\frac{D_k}{X_k}\frac{\partial X_k}{\partial x_i} \quad with \quad D_k = \frac{1 - Y_k}{\sum_{j \neq k} X_j / D_{jk}} \tag{1.27}$$

The Hirschfelder and Curtiss approximation does not respect the mass conservation (Eq. 1.18). In order to retain this approximation, the correction velocity V_c is added (Poinsot and Veynante 2005) and the species diffusion term reads:

$$\rho V_{k,i} Y_k = \rho\left(-D_k \frac{W_k}{W}\frac{\partial X_k}{\partial x_i} + Y_k V_i^c\right) \quad with \quad V_i^c = \sum_{k=1}^{N_s} D_k \frac{W_k}{W}\frac{\partial X_k}{\partial x_i} \tag{1.28}$$

The mixture-averaged Hirschfelder and Curtiss approximation is used in this thesis to conduct 1-D detailed chemistry calculations with REGATH (REal GAs THermodynamics) solver and in the 2-D detailed chemistry done with laminarSMOKE.
It is possible to express the mixture-averaged approximation through a Fick's law. In this case, the diffusion velocity is assumed to be proportional to the

species mass fraction gradient:

$$\rho V_{k,i} Y_k = \rho \left(-D_k \frac{\partial Y_k}{\partial x_i} + Y_k V_i^c \right) \quad with \quad V_i^c = \sum_{k=1}^{N_s} D_k \frac{\partial Y_k}{\partial x_i} \tag{1.29}$$

The effective diffusion coefficient D_k is calculated by using either binary diffusion coefficients 1.27, 1.28 or by using simplified approaches through the knowledge of the dimensionless species Lewis number Le_k and mixture averaged properties:

$$D_k = \frac{D_{th}}{Le_k} \quad with \quad D_{th} = \frac{\lambda}{\rho c_p} \quad with \quad \lambda = \frac{\mu c_p}{Pr} \tag{1.30}$$

Where D_{th} is the thermal diffusion coefficient, c_p is the mixture massic heat capacity, λ and μ respectively the thermal mixture conductivity and mixture viscosity. Pr is the Prandtl number for the mixture. Species Lewis number and Prandtl number slightly changes across the flame front (Poinsot and Veynante 2005) justifying the assumption of retaining constant values. This approach is currently used to capture preferential diffusion effects at reduced computational cost in skeletal and analytically reduced chemistry (Jaravel 2016).
A more simple approach is to assume unity Lewis number and as consequence the species diffusion coefficients are all equal to the thermal one. This simplified approach is employed in the current thesis for the virtual chemistry calculations both for 1D-laminar flames and 3D-turbulent ones.

1.4 Turbulent combustion

1.4.1 Numerical solution of turbulent flows

Industrial flames are usually stabilized using turbulent flows. Turbulent flames allow to increase the volumetric energy density of a system in comparison with laminar ones. For turbulent flows, the numerical solution of the governing balance equations, presented in the previous section, is achieved according to one of the three following strategies (Versteeg and Malalasekera 2007; Pope 2000; Echekki and Mastorakos 2010):

- Reynolds averaged Navier Stokes (RANS) (Launder and Spalding 1983). The balance equations are formulated for the time mean flow quantities. The effect of the turbulence on the mean flow quantities is modeled over the whole energy turbulent spectrum.
- Large Eddy Simulations (LES) (Pope 2000; Sagaut 2006). A spatial filter (box, Gaussian etc.) of size Δ is introduced and applied to the instantaneous flow quantities. The larger turbulent eddies are explicitly resolved whereas the effect of smaller ones on the filtered quantities is modeled.

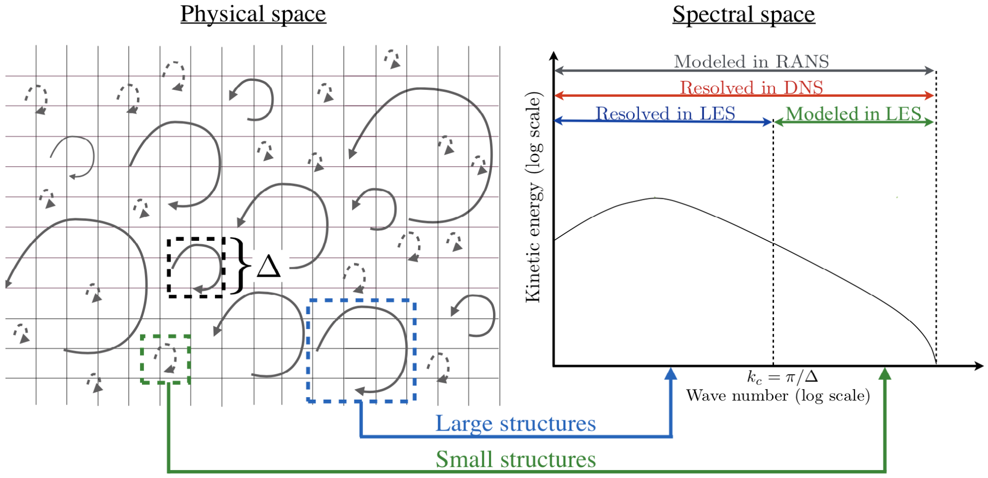

Figure 1.3: *RANS, LES and DNS are summarized in terms of modeled and solved turbulent eddies in spectral and physical space when homogeneous and isotropic turbulence is considered. Δ is the LES filter that correspond to the cut-off wave number k_c in the spectral space. The figure is reproduced from Mercier (2015).*

A cut-off wave number k_c corresponding to the filter size Δ can be also introduced.

- Direct Numerical Simulation (DNS) (Leonard and Hill 1988). The Navier-Stokes equations are solved without any mean and filter operation for the flow variables. In DNS, the whole turbulent energy spectrum is solved. Grid size Δ_x, of the order of the Kolmogorov scale have to be utilized (Pope 2000) to solve the smallest vortex.

Figure 1.3 summarizes the properties of RANS, LES and DNS in terms of solved and modeled turbulent energy in physical and spectral space.

Going from RANS to DNS, the CPU cost associated with the numerical simulation enormously increases because smaller grids size are needed. The CPU cost for a 3-D simulation scales at least with a factor of 16 reducing the grid size by 2, if a fixed Courant number is considered.

DNS is still out reach in term of CPU cost for large scale combustion applications.

In the recent years, due the enormous increase of CPU power, LES is replacing quickly RANS in the simulation of industrial burners, especially for aeronautical applications. LES in comparison to RANS has the advantage to solve most of the turbulent kinetic energy that is associated to the largest vortex (Pope 2000). Furthermore, in combustion applications, LES allows to identify the instantaneous location of cold and burnt gases giving a finer description of the turbulence/flame interactions and species formation (Veynante and Knikker 2006; Poinsot and Veynante 2018). In the present work, the LES approach is retained for the turbulent flame simulations presented in Part III.

1.4.2 Large Eddy Simulation

1.4.2.1 LES quantities

LES provides the resolved space-filtered contribution of the mass, momentum and energy and species fields. Considering an unsteady scalar quantity Q in a reactive flow, the LES space-filtered contribution, denoted by $\overline{Q}$ is obtained by applying a spatial filter G to the scalar Q:

$$\overline{Q} = \int_{-\infty}^{+\infty} Q(\mathbf{x}', t) G(\mathbf{x} - \mathbf{x}') d\mathbf{x}' \tag{1.31}$$

The LES filter G, having characteristic size Δ, is either a box or a Gaussian filters (Poinsot and Veynante 2005). For variable density flows (as in combustion) the filtered balance equations are simplified using the Favre spatial filter or mass-weighted spatial filter (Veynante and Knikker 2006):

$$\widetilde{Q} = \frac{\overline{\rho Q}}{\overline{\rho}} \tag{1.32}$$

1.4.2.2 LES statistics

The LES spatially filtered quantities cannot be directly compared to experimental data (Pope 2004) and time statistical quantities (averaged and resolved variance) are usually considered (Pope 2004). The time or ensemble average of $\widetilde{Q}$ and the corresponding resolved variance are expressed as (Vervisch et al. 2010):

$$\left\langle \widetilde{Q} \right\rangle = \frac{1}{\Delta t} \int_{0}^{\Delta t} \widetilde{Q}(\mathbf{x}, t) dt \tag{1.33}$$

$$\left\langle \widetilde{Q} \right\rangle_{rms} = \sqrt{\left\langle \widetilde{Q}^2 \right\rangle - \left\langle \widetilde{Q} \right\rangle^2} \tag{1.34}$$

$\left\langle \widetilde{Q} \right\rangle$ and $\left\langle \widetilde{Q} \right\rangle_{rms}$ are usually known as Reynolds statistics.
Similarly to Reynolds temporal statistics, the mass weighted time average of $\widetilde{Q}$ and the corresponding resolved variance can be also introduced:

$$\left\{ \widetilde{Q} \right\} = \frac{\left\langle \overline{\rho} \widetilde{Q} \right\rangle}{\left\langle \overline{\rho} \right\rangle} \tag{1.35}$$

$$\left\{\widetilde{Q}\right\}_{rms} = \sqrt{\frac{\left\langle\overline{\rho}\widetilde{Q}^2\right\rangle}{\langle\overline{\rho}\rangle} - \left(\frac{\left\langle\overline{\rho}\widetilde{Q}\right\rangle}{\langle\overline{\rho}\rangle}\right)^2} \tag{1.36}$$

$\left\{\widetilde{Q}\right\}$ and $\left\{\widetilde{Q}\right\}_{rms}$ are usually known as Favre temporal statistics. In the present work, Reynolds and Favre statistics are compared to experiments for the turbulent flames numerically investigated in Part III.

1.4.3 Filtered balance equations

Applying the Favre spatial filter to the system of governing equations presented in Sec. 1.3 the following set of filtered balance equations is obtained:

$$\frac{\partial\overline{\rho}}{\partial t} + \frac{\partial}{\partial x_i}\left(\overline{\rho}\widetilde{u}_i\right) = 0 \tag{1.37}$$

$$\frac{\partial\overline{\rho}\widetilde{u}_i}{\partial t} + \frac{\partial}{\partial x_i}\left(\overline{\rho}\widetilde{u}_i\widetilde{u}_j\right) = -\frac{\partial\overline{p}}{\partial x_i} + \frac{\partial}{\partial x_i}\overline{\rho}\left(\widetilde{u_i u_j} - \widetilde{u}_i\widetilde{u}_j\right) - \frac{\partial\overline{\tau_{ij}}}{\partial x_i} + \overline{F_i} \tag{1.38}$$

$$\frac{\partial}{\partial t}\left(\overline{\rho}\widetilde{h}\right) + \frac{\partial}{\partial x_i}\left(\overline{\rho}\widetilde{u}_i\widetilde{h}\right) = -\frac{\partial\overline{q_i}}{\partial x_i} - \frac{\partial}{\partial x_i}\left(\overline{\rho}\left(\widetilde{hu_i} - \widetilde{h}\widetilde{u}_i\right)\right) \tag{1.39}$$

$$\frac{\partial}{\partial t}\left(\overline{\rho}\widetilde{Y_k}\right) + \frac{\partial}{\partial x_i}\left(\overline{\rho}\widetilde{u}_i\widetilde{Y_k}\right) = -\frac{\partial}{\partial x_i}\left(\overline{\rho V_{k,i} Y_k}\right) - \frac{\partial}{\partial x_i}\left(\overline{\rho}\left(\widetilde{Y_k u_i} - \widetilde{Y_k}\widetilde{u}_i\right)\right) + \overline{\dot{\omega}}_k \tag{1.40}$$

The filtering operation leads to the generation of sub-grid unclosed terms:

- **Reynolds stresses tensor**: $\overline{\rho}\left(\widetilde{u_i u_j} - \widetilde{u}_i\widetilde{u}_j\right)$
- **species and enthalpy enthalpy turbulent fluxes**: $\overline{\rho}\left(\widetilde{Y_k u_i} - \widetilde{Y_k}\widetilde{u}_i\right)$ and $\overline{\rho}\left(\widetilde{hu_i} - \widetilde{h}\widetilde{u}_i\right)$.
- **Filtered laminar diffusive fluxes for species and sensible enthalpy**: $\overline{\rho V_{k,i} Y_k}$ and $\overline{q_i}$
- **Filtered chemical source terms**: $\overline{\dot{\omega}}_k$

The Reynolds stresses tensor is closed with the Boussinesq assumption while the sub-grid laminar and turbulent fluxes are closed with gradient assumption as detailed in Poinsot and Veynante (2005). Instead, the strategy to close the chemical source term depends on turbulent combustion modeling approach.

1.4.4 Turbulent combustion modeling in LES

LES is nowadays a key tool to predict the efficiency of industrial combustion chambers. However, despite the tremendous progress in supercomputing, grids used in practical industrial configurations remain typically coarser than the flame thickness and small scale flame wrinkling patterns. Consequently chemical species cannot be resolved and subgrid scale models are needed for the flame structure and its interactions with the turbulence. As discussed in the recent review of combustion chemistry modeling (Fiorina et al. 2015), different methods have been developed to model, at reduced CPU cost, the instantaneous chemistry reactive layer. This challenging aspect will be addressed in the next Chapter. In addition, dedicated models are required to properly describe the interaction between combustion chemistry and sub-grid turbulent flows motions. In the literature, three approaches are identified for such purpose (Veynante and Vervisch 2002; Fiorina et al. 2015; Poinsot and Veynante 2018):

1. **Turbulent mixing** approach. It is assumed that the turbulence is the limiting process having a characteristic time scale τ_t larger than the chemistry one τ_c. The filtered reaction rate is expressed through algebraic relations and it is assumed proportional to the turbulent mixing (Magnussen and Hjertager 1977; Magnussen 1981), expressed in term of scalar dissipation rate of progress variable or mixture fraction. Introducing the Partially Stirred Reactor (PaSR) model (Chomiak 1990), more advanced expressions (Kärrholm 2008) have been recently proposed to relate the filtered species source term to the chemistry and turbulence time scales. Originally developed for RANS, turbulent mixing models have been recently extended to LES, demonstrating their applicability to MILD combustion applications (Li et al. 2019).
2. **Statistical** approach. A Probability Density Function, named PDF (Pope 1985) or Filtered Density Function (FDF) in LES context (Haworth 2010), is used to establish a one-point statistical relation for each transported scalar. The filtered density function is either presumed from the first moments of selected resolved quantities or calculated as a solution of a balance equation for each scalar. Despite the accuracy, transported FDF methods imply a very high CPU cost and further modeling assumptions for unclosed terms that appears in the FDF transport equations (Raman et al. 2005). Several statistical approaches have been successfully used in the LES context either presuming the FDF function (generally by using a β function) (Cook and Riley 1994; Navarro-Martinez et al. 2005; Ihme and Pitsch 2008) or more recently by transporting it (Raman et al. 2005; Wang and Pope 2011; Rieth et al. 2019).
3. **Geometrical** approach. The flame front is described as a certain entity (iso-surface) propagating from fresh to burnt gases. One approach is the G-equation model (Kerstein et al. 1988) that consists in describing the flame as an infinitely thin propagating surface. Another approach consists

in the direct resolution of the flame reactive layer by:

- artificially thickening the flame front leading to the Thickened Flame model for LES (TFLES) (Colin et al. 2000a)
- explicitly filtering the flame front in the physical space leading to the Filtered-Tabulated Chemistry for LES (F-TACLES) (Fiorina et al. 2010).

The TFLES model is used in the present work to describe the turbulence flame interaction and to deal with the LES under-resolution of the flame front. It is used in combination with both FPI-tabulated chemistry and with virtual transported chemistry in Part III.

TFLES model TFLES is nowadays considered a reliable and robust approach for turbulent combustion modeling. Indeed, it has been successfully applied to complex laboratory scale burners (Ketelheun et al. 2013) (Proch et al. 2017), semi-industrial burners (Benard et al. 2018) (Proch and Kempf 2015) and aeronautical chambers (Felden et al. 2018) (Jaravel et al. 2017) (Lancien et al. 2019).

Typical LES grid ($\Delta_x \approx 0.2 \div 1$ mm) cannot resolve with a sufficient number of mesh points the flame front and intermediate species. TFLES model (Colin et al. 2000a) artificially thickens the flame front to ensure its proper resolution. The diffusion coefficient and the source term of the species equations are respectively multiplied and divided by the thickening factor F. According to the theoretical analysis valid for premixed flame, the laminar flame consumption speed S_l^0 and the thermal flame thickeness δ_l^0 are related to the thermal diffusivity D and to the mean reaction rate $\bar{\dot{\omega}}$:

$$S_l^0 = \sqrt{D\bar{\dot{\omega}}} \tag{1.41}$$

$$\delta_l^0 = \frac{D}{S_l^0} \tag{1.42}$$

As consequence, applying the flame thickening procedure, to the species and enthalpy equations, the flame thickness is enlarged by a factor F while the flame propagate at the same S_l^0.

However, the flame thickening introduces a modification of the interaction between chemistry and turbulence: by increasing the flame thickness to $F\delta_l^0$, the flame becomes less wrinkled and the turbulent flame speed S_T is reduced. Indeed the thickening operation makes the flame insensitive to turbulent eddies smaller than $F\delta^0$ and less sensitive to the larger ones. To compensate this effect, a subgrid scale wrinkling factor Ξ_Δ is introduced in the equations. Applying a uniform thickening factor, the TFLES filtered Favre balance equation for the k^{th} species mass fraction is expressed as (Colin et al. 2000a):

$$\frac{\partial \overline{\rho}\widetilde{Y_k}}{\partial t} + \frac{\partial}{\partial x_i}\left(\overline{\rho}\widetilde{u_i}\widetilde{Y_k}\right) = \frac{\partial}{\partial x_i}\left(\overline{\rho}F\Xi_\Delta\overline{D_k}\frac{\partial\widetilde{Y_k}}{\partial x_i}\right) + \frac{\Xi_\Delta\widetilde{\dot{\omega}_{Y_k}}}{F} \tag{1.43}$$

The subgrid scale wrinkling Ξ_Δ is usually formulated using algebraic expressions (Charlette et al. 2002a; Colin et al. 2000a; Pitsch and De Lageneste 2002), assuming equilibrium conditions between the flame surface density and subgrid turbulence. But this situation is not always achieved especially during the early stages of flame developments (Richard et al. 2007; Veynante and Moureau 2015). To overcome this limitation, dynamic models have been recently designed (Wang et al. 2011; Wang et al. 2012; Volpiani et al. 2016) using Germano-like identities (Germano et al. 1991) to evaluate on-the-fly the controlling parameter of the wrinkling factor.

To avoid an increase of the diffusive fluxes in mixing controlled regions, the thickening operation is dynamically applied only in the flame reactive layer (Legier et al. 2000). The instantaneous flame position is identified by the use of a flame sensor Γ, which equals 1 in the flame front, and 0 elsewhere. Several formulations for the flame sensor have been proposed in the literature: based on the scalar source term (Legier et al. 2000; Franzelli et al. 2013), progress variable gradient (Proch and Kempf 2014) or profile (Durand and Polifke 2007). Chap. 6 gives further details about the dynamic TFLES model and its coupling with virtual and with tabulated chemistry.

Chapter 2

State of the art: combustion chemistry modeling

Contents

Combustion chemistry description is a complex task because it involves a high number of species and reactions that cover a large range of spatial and time scales. Detailed chemistry mechanisms tend to include as much as possible species and elementary reactions to accurately describe the combustion process in multiple operating conditions. But, due to the high number of species and reactions, detailed chemistry mechanisms, are only suitable to perform 0-D reactors and 1-D flame archetypes simulations. Instead, in 3-D large scale computations, to overcome the computational burden, reduced order chemistry models are employed. A brief review of the most used literature reduced order chemistry models is proposed in the present chapter. In particular, global mechanism, tabulated chemistry and systematically reduced mechanisms (skeletal and analytical) are described. The suitability of the various strategies to describe multi-mode and complex combustion regimes is also discussed.

2.1 Introduction

Turbulent combustion simulation needs the introduction of a combustion chemistry model to have access to global flame quantities, temperature and species concentration. For that purpose, the most accurate strategy would consist of the direct inclusion of a detailed chemistry mechanism in the numerical simulation. This choice would include in the flow solver a transported scalar equation for each species in the mechanism, according to the formalism presented in Sec. 1.3.

Unfortunately, this chemistry modeling route cannot be usually afforded for CPU reasons and the only practical solution is to employ reduced order chemistry models.

The choice of the combustion chemistry model directly influence the type of scalars that are transported in the flow solver and the way the scalars source term is computed. For example, in tabulated chemistry techniques, all the thermochemical quantities are tabulated as function of a reduced set of scalars: only the reduced scalars, which coincide with the table dimensions, are transported in the flow solver. On the contrary when a reduced chemistry mechanisms is used, the reduced number of species are transported in the flow solver and the species source term are instantaneously computed using Arrhenius law or analytic laws.

The current chapter gives a short state-of-the art of the most common literature strategies used to model combustion chemistry in LES.

2.2 Detailed chemistry

Detailed thermo-chemistry databases reproduce the oxidation process of hydrocarbon fuels including as much as possible of elementary reactions and species

(Curran et al. 1998).

Thermodynamic species properties and elementary reactions kinetic rate parameters are usually derived either from measurements or from previous literature studies. (Miller et al. 1990; Westbrook et al. 2011).

In a second step, on the basis of sensitivity analysis, they are adjusted to match a large variety of experimental targets such as ignition delay times, flame speeds and species profiles for a series of canonical flame configurations (jet-stirred reactors and 1-D flames) (Frenklach et al. 1992). Another promising approach is to derive the reactions rate constants directly from theoretical studies (Cavallotti et al. 2007; Aguilera-Iparraguirre et al. 2008) using quantum chemistry computations.

Detailed kinetic mechanisms are designed to have access to a fine description of the flame chemical reactive layer, in a wide variety of operating condition: temperature, pressure, mixture composition and flame regimes (Mehl et al. 2011). The effort made by the combustion kinetic research community allows today to have access to detailed kinetic databases, valid for a large variety of hydrocarbon fuels and wide operating conditions (Curran 2018).

The direct inclusion of detailed kinetic in numerical simulations of flames would allow the accurate modeling complex phenomena that are of paramount importance for modern combustion devices:

- Flame heat release and temperature profile, to correctly retrieve the thermal power released by the flame and the instantaneous flame positioning in the burner.
- Extinction and reignition phenomena, that can be caused by low temperature effects or by flame strain.
- Pollutants formation, that is strongly dependent on the operating conditions and from the flame regime.

As anticipated in the introduction, despite the availability of comprehensive detailed reaction mechanisms their applicability to large scale simulation is nowadays limited and complex (Lu and Law 2009). In fact, except for very simple combustion systems (Echekki and Chen 2003), detailed mechanisms, especially for heavier fuels, are too CPU expensive in 3-D LES for several reasons.

The first reason that makes detailed chemistry not directly applicable to large scale simulations in the enormous number of species and reactions that are involved in the mechanism (Lu and Law 2009). For each species involved in the mechanism a scalar must be transported in the flow solver following the formalism expressed in Sec. 1.3.4, while increasing the number of reactions, the size of the reaction matrix grows.

Figure 2.1, reproduced from Curran (2018), is an updated version of the one presented by Lu and Law (2009) and by Egolfopoulos et al. (2014). It shows the size of the most used detailed chemistry mechanisms for typical hydrocarbon fuels. The mechanisms are sorted on the base of the included number of species and reactions.

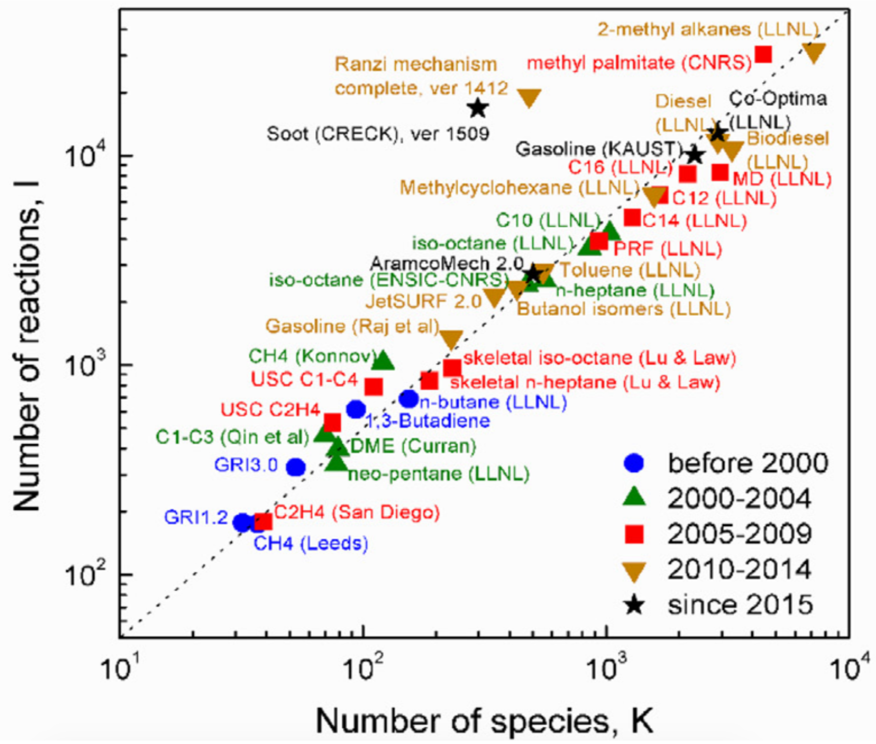

Figure 2.1: *Size of selected detailed mechanisms for the most common hydrocarbon fuels. The mechanisms are positioned in the graph according with the included number of species and reactions. The figure is reproduced from Curran (2018)*

It can be observed that: *i)* mechanisms for C1 and C2 species already include hundred of species and a few hundreds of reactions and *ii)* the size of the mechanisms tremendously increase if heavier hydrocarbons are considered (Dagaut et al. 2014).
The second reason that complicates the inclusion of detailed chemistry in large scale simulations is the large time scales range associated with species formations and/or destruction. The fastest species can feature, in some operating conditions, a destruction time scale that is of the order of 10^{-9} s (Lu et al. 2009), whereas for an LES low Mach solver the typical flow time step is of the order of 10^{-6} s. This makes the detailed kinetic system stiff because fast radicals are rapidly produced or depleted in comparison with other species and in comparison with the convective time step. As consequence, dedicated and CPU costly implicit algorithms must be used to overcome this numerical difficulty.
The third issue, that limits the direct inclusion of detailed chemistry, is related to the coupling of the whole set of species with the turbulent combustion model. Different species feature a large variety of spatial scales. The turbulent combustions model must ensures that all of them are sufficiently resolved on the LES grid to avoid numerical problems.

Detailed chemical mechanisms are easily used to carry-out 0-D reactors and 1-D flame simulations. They are also used in the literature to perform 2-D laminar flame computations, to validate their capability to predict pollutants versus experimental data (Cuoci et al. 2013a; Jin et al. 2015). Instead, the direct crude application, without any type of reduction, of detailed chemistry mechanisms to 3-D turbulent flame simulations is still out of reach for the reasons explained above.

Methane/Air detailed mechanisms GRI-3.0 mechanism (Smith et al. 2011) is a reference detailed mechanism for methane-air oxidation largely used in the literature. It is an optimized mechanism, designed to provide sound basic kinetics, including NO formation and re-burn chemistry. Recently other detailed mechanisms have been developed for methane combustion: for example, the Polimi CRECK mechanism (Ranzi et al. 2012) and the Aramco mechanism (Metcalfe et al. 2013). Typically, mechanisms developed for small hydrocarbon (C_0-C_4) constitute the core for larger hydrocarbon mechanisms (Curran 2018). In this thesis work the results achieved by chemical kinetic modelers will not be discussed but rather assumed as the reference solution to reproduce. The widely used GRI-3.0 mechanism (Smith et al. 2011) is retained as reference.

2.3 Overview on the reduced order models

A review of the most commonly used strategies, to include combustion kinetics, at reduced CPU cost, in numerical simulation of large scale combustion chambers, have been proposed by Fiorina et al. (2015). Recently, an updated state-of-the-art has been also suggested (Fiorina 2019).

Figure 2.2 (Fiorina 2019) shows the main paths that are currently used to derive reduced order models for combustion chemistry description in LES. According to Fiorina (2019), three main routes may be identified:

- **Systematically reduced chemistry**
- **Tabulated chemistry**
- **Optimized chemistry**

Each of the three strategies is characterized by multiple and combined approaches, as described in the following sections. Two of the three routes listed above are sometimes also combined in the literature. An example of hybrid methods has been proposed by Ribert et al. (2014) tabulating fast intermediate species using their self-similar properties while major species are transported in the flow solver. Recently, another hybrid method that combines systematically reduced chemistry and optimization of reaction rate parameters, has been also proposed by Jaouen et al. (2017).

The *virtual chemistry* method, introduced for the first time by Cailler et al. (2017), is also reported among the modeling approaches that make use of op-

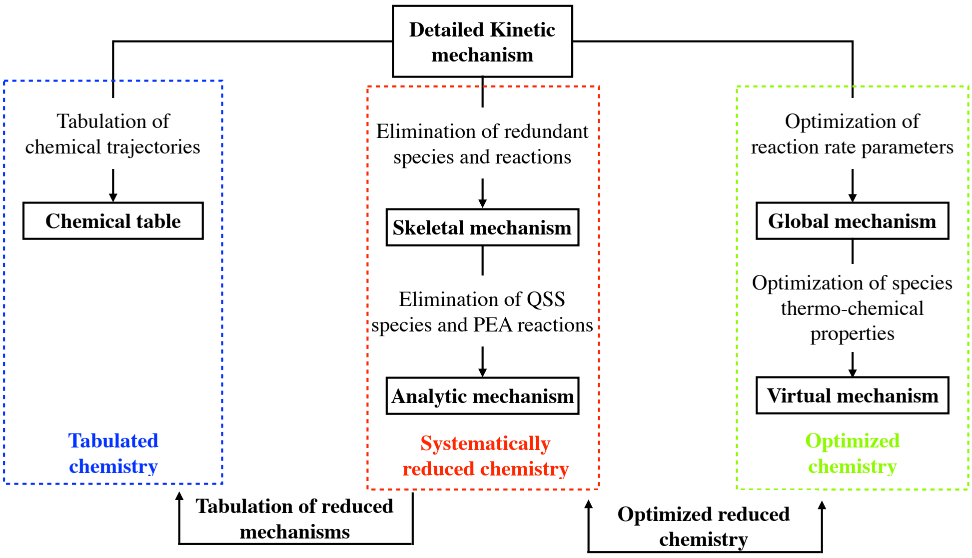

Figure 2.2: *Major routes employed to reduce chemistry for Large Eddy Simulation applications. The scheme is reproduced from Fiorina (2019).*

timization strategies to derive the reduced chemistry model. Being the main topic of the current thesis, virtual chemistry is presented in detail in the next chapter (Chap. 3).

2.4 Systematically reduced chemistry

Systematically reduced mechanisms are derived from reference detailed mechanisms with the aim of reducing the level of complexity associated with chemistry solution. The principal idea is to preserve the main reaction pathways present in the former mechanism, reducing the number of species and reactions and removing the numerical stiffness.

At the end of the simplification process, reduced mechanisms are able to reproduce a certain number of flame quantity of interests (fresh gases temperature, flame speed, ignition delay time, species etc.) for an a-priori chosen range of operating conditions (initial temperature, pressure, equivalence ratios etc.). The comprehensiveness of a reduced mechanism cannot exceed the one of the detailed mechanism from which it is reduced.

The strength of the systematically reduced chemistry approaches is the preservation of the theoretical basis of detailed chemistry: the reaction formalism and the major reaction paths of the detailed mechanism are preserved. In addition, for analytical mechanisms, some ordinary differential equations can be replaced by algebraic ones to further reduce the CPU cost.

The derivation of an analytical reduced mechanism usually consists in two main reduction steps:

- **Skeletal reduction**: species and reactions that are judged unimportant are removed from the former detailed mechanism.
- **Analytic reduction**: a process of stiffness and species removal is applied to the reduced skeletal mechanism, deriving algebraic equations to calculate the concentration of minor species. This step is conducted using QSS (Quasi Stady State) approximation and PE (Partial Equilibrium) assumption.

Skeletal mechanisms may also be directly employed in LES before dimension reduction. However, they still imply an high CPU cost because the species to transport are numerous and some of them induce high numerical stiffness. Consequently, their application to LES computations is still restricted to academic flame configurations (Mukhopadhyay and Abraham 2012; Salehi et al. 2017).

2.4.1 Skeletal reduction

Skeletal reduction consists in removing unimportant species and reactions from the detailed mechanism. It is the most suitable technique to be applied as first reduction step (Lu and Law 2005).

The removal of unimportant species and reactions is usually achieved using different reduction techniques:

- **Graph based methodologies** (Lu and Law 2005)
- **Jacobian-based methodologies** (Tomlin et al. 1997)
- **Lumping** (Ranzi et al. 2001)

The three strategies may also be used in combination, as discussed by Lu and Law (2009).

2.4.1.1 Graph based methodologies

Directed Relation Graph (DRG) was introduced for the first time by Lu and Law (2005). According to the DRG method, a reaction graph is established to describe the interaction between the species involved in a detailed mechanism, reporting the respective interaction magnitude.

Two nodes of the graph, representing the species of the mechanism, are connected each other only if they interact in one reaction at least.

An edge, connecting two nodes, quantifies the contribution of one species to the formation of another one. The magnitude of the contribution is quantified through a normalized interaction coefficient r_{AB}:

$$r_{AB} = \frac{\sum_{i=1}^{N_r} |\alpha_{A,i} q_i \delta_{B,i}|}{\sum_{i=1}^{N_r} |\alpha_{A,i} q_i|} \tag{2.1}$$

$\delta_{B,i}$ is equal to 1 if the species B is involved in the ith reaction and it is equal to 0 otherwise. $\alpha_{A,i}$ is the A species stoichiometric coefficient in the i^{th} reaction.

r_{AB} represents the contribution of species B to the total production rate of the species A.

If the coefficient r_{AB} is lower than a certain threshold, the dependency can be considered negligible and consequently the edge is removed from the graph. To remove edges from the graph, a parameter ε is introduces which represents the accuracy chosen for the final skeletal mechanism.

At the beginning of the procedure, the set of important species are identified: for example fuel, oxidizer and pollutant species. Then, the interaction coefficients are evaluated and after choosing the accuracy ε the DRG is constructed representing a directed edge A→B if and only if $r_{AB} > \varepsilon$. Consequently, the species that does not affect the production of the important species are immediately identified and eliminated from the mechanism.

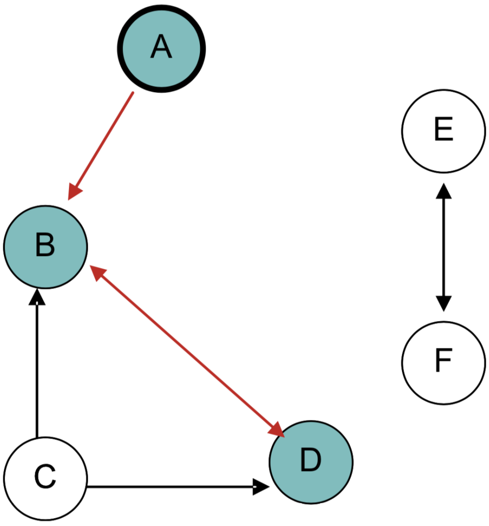

Figure 2.3: *Schematic view of a reaction graph portion after applying the DRG procedure. The nodes correspond to species, while, the edges correspond to normalized interaction coefficients greater than the chosen threshold ε. The figure is reproduced from Lu and Law (2009).*

In Fig. 2.3, a portion of a direct relation graph, proposed by Lu and Law (2009), is shown. Each node represents a species, and each directed edge indicates the dependence of one species on the other. The starting vertex, A, enclosed in the bold circle, represents an important species. The species B and D are necessary species for A prediction while C, E and F can be considered as redundant species.

After removing redundant species from the graph, all the elementary reactions which do not contain any of the important and necessary species are eliminated from the mechanism.

Improvements of the DRG method were proposed by Pepiot-Desjardins and Pitsch (2008) with the DRGEP (DRG with Error Propagation). A new definition of the interaction coefficients is introduced, giving more importance to primary species connected to important ones through the geometrical damping of the error.

The DRG and DRGEP methods have been largely used in the literature to derive skeletal mechanisms for simple and complex fuels: for n-heptane and isooctane (Lu and Law 2006a), methyl decanoate (Herbinet et al. 2008) and for toluene (Stagni et al. 2016). DRG and DRGEP methods are also largely applied as first reduction step in the analytic reduction procedure (Jaravel et al. 2017).

2.4.1.2 Jacobian-based methodologies

The Jacobian matrix **J** contains the rate of change of species concentration in time (Tomlin et al. 1997). Each element J_{ij} of the Jacobian matrix indicates the change in production rate of a species i caused by the fractional change of the concentration of species j. An element of the normalized Jacobian matrix is expressed as:

$$J_{ij} = \frac{\partial \ln \dot{\omega}_i}{\partial \ln [X_j]} \tag{2.2}$$

According to Turanyi (1990), species belonging to a chemical mechanism can be classified into three categories:

- *Important species*: species whose concentration prediction is the scope of the modeling process. For example, they are reactants, products and pollutants.
- *Necessary species*: they have to be accounted in the chemistry model to accurately reproduce the concentration profiles of important species, temperature profile or other important flame quantities.
- *Redundant species*: The remaining ones that may be removed from the mechanism.

If only redundant species are on the lefthand side of a reaction, this reaction can also be eliminated from the mechanism without any effect on the output of the model (Turanyi 1990).

Once the set of important species is defined (N_{target}), the redundant species are identified through the evaluation of the following coefficients:

$$B_j = \sum_{i=1}^{N_{target}} \left(\frac{\partial \ln \dot{\omega}_i}{\partial \ln [X_j]} \right)^2 \tag{2.3}$$

The normalized coefficient B_j evaluates the influence of the concentration change of a species j on the net production rate of all target species. If the coefficient B_j is lower than a certain threshold ε, the species j can be considered as redundant.

A similar approach is used to remove elementary reactions from the former mechanism. For this purpose, normalized sensitivity coefficients have to be evaluated. They characterize the effect of a reaction rate parameter change on the chemical system (Turányi and Bérces 1990):

$$F_{ki} = \frac{\partial \ln \dot{\omega}_k}{\partial \ln k_i} \tag{2.4}$$

An element F_{ki}, of the log-normalized rate sensitivity matrix $\mathbf{F}$, expresses the change of the k species formation rate, caused by the rate coefficient change of the reaction i. It is possible to consider the effect of each reaction rate parameter on the overall production rates of target species using the following least-squares objective function:

$$F_i = \sum_{k=1}^{N_{target}} \left(\frac{k_i}{\dot{\omega}_k} \frac{\partial \ln \dot{\omega}_k}{\partial \ln k_i} \right)^2 \tag{2.5}$$

The overall reaction coefficients F_i can be used to rank the reactions importance in the system, at each reaction time. Consequently, the reactions, less important in the ranking, can be removed from the system.

More sophisticated approaches are used to study the rate sensitivity matrix $\mathbf{F}$ and the Jacobian matrix $\mathbf{J}$, to reduce reaction mechanism, such as principal component analysis (PCA) (Sutherland and Parente 2009) or computational singular perturbation (CSP) (Lam 2013; Valorani et al. 2006).

2.4.1.3 Lumping

Lumping consists in grouping correlated species in order to reduce the number of variables that describe the chemical system. Species lumping may also reduce the number of reactions involved in the mechanism: some reactions are duplicated after applying the lumping species procedure.

Several lumping methodologies are found in the literature (Fournet et al. 2000; Huang et al. 2005; Turányi and Tomlin 2014; Ranzi et al. 2001). Generally lumping is conducted through timescale analysis, projecting the matrix that maps the original vector of variables to a vector space having lower dimensions (Lu and Law 2009). Lumping is particularly useful for large hydrocarbon molecules because of the existence of large number of isomers that have similar thermal and transport properties as shown in Lu and Law (2008b). Reduced skeletal mechanisms using lumping strategies were also used to conduct 2-dimensional CFD simulations for n-heptane and n-dodecane laminar flames (Stagni et al. 2013).

2.4.2 Analytic reduction: from skeletal to analytic chemistry

Dimension reduction is usually applied directly to a skeletal reduced mechanism. The scope is to further decrease the number of transported species and to attenuate the mechanism stiffness.

Analytical mechanisms are usually derived applying quasi steady state (QSS) approximation and partial equilibrium assumption (PEA). These hypothesis allow to relate species concentrations through algebric expressions and successively use them to calculate some intermediate species concentration.

The PEA can be applied to a reaction for which the backward rate quickly balance the forward one and the net reaction rate approximates to zero ($q_i \approx 0$). Consequently, algebraic relations between reactants and products concentrations are derived.

The QSS approximation is instead done for species that are consumed with a reaction rate much faster than the one forming them. In practice, QSS species, as soon as produced, are rapidly consumed. Furthermore, a species can be considered in QSS if the destruction process has a characteristic time scale τ_k that is faster than other processes controlling the flame.

For a QSS species k, the net production rate can be approximated to zero ($\dot{\omega}_k \approx 0$). Consequently, algebraic relations among species concentrations can be derived.

Peters (1993), for the first time, introduced the possibility to compute intermediate species concentration in reduced kinetic mechanisms making use of analytical expressions (Peters 1985) derived from PEA and QSS hypotheses.

More recently automatic procedures to look for PE reactions and QSS species in skeletal mechanisms were introduced (Pepiot 2008). They are usually based on time-scale analysis (Lu and Law 2006b; Lu and Law 2008a; Goussis and Maas 2011).

2.4.3 Application to LES of large scale combustors

The automatic procedures, currently employed to derive analytically reduced mechanisms, combine usually DRG/DRGEP (Pepiot 2008) methodologies with time-scale analysis (Lu et al. 2001) for identification of QSS species and their consequent removal from the set of transported species.

The application of analytic chemistry to LES of semi-industrial scale burners in very recent because of the increase of CPU power availability and the development of automatic procedure to derive reduced mechanisms (Pepiot 2008; Jaravel et al. 2018).

Recently, semi-industrial burners were successfully simulated using analytically reduced mechanisms (Franzelli et al. 2017; Jaravel et al. 2017; Felden et al. 2018; Benard et al. 2018).

2.5 Flamelet based tabulated chemistry

Flamelet based tabulated chemistry approaches rely on the hypotheses that a turbulent flame structure is locally approximated by a of 1-dimensional laminar flame. Using this assumption, the thermochemical state of the combustion process is parametrized as function of a reduced set of variables. The advantage is that only the reduced set of variables have to be transported in the flow solver. The relation between the thermochemical state and the reduced variables cannot be expressed analytically but only through the use of a discrete database (Fiorina et al. 2015).

When tabulated chemistry is employed to conduct numerical simulations of turbulent 3-D flames, two fundamental assumptions are retained:

1. The thermo-chemical state of a 1-D flames collection (premixed or non-premixed) can be projected in a reduced phase space.
2. The 3-D turbulent flame structure stays locally close to the tabulated flame archetype.

Tabulated chemistry approaches have been derived by making use of different theoretical analysis for premixed and non premixed flames. The two approaches are detailed below.

More emphasis is given to the FPI/FGM (Gicquel et al. 2000; Van Oijen et al. 2001) premixed based tabulation technique since it is used in the present thesis to conduct LES of the Sydney Inhomogeneous burner. A detailed description of chemtable generation in several flame conditions can be found in Fiorina et al. (2015) and in Van Oijen et al. (2016).

2.5.1 Premixed based tabulation

The theoretical base of tabulating premixed flames is derived from the work of Maas and Pope (1992a) and Maas and Pope (1992b). Analysing homogeneous chemical 0-D reactor solutions, Maas and Pope (1992b) identified a low-dimensional manifold that has the property to attract all chemistry trajectories. This manifold is governed by slow time scales associated to the evolution of only few species. Based on the Jacobian reaction matrix eigenvector and eigenvalues analysis, the governing slow time scales are identified. Once the species associated to the slow time scales are known, all the others are mapped as function of them and the ILDM (Intrinsic Low-Dimensional manifold) is build-up.

An example of attractive sub-space (ILDM manifold) from the work of Maas and Pope (1992b) is presented in Fig. 2.4. The attractive subspace is projected in the OH-CO_2 space.

Starting from the ILDM theory, Gicquel et al. (2000) showed that building-up the manifold from 1-D laminar premixed flames, at the place of 0-D reactors, allows a better description of the low temperature flame region. The proposed model is named FPI (Flame Prolongation of ILDM).

Van Oijen et al. (2001) simultaneously suggested the possibility to tabu-

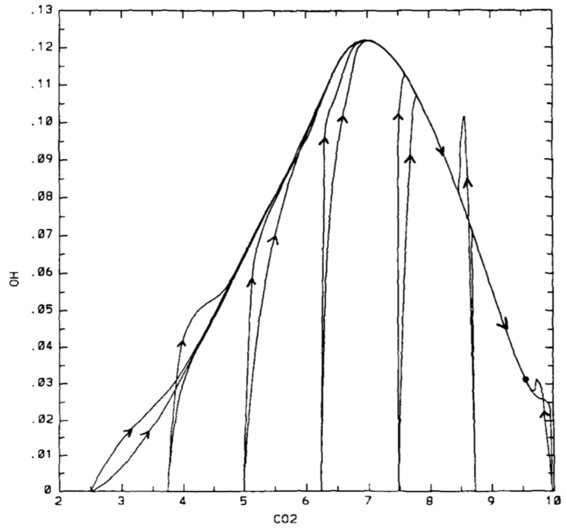

Figure 2.4: *Example of chemical trajectories analysis projected in the OH-CO_2 space. The figure is reproduced from Maas and Pope (1992b)*

late 1-D premixed flames as function of a unique progress variable in the pre-processing phase of a CFD computation and he called the model FGM (Flamelet-Generated Manifold).

In the FPI-FGM approach, the basic idea is the description of combustion chemistry as a collection of unstrained laminar one-dimensional premixed flames. The chemical trajectories are tabulated, from premixed flamelets, in phase space as a function of two variables: the progress variable Y_c (or the normalized one c) and the mixture fraction Z. Only the phase variables are transported in the flow solver leading to a drastic reduction of the CPU simulation cost.

The progress variable Y_c describes the reaction advancement from fresh gases to fully burnt gases. The mixture fraction Z, in gas-phase combustion, is considered a passive scalar that describes the degree of mixing between fuel and oxidized.

Reaction progress variable Y_c must evolve monotonically between fresh and bunt gases, to ensure a bijective relation $f(Y_c)$ with the other thermochemical flame quantities. Y_c is usually defined as a normalized temperature or as a linear combination of reactive species. In this last case it can be normalized by its equilibrium value ($c = Y_c/Y_c^{eq}$) to be bounded between 0 and 1. The progress variable is transported in the flow solver using a classical reactive scalar transport equation:

$$\frac{\partial \rho Y_c}{\partial t} + \frac{\partial}{\partial x_i}\left(\rho u_i Y_c\right) = \frac{\partial}{\partial x_i}\left(\rho D_{Y_c} \frac{\partial Y_c}{\partial x_i}\right) + \dot{\omega}_{Y_c} \tag{2.6}$$

The chemical source term is locally extracted from the look-up table and the

diffusion coefficient is classically closed with a unity Lewis assumption.
Mixture fraction instead features the following transport equation:

$$\frac{\partial \rho Z}{\partial t} + \frac{\partial}{\partial x_i}(\rho u_i Z) = \frac{\partial}{\partial x_i}\left(\rho D_Z \frac{\partial Z}{\partial x_i}\right) \tag{2.7}$$

As for progress variable, a unity Lewis number assumption is usually retained for the diffusion coefficient D_Z calculation.
To ensure a one to one relation, mixture fraction has to be defined to be conserved along a constant equivalence ratio flame front. It is usually defined either from N_2 mass fraction or from elements conservation (Bilger et al. 1990). Mixture fraction is usually normalized to be one in pure fuel and zero in pure oxidizer.
Afrter defining Y_c and Z, any thermochemical variable φ may be mapped uniquely as a function of the two coordinate $\varphi = f(Y_c, Z)$ and stored in a look-up table. Fiorina et al. (2003) enlarged the FPI applicability to non adiabatic stratified flame conditions, including the enthalpy coordinate to the chemtable. The suitability and limitation of FPI tabulation to describe partially premixed and non premixed flame conditions has been also discussed in Fiorina et al. (2005) and in Vreman et al. (2008).

2.5.2 Non-premixed based tabulation

The steady flamelet model, for non-premixed diffusion flames, was proposed for the first time by Peters (1984). From a physical hypothesis, Peters (1984) affirmed that the combustion process in a turbulent diffusion flame occurs in flamelets, whose properties are the same as those of steady, 1-D diffusion counterflow flames. The hypothesis is that the flame remains locally thin compared to turbulent scales.
In the flamelet model, for a given compositions of fuel and oxidizer streams, the mixing is typically characterized through a single parameter: the mixture fraction, whose transport equation is defined as in Eq. 2.7.
The steady flamelet chemistry table is obtained by solving the governing equations for each scalar φ together with mass and momentum in Z space, in 1-D diffusion counter-flow flames.
Each scalar equation is written in Z space as follows:

$$-\frac{\chi_Z}{2}\frac{\partial^2 \phi}{\partial Z^2} = \dot{\omega}_\phi \tag{2.8}$$

where $\chi_Z = 2D_Z \nabla_Z \cdot \nabla_Z$ is the scalar dissipation rate which depends from the imposed flow conditions. The steady flamelet table is built solving the scalars Eq.s 2.8 together with mass and momentum for a set of discrete values of the scalar dissipation rate, defined at stoichiometric conditions ($\chi_{Z,st}$).

The thermochemical state of the mixture is then parametrized as function of Z and χ_Z. Pierce and Moin (2004) proposed an improvement of the flamelet model to take into account also unsteady phenomena. A progress variable Y_c together with mixture fraction Z are used to track the mixture thermochemical state. The model is called Flame-Progress Variable (FPV) (Pierce and Moin 2004).

2.5.3 Application to LES of large scale combustors

Tabulated chemistry have been for several years the most used strategies to conduct LES of laboratory scale flames and industrial configurations for two main reasons:

1. The low CPU cost: just a few number of scalars coinciding with the coordinates of the table need to be transported in the flow solver.
2. The absence of numerical issues related to species source term calculation: the scalar source term is precomputed and stored in the chemtable.

Premixed based tabulated chemistry has been widely applied to simulate various flame configurations in the LES framework (Proch and Kempf 2015; Pecquery et al. 2014) even including flame heat losses in semi-industrial flame configurations (Chatelier et al. 2019). Recently a joint comparison have shown that FPI-FGM tabulated chemistry methods are able to reproduce the flame structure of a weakly stratified turbulent flame configuration (Fiorina et al. 2015).

Non-premixed based tabulated chemistry has been also extensively used in LES in jet flame configuration (Perry et al. 2017) and complex burners (Ihme and Pitsch 2008).

Despite the CPU efficiency, tabulated chemistry shows several limitation when the flame regime is complex and/or not perfectly apriori identified.

For example, coexistence of premixed, non-premixed and partially premixed flame regimes arise when fuel and air are partially premixed or separated at the burner injection. Furthermore, in modern combustion chambers, the presence of strong recirculation of burnt gases lowers the combustion temperature, promoting the development of complex flame regimes characterized by flame heat losses (Lamouroux et al. 2014; Benard et al. 2018).

These complex and multiple phenomena tremendously complicate the generation of the chemtable because several flame archetypes have to be considered and combined requiring further modeling assumptions (Lamouroux et al. 2014; Ribert et al. 2006).

2.6 Optimized-global chemistry

Simplified reactions mechanisms including a few number of species and reactions, were introduced for the first time in the work of Westbrook and Dryer (1981) and successively in the work of Jones and Lindstedt (1988). From two to four reaction steps are considered and the respective reaction rate parameters are optimized to achieve a satisfactory description of the two layer flame structure encountered in premixed laminar flames: a fast fuel decomposition and a slow oxidation of intermediate species. A sufficient number of species need to be also added to the reduced scheme to adequately describe adiabatic equilibrium conditions up to moderately rich equivalence ratios.

The final scope of global mechanisms is to reproduce overall flame quantities such as equilibrium temperature and flame consumption speed for a limited range of operating conditions.

In global mechanisms, reaction rate parameters are either empirically or systematically adjusted to match a reference detailed chemistry ensemble of solutions and/or experimental data for 1-D premixed and 1-D diffusion flames. Arbitrary reaction orders, as in Eq. 1.15, are also retained by Jones and Lindstedt (1988). Fernandez-Tarrazo et al. (2006) for 1-step chemistry and subsequently Franzelli et al. (2010) for two-step chemistry proposed a methodology to adapt some reaction rate parameters, as function of the local mixture equivalence ratio, in order to significantly improve the laminar flame consumption speed prediction over the whole flammability limit.

Global mechanisms have been extensively used in the recent years to conduct LES of industrial scale combustion chambers reaching a good compromise between mean flame position prediction and CPU cost efficiency (Franzelli et al. 2012; Volpiani et al. 2017; Hermeth et al. 2014). Recently the ignition process of an annular chamber has been also reproduced (Philip et al. 2015; Lancien et al. 2018) using two-step chemistry.

Polifke et al. (1998) developed a more systematic approach to derive the reaction rate parameters for the global reactions. Optimization algorithms (for example evolutionary algorithms) are used to optimize the reaction rate parameters of the global mechanisms, aiming at capturing heat release and species profiles. Issue in reproducing intermediate species were however encountered. Eventually, using global mechanisms, pollutant species and accurate inner flame structure description are out of reach (Franzelli et al. 2013).

2.7 Combustion regimes

The literature on reduced chemistry models, described in the present chapter, has been developed and a-posteriori validated over 0-D reactors and 1-D flame configurations. Reduced chemistry results are compared versus reference detailed chemistry solutions. 1-D premixed and 1-D non-premixed flames are usually retained as canonical simplified flame configurations. They allow to reproduce the chemical flame structure and its interaction with the thermal and molecular diffusion simplifying the governing balance equations solution. Furthermore, they are a simplified representation of the local flame structure that can be encountered in a practical combustor.

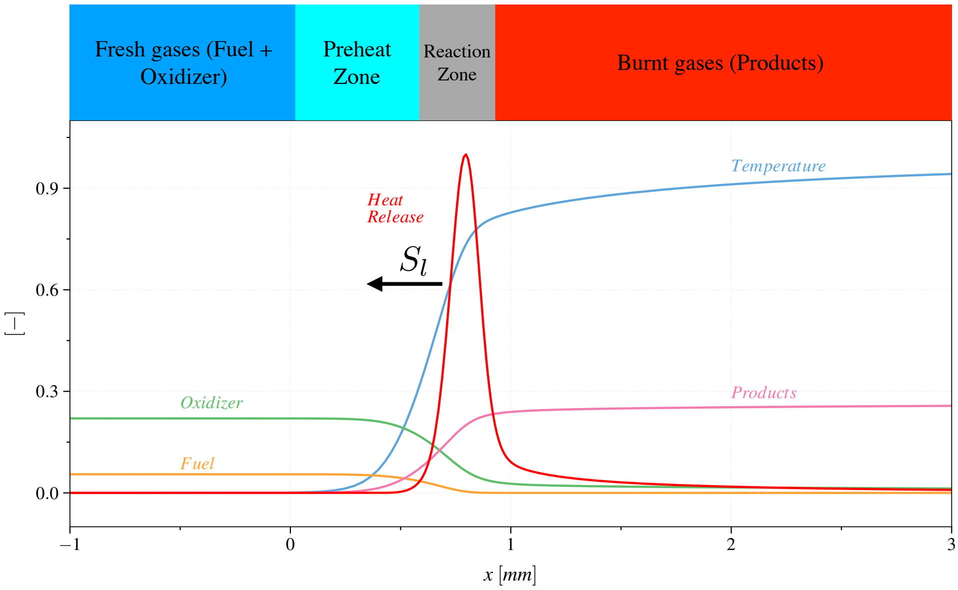

Figure 2.5: *CH_4/Air stoichiometric 1-dimensional premixed laminar flame at atmospheric pressure. The flame is computed with the code REGATH (Darabiha 1992). Mass fraction of fuel (CH4), oxidizer (O_2) and major products(CO + CO_2 + H_2O) are reported using different colors. Normalized temperature and heat release are also reported. The main flame regions are schematically shown in the upper part of the figure.*

The 1-D premixed and non-premixed flames are hereafter briefly reminded along with their main flame quantities. Eventually, the suitability of the various reduced order chemistry models to predict the various combustion regimes is discussed

2.7.1 Premixed flame

The 1-D unstretched prenfectly premixed freely propagating flame structure is presented in Fig. 2.5 . A flame front separates the fresh gases from the burnt one. The flame front propagates at the velocity S_l (laminar flame consumption speed) toward the fresh gases. Fuel and oxidizer are mixed in burnable proportions at the inlet. The key parameter that controls the proportions of fuel and air, in fresh gases, is the equivalence ratio ϕ.
In the flame region three main zones can be identified:

- **Preheat zone**: Fresh gases are heated by thermal fluxes.
- **Reaction zone**: Fuel and Oxidizer decompose in radicals, successively

consumed to form secondary fuels. This zone features a characteristic thickness size δ_r that changes as function of the operating conditions.

- **Post-flame zone**: The intermediates are converted into major combustion products (CO, CO_2, H_2O etc.). Slow combustion processes continue in the post-flame region as well (e.g. NO_x chemistry).

The mixing between fuel and oxidizer is characterized by the equivalence ratio ϕ, defined as:

$$\phi = s \frac{Y_{F,0}}{Y_{O,0}} \tag{2.9}$$

$Y_{F,0}$ and $Y_{O,0}$ are the fuel and oxidizer mass fractions in the fresh gases streams while s is the stoichiometric ratio, defined as:

$$s = \frac{\nu_O W_O}{\nu_F W_F} \tag{2.10}$$

ν_O and ν_F are the stoichiometric coefficients when a global reaction is considered.

For a premixed flame some fundamental quantities (laminar flame speed and flame thickness) are defined. These quantities characterize a premixed flame structure and depend on the operating conditions such as equivalence ratio, fresh temperature, pressure etc. The premixed flame consumption speed is usually defined as follows (Poinsot and Veynante 2005):

$$S_l = \frac{1}{\rho_0 \left(Y_{F,-\infty} - Y_{F,\infty}\right)} \int_{-\infty}^{\infty} \dot{\omega}_F(x) dx \tag{2.11}$$

Where $Y_{F,-\infty}$ and $Y_{F,\infty}$ are the fuel mass fraction in the fresh and burnt gases, respectively and $\dot{\omega}_F$ is the fuel source term.

The laminar flame thickness is usually considered equal to the thermal thickness of the flame (Poinsot and Veynante 2005) and it is computed from the knowledge of the flame temperature gradient:

$$\delta_l = \frac{T_b - T_f}{\max\left(\left|\frac{dT}{dx}\right|\right)} \tag{2.12}$$

T_f and T_b are the temperature is fresh and burnt gases, respectively.

2.7.2 Non premixed counterflow flame

The chemical and thermal structure of a non premixed diffusion flame in counterflow configuration is illustrated in Fig. 2.6.

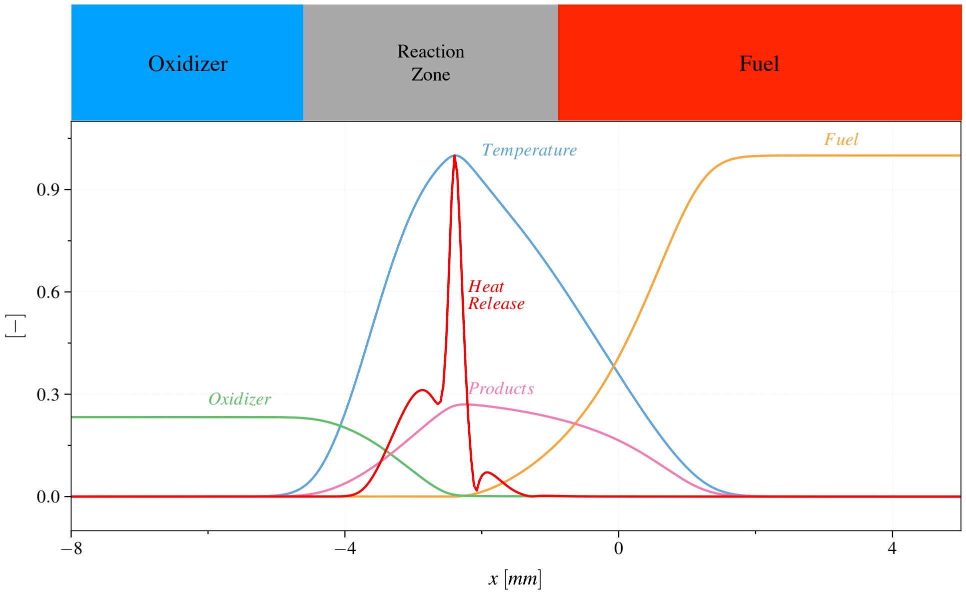

Figure 2.6: *CH4/air conterflow diffusion flame at atmospheric pressure. Mass fraction of fuel (CH4), oxidizer (O_2) and major products($CO + CO_2 + H_2O$) are reported using different colors. Normalized temperature and heat release are also reported. The various flame regions are schematically reported in the upper part of the figure.*

Fuel and oxidizer diffuse toward the reaction zone, where the heat is released. The reaction zone does not propagate but it is localized at the stagnation plate close to the stoichiometric mixture point.
Diffusion flames are controlled by the mixing that brings fresh reactants toward the flame region.
In a counterflow flame configuration, the mixing strength is characterized by the scalar dissipation rate χ, that measures the molecular and heat diffusion strength. The scalar dissipation rate of the flame is linked to the external velocity boundary conditions defined in term of flame strain rate a (Peters 2000). In the present thesis the flame strain rate is used to control the velocity at the streams inlet for the diffusion counter-flow flames (Darabiha 1992).

2.7.3 Flame structure in practical applications

The two ideal cases, detailed above, are rarely achieved in a practical combustion chamber but a coexistence of them is usually encountered. Nowadays, industrial burners operates in complex flame regimes (Masri 2015) (premixed and non-premixed and partially premixed) including heat losses and fresh gases dilution.

On one side, the not perfect premixing between fuel and air in the injection system causes mixture stratification and consequently the developed flame exhibits local equivalence ratio inhomogeneity. On the contrary, when fuel and air are injected separately, the mixing process causes the development of partially premixed flames. In such environment, coexistence of premixed and non premixed flame structures exist.

A recent joint experimental study conducted by Sydney (Meares and Masri 2014) and Sandia (Barlow et al. 2015) over a jet burner configuration confirms that the inhomogeneous mixing between fuel and oxidizer causes the development of multiple flame structure and flame stability enhancement. The Inhomogeneous jet burner, proposed by Meares and Masri (2014), is numerically investigated in the present thesis in Chap. 6.

Flame heat losses also causes a departure from the two ideal flame archetypes. Indeed, heat losses lower the flame enthalpy and consequently chemistry trajectories are modified, as will be shown in Chap. 4.

2.7.4 Reduced models suitability

The reduced chemistry models described in the present chapters (i.e. systematically reduced, tabulated and global optimized chemistry) are often designed to reproduce detailed chemistry results on a single flame elementary regime in adiabatic conditions. As consequence, when the local flame structure departs from the targeted one, important discrepancies can arise. In particular, premixed based tabulated chemistry and global optimized chemistry are efficient to describe premixed and weakly stratified combustion regimes. On the contrary, non-premixed based tabulated chemistry is very efficient when a non-premixed or a partially premixed two-streams injection is modeled.

To overcome the above limitations hybrid tabulated chemistry methods were proposed in the literature: combining premixed and non-premixed flame archetypes (Bykov and Maas 2009; Hasse and Peters 2005; Knudsen and Pitsch 2009; Nguyen et al. 2010), tabulating partially premixed flames (Franzelli et al. 2013) or combining transported and tabulated chemistry (Ribert et al. 2014). However, the tabulation of the multiple flamelet ingredients need additional hypotheses (Ribert et al. 2006; Ihme et al. 2012) and causes numerical and storage issues (Lamouroux et al. 2014; Fiorina et al. 2015). Furthermore flame index and ad-hoc formulations must be provided to close the scalar source terms to combine the several flamelet ingredients (Knudsen and Pitsch 2012).

A recent comparison proposed by Cailler (2018) showed the limitation of global optimized chemistry and tabulated chemistry to describe pollutant species profiles on mixed combustion regimes.

As reported in Fig. 2.7 (Cailler 2018), among the canonical routes, only the model that is based on systematically reduced chemistry (LU19) allows to accurately capture CO formation on multiple combustion regimes.

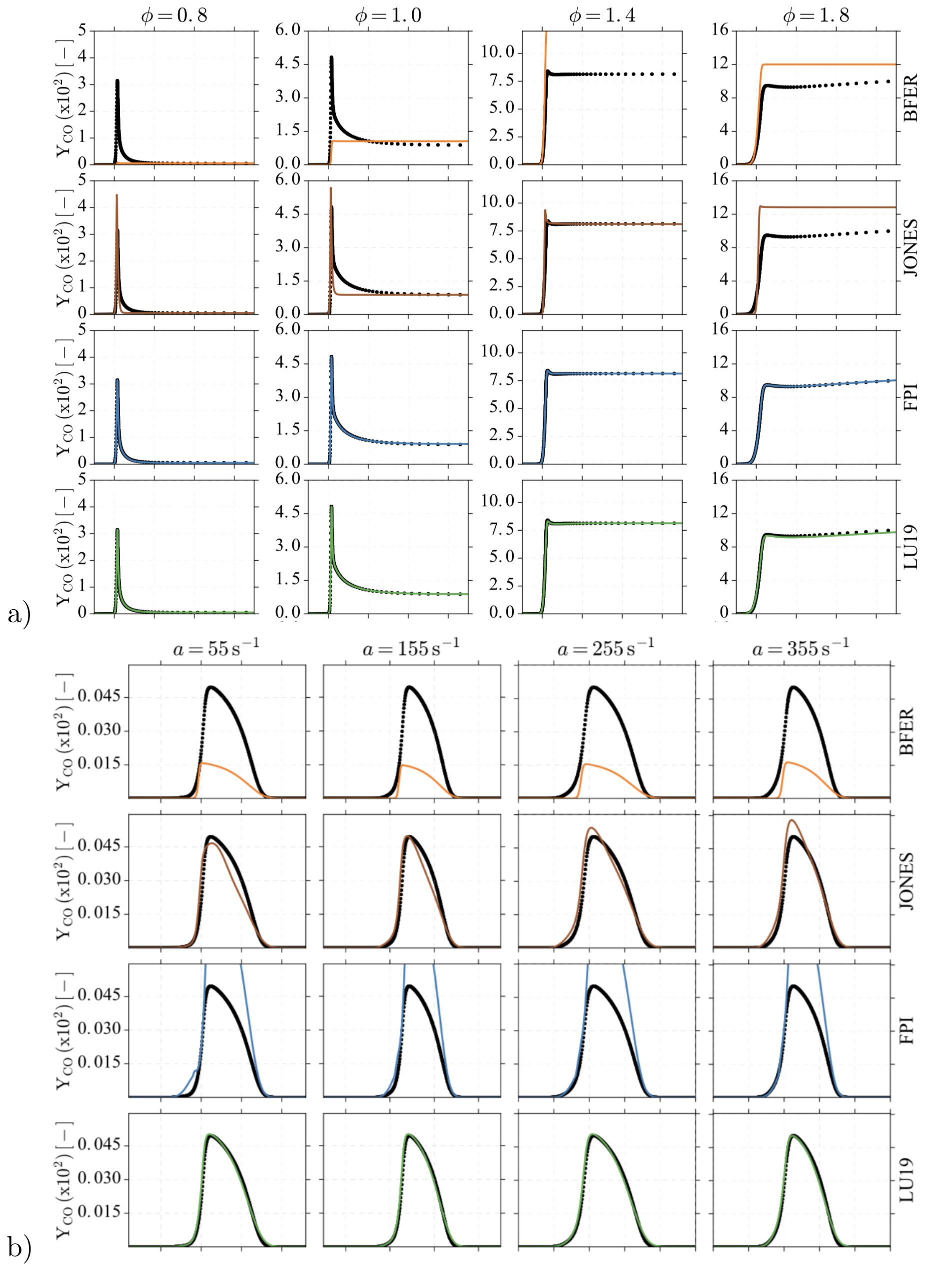

Figure 2.7: *CO mass fraction prediction in 1-D premixed (Fig. a) and non-premixed counterflow (Fig. b) flames. Different literature combustion chemistry models are compared versus detailed chemistry (black dots). BFER-2 steps (Franzelli et al. 2010) and JONES-4 steps(Jones and Lindstedt 1988) global optimized mechanisms, FPI-premixed based tabulated (Gicquel et al. 2000) and LU19 (Lu and Law 2008a) analytically reduced chemistry are compared using different colors. The figure is reproduced from Cailler (2018)*

In addition, difficulties for global optimized chemistry and tabulated chemistry arise when more complex pollutants such as NO_x and soot have to be described. In particular, the limitations shown by global optimized chemistry and tabulated chemistry in the NO_x prediction are discussed in Chap. 5.
These reasons, combined with increased computational resources and progresses in numerical methods for reducing chemical kinetics, lead toward a fast-growing interest for including semi-detailed transported finite-rate chemistry in LES.
Today, the only strategy that is currently CPU affordable, for large scale application, is the use of analytic chemistry (Jaravel 2016; Felden 2016; Benard et al. 2018). However, the CPU cost associated with these simulations is higher than tabulated and global chemistry especially when heavy hydrocarbons are considered (Cailler 2018).
The new *virtual chemistry* model, recently proposed by Cailler et al. (2017), could represent a worthy alternative to the above strategies. It allows to ensure a compromise between accurate flame structure description and CPU efficiency. Furthermore, Cailler et al. (2017) have shown the potentiality of virtual chemistry to capture CO emissions in multiple combustion regimes. The virtual chemistry approach is described in the next chapter and it is retained as the modeling strategy in the present work.

Chapter 3

Virtual chemistry

Contents

In the present chapter, the recently developed virtual chemistry approach is described presenting its novelties compared to the others combustion chemistry reduced modeling routes. The chapters details the virtual chemistry general architecture and the optimization procedures to build-up the main mechanism and the CO satellite one. At the end of the chapter, it is proposed a focus on the virtual chemistry modeling new challenges that are then the focus of the thesis

3.1 Introduction

A new and original reduced order model for combustion chemistry description, called *virtual chemistry* (Cailler et al. 2017), has been recently introduced, at EM2C laboratory, in the Phd thesis of Cailler (2018). Virtual chemistry aims at modeling combustion kinetic, combining low CPU cost and accurate flame structure description including the prediction of pollutant species.

Virtual chemistry is formulated as a transported chemistry reduced model as well as global chemistry and systematically reduced chemistry. Indeed, just a few species are transported in the flow solver in comparison with detailed chemistry that is instead the reference to reproduce.

Compared to systematically reduced approaches that gradually downsize the mechanism dimension, virtual chemistry approach gradually increases the dimension of the model (Cailler et al. 2017).

In the classification proposed in the previous chapter, virtual chemistry is included among the optimization based methodologies (Fiorina 2019). Indeed, the idea of systematically fit the reaction rate parameters to reproduce a selection of flame quantities of interest is similar to the global mechanism approaches. However, several novelties are introduced in comparison to global optimized chemistry:

- The building-up of a network of an optimized number of virtual species interacting through virtual elementary reactions.
- The optimization of virtual species thermodynamic properties.
- The use of dedicated sub-mechanisms to predict flame quantities of interest, for example pollutant species.

Despite the use of virtual species and reactions, virtual chemistry still retains the classical reaction formalism, presented in Chap. 1, for elementary gas kinetics.

$$\sum_{k=1}^{N_s} \alpha_{ki}^{'} \chi_k^v \rightarrow \sum_{k=1}^{N_s} \alpha_{ki}^{''} \chi_k^v \quad (i = 1, ..., N_r) \tag{3.1}$$

The virtual species χ_k^v interact through virtual reactions r_i^v and the chemical reaction rates are closed with an Arrhenius like formulation as in Eq. 1.12.

A main virtual mechanism is optimized to give access to temperature and heat release and it is coupled with the governing Navier-Stocks equations. In addition, dedicated pollutant sub-mechanisms are added to model the targeted pollutants species. Each pollutant sub-mechanism features a characteristic time scale associated to the target species.

3.2 Methodology and optimization

3.2.1 Architecture

As proposed by Cailler (2018), the procedure to build-up the virtual chemistry mechanisms is summarized in the scheme presented in Fig. 3.1.

A reference flame library is pre-computed using a detailed chemistry thermochemical database. It is made of an ensemble of target flame configurations that, in principle, can include equilibrium computations and a selection of 0-D reactors and 1-D flame archetypes. Reference equilibrium computations are

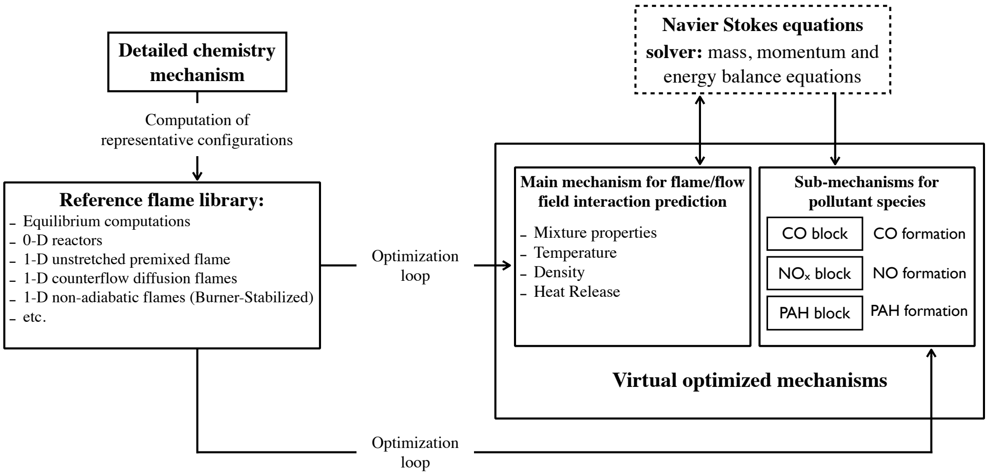

Figure 3.1: *Overview on the procedure to build-up virtual optimized chemical mechanisms. The figure is adapted from Cailler (2018).*

used to optimize the virtual species thermodynamic properties. 1-D premixed flames spanning the whole fresh gases equivalence ratio range bounded between the lean and rich flammability limits allows to recover temperature and heat release. Furthermore, enlarging the flamelet database, including 1-D premixed and 1-D non premixed flamelets allows to recover CO formation in multi-regime flames (Cailler 2018).

In a first optimization loop, the main virtual mechanism, dedicated to temperature and heat release rate prediction, is derived. Virtual species thermodynamic and transport properties are optimized to reproduce the mean flame properties of the reference mixture in fresh and burnt gases. Then, kinetic rate parameters for the main mechanism are optimized to retrieve temperature and laminar flame consumption speed of the reference solutions.

Once the virtual main mechanism is build-up, virtual chemistry is able to reproduce with a certain accuracy mean mixture properties, temperature, density and heat release of the reference database.

In the second optimization loop, as shown in Fig. 3.1, the virtual satellite mechanisms dedicated to pollutants specie prediction (CO, NOx, PAH, etc.) are derived. Kinetic rate parameters for the pollutant sub-mechanisms are optimized to reproduce the desired pollutant mass fraction for the ensemble of operating conditions considered in the reference database.

As shown in the Fig. 3.1, only the main virtual mechanism is coupled with the flow solver balance equations (mass, momentum and energy). On the contrary, for pollutant sub-mechanisms, only species balance equations are solved and they do not retro-act in the closure of mass, momentum and energy governing

equations.
As consequence, virtual species involved in pollutant sub-mechanism do not need thermodynamic properties because they are not involved in the closure of the energy balance equation. Hence, just kinetic rate parameters have to be derived in pollutant dedicated sub-mechanisms.

3.2.2 Optimization problem

The virtual species properties and the kinetic rate parameters of the virtual reactions are optimized through an evolutionary algorithm designed by Cailler et al. (2017). The optimization problem can be formalized as a classical minimization of a cost function C:

$$C = f\left(\mathbf{w}^v(\chi^{\mathbf{v}}), \mathbf{w}^d(\chi^{\mathbf{d}})\right) \tag{3.2}$$

where $\mathbf{w} = (\rho u, \rho v, \rho w, \rho Y_k, T)$ is the state vector, defined as the solution of momentum, species and energy governing balance equations, function of the vector of parameters χ. Detailed state vector $\mathbf{w}^d$ and virtual one $\mathbf{w}^v$ are constrained by the set of governing balance equations defined in Chap. 1.
χ is the vector containing the thermo-chemistry parameters of the mixture. It is known for the reference flame library ($\chi^{\mathbf{d}}$) and consequently it constitutes an input of the optimization problems. $\chi^{\mathbf{v}}$, on the contrary, represents the vector containing the thermochemical variables for the virtual mechanisms and therefore it is the unknown of the problem (i.e. the output of the optimization procedure).
Each thermochemical variable contained in the vector $\chi^{\mathbf{v}}$ is bounded between a lower and an upper bound which are user input parameters.
In practice, the cost function C is given, through the function f, by a linear combination of normalized differences of selected flame quantities calculated with the virtual mechanisms $f(\mathbf{w}^v(\chi^{\mathbf{v}}))$ and reference chemistry $f(\mathbf{w}^d(\chi^{\mathbf{d}}))$, respectively.
At each optimization step (thermodynamic properties, kinetic rate parameters for the main and pollutant sub-mechanism) the cost function is defined using different target quantities. The various optimization step with the respective cost function are detailed in the following sections.

3.2.3 Optimization algorithm

The evolutionary algorithm designed by Cailler (2018), implemented in the in-house code MelOptim (Cailler 2018), is used in the present thesis to perform all the virtual chemistry optimizations. Optimization algorithm are usually classified between local and global ones. Genetic optimization is included among the global optimization strategy. The use of a global algorithm rather than a local one is preferred in the context of the chemical kinetics optimization, for several reasons:

- The cost function f does not have an analytical expression.
- The random individuals generations used in global algorithm allows to better span the validity domain of the parameters to optimize, preventing to hand up in local optima.
- For local algorithm an initial guess must be provided for each thermochemical parameter. The definition of this initial guess is not straightforward for virtual species and reactions parameters.

Details about the evolutionary algorithm implemented in the in-house code MelOptim are given in Cailler et al. (2017) and in Cailler (2018)

The code MelOptim is coupled with the flame solver REGATH (Darabiha 1992) to solve the governing balance equations and successively compute the fitness function at each iteration of the optimization procedure.

3.3 Main-temperature mechanism

A 2-step main virtual mechanism is retained, as proposed by Cailler (2018), to predict temperature and heat release. It has the following structure:

$$\alpha^v_F F + \alpha^v_{Ox} Ox \rightarrow \alpha^v_I I \tag{R^T_1}$$

$$\alpha^v_I I \rightarrow \sum_{k=1}^{N^v_P} \alpha^v_{P_k} P_k \tag{R^T_2}$$

where α^v_χ are the stoichiometric coefficients per mass unit of the virtual species χ. The symbols F, Ox and I, respectively, denote the fuel, the oxidizer and a virtual intermediate species. The burnt gases composition is modeled by a mixture of N^v_P virtual products P_k. A non reactive dilutant species D is also added to the virtual mixture. Two irreversible reactions steps are considered: fuel and oxidized are transformed in an intermediate species that is successively transformed in the virtual product mixture. Cailler et al. (2017) have shown that a two step virtual mechanism allows to well retrieve the two layer premixed flame structure and laminar flame speed, for the whole flammability limit, with a sufficient accuracy.

The main virtual mechanism enables the proper capture of the temperature and heat release profiles of the reference flame archetypes.

The building up of the main virtual mechanism involves two consecutive optimization sub-steps:

1. It aims at optimizing transport and thermodynamic properties of the virtual species in order to reproduce the mean properties of the reference mixture in fresh and burnt gases respectively. In the thermodynamic optimization stage, the mass stoichiometric coefficients of the virtual products $\alpha^v_{P_k}$ are also computed.

2. It aims at optimizing the kinetic rate parameters for the virtual reactions to reproduce the correct thermal inner flame structure and flame flow-field interaction.

The second optimization step is performed only once the first one is completed because species thermodynamic and transport properties are needed at the second stage.

The different objective cost function C, employed at the different optimization stages are detailed below.

3.3.1 Virtual species thermodynamic properties

The thermodynamic properties of each virtual species k is defined by the vector $\psi_k^v = (c_{p_k}^v, h_k^v)$, where $c_{p_k}^v$ and h_k^v denote the heat capacity and the enthalpy, respectively.

The virtual species thermodynamic properties $c_{p_k}^v$ and h_k^v are expressed by using the same NASA temperature dependent polynomial functions (McBride et al. 1993) used for real species:

$$\frac{C_{pk}}{R} = a_{1k} + a_{2k}T + a_{3k}T^2 + a_{4k}T^3 + a_{5k}T^4 \tag{3.3}$$

$$\frac{H_k}{RT} = a_{1k} + \frac{a_{2k}}{2}T + \frac{a_{3k}}{3}T^2 + \frac{a_{4k}}{4}T^3 + \frac{a_{5k}}{5}T^4 + \frac{a_{6k}}{T} \tag{3.4}$$

Each NASA thermodynamic coefficient a_{lk}^v for each virtual species k is optimized to correctly reproduce the mean thermodynamic properties of the reference mixture in fresh and burnt gases.

The following cost function is considered:

$$C^{thermo} = \left(\psi^v - \psi^d\right) \tag{3.5}$$

Where ψ^v and ψ^d are the mean mixture thermodynamic properties for the virtual and reference chemistry computed as follows:

$$\psi^v = \sum_{k=1}^{N_v} Y_k^v \psi_k^v; \qquad \psi^d = \sum_{k=1}^{N_d} Y_k^d \psi_k^d \tag{3.6}$$

Y_k^v and Y_k^d are the k^{th} species mass fractions for the virtual and detailed mixture respectively. N_v and N_d are the number of species involved in the virtual and detailed mechanisms, respectively. ψ_k^v and ψ_k^d represent the thermodynamic properties for the kth species in the virtual and detailed mixture, respectively.

Thermo-chemical equilibrium is recovered if the mixture, composed of N^v_P *virtual* products plus F, Ox, I and D, matches the mean thermodynamic properties of the reference mixture, composed by N_d *real* species.
In practise, the cost function C^{thermo} is minimized to achieve a correct reproduction of the mean mixture thermodynamic properties in fresh and burnt gases.
In fresh gases, the optimization is automatically fulfilled if real thermodynamic properties are attributed to F, Ox and D. For example in CH_4/Air combustion the thermodynamic properties of CH_4, O_2 and N_2 are retained.
The virtual intermediate species I is fully consumed by reaction R^T_2 and therefore not present at equilibrium.
In the fully burnt gases, the chemical equilibrium is recovered if the mixture composed of N^v_P virtual products together with the remaining fuel F, oxidizer Ox and dilutant D matches, the mean thermodynamic properties of the reference detailed chemistry mixture, composed of N^d_s real species.
Then, the cost function at equilibrium condition is formalized with the following relation:

$$C^{thermo} = \sum_{k=1}^{N^v_s} \psi^v_k Y^v_k|^{eq} - \sum_{k=1}^{N^d_s} \psi^d_k Y^d_k|^{eq} \tag{3.7}$$

The symbol $|^{eq}$ specifies that the quantity are considered at chemical equilibrium conditions. Separating the virtual products contribution from F, Ox and D ones, Eq. 3.7 is rewritten as:

$$C^{thermo} = \sum_{k=F,Ox,D} \psi^v_k Y^v_k|^{eq} + \sum_{k=1}^{N^v_p} \psi^v_{P_k} Y^v_{P_k}|^{eq} - \sum_{k=1}^{N^d_s} \psi^d_k Y^d_k|^{eq} \tag{3.8}$$

$Y^v_{P_k}$ is the mass fraction of each virtual product P_k and ψ_{P_k} its thermodynamic property.
The virtual products mass fraction is equal to $Y^v_{Pk} = \alpha_{Pk} Y^v_P$, where α_{Pk} is the product stoichiometric coefficients per mass unit and Y^v_P the total virtual products mass fraction. By using the polynomial NASA relations, the fitness function in 3.8 is compactly re-written as:

$$C^{thermo} = \sum_{l=1}^{N_T} \left[\sum_{k=1}^{N^v_p} a^v_{lP_k} \alpha_{Pk} - \sigma_l / Y^v_P|^{eq} \right] \tag{3.9}$$

where σ_l is expressed as:

$$\sigma_l = \sum_{k=1}^{N^d_s} a^d_{lk} Y^d_k - \sum_{k=F,Ox,D} a^v_{lk} Y^v_k \quad for \quad l = 1,..,N_T \tag{3.10}$$

N_T is the number of NASA polynomial coefficients that are considered. In virtual chemistry considering $N_T = 6$, heat capacity and the enthalpy are defined.
σ_l is a known quantity because combination of information from the detailed chemistry library and informations from Fuel, Oxidizer and Dilutant. The total virtual product mass fraction at the equilibrium condition $Y_P^v|^{eq}$ is also a known quantity from the stoichiometry.
Virtual product NASA thermodynamic coefficients $a^v_{lP_k}$ and the virtual products stoichiometric coefficient α_{Pk} are the unknowns of the problem. The cost function C^{thermo}, written in Eq. 3.9 only for one operating condition, is easily generalized for the whole set of operating conditions included in the flame library, by using the sum of them:

$$\left(C^{thermo}\right)^{tot} = \sum_{j=1}^{N_c} C_j^{thermo} \tag{3.11}$$

where N_c is the number of operating conditions (fresh gases equivalence ratios) considered in the flammability range.
The genetic algorithm minimizes the cost function $\left(C^{thermo}\right)^{tot}$, optimizing the $a^v_{lP_k}$ coefficients and successively computing the α_{Pk} coefficients. Further details about the thermodynamic optimization algorithm are detailed in Cailler (2018) Phd thesis.
As shown by Cailler et al. (2017), the original idea of optimizing the thermodynamic properties of some virtual species allows to excellently capture the equilibrium flame temperature over the whole flammability limit (Fig. 3.2).

3.3.2 Virtual species transport properties

The transport properties for virtual species are closed with a simplified model assuming $Le_k = 1$. Consequently, the diffusion velocities, in the species transport equations, are expressed using the Fick's law approximation proposed in Eq. 1.29. The species diffusion coefficients D_k are assumed all equal to the the thermal one D_{th} and they are computed through the knowledge of mean mixture average dynamic viscosity as detailed in Eq. 1.30. The mixture averaged dynamic viscosity is computed through a power law:

$$\mu^v = \mu_0 \left(\frac{T}{T_0}\right)^{\beta} \tag{3.12}$$

μ_0 is the dynamic viscosity at the reference temperature T_0 (the fresh gases temperature) and it is computed from the reference mixture.

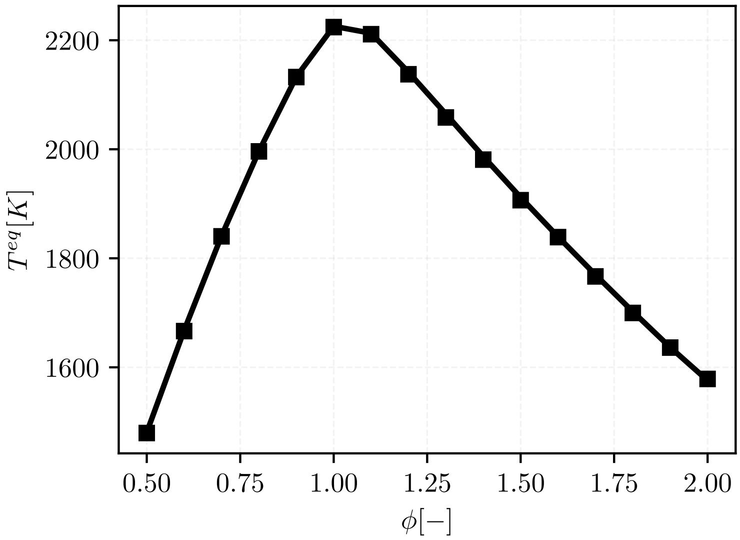

Figure 3.2: *Adiabatic equilibrium temperature over the whole flammability limit for* CH_4*/air combustion at atmospheric pressure and 300K initial temperature. Virtual chemistry solution (squared symbols) is compared versus the adiabatic temperature computed using a mixture of 53 species (continuous line).*

In practice, the optimization of the virtual species transport properties with the hypothesis of $Le_k = 1$ is formalized using the following cost function:

$$C^{tran} = \left(\mu^v - \mu^d\right) \tag{3.13}$$

Where μ^v and μ^d are the mean mixture average evaluated at stoichiometric conditions for virtual and detailed chemistry, respectively. μ^d is a known quantity. β is the optimized parameter that enable to fit the temperature dependency of the dynamic viscosity at atmospheric pressure. This approach for computing the dynamic viscosity has been already validated in global chemistry by Franzelli et al. (2010).
For CH_4/Air combustion, $\mu_0 = 1.8405[kg/(m.s)]$ and $\beta = 0.6759$.

3.3.3 Kinetic rate parameters

The rate of progress of the two irreversible reactions R_1^T and R_2^T is closed with an Arrhenius like formulation using arbitrary reaction orders:

$$q_1 = A_1(\phi)\exp\left(\frac{-E_a^1}{RT}\right)[F]^{F_F^1}\,[O]^{F_{Ox}^1} \tag{3.14}$$

$$q_2 = A_2\exp\left(\frac{-E_a^2}{RT}\right)[I]^{F_I^2(\phi)} \tag{3.15}$$

where A_i and $E_{a,i}$ are the pre-exponential factor and activation energy of reaction i, respectively. $F_{k,i}$ is the kth species forward reaction order for the reaction i and $[k]$ is the kth species molar concentration. A_1 and F_I^2 are tabulated as function of the mixture equivalence ratio to satisfactorily retrieve the laminar flame speed and temperature profile for the whole flammability limit.
A_i, $E_{a,i}$ and $F_{k,i}$ are optimized to minimize the following fitness function:

$$C_{main}^{kinetic} = \alpha_1\frac{|S_L^v - S_L^d|}{S_L^d} + \alpha_2\frac{\|T^v(x) - T^d(x)\|_{L_2}}{\|T^d(x)\|_{L_2}} \tag{3.16}$$

Where S_L and $T(x)$ denote the laminar flame consumption speed and the temperature profile along the 1-dimensional domain, respectively.
If multiple operating conditions are considered in the optimization procedure (equivalence ratio, enthalpy or pressure), a global cost function is computed by summing the ones evaluated for each operating condition.
The weights α_1 and α_2 are used to give appropriate importance to each variable involved in the cost function evaluation.
Including in the optimization database 1-D premixed flames, whose equivalence ratios cover whole flammability limit, Cailler et al. (2017) showed that the virtual main mechanism is able to accurately reproduce:

- Laminar flame consumption speed over the whole flammability limit. Figure 3.3 compares the laminar flame consumption speed for virtual and detailed chemistry showing that virtual chemistry enables a good reproduction of laminar flame speed in the whole flammability limit.
- Temperature profiles for 1-D premixed laminar flames over the whole flammability limit. Figure 3.4 shows a comparison of the temperature profiles for 1-D premixed flames computed with virtual and detailed chemistry for various equivalence ratios.
- Temperature profiles in 1-D diffusion counter-flow flames. Figure 3.5 shows a comparison of the virtual and detailed temperature profiles in a 1-D counter-flow diffusion flame.

3.4 Pollutant sub-mechanisms

The second optimization loop, presented in Fig. 3.1, is dedicated to the pollutant sub-mechanisms optimization.

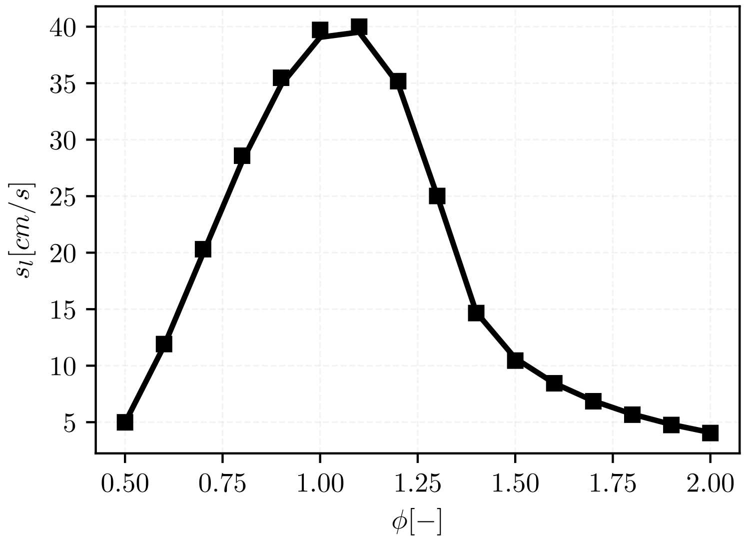

Figure 3.3: *1-D laminar flame consumption speed for CH_4/Air combustion at atmospheric pressure. Detailed chemistry (continuous line) is compared with virtual chemistry (squared dots).*

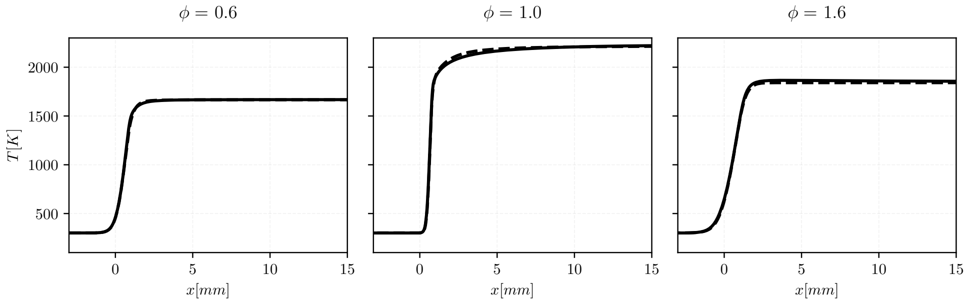

Figure 3.4: *1-D premixed temperature profiles for CH_4/Air combustion at atmospheric pressure. Results are shown for various equivalence ratios ϕ: lean, stoichiometric and rich flames. Detailed chemistry (continuous line) is compared with virtual chemistry solution (dashed line).*

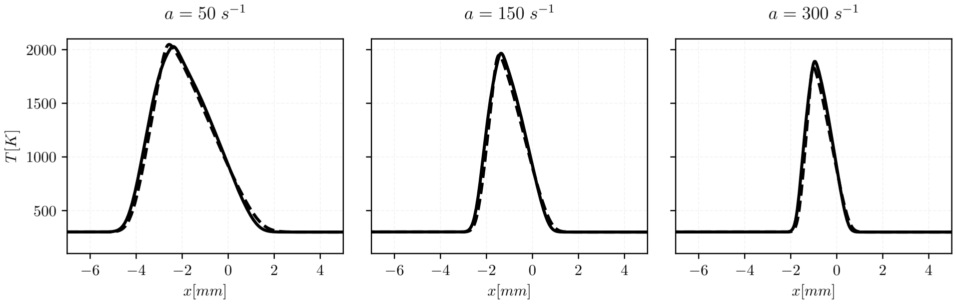

Figure 3.5: *1-D diffusion counter-flow temperature profiles for CH_4/Air combustion at atmospheric pressure. Results are shown for various values of the flame strain rate a. Detailed chemistry (continuous line) is compared with virtual chemistry solution (dashed line).*

Pollutant sub-mechanisms aim to reproduce only detailed chemistry solutions of targeted species (for example CO or NO).

The species diffusive fluxes are computed with the same simplified hypothesis used for the main mechanism, considering $Le_k = 1$.

The design of the virtual reactions network, in the pollutant dedicated sub-mechanisms, is based on a pure physical analysis of the main chemical formation paths affecting the considered pollutant.

3.4.1 CO sub-mechanism

As proposed by Cailler (2018), the following 3-steps mechanism is used to predict the CO:

$$\alpha_F^v F + \alpha_{Ox}^v Ox \rightarrow \alpha_{CO}^v CO + (1 - \alpha_{CO}^v)\, V_1 \qquad (R_1^{CO})$$

$$F + V_1 \rightarrow F + CO \qquad (R_2^{CO})$$

$$CO \leftrightarrow V_2 \qquad (R_3^{CO})$$

Fuel F and Oxidizer Ox are the same species involved in the main virtual mechanism. To reduce the computational cost, F and Ox concentrations are imposed in the CO mechanism computation since their profiles are already known from the solution of the main mechanism.

V_1 and V_2 are two virtual species while CO aims at reproducing, with a certain accuracy, the real CO profile given from detailed chemistry.

The mechanism was designed by Cailler et al. (2019) to describe the principal CO formation and consumption chemical time scales:

- The first reaction R_1^{CO} describes the fast CO production from fuel oxidation.
- The second reaction R_2^{CO} converts V1 into CO to capture the slow CO formation processes occurring in rich conditions.

- The reversible reaction R_3^{CO} between CO and V2 models the slow recombination processes observed in the post-flame zone. In addition, the inclusion of an equilibrium reaction ensures the proper capture of the CO equilibrium concentration.

The coefficient α_{CO} is smaller than 1 only if $\phi >= 1.4$. It activates the reaction R_3^{CO} only for rich conditions.
The rate of progress for the three reactions are expressed using and Arrhenius-like formulation:

$$q_1^{CO} = A_1(\phi) \exp\left(\frac{-E_{a,1}}{RT}\right) [F]^{F_F^1} [Ox]^{F_{Ox}^1} \tag{3.17}$$

$$q_2^{CO} = A_2(\phi) \exp\left(\frac{-E_{a,2}}{RT}\right) [F]^{F_F^2} [V_1]^{F_{V_1}^2} \tag{3.18}$$

$$q_3^{CO} = A_3(\phi) \exp\left(\frac{-E_{a,3}}{RT}\right) \left([CO]^{F_{CO}^3} [V_2]^{F_{V_2}^3} - \frac{[CO]^{R_{CO}^3} [V_2]^{R_{V_2}^3}}{K_{c,3}^{CO}}\right) \tag{3.19}$$

q_3 has the same expression as q_1 (Eq. 5.6) and it conserves the same kinetic rate parameters as well.
$R_{k,i}$ represents the kth species reverse reaction order for the reaction i. Reverse reaction orders are considered just for the reaction R_3^{CO} as it follows an equilibrium formalism. All the kinetic rate parameters involved in Eq.s 3.18 and 3.19 and the stoichiometric coefficient α_{CO} are optimized, by using the following cost function:

$$C_{CO}^{kinetic} = \frac{\| Y_{CO}^v(x) - Y_{CO}^d(x) \|_{L_2}}{\| Y_{CO}^d(x) \|_{L_2}} \tag{3.20}$$

A_2 and A_3 have to be tabulated as function of the fresh gases equivalence ratio, to satisfactorily retrieve the CO peak value and the CO post-flame formation in rich conditions.
The equilibrium constant $K_{c,3}^v$ for the reaction 3.19 is calculated in concentration units according to the equilibrium theory presented in 1.16:

$$K_{c,3} = \frac{[V_2]^v |^{eq}}{[CO]^d |^{eq}} \tag{3.21}$$

where $[V_2]^v |^{eq}$ and $[CO]^d |^{eq}$ are the molar species concentration, at equilibrium conditions, for the species $V2$ and CO, respectively. $[CO]^d |^{eq}$ is extracted from detailed chemistry equilibrium computations while $[V_2]^v |^{eq}$ can be computed from mass conservation.

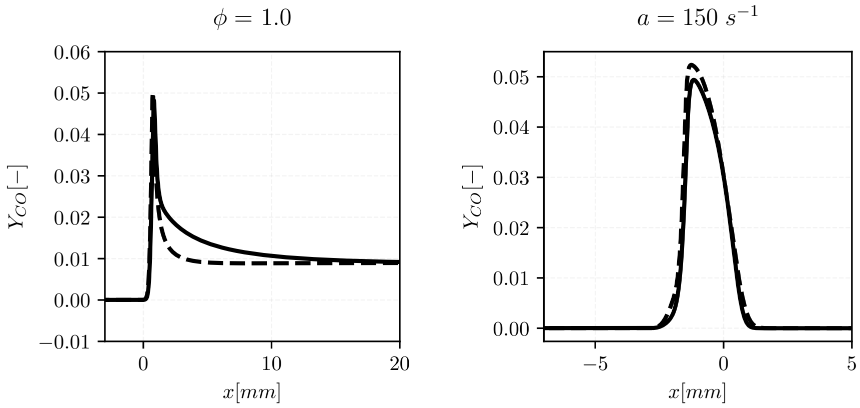

Figure 3.6: *CO mass fraction profile in an adiabatic premixed laminar flame for* $\phi = 1$ *and in a counterflow diffusion flame at* $a = 150s^{-1}$*. Detailed chemistry (continuous line) is compared with virtual chemistry solution (dashed line).*

3.4.2 Validation results

Cailler (2018) showed that the above CO sub-mechanism structure allows a proper capture of CO formation in mixed combustion regimes: premixed and diffusion flames. This results is achieved only is the two flame archetypes are added to the flamelet learning library.

Figure 3.6 shows CO mass fraction comparison between virtual and detailed chemistry for both a 1-D premixed laminar flame and a 1-D counterflow diffusion flame. Indeed, satisfactory results are achieved.

3.5 Conclusion

As introduced by Cailler (2018), virtual chemistry is a new and promising methodology to model combustion chemistry in flame numerical simulations combining low CPU cost and pollutant description. Cailler (2018) has shown that virtual chemistry allows to describe in multi-mode combustion regimes:

- temperature profile and heat release,
- CO emissions,

by using a few number of virtual species and reactions.

However, the potentialities of the approach are numerous and yet unexplored. The capability to describe more complex flame conditions such as the non-adiabatic ones need to be assessed. In addition to CO emissions, the potentiality to describe slow chemistry pollutants such as NO_x need also to be demonstrated. Finally, the application of the virtual chemistry approach to turbulent flame LES need to be further validated.

The present thesis work gives answer to the above research key points.

In Part II:

- Chap. 4 extends virtual chemistry to non adiabatic laminar flame conditions.
- Chap. 5 proposes a new pollutant satellite sub-mechanism for NO emission prediction. The mechanism is validated in 2-D laminar flame simulations including several flame conditions (premixed, non-premixed and partially premixed).

In Part III, the suitability of the virtual chemistry approach to conduct LES is demonstrated. In particular, the two following turbulent flame configurations are numerically investigated:

- in Chap 6, the Sydney compositionally inhomogeneous jet burner (Meares and Masri 2014; Barlow et al. 2015). It is characterized by the coexistence of premixed and non-premixed flame structures.
- in Chap. 7, the Preccinsta semi-industrial chamber. In this configuration, the flame is exposed to wall heat losses. A comparison of the virtual chemistry results versus the most advanced analytic chemistry computation, conducted by Benard et al. (2018), is also shown.

Part II

Extending the Virtual Chemistry range of applications

Chapter 4

Virtual chemistry for non adiabatic flame conditions

Contents

The aim of the present chapter is the development of a comprehensive reduced chemistry model able to account for the impact of heat losses on chemical flame structure. Virtual chemistry is trained to recover flame quantities of an ensemble of target flames including non adiabatic conditions. Burner-stabilized flamelets are added in the reference optimization database to capture the influence of heat-losses on flame heat release and CO pollutant formation. The approach is a-posteriori validated in 1-D laminar burner stabilized flames and further assessed in a radiative freely propagating flame configuration.

4.1 Introduction

By reducing the temperature and the flame consumption speed, heat exchanges affect the flame stabilization mechanisms (Fiorina et al. 2015; Mercier et al. 2016) as well as major species and pollutant formation (Jainski et al. 2017). In addition, heat losses promote local extinction, at the origin of incomplete fuel consumption (Guiberti et al. 2015). The proper capture of flame heat losses is therefore crucial for chemistry models employed in numerical simulations of industrial combustion chambers (Proch and Kempf 2015).

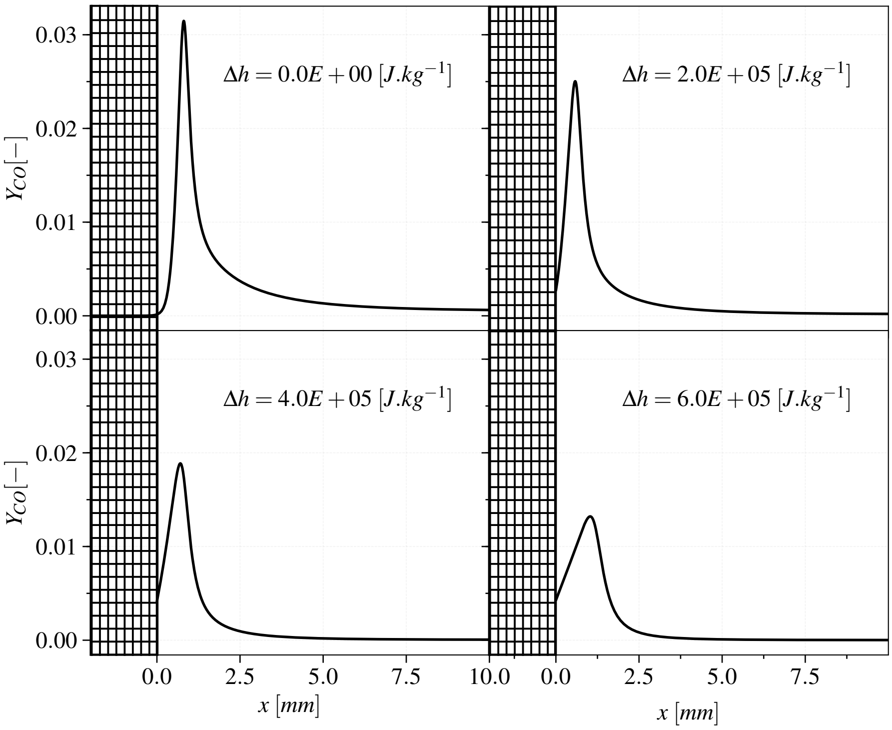

Figure 4.1: *CO mass fraction profiles for burner stabilized flame computed at constant equivalence ratio ($\phi = 0.8$), atmospheric pressure and fresh gases temperature of 300K with REGATH code (Darabiha 1992) using GRI3.0 mechanism (Smith et al. 2011). The four flames are computed for different enthalpy defect values with respect to a freely propagating adiabatic flame.*

For example, heat losses strongly affect CO formation. Figure 4.1 shows the CO mass fraction profiles for a series of constant pressure premixed burner stabilized flames (Kee et al. 1985) computed with detailed chemistry. Different flame enthalpy values are considered from near adiabatic conditions ($\Delta h = 0.0$ $J.kg^{-1}$) to near extinction ($\Delta h = 6.0E + 05$ $J.kg^{-1}$). Indeed, Increasing heat losses, the CO peak reduces up to 50% and the thickness of the CO layer is modified.

As argued in previous Chapters, detailed chemistry cannot be employed to conduct 3-D large scale LES computations. Reliable reduced order chemistry models that aims at capture non-adiabatic flame conditions must correctly account for flame heat losses sensitivity, as in detailed chemistry.

As widely discussed in Chap. 2, three main reduction routes are currently employed (Fiorina et al. 2015). i) Mechanism reduction leading to analytically reduced mechanism (Lu and Law 2008a; Pepiot-Desjardins and Pitsch 2008). Despite the recent promising application of analytic chemistry to a swirled combustor (Jaravel et al. 2017), the computational costs along with numerical stiffness remain restrictive. ii) Chemistry tabulation (Fiorina et al. 2015;

Van Oijen et al. 2016). Heat transfers are handled by adding a dedicated coordinate (usually the enthalpy) to the look-up table (Van Oijen et al. 2001; Fiorina et al. 2003; Ihme and Pitsch 2008). However, tabulated chemistry shows some limitations when the encountered flame structures differ from the tabulated archetype (Fiorina et al. 2005). Multiple flame archetypes have to be considered, which both complicates the generation of the chemical look-up table (Bykov and Maas 2007a; Nguyen et al. 2010; Franzelli et al. 2013) and causes memory issues (Ihme et al. 2007; Veynante et al. 2008). iii) Empirically reduced global mechanisms (Westbrook and Dryer 1981; Jones and Lindstedt 1988) constitute another CPU efficient strategy, currently used to perform LES of industrial scale combustion chambers (Berger et al. 2016; Franzelli et al. 2010). However, these schemes only capture global flame properties on a limited range of operating condition and cannot predict pollutants.

Virtual chemistry (Cailler et al. 2017; Cailler et al. 2019), as introduced in Chap. 3, is an alternative reduced chemistry model that can allow to face some of the above limitations.

The aim of the present chapter is the development of a comprehensive virtual chemistry model able to account for the impact of heat losses on flame structure (temperature and heat release) and CO prediction in premixed stratified flame conditions.

Main and CO virtual mechanisms are trained to recover the properties of an ensemble of adiabatic and non-adiabatic target flames. Burner-stabilized flamelets, in addition to freely propagating, are introduced in the reference database to capture the influence of heat-losses on temperature and CO formation of premixed stratified flames.

The main virtual mechanism and the CO dedicated sub-mechanism are re-optimized to capture non adiabatic flame conditions. A dependency to flame enthalpy of products mass stoichiometric coefficients and kinetic rate parameters is added.

The virtual schemes are developed in Sec 4.3 and a-posteriori validated in 1-D laminar flame configurations primarily included in the optimization database such as burner stabilized flames from nearly adiabatic conditions to extinction. In Sec. 4.4, a radiative freely propagating flame configuration, not included in the training database, is computed. It is considered an intermediate test, for the developed non-adiabatic virtual mechanism, before moving to a turbulent flame application in Chap 7.

4.2 Burner stabilized flame archetype

1-D flame configuration representative of non adiabatic conditions must be introduced in the virtual chemistry learning database to take into account of flame heat losses. Laminar premixed flames stabilized on a porous isothermal burner (Kee et al. 1985) are chosen to study heat losses impact on chemistry.

In steady state conditions, 1-D burner stabilized premixed flames are governed by the following set of equations (Fiorina et al. 2003):

$$\dot{m} = \rho u \tag{4.1}$$

$$c_p \dot{m} \frac{\mathrm{d}T}{\mathrm{d}x} = \frac{\mathrm{d}}{\mathrm{d}x}\left(\lambda \frac{\mathrm{d}T}{\mathrm{d}x}\right) - \frac{\mathrm{d}T}{\mathrm{d}x} \sum_{k=1}^{N_s} \left[C_{pk} J_k\right] - \sum_{k=1}^{N_s} \left[\dot{\omega}_k h_k\right] \tag{4.2}$$

$$\dot{m} \frac{\mathrm{d}Y_k}{\mathrm{d}x} = -\frac{\mathrm{d}}{\mathrm{d}x}\left(J_k\right) + \rho \dot{\omega}_k \quad (k = 1, ..., N_s) \tag{4.3}$$

$$p = \rho \frac{R}{\overline{\overline{W}}} T \tag{4.4}$$

where x is the spatial coordinate, $\dot{m} = \dot{M}/A$ the mass flow rate per unity area. u denotes the fluid velocity, ρ the density, T the temperature and Y_k the species mass fractions. λ is the mixture thermal conductivity, c_p the constant pressure heat capacity and h_k the enthalpy of kth species. $\dot{\omega}_k$ and $J_k = \rho Y_k V_k$ denote respectively the source term and molecular diffusive flux of species k.
The prescription of heat fluxes at the burner nozzle, is ensured by imposing the following boundary conditions on the left flame side:

$$\rho^n u^n = \dot{m} \tag{4.5}$$

$$Y_k^n = Y_k^f - \frac{J_k^n}{\dot{m}} \tag{4.6}$$

$$T^n = T^f \tag{4.7}$$

where the superscript f denotes the state of the fresh gases entering the porous isothermal burner while the superscript n refers to the gas state at the nozzle which coincides with the first point of the simulated domain at $x = 0$. The user-imposed mass flow rate per unit area $\dot{m}$ controls the amount of heat losses submitted to the flame. When $\dot{m}$ is reduced below the adiabatic limit, the flame anchoring shifts on the first point of the computational domain. Because of a non zero temperature gradient at the nozzle, conductive heat fluxes, associated to species fluxed, take place between the burner nozzle and the edge of the flame. As a consequence, the enthalpy level of the flame is reduced in comparison with the adiabatic conditions. The enthalpy defect can be evaluated by integrating the temperature balance equation (Eq. 4.2) along the computational domain:

$$\Delta h = h^f\left(\phi\right) - h^{eq}\left(\phi, \dot{m}\right) = \left[\frac{\lambda}{\dot{m}} \frac{\mathrm{d}T}{\mathrm{d}x}\right]_{x=0} \tag{4.8}$$

where $h^{eq}(\phi, \dot{m})$ is the enthalpy of the fully burnt gases. The adiabatic case $(\Delta h = 0)$ is obtained for a mass flow rate $\dot{m} = \rho^f S_l^0$, where ρ^f is the fresh gases density and S_l^0 the laminar flame speed. The adiabatic flame degenerates into a 1-D freely propagating flame and no heat exchange occurs between the flame and the porous burner.

The adiabatic laminar flame consumption speed S_l^0 is defined as the integral of the burning rate across the flame brush (Poinsot and Veynante 2005). This definition can be extended to burner stabilized flames, as introduced in Mercier et al. (2014), by integrating, for the fuel, Eq. 4.3 along the direction normal to the flame front:

$$S_l = \frac{1}{\rho^f \left(Y_F^{eq} - Y_F^n\right)} \left(\int_0^{+\infty} \rho \dot{\omega}_F \left(x, \phi, \Delta h\right) dx + J_F^n \right) \tag{4.9}$$

Y_F^{eq} and Y_F^n are the fuel mass fractions respectively in the fully burnt gases and at the burner nozzle. J_F^n is the molecular diffusive flux of fuel at the burner nozzle. This formula degenerates to the classical definition in case of a freely propagating flame for $J_F^n = 0$.

4.3 Non-adiabatic virtual chemical scheme

As detailed in Chap. 3, a virtual chemical scheme is decomposed into a main mechanism and satellite sub-mechanisms dedicated to pollutant formation prediction.

Here, the main 2-step mechanism, which aims to predict the heat release and the flame temperature has the same structure, presented in Chap. 3:

$$\alpha_F^v F + \alpha_{Ox}^v Ox \rightarrow \alpha_I^v I \tag{R_1^T}$$

$$\alpha_I^v I \rightarrow \sum_{k=1}^{N_P^v} \alpha_{P_k}^v P_k \tag{R_2^T}$$

The burnt gases composition is modeled by a mixture composed of 4 virtual products P_k. A non reactive dilutant species D is added to the virtual mixture having the same thermo-chemical properties as the real species N_2. Real thermo-chemical properties are attributed to fuel F and oxidizer Ox, as well.

As detailed in Chap. 3, the 3-step mechanism is retained to predict CO formation:

$$\alpha_F^v F + \alpha_{Ox}^v Ox \rightarrow \alpha_{CO}^v CO + \left(1 - \alpha_{CO}^v\right) V_1 \tag{R_1^{CO}}$$

$$F + V_1 \rightarrow F + CO \tag{R_2^{CO}}$$

$$CO \leftrightarrow V_2 \tag{R_3^{CO}}$$

4.3.1 Thermochemical equilibrium

Enthalpy losses impact on the thermochemical equilibrium state. Indeed, fixing the equivalence ratio and the initial temperature and lowering the flame enthalpy, equilibrium temperature reduces and consequently chemical equilibrium composition changes. Virtual chemistry mechanisms have to account for such phenomena if non adiabatic flame conditions are faced. The strategies retained here to correctly recover the enthalpy defect effect on equilibrium temperature and on CO equilibrium concentration are detailed below.

4.3.1.1 Temperature

As introduced in Chapter 3, the thermodynamic properties of each species k are defined by the vector $\psi_k = (c_{p_k}, h_k)$. c_{p_k} and h_k, denote the heat capacity and the enthalpy, respectively. Thermochemical equilibrium is properly recovered if the mixture composed of N_P^v *virtual* species plus the fuel F, the oxidizer Ox and the dilutant D matches the thermodynamic properties given by the reference detailed scheme composed of N_s^d *real* species. This condition is formalized by the following relation:

$$\sum_{k=1}^{N_s^d} \psi_k^d Y_k^d|^{eq} = \sum_{k=F,Ox,D} \psi_k^v Y_k^v|^{eq} + \sum_{k=1}^{N_p^v} \psi_{P_k}^v Y_{P_k}^v|^{eq} \tag{4.10}$$

The virtual intermediate species I is fully consumed by reaction R_2^T and therefore not present at equilibrium. The equality 4.10 is applied to each equilibrium state of the mixture (characterized at constant pressure, by the equivalence ratio ϕ and enthalpy h). In the Eq. 4.10, the reference burnt gas composition $Y_k^d(\phi, \Delta h)$ is given by thermochemical equilibrium computations, where $\Delta h = h^{ad} - h$ is the enthalpy defect with respect to adiabatic conditions h^{ad}. ψ_k are in practice modeled by a NASA (Chase et al. 1975) temperature dependent polynomial functions of coefficient $a_{l,k}$, suitable for ideal gas states, as detailed in Chapters 1 and 3. By identifying each polynomial term, Eq. 4.10 is then recast into the following system of equations, valid for each state of the mixture:

$$\sum_{k=1}^{N_p^v} a_{lP_k}^v \alpha_{Pk} = \frac{\sigma_l(\phi, \Delta h)}{Y_P^v(\phi)} \quad \text{for} \quad l = 1, ..., 6 \tag{4.11}$$

where

$$\sigma_l(\phi, \Delta h) = \sum_{k=1}^{N_s^d} a_{lk}^d Y_k^d(\phi, \Delta h) - \sum_{k=F,Ox,D} a_{lk}^v Y_k^v(\phi) \tag{4.12}$$

Y_P^v is the total mass fraction of virtual products and $Y_{P_k}^v = \alpha_{Pk} Y_P^v$ where α_{Pk} are the product stoichiometric coefficients per mass unit. The strategy to recover the equilibrium thermodynamical state for all equivalence ratio ϕ and enthalpy defect Δh conditions consists in the two following steps:

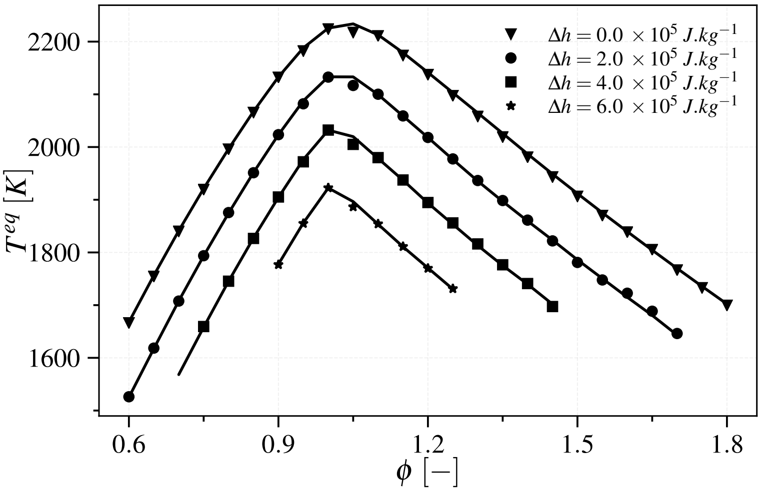

Figure 4.2: *Non-adiabatic equilibrium temperature versus equivalence ratio for different enthalpy defects, where $\Delta h = 0$ corresponds to adiabatic conditions. The mixture is composed of methane and air at an initial temperature of 300 K under atmospheric pressure conditions. Lines is the reference detailed thermochemical equilibrium solution obtained with 53 species whereas the symbols are the virtual chemistry prediction, using 4 virtual products.*

- *Equilibrium temperature under adiabatic conditions.* For that purpose, as detailed in Chap. 3 (Cailler et al. 2017), the number of virtual species N_P^v, the stoichiometric coefficients $\alpha_{P_k}^v(\phi)$ and the thermodynamic properties ψ_k^v of virtual products are optimized to minimize the cost function 3.8 in adiabatic conditions ($\Delta h = 0$) with the arbitrary constraint $\sum_{k=1}^{N_p^v} \alpha_{Pk}(\phi) = 1$. For methane/air combustion, an accurate estimation of the adiabatic flame temperature is obtained with four virtual products, i.e. with $N_p^v = 4$ (Cailler et al. 2017).
- *Equilibrium temperature under non-adiabatic conditions.* The number of virtual species N_P^v and their thermo-properties ψ_k^v identified under adiabatic conditions are conserved. A dependency on enthalpy defect is added to the stoichiometric coefficients $\alpha_{Pk}(\phi, \Delta h)$, retaining the arbitrary constraint $\sum_{k=1}^{N_p^v} \alpha_{Pk}(\phi, \Delta h) = 1$. $\alpha_{Pk}(\phi, \Delta h)$ are computed by inverting the system of algebraic equations Eqs. 4.11 for each operating condition $(\phi, \Delta h)$. This formalism adapts the virtual species composition to mimic the "real" thermo-chemical equilibrium state dependency to heat losses.

Figure 4.2 shows that the non-adiabatic flame temperature is indeed well retrieved by a virtual product mixture composed by 4 species over a wide range of equivalence ratio and enthalpy defect conditions.

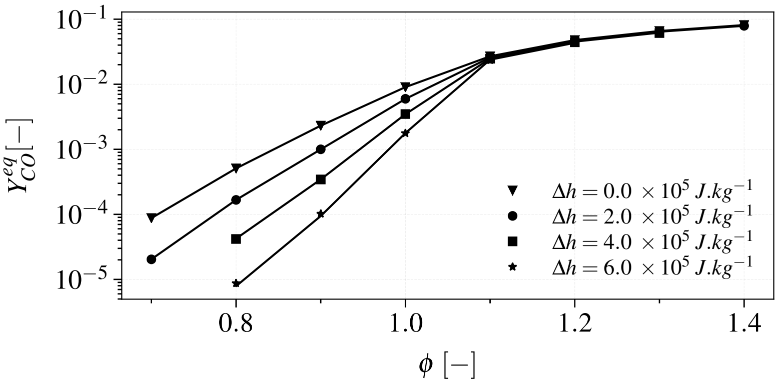

Figure 4.3: *Non-adiabatic equilibrium CO mass fraction versus equivalence ratio for different enthalpy defects, where $\Delta h = 0$ corresponds to adiabatic conditions. The mixture is composed of methane and air at an initial temperature of 300 K under atmospheric pressure conditions. Lines is the reference detailed thermochemical equilibrium solution obtained with 53 species while symbols are the virtual chemistry prediction.*

4.3.1.2 CO mass fraction

The CO mass fraction at equilibrium is given by the equilibrium constant $K_{c,3}^{CO}$ (Cailler et al. 2019) of the reversible reaction R_3^{CO}. Function of equivalence ratio for adiabatic condition, a dependency on the enthalpy defect is added to account for heat losses, as follows:

$$K_{c,3}^{CO}(\phi, \Delta h) = \frac{[V_2]^v|^{eq}(\phi, \Delta h)}{[CO]^d|^{eq}(\phi, \Delta h)} \tag{4.13}$$

where $[CO]^d|^{eq}(\phi, \Delta h)$ is obtained from reference thermochemic equilibrium computations. As V_1 is entirely consumed in the burnt gases, $[V_2]^v|^{eq}(\phi)$ is deduced from mass conservation. As shown in Fig. 4.3, the equilibrium predicted by virtual CO sub-mechanism agrees with complex detailed chemistry equilibrium computations.

4.3.2 Chemical kinetics

4.3.2.1 Heat release and flame consumption speed

The rate of progress of reactions R_1^T and R_2^T reads:

$$q_1 = A_1(\phi, \Delta h)\exp\left(\frac{-E_{a,1}}{RT}\right)[F]^{F_{F,1}}[O]^{F_{Ox,1}} \tag{4.14}$$

$$q_2 = A_2 \exp\left(\frac{-E_{a,2}}{RT}\right)[I]^{F_{I,2}(\phi,\Delta h)} \tag{4.15}$$

where A_r and $E_{a,r}$ are the pre-exponential factor and activation energy of reaction r, respectively, A_1 and $F_{I,2}$ being both function of equivalence ratio and enthalpy defect. $F_{k,r}$ is the kth species reaction order for the reaction r and $[k]$ is the kth species molar concentration. All these parameters are optimized by using a genetic algorithm in order to minimize the following fitness function:

$$C^{kinetic}_{main}\left(A_r, E_{a,r}, F_{k,r}\right) = \sum_{j=1}^{N_c} \alpha_1 \frac{|S^v_{L_j} - S^d_{L_j}|}{S^d_{L_j}} + \alpha_2 \frac{\|T^v_j\left(x\right) - T^d_j\left(x\right)\|_{L_2}}{\|T^d_j\left(x\right)\|_{L_2}}, \quad (4.16)$$

where S_{L_j} and $T_j\left(x\right)$ are the laminar flame consumption speed and the temperature profile of the j^{th} set of operating conditions $(\phi, \Delta h)$. The weights α_1 and α_2 are imposed equal to 0.01 and 0.99, respectively, to give appropriate influence to both criteria.

The optimization of kinetic rate parameter $(A_r, E_{a,r}, F_{k,r})$ is first performed by targeting a set of adiabatic freely-propagating 1-D flames computed with the GRI 3.0 (Smith et al. 2011) detailed mechanism (Cailler et al. 2017), as detailed in Chap. 3.

Then, to identify the dependency on A_1 and $F_{I,2}$ to heat losses, a second optimization step is realized by targeting non-adiabatic flamelets. The archetype retained for that purpose is the 1-D burner stabilized flame configuration described in 4.2, used in many non-adiabatic chemistry tabulation methods (Van Oijen et al. 2001; Fiorina et al. 2003; Mercier et al. 2014).

By acting on the fresh gases mass flow rates, the range of enthalpy defect is covered from adiabatic ($\Delta h = 0$) up to the extinction limit ($\Delta h = \Delta h^q$). During the optimization step, the objective function $C^{kinetic}_{main}$ is computed through Eq. 4.16 by using the definition of flame consumption speed, valid in both freely-propagating and burner-stabilized flame configurations introduced in Sec. 4.2.

A series of burner stabilized flames, computed at $\phi = 0.8$ with the non-adiabatic virtual scheme, are compared against detailed chemistry solutions in Fig 4.4 for three ratios $\Delta h/\Delta h^q$. With only 4 virtual species and 2 virtual reactions the temperature profiles are fairly reproduced compared to the detailed chemistry prediction which includes instead 53 species and 325 reactions.

As shown in Fig 4.6, the flame consumption speed given by Eq. 4.9, *a-posteriori* predicted by the non-adiabatic virtual mechanism, compares well against the detailed chemistry reference solution.

Burner stabilized flames are also computed with the original adiabatic virtual mechanism developed in Cailler et al. (2017). In this last case, the flame consumption speed shown by empty circles in Fig.4.6 presents significant bias whose magnitude increases with Δh. Indeed, as the adiabatic formulation of the virtual chemistry involves temperature dependent Arrhenius reaction rates, a sensitivity of the flame speed to the mixture enthalpy is expected. However, as shown in Fig. 4.6, the prediction is not accurate and the non-adiabatic developments correct this mis-prediction.

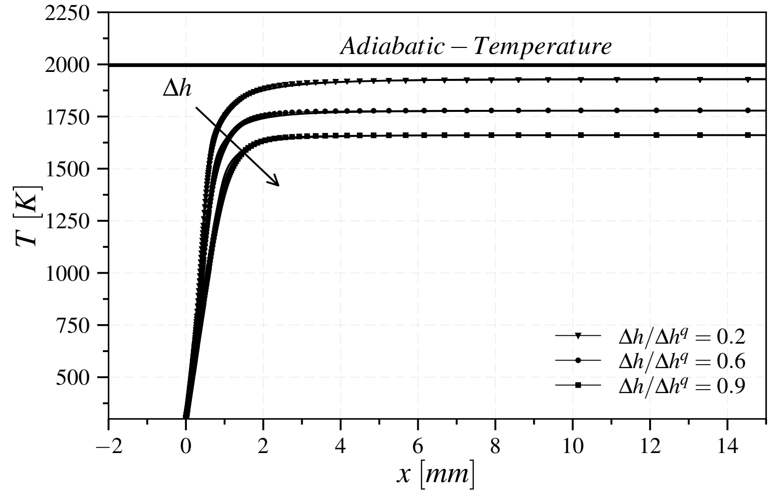

Figure 4.4: *Temperature profiles computed for burner stabilized flames at* $\phi = 0.8$. Δh *is normalized using the quenching maximum value* ($5.7 \times 10^5 J.kg^{-1}$)*. Lines: detailed chemistry solutions. Symbols: virtual chemistry solutions.*

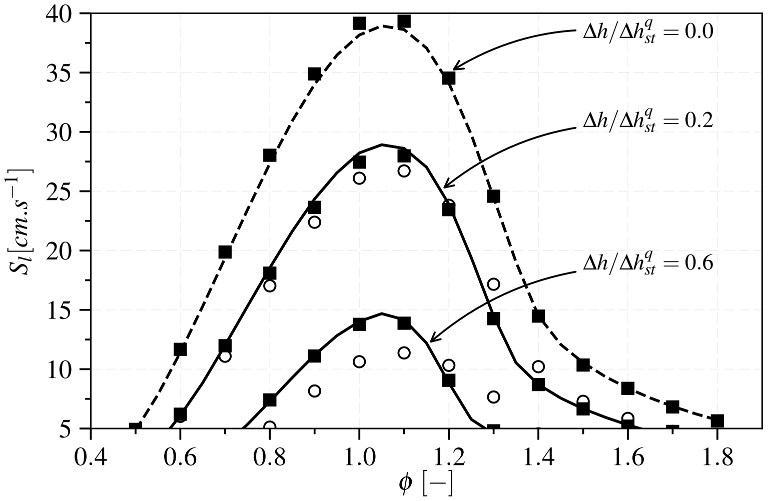

Figure 4.5: *Laminar flame consumption speed computed on freely propagating adiabatic (dashed-line) and burner stabilized (solid line) configurations versus equivalence ratio for different enthalpy defects.* Δh *is normalized using the quenching maximum value at stoichiometry* ($8.1 \times 10^5 J.kg^{-1}$)*. Lines: detailed chemistry. Squares: non-adiabatic virtual chemical scheme. Empty circle: adiabatic virtual scheme.*

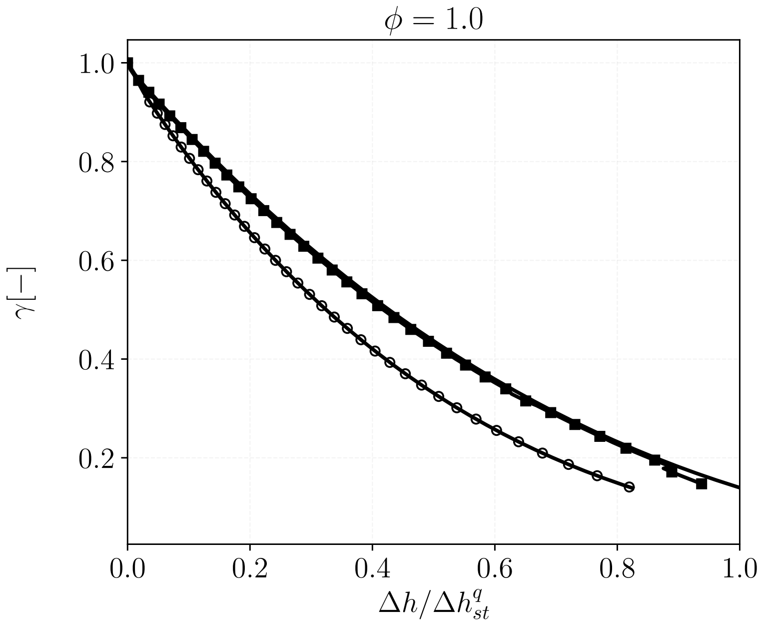

Figure 4.6: *Dimensionless laminar flame speed computed at stoichiometric conditions for different flame enthalpy losses.* Δh *is normalized using the quenching maximum value at stoichiometry (*$8.1 \times 10^5 J.kg^{-1}$*). Lines: detailed chemistry. Squares: non-adiabatic virtual chemical scheme. Empty circle: adiabatic virtual scheme.*

According to Mercier et al. (2014), the dimensionless laminar flame speed γ is introduced:

$$\gamma\left(\phi, \Delta h\right) = \frac{S_l(\phi, \Delta h)}{S_l^{ad}(\phi)} \tag{4.17}$$

The superscript *ad* denotes the adiabatic flame conditions.
Figure 4.6 shows the evolution of γ factor as function of the enthalpy defect at stoichiometric conditions. Virtual mechanism reproduces well the laminar flame consumption speed up to extinction, only if non adiabatic flamelets are added in the optimization database.

4.3.2.2 CO formation

The rate of progress of reactions R_1^{CO}, R_2^{CO} and R_3^{CO} are modeled by retaining the formulation along with the adiabatic kinetic rate parameters proposed in Chap. 3, according to Cailler et al. (2019). Extension to heat losses is achieved by applying the optimization procedure developed for the main mechanism and described in section 4.3.2.1, with pre-exponential constants $A_1(\phi, \Delta h)$, $A_2(\phi, \Delta h)$ and $A_3(\phi, \Delta h)$ tabulated in terms of both equivalence ratio and enthalpy defect:

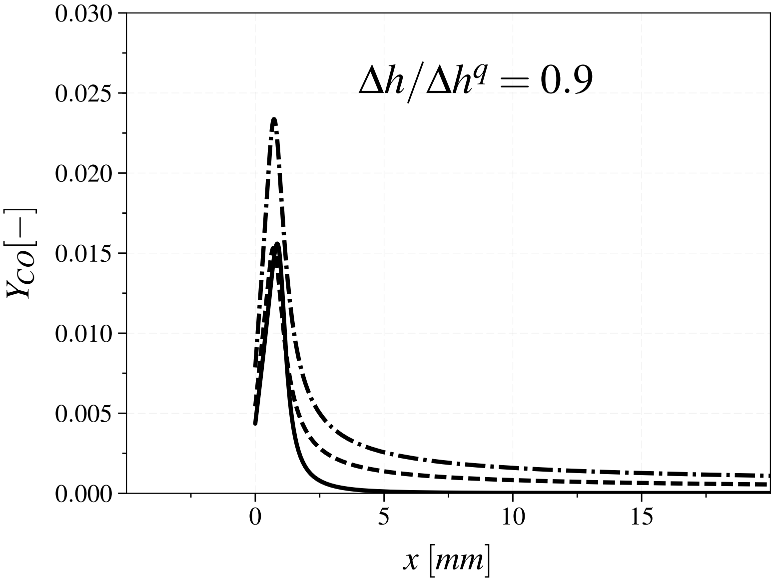

Figure 4.7: *CO mass fractions profiles computed for a burner stabilized flame at $\phi = 0.8$ and at fixed $\Delta h/\Delta h^q$. Continuous line: Detailed chemistry calculations. Dashed dot line: Adiabatic virtual chemistry calculation. Dashed line: Non adiabatic virtual chemistry calculations.*

$$q_1^{CO} = A_1 f_1(\phi, \Delta h)\exp\left(\frac{-E_{a,1}}{RT}\right)[F]^{F_F^1}\,[Ox]^{F_{Ox}^1} \tag{4.18}$$

$$q_2^{CO} = A_2 f_2(\phi, \Delta h)\exp\left(\frac{-E_{a,2}}{RT}\right)[F]^{F_F^2}\,[V_1]^{F_{V_1}^2} \tag{4.19}$$

$$q_3^{CO} = A_3 f_3(\phi, \Delta h)\exp\left(\frac{-E_{a,3}}{RT}\right)\left([CO]^{F_{CO}^3}\,[V_2]^{F_{V_2}^3} - \frac{[CO]^{R_{CO}^3}\,[V_2]^{R_{V_2}^3}}{K_{c,3}^{CO}(\phi, \Delta h)}\right) \tag{4.20}$$

In the optimization process, burner-stabilized flames are retained to constitute the target database with a fitness function based on the CO mass fraction profiles:

$$C_{CO}^{kinetic} = \frac{\|Y_{CO}^v(x) - Y_{CO}^d(x)\|_{L_2}}{\|Y_{CO}^d(x)\|_{L_2}} \tag{4.21}$$

where $Y_{CO_j}^v$ and $Y_{CO_j}^d$ are the the CO mass fraction for virtual and detailed chemistry. The cost function is evaluated for each operating condition (ϕ, Δh) included in the flamelet library.
Figure 4.7 compares, for a 1-D burner stabilized flame at fixed ϕ and enthalpy defect, the computed CO mass fractions profiles obtained with the

non-adiabatic virtual scheme and with the adiabatic one versus the reference solution. Significant differences are observed between the two solutions demonstrating the value of the developments. In particular, the influence of heat losses on the Y_{CO} peak is well predicted only with non adiabatic scheme.

4.4 1-D radiative flames

The non-adiabatic temperature and CO virtual schemes are challenged in a 1-D laminar premixed flames submitted to radiative heat losses, which have not been considered during the optimization step. Radiative fluxes modeled by $\dot{q} = \epsilon\sigma(T^4 - T_0^4)$ are added to the energy balance equation of the 1-D flame solver REGATH (Darabiha 1992) according to the following equation:

$$u\rho c_p \frac{dT}{dx} - \frac{d}{dx}\left(\lambda \frac{dT}{dx}\right) + \sum_k \left(\rho Y_k V_k c_{p_k}\right) \frac{dT}{dx} + \sum_k h_k \dot{\omega}_k + \sigma\epsilon \left(T^4 - T_0^4\right) = 0 \quad (4.22)$$

σ is the Stefan-Boltzmann constant, ϵ the gas emissivity, T is the local gas temperature and T_0 the fresh gases temperature. Detailed chemistry simulations, performed with this basic radiative model, will serve as a reference. Even not realistic, this crude radiative model is however sufficient to verify the ability of non adiabatic virtual chemistry to capture the impact of radiative heat losses on the chemical flame structure.

Figures 4.8 and 4.9 compare temperature and Y_{CO} predicted by detailed and virtual chemistry for different values of gas emissivity ε. Temperature comparisons show reasonably good agreement between virtual and detailed chemistry, with small discrepancies observed for high emissivity values. The flame front is not affected by radiative heat losses and consequently all CO profiles converge toward the ones obtained for $\varepsilon = 0$ (i.e. no radiative flame). In the post flame region, instead, radiative heat losses affect the burnt gases composition and consequently CO profiles. Virtual chemistry predicts well the CO sensitivity to radiative heat losses in the post flame.

The virtual chemical scheme still perform well in non-adiabatic configurations not included in the target learning database. This confirms that enthalpy variations act identically on the chemical flame structure regardless of the origin of heat losses as observed in Fiorina et al. (2003).

4.5 Conclusion

Virtual chemistry has been extended to account for the effect of heat losses on flame temperature profiles, laminar flame speed and CO production. The validity domain of the model has been enlarged without adding species and reactions to the reduced schemes. Detailed chemistry phenomena are well reproduced in non adiabatic premixed laminar flame simulations. After the

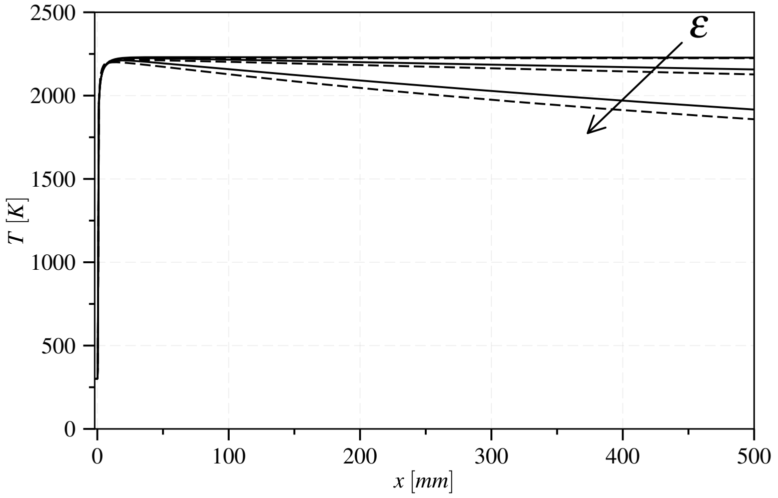

Figure 4.8: *Temperature mass fraction profiles for a series of 1D stoichiometric premixed laminar flame submitted to radiative heat losses for 3 different values of gas emissivity, respectively, $\varepsilon = 0.0$, $\varepsilon = 0.1$, $\varepsilon = 0.5$. Continuous lines: detailed chemistry. Dashed lines: non adiabatic virtual chemistry.*

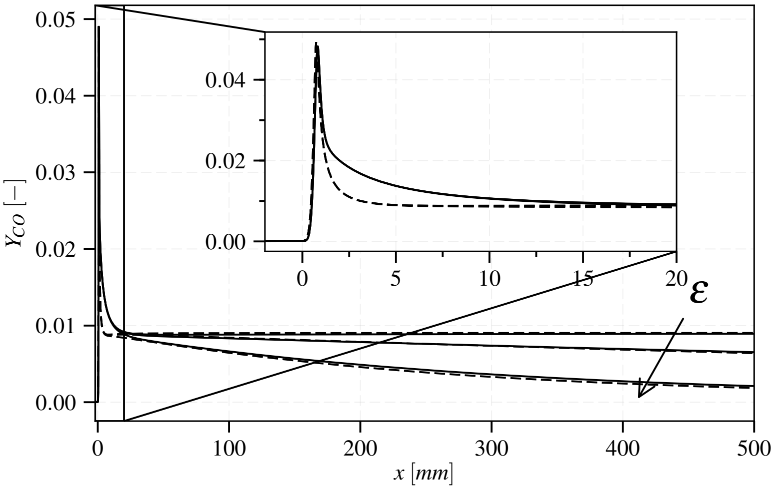

Figure 4.9: *CO mass fraction profiles for a series of 1D stoichiometric premixed laminar flame submitted to radiative heat losses for 3 different values of gas emissivity, respectively, $\varepsilon = 0.0$, $\varepsilon = 0.1$, $\varepsilon = 0.5$. A zoom close to the flame region is done for CO mass fraction profiles. Continuous lines: detailed chemistry. Dashed lines: non adiabatic virtual chemistry.*

improvements, virtual chemistry predicts well CO even in non-adiabatic laminar flame configurations (1-D radiative flame) that are not included in the optimization database.
In Chap. 7 the non adiabatic virtual scheme is used to perform a 3-D turbulent computation to further validate the approach.

Chapter 5

NO virtual sub-mechanism

Contents

A reduced order kinetic model for NO (Nitric Oxide) prediction, based on the recent virtual chemistry methodology, is developed. Two virtual chemistry mechanisms are here employed: a main mechanism for calculating the temperature and heat release rate and a second mechanism dedicated to NO prediction. To recover the chemical structure of multi-mode combustion, both premixed and non-premixed flamelets are included in the learning database used to optimize the virtual NO mechanism. A multi-zone optimization procedure is developed to accurately capture both fast and slow NO chemistry that include prompt, thermal and reburning pathways. The proposed NO sub-mechanism and optimization methodology are applied to CH_4/air combustion. Laminar 1-D premixed and non-premixed flamelet configurations are first tested. The approach is then further assessed in 2-D CFD laminar flame simulations, by providing a direct comparison against detailed chemistry. 2-D premixed, non-premixed and partially premixed flame configurations are numerically investigated. For all cases, the virtual mechanism fairly captures temperature and NO_x chemistry with only 12 virtual species and 8 virtual reactions with a drastic CPU time reduction compared to detailed chemistry.

5.1 Introduction

Nitrogen oxides (NO_x) emitted in the atmosphere, even in small quantities, cause problems to the local quality of the air. They contribute to acid rain, ozone production and smog formation. Combustion processes are the main source of nitrogen oxides emissions (International Energy Agency 2016). To limit their production engineers need numerical tools to design and optimize combustion devices. The numerical prediction of NO_x emission is a challenging task for three main reasons: *i*) NO_x are produced in very small quantities; *ii*) NO_x formation and consumption feature multiple chemical time scales and *iii*) NO_x chemical paths vary with the operating conditions (fuel, temperature, pressure, equivalence ratio, etc.). At the combustion chamber exit, NO_x are mainly composed of NO (Lefebvre 1998), whose chemistry complexity is well illustrated in Fig. 5.1. The detailed chemistry solutions of stoichiometric and rich ($\phi = 1.6$) premixed 1-D freely propagating laminar flames, obtained using REGATH solver (Darabiha 1992) and GRI3.0 detailed mechanism (Smith et al. 2011) for CH_4/air combustion, are shown. A thin flame front region zone, of the order of the millimeter, is first identified within the thermal flame thickness. NO chemistry has here a characteristic time scale comparable to the fuel oxidation process. The chemical pathway, leading to this flame front NO formation, is identified as *prompt* route (Fenimore 1971; Hayhurst and Vince 1980). A second zone is observed in the post-flame region where temperature and major species reach chemical equilibrium, while NO mass fraction still

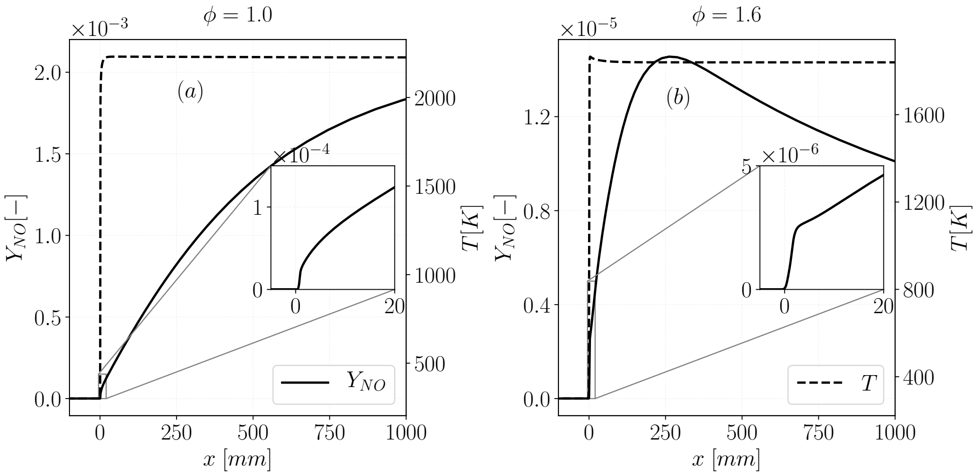

Figure 5.1: *Temperature and NO mass fraction profiles from CH_4/air 1-D premixed flames computed at two different equivalence ratios (stoichiometric and rich) with the GRI3.0 mechanism Smith, Golden, Frenklach, Eiteener, Goldenberg, Bowman, Hanson, Gardiner, Lissianski, and Qin (2011). Pressure is equal to 1 atm and the initial temperature equals 300K. The computational domain covers 1 m and includes the flame front and post-flame regions. The inner zoom plots show the NO mass fraction with a domain length comparable with the flame thermal thickness.*

evolves slowly. Furthermore, in the post-flame zone, NO chemistry exhibits two different behaviours:

- For lean, stoichiometric and moderately rich conditions: a slow, monotonic, NO production is observed until the chemical equilibrium is reached. This process is mainly governed by the *thermal* (Zeldovich 2014) route.
- For very rich conditions ($\phi \geq 1.4$): the slow NO formation competes with NO recombination (Kuo 2005) causing a non-monotonic evolution of NO mass fraction. The NO consumption is known as *reburning* process (Faravelli et al. 2003; Frassoldati et al. 2003).

Detailed chemistry mechanisms currently include and combine *prompt*, *thermal* and *reburning* pathways, to describe NO formation in as many as possible flame conditions (Glarborg et al. 2018). However hydrocarbons detailed chemical mechanisms involve hundreds of species and reactions (Lu and Law 2009) and their size further increase with the consideration of NO chemistry. For example in the GRI3.0 mechanism (Smith et al. 2011), widely used to describe CH_4 oxidation, the NO_x chemistry subset adds 17 species and 108 reactions to the initial mechanism made of 36 species and 217 reactions. As detailed in Chap. 2, the direct inclusion of detailed chemistry in CFD simulations causes CPU cost issues (Lu et al. 2009). Consequently, reduced order models are needed to mitigate the computational burden (Wang and Frenklach 1991; Lu and Law 2009; Fiorina et al. 2015). Three main modeling strategies are currently employed in the literature to model combustion chemistry at reduced

CPU cost (Fiorina et al. 2015; Fiorina 2019): global mechanisms (Westbrook and Dryer 1981; Jones and Lindstedt 1988), tabulated chemistry (Peters 1984; Gicquel et al. 2000; Van Oijen et al. 2001) and analytically reduced chemistry (Lu and Law 2008a; Pepiot-Desjardins and Pitsch 2008).

A widely used technique to capture main combustion chemistry properties is to develop and optimize empirical global and semi-global mechanisms (Fernandez-Tarrazo et al. 2006; Franzelli et al. 2010), containing from 1 to 4 reaction steps. Unfortunately these mechanisms are not suitable to predict NO because, including only a few number of species, they do not contain NO chemistry species.

An alternative strategy is the systematic reduction of detailed mechanisms. Analytically reduced mechanisms (Lu and Law 2009) have been especially developed to capture NO formation (Jaravel et al. 2017). This strategy allows to predict NO formation (Lu and Law 2008a) over multiple flame regimes with an acceptable error. However, the application of analytically reduced mechanisms to large scale simulations (Jaravel et al. 2017; Jaravel et al. 2018) is still CPU costly.

The last standard route for chemistry reduction is the “tabulated chemistry” formalism (Peters 1984; Maas and Pope 1992a). It aims at pre-computing, in a preliminary step, the reduced manifold in which the chemical subspace evolves. The manifold is finally coupled with a CFD solver to model the combustion process. In flamelet based tabulated chemistry methods, all detailed chemistry ingredients are included within a chemical table build-up from a collection of 0-D reactors or 1-D flame archetypes (Gicquel et al. 2000; Van Oijen et al. 2001; Bykov and Maas 2007b). The definition and the coordinates of the chemical database depend on the complexity of the targeted computed flame regime. In the literature, the potential of tabulated chemistry for NO formation prediction has been investigated first by Nafe and Maas (2002). Analysing PSRs (Perfectly Stirred Reactors) solutions, using the ILDM (intrincsic low-dimensional manifolds) (Maas and Pope 1992a) approach, they conclude that additional slow time scales associated with NO chemistry exist.

In the flamelet framework one strategy, to model NO formation, is to include nitrogen species the progress variable definition and to add a dedicated transport equation for NO mass fraction in the flow solver (Godel et al. 2009; Vreman et al. 2008). Another strategy, originally developed in the FPV formalism (flamelet/progress variable) (Ihme and Pitsch 2008) and then adapted to the FGM model (flamelet generated manifolds) (Ketelheun et al. 2011), consists in splitting the NO chemical source term in a production and a consumption contributions and in adding an additional transport equation for the NO mass fraction in the flow solver. An original tabulated chemistry approach, called NOMANI model, has been proposed by Pecquery et al. (2014) in the FPI (flame prolongation of ILDM) context. In the NOMANI model, the NO source term is split in a flame front contribution and in a burnt gases contribution which are extracted from two separate look-up tables (carbon and nitrogen), parametrised from two different progress variables. The NORA model (NO Relaxation Approach) (Vervisch et al. 2011), dedicated to thermal NO prediction in internal combustion engines, is another example of tabulated chemistry application to NO prediction using a collection of PSRs solutions. However particular attention is required when NO mass fraction is retained as a progress variable in the post-flame region. As shown in Fig 5.1b, in rich conditions, NO mass fraction is not strictly monotonous and cannot be considered as progress variable. Godel et al. (2009) overcame this limitation, by using an optimized combination of N-species to build-up an appropriate NO chemistry progress variable valid also for rich conditions.

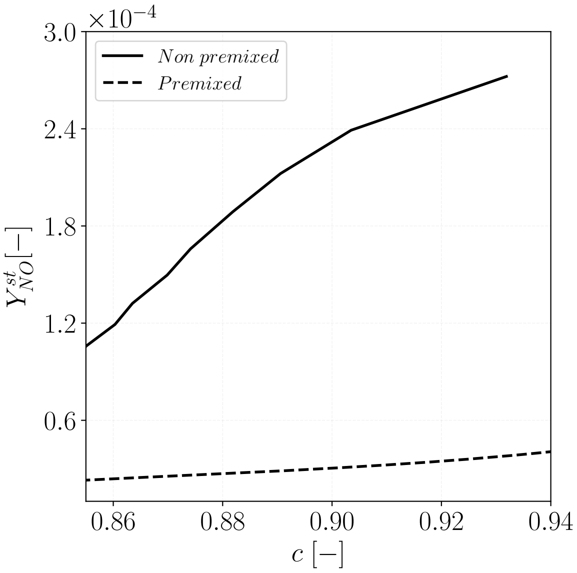

Figure 5.2: *NO mass fraction flamelet trajectories for a CH_4/air mixture, at atmospheric pressure and initial temperature of 300K, computed with GRI3.0 mechanism (Smith et al. 2011). The data are plotted as a function of progress variable (c) over the stoichiometric mixture fraction (Z_{st}) cut-plane. Data are extracted from a premixed and a non-premixed database.*

Despite the extensive and successful applications, tabulated chemistry fails when the local flame structure differs from the tabulated archetype (Fiorina et al. 2005; Nguyen et al. 2010; Bykov and Maas 2009). As an example, Fig. 5.2 shows the trajectories projection in the Y_{NO}-progress variable (c) sub-space over the stoichiometric cut-plane ($Z = Z_{st}$), of both premixed and non-premixed 1-D flamelets. The 1-D flames are computed using REGATH solver (Darabiha 1992) and GRI3.0 detailed mechanism (Smith et al. 2011) for CH_4/air mixture. The NO mass fraction trajectories show significant differences (up to an order of magnitude) between the two databases for the same mixture fraction (Z_{st}) and the same progress variable (c) values. This demonstrates that tabulated chemistry, does not perform well for NO formation in multi-mode combustion, if a single flame regime is accounted in the database generation.

An alternative reduction chemistry route, named *virtual chemistry*, has been recently developed by Cailler et al. (2017), as described in previous chapters. The method consists in building-up empirical mechanisms made of virtual species and reactions. As in tabulated chemistry, an ensemble of reference flame archetypes is first computed. However instead of "tabulating" low-dimensional manifolds, thermodynamic and chemical properties of the virtual components are optimized to fit an ensemble of targeted flame solutions. It has been observed by Cailler et al. (2019) that multi-mode combustion regimes are well captured with a limited number of virtual species and virtual reactions an soon as both premixed and non-premixed flame elements are included in the learning database. CO emissions have been accurately predicted in a turbulent confined aeronautical combustor exposed to heat losses (Maio et al. 2019). Virtual chemistry is then a good candidate to model NO formation in hybrid flame structures.

The objective of the present study is to propose a new reduced mechanism in the virtual chemistry formalism able to predict NO in hybrid combustion regimes. The challenge is to account for all the NO chemistry pathways, included in detailed chemistry for premixed and non-premixed flames. In section 5.2, the NO mechanism is introduced whereas the optimization strategy and the application to CH_4/air combustion are described in section 5.3. Section 5.4 shows and discusses the validation results in 1-D premixed freely propagating flames and in non-premixed counterflow flames, comparing the virtual chemistry results against simulations carried out with the detailed kinetic mechanism. In section 5.5, the proposed mechanism is further assessed in 2-D CFD laminar flame simulations, employing the open source solver laminarSMOKE (Cuoci et al. 2013a). A premixed, a non-premixed and a partially premixed flame configuration are studied.

5.2 Virtual mechanism architecture

5.2.1 Principle

Virtual chemistry architecture and theoretical bases, already described in Chap. 3, are here briefly reminded. Virtual chemistry is a reduced order model which aims to describe global flame quantities, temperature and pollutant formation (Cailler et al. 2017; Cailler et al. 2019; Maio et al. 2019). The strategy consists in designing virtual mechanisms composed of a reduced set of virtual species interacting through a reduced number of virtual reactions (Cailler et al. 2017). Virtual species thermo-chemical properties and virtual reactions kinetic constants are optimized to target “real” flame properties of interest such as temperature, heat release and pollutant concentration. As discussed in Cailler et al. (2019), a virtual chemical mechanism is composed of one main mechanism and several satellite virtual sub-mechanisms. The virtual main mechanism is trained to reproduce the mean mixture properties, temperature, density and heat release rate. The learning database is made of an ensemble of flame archetypes computed with detailed chemistry. The main mechanism is coupled with the flow solver through the mass, momentum and energy equations. Detailed chemistry ingredients are accounted for during the optimization stage of the main mechanism but, as integrated flame quantities (flame speed, heat release, etc.) and temperature are targeted, individual species informations are not accessible anymore. Satellite virtual sub-mechanisms have therefore been introduced to access specific species mass fractions of interest. As an example, a virtual sub-mechanism dedicated to CO prediction has been developed in Cailler et al. (2019).

A virtual mechanism for NO prediction is designed in this section. For that purpose, the virtual chemistry formalism is first presented (section 5.2.2) and the main virtual mechanism is then briefly reminded in section 5.2.3. A novel virtual chemistry architecture dedicated to NO prediction is discussed in section 5.2.4.

5.2.2 Virtual chemistry theoretical base

A virtual mechanism X includes N_s virtual species and N_r virtual reactions. The virtual mechanism X is composed by an ensemble of reversible virtual reactions R_i^X:

$$\sum_{k=1}^{N_s^i} \alpha_{ki}^{'} \nu_k \leftrightarrow \sum_{k=1}^{N_s^i} \alpha_{ki}^{''} \nu_k \tag{5.1}$$

where N_s^i is the number of virtual species involved in the virtual reaction R_i^X. ν_k denotes the k^{th} virtual species whereas $\alpha_{ki}^{'}$ and $\alpha_{ki}^{''}$ are the reactant and product mass stoichiometric coefficients, respectively. The reaction progress q_i, for the reaction R_i^X, is closed using a finite rate formulation with modified reaction orders:

$$q_i = k_{fi} \prod_{k=1}^{N_s} [X_k]^{F_k^i} - k_{bi} \prod_{k=1}^{N_s} [X_k]^{B_k^i} \quad i = R_i^X \tag{5.2}$$

$[X_k]$ is the k^{th} molar species concentration, F_k^i and B_k^i are the forward and backward reaction orders corresponding to the k^{th} species in the i^{th} reaction. k_{fi} and k_{bi} are the forward and backward rate constants. k_{fi} is expressed using an Arrhenius-like formulation:

$$k_{fi} = A_i T^{\beta_i} \exp\left(\frac{-E_a^i}{RT}\right) \quad i = R_i^X \tag{5.3}$$

A_i is the pre-exponential factor, E_a^i is the activation energy and in the modified Arrhenius law a temperature exponent β_i is added. When R_i^X is a reversible reaction, the backward rate constant is related to the forward one through the equilibrium constant $K_{eq,i}$:

$$k_{bi} = \frac{k_{fi}}{K_{eq,i}} \quad i = R_i^X \tag{5.4}$$

The kinetic rate parameters of virtual reactions in the virtual mechanism X are optimized through the evolutionary algorithm proposed by Cailler et al. (2017). The optimization problem consists in minimizing the following cost function C:

$$C = f\left(\mathbf{w}^v\left(\chi^{\mathbf{v}}\right), \mathbf{w}^d\left(\chi^{\mathbf{d}}\right)\right) \tag{5.5}$$

where $\mathbf{w} = (\rho u, \rho v, \rho w, \rho Y_k, T)$ is the state vector, defined as the solution of momentum, species and energy governing balance equations, function of the vector of parameters χ. The vector χ includes the set of thermodynamic, transport and kinetic rate parameters, whereas ^{d} and ^{v} superscripts refer to detailed and virtual chemistry, respectively. The cost function C aims to compare the virtual and detailed chemistry solutions through a linear combination of selected normalized flame quantities. $\chi^{\mathbf{d}}$ is given by the detailed thermo-chemistry database, retained as a reference, whereas $\chi^{\mathbf{v}}$ is the set of thermo-chemistry and transport parameters to optimize, which constitutes the output of the optimization procedure.

5.2.3 Main mechanism

The 2-step main virtual mechanism proposed in (Cailler et al. 2017) is retained:

$$\alpha_F^1 F + \alpha_{Ox}^1 Ox \rightarrow I \tag{R_1^T}$$

$$I \rightarrow \sum_{k=1}^{N_P^v} \alpha_{P_k}^2 P_k \tag{R_2^T}$$

A non reactive dilutant species D is added to the mixture. The reaction progresses of the two irreversible reactions R_1^T and R_2^T are closed with an Arrhenius-like formulation as follows:

$$q_1 = A_1\left(Z\right)\exp\left(\frac{-E_a^1}{RT}\right)\left[F\right]^{F_F^1}\left[O\right]^{F_{Ox}^1} \tag{5.6}$$

$$q_2 = A_2 \exp\left(\frac{-E_a^2}{RT}\right)\left[I\right]^{F_I^2(Z)} \tag{5.7}$$

The pre-exponential constant A_1 and the forward reaction order F_I^2 are tabulated as a function of the local mixture fraction. In practice, the local mixture fraction Z is identified from the non reactive dilutant mass fraction Y_D as no preferential species diffusion is considered. A one-to-one relation can be established between Y_D and Z, according to the following equation:

$$Z = \frac{Y_D - Y_D|^{Ox}}{Y_D|^F - Y_D|^{Ox}} \tag{5.8}$$

where the superscripts F and Ox denotes the conditions in pure fuel and oxidizer, respectively.
This 2-step structure captures equilibrium flame properties, laminar flame consumption speed and temperature in both lean and rich regimes. Further details and validation cases are developed in Cailler et al. (2017).

5.2.4 NO mechanism

A mechanism architecture is proposed to account for the whole NO chemical pathways evidenced previously in Fig. 5.1: *prompt*, *thermal* and *reburning*. For that purpose, the following NO virtual sub-mechanism, composed of 6 reactions, is proposed:

$$\begin{aligned}
\alpha_F^1 F + \alpha_{Ox}^1 Ox &\rightarrow \alpha_{V_1}^1 V_1 + \alpha_{V_2}^1 V_2 + \alpha_{V_3}^1 V_3 && (R_1^{NO})\\
V_1 + F + Ox &\rightarrow \alpha_{NO}^2 NO + \alpha_{V_2}^2 V_2 + F + Ox && (R_2^{NO})\\
F + NO &\rightarrow F + V_2 && (R_3^{NO})\\
V_3 &\rightarrow NO && (R_4^{NO})\\
V_3 &\rightarrow V_2 && (R_5^{NO})\\
V_2 &\leftrightarrow NO && (R_6^{NO})
\end{aligned}$$

where α_k^i are the mass stoichiometric coefficients associated to species k in the reaction R_i. An ensemble of virtual species V_1, V_2 and V_3 is first produced through the initiation reaction R_1^{NO}. To ensure consistency in fuel (F) and oxidizer (Ox) consumption, the kinetic rate parameters of reaction R_1^{NO} are identical to those of the initiation reaction R_1^T of the main virtual mechanism. Reactions R_2^{NO} and R_3^{NO} are dedicated to model the fast NO chemistry, which is dominant at the flame front scale. R_3^{NO} is designed to reproduce the fast NO reburning that is especially relevant when an excess of hydrocarbon radicals is present in the system (Frassoldati et al. 2003). In addition, as it will be shown in section 5.4.3, using two reactions (R_2^{NO}-R_3^{NO}) to model fast NO formation, instead of one (R_2^{NO}), enables a better prediction of both premixed and non-premixed NO profiles.
Virtual reactions R_4^{NO} to R_6^{NO} describe the NO formation associated with slow post-flame chemistry. It includes thermal NO pathway and slow NO reburning

phenomena. As discussed later in section 5.4.2, the combination of three reactions allows an efficient description of slow NO post-flame pathways in both lean and rich regimes. Finally, the equilibrium reaction R_6^{NO} ensures that the chemical equilibrium conditions are well retrieved.
The rate of progress for the reactions set R_1^{NO}-R_6^{NO} are closed using the following Arrhenius-like expressions:

$$q_1 = A_1 \exp\left(\frac{-E_{a,1}}{RT}\right) [F]^{F_{F,1}} [O]^{F_{Ox,1}} \tag{5.9}$$

$$q_2 = A_2\,(Z) \exp\left(\frac{-E_a^2}{RT}\right) T^{\beta_T^2} [V_1]^{F_{V_1}^2} [F]\,[Ox] \tag{5.10}$$

$$q_3 = A_3 \exp\left(\frac{-E_a^3}{RT}\right) [F]\,[NO]^{F_{NO}^3} \tag{5.11}$$

$$q_4 = A_4\,(Z) \exp\left(\frac{-E_a^4}{RT}\right) [V_3]^{F_{V_3}^4} \tag{5.12}$$

$$q_5 = A_5\,(Z) \exp\left(\frac{-E_a^5}{RT}\right) [V_3]^{F_{V_3}^5} \tag{5.13}$$

$$q_6 = A_6\,(Z) \exp\left(\frac{-E_a^6}{RT}\right) \left([NO]^{F_{NO}^6} [V_2]^{F_{V_2}^6} - \frac{[NO]^{B_{NO}^6} [V_2]^{B_{V_2}^6}}{K_c^6}\right) \tag{5.14}$$

The equilibrium constant for the reversible reaction R_6^{NO} is computed as follows:

$$K_c^6 = \frac{[NO]^d\,|^{eq}}{[V_2]^v\,|^{eq}} \tag{5.15}$$

where $[NO]^d\,|^{eq}$ is the equilibrium NO molar concentration obtained from detailed thermodynamical equilibrium computations. $[V_2]^v\,|^{eq}$ is computed from the knowledge of V_2 mass fraction at equilibrium condition. By convention, the sum of virtual species mass fractions equals one Cailler, Darabiha, and Fiorina (2019), therefore:

$$\sum_{k=1}^{N_s^{NO}} Y_k = 1 \tag{5.16}$$

N_s^{NO} is the number of species involved in the NO virtual sub-mechanism. Consequently, Y_{V_2} is computed from Eq. 5.16 as:

$$Y_{V_2}|^{eq} = 1 - Y_F|^{eq} - Y_{Ox}|^{eq} - Y_{NO}|^{eq} - Y_D|^{eq} - Y_{V_1}|^{eq} - Y_{V_3}|^{eq} \tag{5.17}$$

$Y_{V_1}|^{eq}$ and $Y_{V_3}|^{eq}$ are theoretically equal to zero at equilibrium since the species V_1 and V_3 are completely consumed through the reactions R_2^{NO}, R_4^{NO} and R_5^{NO}. $Y_F|^{eq}$, $Y_{Ox}|^{eq}$ and $Y_D|^{eq}$ are known quantities from the main virtual mechanism solution while $Y_{NO}|^{eq}$ is assumed equal to the reference one.

However, it has been noticed that for very lean and rich conditions $Y_{V_1} \neq 0$ at equilibrium. In the 2ZONE optimization, detailed in section 5.3.3, $Y_{V_1}|^{eq}$ is however a known quantity at the end of the flame-front block optimization and it is easily accounted for in Eq. 5.17 for computing $Y_{V_2}|^{eq}$, before performing the post-flame block optimization.

R_6^{NO} reaction orders are constrained by the following equations to ensure a net reaction rate equal to zero at equilibrium:

$$B_{NO}^6 = F_{NO}^6 + 1 \tag{5.18}$$

$$B_{V_2}^6 = F_{V_2}^6 - 1 \tag{5.19}$$

The set of kinetic rate parameters to optimize includes the pre-exponential constants A_i the activation energies E_a^i, forward reaction orders F_k^i and species stoichiometric coefficients α_k^i for reactions R_1^{NO} to R_6^{NO} and the temperature exponent β_T^2. To limit the number of parameters to optimize, F and Ox reaction order are set equal to 1 and the kinetic parameters for the reaction R_1^{NO} are kept equal to the R_1^T ones. To capture the dependency of NO mass fraction production/consumption to the equivalence ratio the pre-exponential constants A_2, A_4, A_5 and A_6 depend on the mixture fraction Z, computed from the local dilutant mass fraction Y_D (as in Eq. 5.8).

Reactions R_4^{NO} and R_5^{NO} are needed to retrieve the slow NO formation and its successive recombination characterizing rich flame conditions, as discussed in section 5.1. This phenomenon is observed in the NO detailed profiles starting from $\phi = 1.4$. In practice, reactions R_4^{NO} and R_5^{NO} are activated for $\phi \geq 1.4$ through the stoichiometric coefficient $\alpha_{V_3}^1$. Section 5.4.2 discusses the importance of adding reactions R_4^{NO} and R_5^{NO} for rich conditions. The following section 5.3 gives details about the optimization procedure.

5.3 Optimization of the NO virtual scheme

5.3.1 Principle

Figure 5.3 summarizes the general NO mechanism optimization procedure. The vector χ^v contains the ensemble of selected kinetic rate parameters for the virtual NO sub-mechanism, as discussed in the previous section. N random individuals, corresponding to N χ_n^v vectors, evolve for a certain number of generations N_{gen}, in the optimization loop, according to the evolutionary algorithm designed by Cailler et al. (2017). Each parameter of the vector χ_n^v may mutate in the genetic optimization loop within user-defined lower and upper bounds.

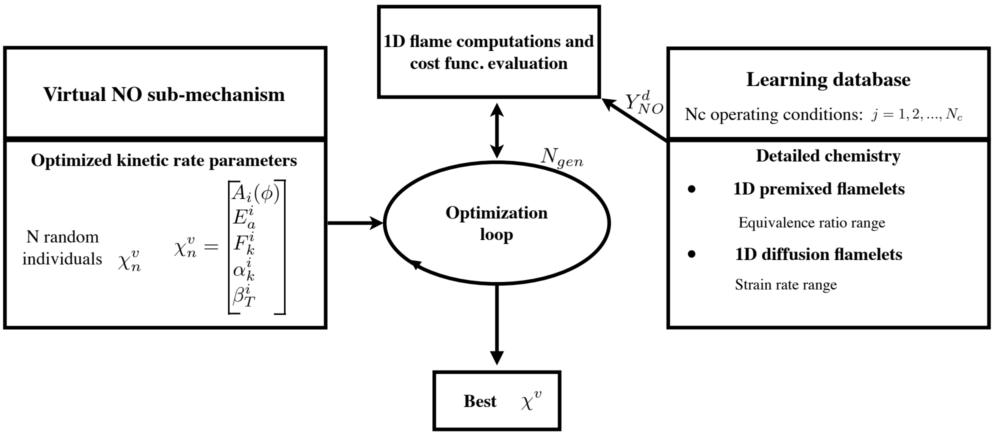

Figure 5.3: *Schematic view of the general procedure employed to optimize the kinetic rate parameters of the NO virtual mechanism.*

After a pre-defined number of genetic generations N_{gen}, the best individual (best χ^v vector) is identified as output.
As discussed in Cailler et al. (2019), to capture pollutant formation in multi-mode combustion, the learning database must include informations from both 1-D premixed flames and 1-D non-premixed counterflow flames. To account for these two different flamelet archetypes, the cost function C_{NO} used in the optimization procedure is computed as:

$$C_{NO} = C_{NO}^{P} + C_{NO}^{NP} \tag{5.20}$$

where C_{NO}^{P} and C_{NO}^{NP} are the cost functions relative to premixed flamelet library and non-premixed one, respectively. C_{NO}^{P} is defined from the NO mass fraction L_2 norm as follows:

$$C_{NO}^{P} = \sum_{i=1}^{N_\phi} \frac{\| Y_{NO}^{P,v}\left(x, \phi_i^0\right) - Y_{NO}^{P,d}\left(x, \phi_i^0\right) \|_{L_2}}{\| Y_{NO}^{P,d}\left(x, \phi_i^0\right) \|_{L_2}} \tag{5.21}$$

where $Y_{NO}^{P,v}$ and $Y_{NO}^{P,d}$ are the NO mass fraction of a freely propagating premixed flame computed with the virtual and detailed mechanism, respectively. N_ϕ is the number of premixed flamelets included in the learning database. ϕ_i^0 is the fresh gases equivalence ratio of the ith flamelet. x is the premixed flame coordinate normal to the flame front. $x \in \mathcal{A}^P$, where $\mathcal{A}^P$ is the spatial subspace targeted during the optimization procedure for each premixed flamelet. If the whole flame domain is targeted during the optimization process, then $\mathcal{A}^P = [-\infty, +\infty]$, where $x = -\infty$ and $x = +\infty$ correspond to fresh and burn gases conditions, respectively.

C_{NO}^{NP} is defined from the NO mass fraction maximum value along the non-premixed flame domain:

$$C_{NO}^{NP} = \sum_{j=1}^{N_a} \frac{\max_y \left| Y_{NO}^{NP,v}(y, a_j) \right| - \max_y \left| Y_{NO}^{NP,d}(y, a_j) \right|}{\max_y \left| Y_{NO}^{NP,v}(y, a_j) \right|} \tag{5.22}$$

where $Y_{NO}^{NP,v}$ and $Y_{NO}^{NP,d}$ are the NO mass fraction of a non-premixed counterflow flame computed with the virtual and detailed mechanism, respectively. N_a is the number of non-premixed flamelets included in the learning database and a_j is the strain rate of the jth flamelet. $a_j \in \mathcal{A}^{NP}$, where $\mathcal{A}^{NP}$ is the range of strain rates targeted. If the whole non-premixed flamelet library is considered, then $\mathcal{A}^{NP} = [a_0, a_{N_a}]$, where a_0 and a_{N_a} correspond to null and quenching strain rates a_q, respectively. y is the 1-D flame coordinate. Two optimization strategies, based on 1 or 2 zones, are now compared in the following sections.

5.3.2 Single zone optimization (1ZONE)

The 1-zone optimization (1ZONE) is a brute-force approach that consists in optimizing all reactions rate parameters included in the vector χ^v in one step. During this step, the whole spatial dimension of the N_ϕ reference premixed flames is targeted: $\mathcal{A}^P = [-\infty, +\infty]$. Simultaneously the entire range of steady state strained non-premixed flamelets is also considered: $\mathcal{A}^{NP} = [a_0, a_q]$. During this step, all kinetic parameters of reactions R_1^{NO}-R_6^{NO} are optimized. As it will be shown further, the too high number of kinetic rate parameters optimized in a single step causes the failure of the optimization algorithm. A 2-zone optimization method is therefore introduced.

5.3.3 2-zone optimization (2ZONE)

The optimization procedure is split into two consecutive steps dedicated to the optimization of fast and slow NO formations process, respectively. To reduce the number of free kinetic rate parameters to account at each step, reaction R_1^{NO}-R_6^{NO} are optimized through the two following steps:

1. *Flame front block* optimization. Virtual elementary reactions R_1^{NO}-R_3^{NO} designed to capture flame front NO formation are trained to reproduce only fast time scales phenomena. Fast time scales learning regions representative of NO formation need to be extracted from the whole set of target flames, which gathers here premixed and non-premixed flames.
2. *Post-flame block* optimization. The virtual elementary reactions R_4^{NO}-R_6^{NO} are optimized to recover the post-flame NO formation which mostly characterize premixed flames burnt gases. During the post-flame block optimization, kinetic parameters of reactions R_1^{NO}-R_3^{NO}, issued from the first step, are conserved.

A criterion is required to distinguish the learning subspaces dedicated to the *Flame front* and *Post-flame* optimization steps, respectively. The definition of the criterion and the subspaces separation procedure is detailed in Appendix A. For that purpose, two physical quantities (δ_{FF} and a_{FF}), dedicated respectively to premixed and non-premixed flamelets, are defined to distinguish the fast NO formation time scale from the slow one. δ_{FF} is the critical length scale for premixed flamelets. For $x \in [-\infty, \delta_{FF}]$, fast time scales, characteristics of *prompt* NO, dominate. At the opposite *thermal* and *reburning* are more important for $x \in [\delta_{FF}, +\infty]$. a_{FF} is the critical strain rate for non-premixed strained flamelets. For $a \in [a_{FF}, a_q]$ fast NO time scales dominate while for $a \in [0, a_{FF}]$ slow time scales are more important.
The optimization process is then split into two steps:

Step 1 The *Flame front block* is optimized using flame data characteristic of *prompt* NO process. In practice, the cost functions C^P_{NO} and C^{NP}_{NO}, computed by Eq.s 5.21 and 5.22, are restricted to the subspaces $\mathcal{A}^P = [-\infty, \delta_{FF}]$ and $\mathcal{A}^{NP} = [a_{FF}, a_q]$. During this step, only kinetic parameters of reactions R^{NO}_1-R^{NO}_3 are optimized.

Step 2 The *Post-flame block* is optimized using flame data characteristic of *slow* NO processes. In practice, the cost functions C^P_{NO} and C^{NP}_{NO}, computed by Eq.s 5.21 and 5.22, include the entire premixed flamelet space $\mathcal{A}^P = [-\infty, +\infty]$. Analysis of DNS of partial-oxidation processes have shown than, in post-flame regions characterized by slow chemistry phenomena, molecular diffusion is less important than chemical reactions (Caudal et al. 2015). According to ILDM theory Maas and Pope (1992a), chemical trajectories followed by premixed and non premixed flames in the composition space are therefore identical. In the present work, only premixed flamelets are therefore targeted to optimize slow NO chemistry: $\mathcal{A}^{NP} = \varnothing$. During this step, only kinetic parameters of reactions R^{NO}_4-R^{NO}_6 are optimized. The two learning procedures, 1ZONE and 2ZONE, are now compared on a simple test case.

5.3.4 Comparison of 1ZONE and 2ZONE optimization procedures

The learning database retained to optimize the NO virtual mechanism is made of a single stoichiometric CH_4/air premixed flamelet. Both 1ZONE and 2ZONE optimized solutions are *a-posteriori* compared against the targeted solution in Fig. 5.4. The slow NO formation, visible over the entire computational domain, from $x = 0$ to $x = 5$ m, is fairly well captured by the two algorithms. But the 1ZONE (dashed line) optimized scheme fails to capture the prompt NO formation, as evidenced in the inner graph which focuses on the thermal flame thickness (from $x = 0$ to $x = 25$ mm). This inaccuracy is corrected by the

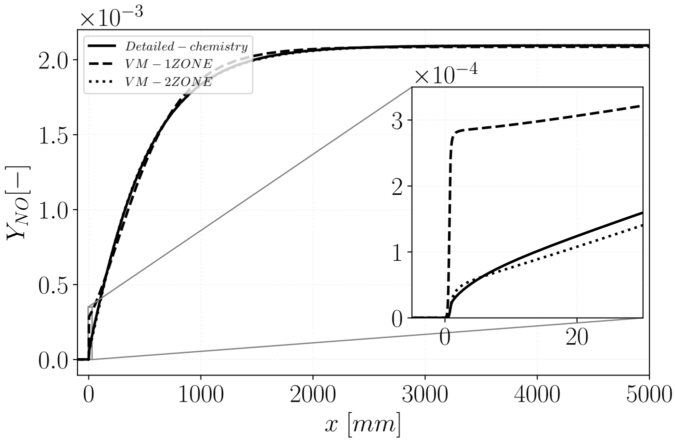

Figure 5.4: *Comparison of the NO mass fraction computed with virtual chemistry and reference detailed chemistry, at stoichiometric conditions. Virtual chemistry results are shown for the 1-zone optimization (1ZONE) and the 2-zone optimization (2ZONE). The comparison is proposed either over the whole computational domain and in the flame front region.*

2ZONE (dotted line) algorithm which is able to predict both fast and slow NO chemistry.

To understand the difference between 1ZONE and 2ZONE, the error ϵ between the targeted flame data and the two optimized solutions *a-posteriori* obtained with the virtual mechanism is introduced:

$$\epsilon(\mathcal{A}') = \frac{\| Y_{NO}^{P,v}\left(x, \phi^0\right) - Y_{NO}^{P,d}\left(x, \phi^0\right) \|_{L_2}}{\| Y_{NO}^{P,d}\left(x, \phi^0\right) \|_{L_2}} \qquad \text{for} \quad x \in \mathcal{A}' \tag{5.23}$$

where $\mathcal{A}'$ is the 1-D spatial subspace on which the error ϵ is computed. The three subspaces $\mathcal{A}' = [-\infty, +\infty]$, $\mathcal{A}' = [-\infty, \delta_{FF}]$ and $\mathcal{A}' = [\delta_{FF}, +\infty]$ are retained to measure ϵ along the the *whole flame*, *flame front* region and *post-flame* region, respectively.

Figure 5.5 plots the evolution of these three errors as function of the generation number N_{gen} for both 1ZONE and 2ZONE algorithms. The error computed over the *whole domain* decreases as expected with the 1ZONE procedure during 15-20 generations and then it reaches a plateau around 2% (Fig. 5.5, left). However, better results are observed with the 2ZONE mechanism. With the 1ZONE procedure, a very poor convergence of the error is observed in the *flame front*, which stays above 1000% (Fig. 5.5, center). The limited accuracy of the 1ZONE solution is actually due to failure of the optimization process, where the number of kinetic rate parameters optimized in a single step is too high.

Results are greatly improved by the 2ZONE algorithm where the convergence of the error in the *flame front* is ensured. As a consequence, the error on the prompt NO prediction decreases below 5% after 20 generations. In addition,

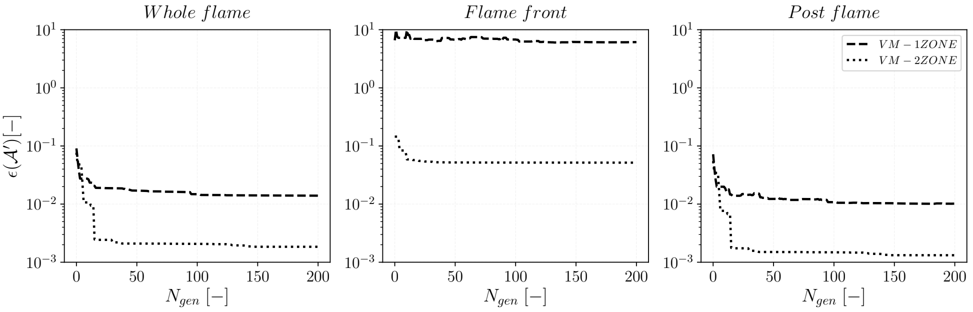

Figure 5.5: *Error evolution during the optimization procedure. N_{gen} is the generation number performed by the evolutionary algorithm. The error is shown for the single zone optimization (VM-1ZONE) and for the two zone optimization (VM-2ZONE) and it is computed using three subspaces: whole flame, flame front and post-flame regions.*

the *post-flame* error of the 2ZONE optimization procedure is also decreased by more than an order of magnitude compared with the 1ZONE (Fig. 5.5, right).

5.4 Results: 1-D flames

This section presents the 1-D results of the R_1^{NO}-R_6^{NO} NO virtual mechanism optimized according to the 2ZONE strategy over CH_4/air hybrid flamelets. Results for premixed freely propagating flames, for several mixture equivalence ratios, and for diffusion flames for several flame strain rates are presented and compared to simulations carried out with the detailed kinetic mechanism.

5.4.1 Virtual mechanism optimization for multi-mode combustion

Figure 5.6 describes the 2ZONE optimization procedure. The reference detailed chemistry premixed and non-premixed flamelets are computed using the GRI3.0 mechanism (Smith et al. 2011).

The N_ϕ premixed flamelets retained to compute the cost function C_{NO}^P from Eq. 5.21 cover the whole flammability limit: 0.6< ϕ_0 <1.8. The equivalence ratio step between two flamelets ($\Delta\phi$) is equal to 0.1. For 1-D non-premixed counterflow flames, NO profiles representative of flames having a strain rate a greater than the critical value $a_{FF} = 50s^{-1}$ are included. For this application, the subspace $\mathcal{A}^{NP} = \{50, 150, 300\}$ s^{-1} is retained to build up the non-premixed learning library.

Three virtual mechanisms of different sizes are generated in order to assess the influence of the number of virtual species and reactions. The complete virtual mechanism R_1^{NO}-R_6^{NO} is indicated with the abbreviation VM-6R. Two smaller mechanisms VM-4R and VM-5R are also considered. VM-4R is obtained by removing R_4^{NO} and R_5^{NO} from the VM-6R mechanism before the optimization

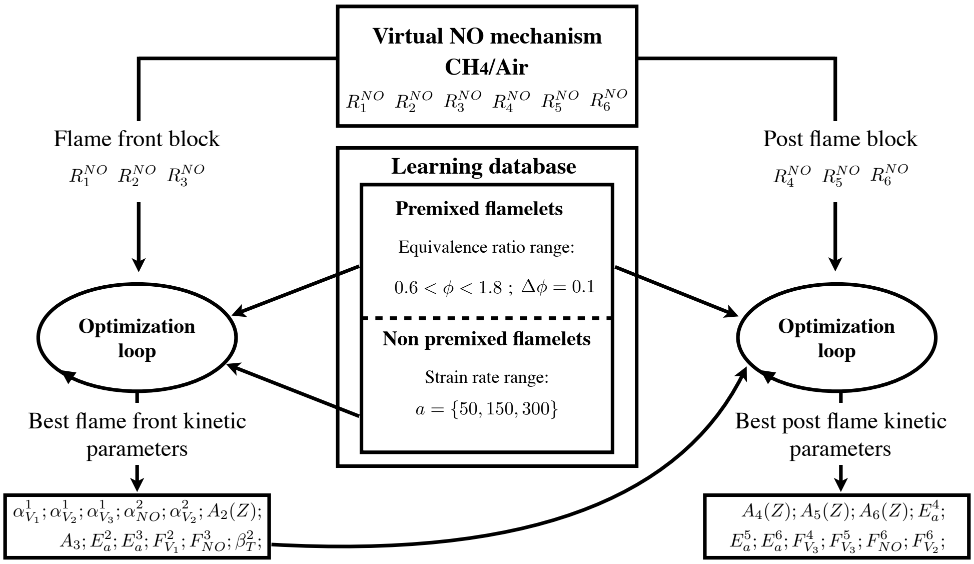

Figure 5.6: *Virtual NO mechanism optimization procedure applied to CH_4/air combustion. The 2ZONE optimization is applied.*

Table 5.1: *Summary of the three optimized virtual NO mechanisms. The virtual reactions that are included in each mechanism are indicated.*

Mechanism	Reactions	Nb of reactions for *Flame front*	Nb of reactions for *Post flame*	Nb of species
VM-6R	R_1^{NO}-R_6^{NO}	3	3	6
VM-4R	R_1^{NO}-R_3^{NO} R_6^{NO}	3	1	5
VM-5R	R_1^{NO}-R_2^{NO} R_4^{NO}-R_6^{NO}	2	3	6

procedure. Whereas three reactions R_1^{NO}-R_3^{NO} are dedicated to capture fast processes, only R_6^{NO} is kept to handle slow time scales and to retrieve equilibrium conditions. At the opposite VM-5R is designed by removing R_3^{NO} from the VM-6R mechanism. The three elementary reactions R_4^{NO}-R_6^{NO} are retained for slow process but the number of "fast" elementary reactions is restricted to R_1^{NO} and R_2^{NO}. Table 5.1 presents a summary of the three mechanism's properties. Molecular diffusive fluxes of species belonging to both main and NO virtual schemes are modeled with a unity Lewis number assumption. However, as discussed in Cailler et al. (2019), this assumption still enables a correct prediction of unstretched laminar flame consumption speed and species profiles across planar flame fronts, as the targeted 1-D flame solutions used to calibrate the main virtual scheme include differential diffusion effects.

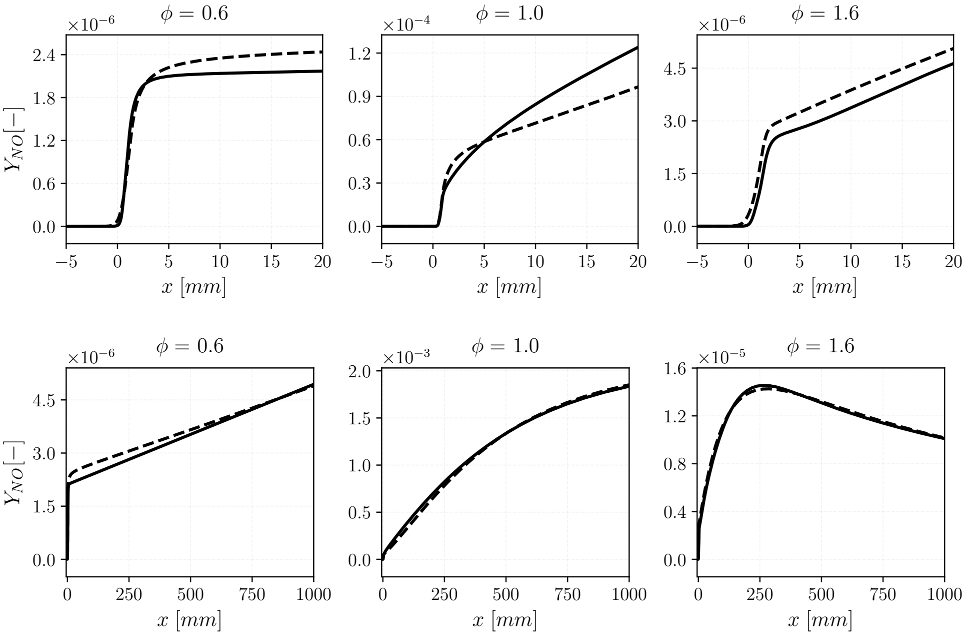

Figure 5.7: *NO mass fraction profiles for a lean ($\phi = 0.6$), a stoichiometric ($\phi = 1.0$) and a rich ($\phi = 1.6$) equivalence ratio. Virtual chemistry VM-6R NO solution is compared versus the reference detailed chemistry one. Results are presented at the flame front (upper figures) and post-flame (lower figures) spatial scales.*

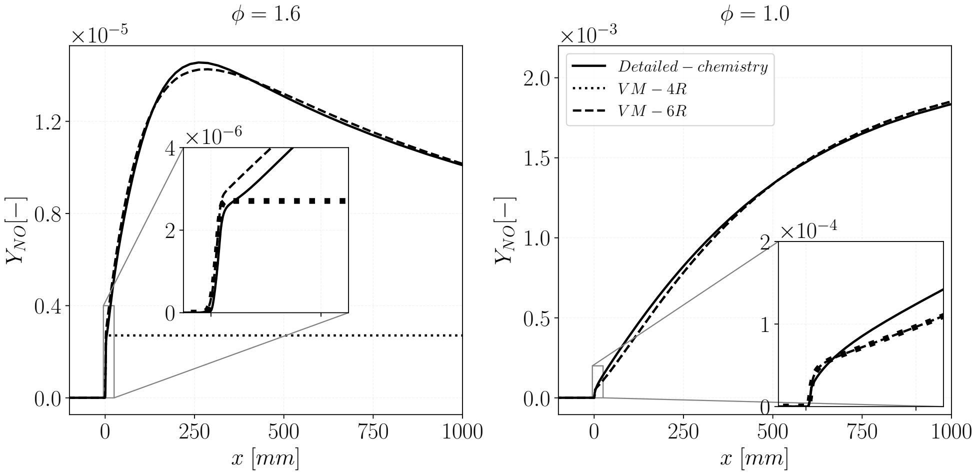

Figure 5.8: *Comparison of NO mass fraction from detailed chemistry and virtual chemistry for a rich (left) and a stoichiometric (right) 1-D premixed flames. Two virtual mechanism are shown: the first retains 1 reaction only in the post-flame block (VM-4R) and the second retains the whole post-flame block (VM-6R).*

5.4.2 Premixed flames

VM-6R results are *a-posteriori* compared versus the reference detailed chemistry solutions, for three different equivalence ratios: lean ($\phi = 0.6$), stoichiometric ($\phi = 1.0$) and rich ($\phi = 1.6$). The results are presented in the flame front and in the post-flame regions in Fig.5.7. The proposed 6-reactions mechanism allows to correctly reproduce prompt and thermal post-flame NO formation characterizing lean and stoichiometric conditions. The post-flame NO re-burning phenomena, encountered in rich flame conditions, are also correctly described.

A comparison is proposed to stress the role of reactions R_4^{NO} and R_5^{NO} in the mechanism. Figure 5.8 compares, for a rich (at $\phi = 1.6$) and a stoichiometric flames, the results obtained with the two mechanisms VM-4R and VM-6R versus the detailed chemistry solutions. It is evident that the two reactions R_5^{NO} and R_6^{NO} are required to capture the slow NO reburning already illustrated in Fig. 5.1. These reactions are not needed in lean, stoichiometric and moderately rich conditions ($\phi < 1.4$), where reburning phenomena do not occur. Consequently VM-4R and VM-6R solutions collapse on the same one for $\phi < 1.4$ as illustrated in Fig. 5.8 (right).

5.4.3 Non-premixed flames

1-D non-premixed counterflow flames are *a-posteriori* computed with the entire optimized virtual mechanism VM-6R. Figure 5.9 shows the NO profile computed with the whole virtual NO mechanism VM-6R, compared to the reference

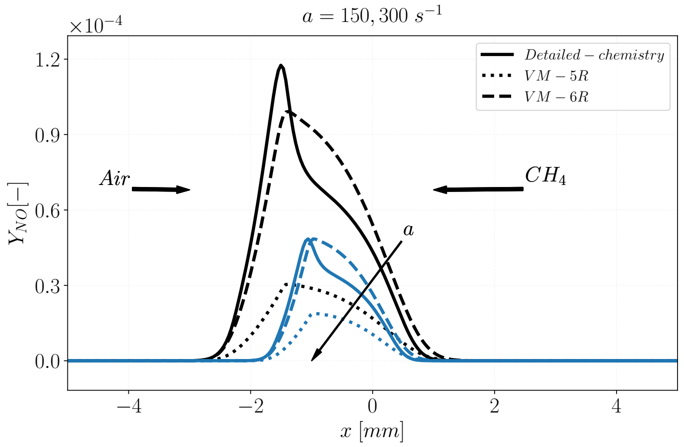

Figure 5.9: *Diffusion opposed jet flames NO mass fraction profiles. Detailed chemistry and virtual chemistry results are compared. Two virtual mechanisms are shown: the first considers 1 reaction only in the flame front block (VM-5R) and the second considers the whole flame front block (VM-6R). Different colors are used for different stain rates.*

profiles, for two different flame strain rates.
The proposed virtual NO mechanism optimized to fit both premixed and non-premixed flame archetypes retrieves the high sensitivity of the NO profile to the flame strain rate. Decreasing the flame strain rate, the residence time increases and consequently the NO formation is higher.
However, virtual NO mechanism VM-6R does not perfectly describe the fast NO mass fraction decay on the flame rich side, which characterizes detailed chemistry profiles. It turns out difficult to find a better compromise between premixed and non-premixed flames in the flame front region with only two reactions (R_2^{NO}-R_3^{NO}).
Comparison between VM-6R and VM-5R, in which reaction R_3^{NO} has been removed before the optimization process, is also shown in Fig. 5.9. The large discrepancy observed between VM-5R and the detailed chemistry solutions confirms that R_3^{NO} is required in the flame front block to capture NO formation in non-premixed flames. Without it, the virtual mechanism does not have enough degree of freedom to capture NO formation in both premixed and non-premixed flame regimes.

5.5 2-D slots burner flames

In the current section, virtual chemistry is challenged in 2-D CFD computations and compared against detailed chemistry simulations. The simulations are carried out for several 2-D laminar flame benchmarks including a premixed, a non-premixed and a partially premixed flame.

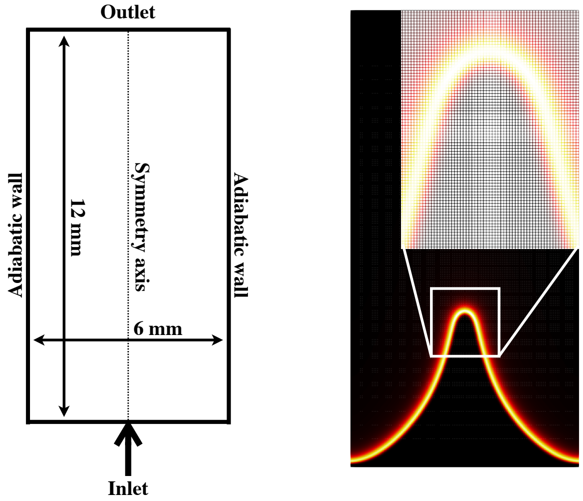

Figure 5.10: *2-D premixed slot burner numerical set-up. On the left schematic view of the computational domain with the corresponding dimensions and the boundary conditions. On the right the normalized heat release rate from numerical simulation shown on the computational grid.*

The CFD code laminarSMOKE (Cuoci et al. 2013a) is used to perform the computations for both detailed chemistry and virtual chemistry. The laminarSMOKE code is based on the open-source suite OpenFOAM (OpenFOAM 2019). It has already shown capability to accurately model laminar flames including detailed chemistry using hundreds of species and reactions (Cuoci et al. 2013b; Stagni et al. 2013). The transport equations of mass, momentum, energy, and species are solved based on the operator-splitting approach (Day and Bell 2000).

5.5.1 Premixed flame

The premixed single slot burner geometry consists of a 2-D rectangular computational domain whose dimensions are shown in Fig. 5.10. The boundary conditions include an inlet, an outlet and adiabatic walls. Since the configuration is axial-symmetric only a half of the computational domain is simulated. The other half of the computational domain is obtained by symmetric reflection of the first part. Therefore a symmetry boundary condition is imposed along the axis.
At the inlet, a developed laminar parabolic velocity profile is prescribed in the axial direction using a mean value $U_m = 0.6\ m/s$, whereas the others velocity components are set equal to zero. A cartesian grid is considered in the simulation. The characteristic cell size is of about $\sim$ 0.015 mm. This cell size allows to fully resolve the thermal flame thickness and the heat release rate of a premixed laminar flame. In particular, the employed mesh size ensures 15 to

20 cells across the thermal flame thickness.
A zoom on the computational grid, in the flame tip region, is made in Fig. 5.10 and an example of normalized heat release rate is also shown on the computational grid. Indeed the heat release rate is properly solved over the employed grid.
Figure 5.11 shows the temperature and NO field for the 2-D premixed burner at three different equivalence ratios (0.8, 1.0 and 1.2). Virtual chemistry results are directly compared to detailed chemistry ones.
The temperature field predicted by the main virtual mechanism is in good agreement with the detailed chemistry, for the three equivalence ratios. It is remarkable that the flame height is properly captured by virtual chemistry. At $\phi = 1.2$ the height is slightly underestimated by about 10%. Virtual chemistry correctly reproduces the temperature evolution, from fresh to burnt gases with a small difference in flame curvature description.
The virtual NO field agrees well with the temperature field: when temperature increases earlier for virtual chemistry (as for $\phi = 1.2$), NO increases earlier too. The 2-D slot burner configuration, retained in the present work allows to observe mostly the whole prompt NO formation and the first part of the thermal one. However, as observed in the 1-D premixed profiles in Fig. 5.8, NO is further produced in the burnt gases, for longer residence time, through the thermal route. A slight underestimation of the NO level is observed at $\phi = 0.8$ and 1.0, whereas a better prediction is observed for $\phi = 1.2$. This behaviour is in accordance with the 1-D profiles shown in Fig. 5.7 at the flame front scale.
For the stoichiometric slot burner flame, 1-D temperature and NO mass fraction profiles are extracted from the 2-D field over both axial and a radial directions. The 1-D sections, used for the comparison, are indicated by white lines in Fig. 5.11. Figure 5.12 shows the temperature and NO profiles from virtual and from detailed chemistry computations along the two lines in the axial (r=0 mm) and for a radial section (x= 2 mm).
The excellent temperature agreement in the axial direction confirms that the flame height is well retrieved even if a slight shifting in the radial direction is observed. This discrepancy is due to the not perfect reproduction of the flame curvature. Indeed preferential diffusion effects coupled to flame stretch are not well captured by virtual chemistry because of simple assumptions for diffusive fluxes closure. NO virtual profiles are consistent with the results obtained in 1-D flame computations shown in Fig. 5.7.

5.5.2 Non-premixed flame

A 2-D non-premixed laminar coflow flame is simulated in the present section. The considered configuration along with the main burner dimensions and the boundary conditions set-up are schematized in Fig. 5.13. The figure also shows a normalized heat release rate field over half of the computational domain region close to the burner nozzle. A fuel jet is surrounded by a pure air coflow

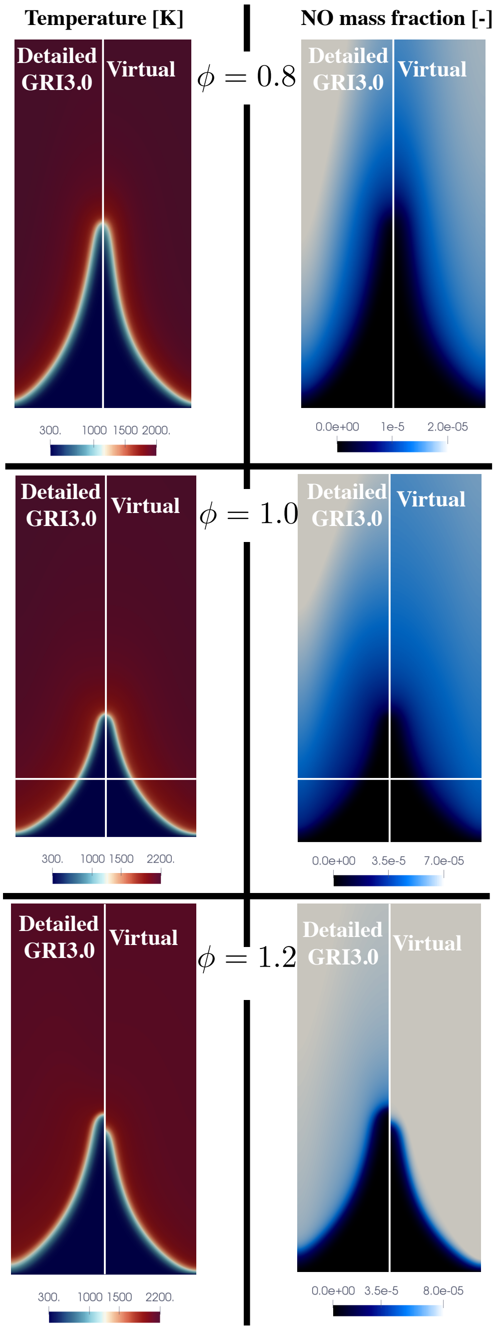

Figure 5.11: *Temperature and NO mass fraction colormaps for the 2-D laminar single slot burner (Bunsen flame). Virtual chemistry solution is compared with detailed chemistry one.*

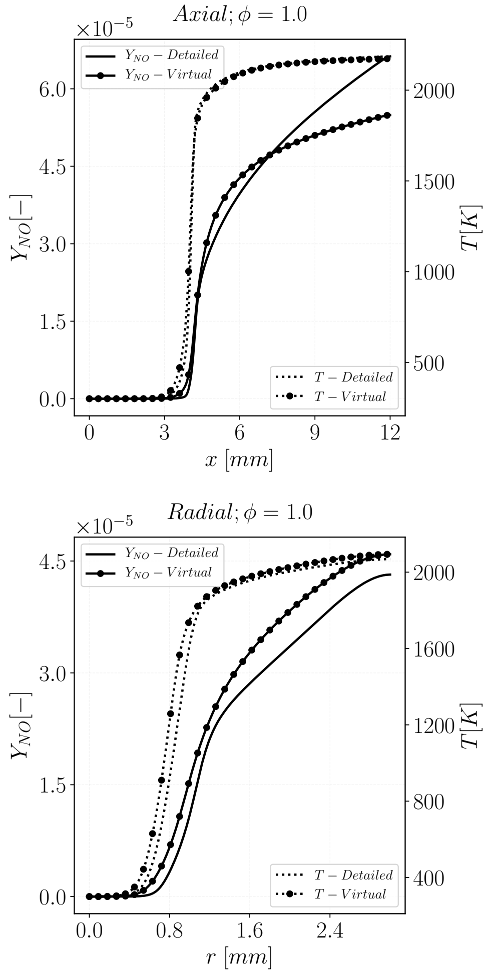

$Axial; \phi = 1.0$

$Radial; \phi = 1.0$

Figure 5.12: *Virtual chemistry (symbols + lines) is compared against detailed chemistry (lines) for temperature (dashed lines) and NO mass fraction (solid lines). Top: axial profiles. Bottom: radial profiles at the centerline distance x= 2 mm.*

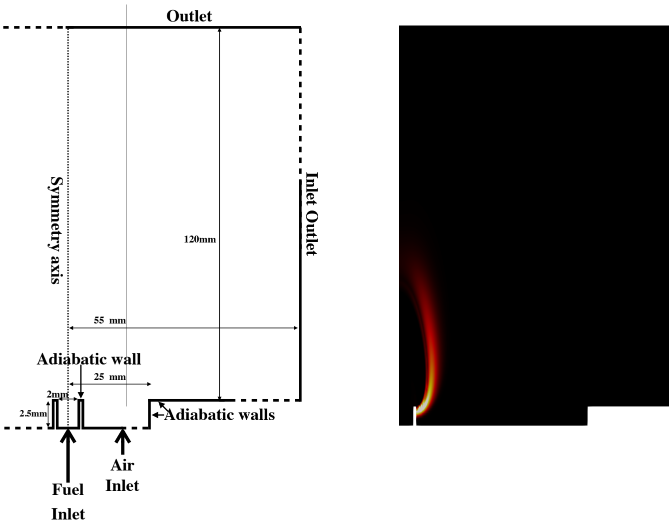

Figure 5.13: *Numerical set-up of the coflow diffusion flame burner. On the left a schematic view of the 2-D simulated domain is presented. The main burner dimensions and the prescribed boundary conditions type are shown. On the right an example of normalized heat release rate computed from detailed chemistry simulation is shown.*

allowing the development of a non-premixed diffusion flame. The computational geometry is symmetric with respect to the centreline axis, as for the premixed single slot burner; consequently, just a half of the computational domain is computed. Adiabatic walls are imposed close to the air inlet whereas an inlet/outlet boundary condition (OpenFOAM 2019) is prescribed on the burner side.

A 2-D non uniform structured rectangular mesh is used in the simulations as proposed by Cuoci et al. (2013a), Cuoci et al. (2013b). The characteristic mesh size in the flame front region is of about ~ 0.05 mm which is sufficient to ensure a proper flame resolution in diffusion flame conditions. Velocity boundary conditions are tuned to ensure the flame attachment to the burner lip avoiding any flame lift-off. Flat velocity profiles at 0.15 m/s are prescribed in the two streams. Pure CH_4 and pure air at 300 K are injected in the *Fuel Inlet* and the *Air Inlet*, respectively.

Figure 5.14 shows the temperature and NO mass fraction fields for the 2-D diffusion flame configuration, comparing virtual chemistry to the detailed chemistry results. The virtual chemistry flame shape is close to the detailed chemistry one, but it appears slightly more compact. In the virtual chemistry simulation, temperature increases faster than with detailed chemistry.

The NO mass fraction field predicted by virtual chemistry is correctly located in the computational domain with respect to temperature field.

Figure 5.15 compares the temperature and NO mass fraction along the flame axis. As virtual chemistry temperature rises faster, NO mass fraction presents an early peak at $x = 0$ mm. Successively the small NO reburning corresponding

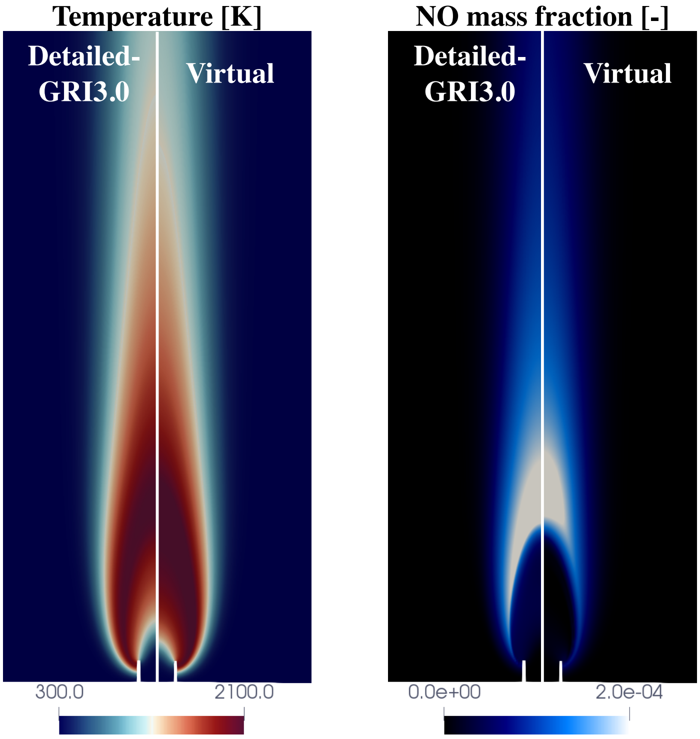

Figure 5.14: *Temperature and NO mass fraction fields from numerical simulations for the diffusion flame. The virtual chemistry results are compared versus the reference GRI3.0 solutions.*

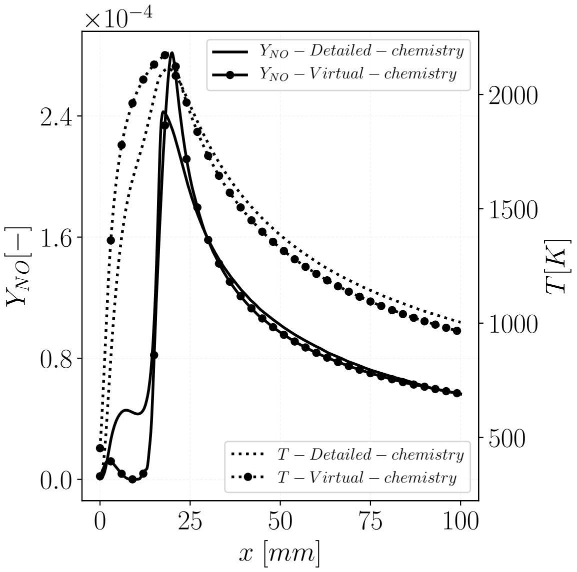

Figure 5.15: *Temperature (dashed lines) and NO mass fraction (solid lines) along the centerline axis (x=0 mm) of the 2-D coflow non-premixed flame. Virtual chemistry (symbols + lines) is compared against detailed chemistry (lines).*

to detailed chemistry is overestimated by virtual chemistry. This reburning phenomenon in coflow flame configuration has been already observed by Cuoci et al. (2013a).

The max NO peak prediction, corresponding to the temperature peak is correctly predicted. However, the amplitude of NO mass fraction is relatively overestimated. This phenomenon is attributed to the slight temperature overestimation. After the peak zone, the NO reduction due to consumption and/or dilution effects is correctly captured.

5.5.3 Partially-premixed flame

The developed NO virtual mechanism is finally assessed in a partially premixed flame configuration. The considered geometry and mesh are the same as the diffusion flame configuration, described in the previous section. In the central jet (*Fuel Inlet*) a premixed mixture of fuel and air, above the flammability limit, is injected. An equivalence ratio equal to 2.5 and a temperature of 300K are prescribed.

Pure ambient air at 300K, as for the diffusion flame configuration, is injected through the *Air Inlet* tube. Inlet velocities are tuned to stabilize the flame at the burner lips, without having any lift-off. A flat velocity profiles of 0.35 m/s and 0.05 m/s are prescribed at the *Fuel Inlet* and the *Air Inlet*, respectively.

Figures 5.16 shows the temperature and NO mass fraction 2-D fields for the partially premixed flame. The flame is stabilized at the same position with

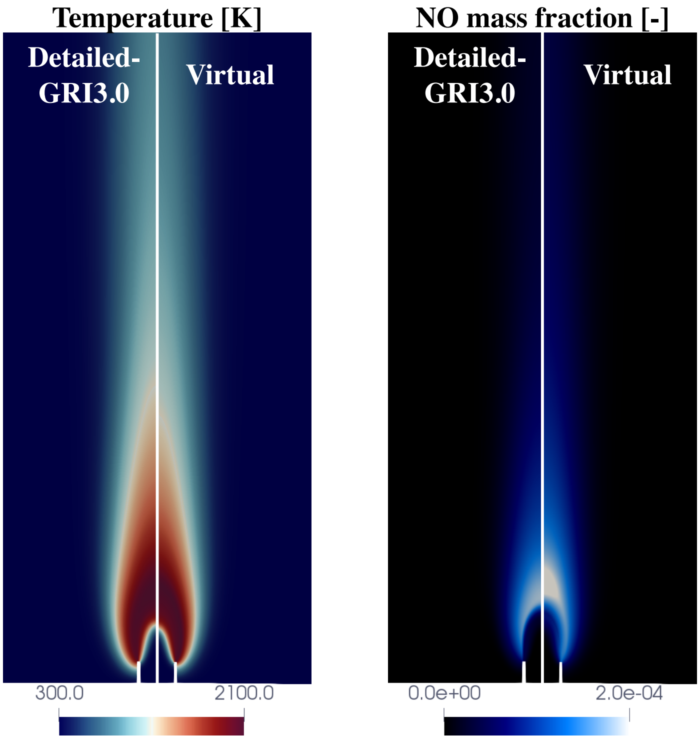

Figure 5.16: *Temperature and NO mass fraction fields from numerical simulations for the partially-premixed flame. The virtual chemistry results are compared versus the reference GRI3.0 solutions.*

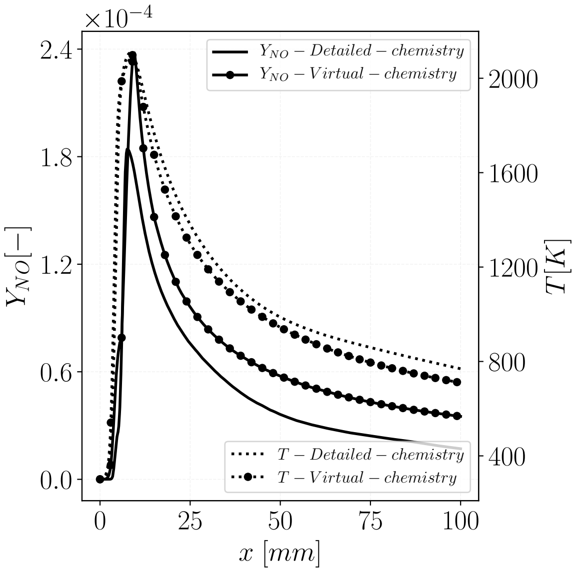

Figure 5.17: *Temperature (dashed lines) and NO mass fraction (solid lines) along the centerline axis (x=0 mm) of the 2-D coflow partially premixed flame. Virtual chemistry (symbols + lines) is compared against detailed chemistry (lines).*

Table 5.2: *CPU cost comparison between detailed reference chemistry and virtual chemistry computations. Main temperature mechanism and the NO one are considered for virtual chemistry.*

Mechanism	**Nb. species**	$C = t/t^v$
GRI3.0 (Smith et al. 2011)	53	39
Virtual Mech.	12	1

detailed and virtual chemistry. NO field is correctly located over the computational domain, but the NO peak value is overestimated.

Figure 5.17 shows the temperature and NO profiles along the axis. The NO 1-D profile confirms the correct prediction of the NO peak position but its value is overestimated.

5.5.4 CPU cost comparison

A comparison to evaluate the CPU ratio between detailed chemistry and virtual chemistry simulation was carried out. The stoichiometric 2-D premixed slot burner is computed for the same physical time (10 ms), using the same numerical set-up and employing the same numbers of processors for virtual and detailed chemistry. Table 5.2 summarizes the results of the comparison. The CPU time ratio $C = t^d/t^v$ that compares the detailed (t^d) and virtual chemistry (t^v) computational time, is equal to = 39. The drastic CPU cost reduction is mainly due to the species and reactions reduction. The observed CPU speed-up is equal to:

$$C = \frac{t^d}{t^v} \simeq \left(\frac{n^d}{n^v}\right)^{2.5} \tag{5.24}$$

where n^d (=53) and n^v(=12) are respectively the number of species included in the detailed and virtual mechanisms. This result is in accordance with previous numerical studies that use implicit solvers. (Law 2007; Lu and Law 2007; Pepiot 2008). This CPU result analysis is valid for any 2-dimensional laminar computation (premixed, non-premixed and partially premixed) performed with laminarSMOKE solver (Cuoci et al. 2013a).

5.6 Conclusions

The virtual chemistry strategy has been retained to develop a new pollutant reduced mechanism devoted to NO prediction. The original virtual chemistry formulation has been used to predict flame temperature and heat release rate. An NO virtual mechanism has been designed using a reduced set of virtual species and reactions and trained over a hybrid flamelet database, made of premixed and non-premixed 1-D flames.

A two-step optimization strategy has been developed to separate and to independently optimize the virtual reactions dedicated to flame front and post-flame NO chemistry, respectively. The proposed model is able to describe all the NO chemistry pathways exhibited by the reference flame solution. In particular *prompt* NO, *thermal* NO and post-flame NO *reburning* are correctly described by the virtual chemistry model. The developed NO virtual mechanism has been tested in 2-D laminar premixed, non-premixed and partially premixed flame computations. A comparison to detailed reference chemistry has also been proposed. In the CFD computations, the final CPU cost associated with the virtual chemistry simulation is drastically smaller than with detailed chemistry one (of about 40 times).

Despite the accurate and promising results, at the current stage, the number of virtual species along with the virtual reactions network are empirically designed. The virtual chemistry architecture is based on the pure observation of the physical phenomenon to account for. Consequently, the number of degree of freedom (virtual species and reaction) may be not the optimal one and/or some important chemical pathways may be missed. To overcome this current limitation, new modeling strategies that provide an automatic build-up of the virtual chemistry network, from a time scale analysis of the reference chemical system, are in progress.

Part III

Application to turbulent flames

Chapter 6

LES of the Sydney Inhomogeneous burner

Contents

The present chapter focuses on the LES study of the piloted jet flame with inhomogeneous inlet called "Sydney inhomogeneous burner" or "Inhomogeneous piloted burner". Virtual chemistry is here tested for the first time to model combustion chemistry in a multi-mode turbulent flame configuration. The virtual chemistry-LES results are compared to a FPI-LES tabulated chemistry simulation. Eventually, the computations are compared to the available measurements to evaluate the impact of the chemical description on temperature and CO prediction.

6.1 Introduction

In industrial combustion chambers, fuel and air are usually injected separately and consequently the fuel-air mixing promotes the development of multiple-flame structures: premixed, non-premixed and partially premixed (Masri 2015). The description of such complex combustion regime represents a big challenge for the turbulent combustion modeling community (Barlow 2018). Indeed, the chemistry modeling of combined multiple flame structures causes numerous modeling difficulties (Knudsen and Pitsch 2012): heat release, temperature and species concentrations have to be reproduced according to the different encountered flame trajectories (Fiorina 2019). In particular, in a multi-mode flame environment, pollutants formation is very sensitive to the local combustion regime and then extremely difficult to model. Fiorina et al. (2005) and more recently Cailler et al. (2019) have shown that predicting CO in non-premixed combustion regime using premixed based flamelets trajectories or vice-versa leads to important bias. The same observation is valid for nitric oxide (NO) as shown in Chap. 5.

Most of the available literature combustion chemistry models are based on tabulated chemistry (Peters 1988; Maas and Pope 1992b; Gicquel et al. 2000; Van Oijen et al. 2001) and they are derived to target a single flame regime (Gicquel et al. 2000; Van Oijen et al. 2001; Pierce and Moin 2004). Consequently, they are often not efficient outside the tabulated flamelet trajectories (Cailler et al. 2019), especially for pollutant prediction (Fiorina 2019).

Reduced chemistry models, based on transported finite rate chemistry, have demonstrated to be more suitable for complex flame environment (Felden et al. 2018). Reduced mechanisms can be derived mixing informations from premixed and non premixed flames (Lu and Law 2008a). Furthermore, they do not need additional modeling assumptions to simulate multi-injector problems and flame heat losses, differently from tabulated chemistry (Hasse and Peters 2005; Fiorina et al. 2003; Franzelli et al. 2010).

One finite rate chemistry strategy consists in the use of global optimized mechanisms (Westbrook and Dryer 1981; Jones and Lindstedt 1988). Although robust for global flame quantities and CPU efficient (Franzelli et al. 2010), they are not suitable for accurate flame structure and pollutants description. Two possible finite rate chemistry strategies are instead currently used to conduct LES of complex burners combining flame structure and pollutant predictions, at an affordable CPU cost. One consolidated strategy consists in the use of non-stiff Analytically Reduced Chemistry (ARC). ARC mechanisms have been recently used to perform simulations of complex burners (Jaravel et al. 2017; Felden et al. 2018), demonstrating also the importance of retaining finite rate chemistry effects for CO modeling (Benard et al. 2019). A second emerging finite rate chemistry approach is the *virtual chemistry* methodology (Cailler et al. 2017; Cailler et al. 2019). Its suitability to model CO emissions in LES have been recently demonstrated for a turbulent confined aeronautical combustor exposed to heat losses (Maio et al. 2019). But, its capability to reproduce multi-mode turbulent flame condition need to be fully explored. *Virtual chemistry* (Cailler et al. 2017), as presented in Chap. 3, has shown the ability to describe flame structure and CO formation (Cailler et al. 2019) in combined laminar premixed and non premixed combustion regimes.

The objective of the present chapter is to challenge, for the first time, virtual chemistry in turbulent mixed combustion regimes in LES.

Sydney Inhomogeneous burner, designed at Sydney University (Meares and Masri 2014) and experimented at both Sydney University (Meares et al. 2015) and Sandia National Laboratories (Barlow et al. 2015) is an academic jet flame configuration operating in multi-regime flame conditions. The burner set-up and the inflow conditions are designed to promote mixed combustion regimes. Therefore, it is a well-suited test case candidate to validate virtual chemistry in multi-regime turbulent flame conditions.

The virtual chemistry LES computation is also compared with an FPI-FGM (Gicquel et al. 2000; Van Oijen et al. 2001) tabulated chemistry LES simulation. FPI-FGM is instead a well established literature combustion chemistry approach.

The two combustion chemistry models are coupled with the thickened flame model for LES to deal with the under-resolution of the flame front and to account for chemistry turbulence interaction at the sub-grid scale.

The two LES computations are performed with the unstructured finite-volume low Mach number code YALES2 (Moureau et al. 2011a).

In the present chapter, first a brief state of the art on the recent numerical studies on the Sydney Inhomogeneous burner is discussed. Then, the employed combustion modeling strategies are presented. Successively, an overview on the burner configuration and on the most relevant experimental studies is given. After presenting the numerical set-up, non reactive inert simulations and reactive ones are shown and compared to experiments.

Table 6.1: *Literature modelling studies on the Sydney Inhomogeneous piloted burner.*

Publication	Chemistry model	Combustion model
Meares et al. (2015)	reduced chemistry	Eulerian stochastic field
Wu and Ihme (2016)	premixed or non-premixed flamelet	presumed-PDF
Kleinheinz et al. (2017)	multi-regime flamelet	presumed-PDF
Johnson et al. (2017)	non-premixed flamelet	presumed-PDF
Perry et al. (2017)	partially premixed diffusion flamelet	presumed-PDF
Galindo et al. (2017)	non-premixed flamelet	MMC-LES
Perry and Mueller (2018)	partially premixed diffusion flamelet	presumed-PDF
Tian and Lindstedt (2018)	reduced chemistry	transported PDF
Rieth et al. (2019)	reduced chemistry/premixed flamelet	transported PDF

6.2 State of the art

Sydney inhomogeneous burner have been recently numerically investigated in the literature by several research groups, using Large Eddy Simulation models (Meares et al. 2015; Wu and Ihme 2016; Kleinheinz et al. 2017; Johnson et al. 2017; Perry et al. 2017; Galindo et al. 2017; Tian and Lindstedt 2018; Rieth et al. 2019). Different combustion chemistry and turbulent combustion models are employed in these studies. A summary, of the recently published works with the corresponding combustion modeling approaches, is presented in Tab. 6.1.

It shows that most of the studies make use of flamelet libraries combined with presumed PDF (Wu and Ihme 2016; Kleinheinz et al. 2017; Johnson et al. 2017; Perry et al. 2017; Perry and Mueller 2018) or transported PDF (Rieth et al. 2019) turbulent combustion models. While only few studies employ transported complex chemistry combined with transported PDF (Kleinheinz et al. 2017; Tian and Lindstedt 2018) because of the very high CPU cost associated. An hybrid model, that combines reduced transported chemistry and tabulated chemistry with PDF transport, has been recently introduced by Rieth et al. (2019) to limit the CPU cost. Compared to transported chemistry models, tabulated chemistry has the advantage to be less CPU demanding. But, when used in complex flame conditions such as Sydney inhomogeneous burner, it requires important modeling assumptions and simplifications that are not needed by a reduced mechanism: the choice of the flame archetypes to tabulate (Perry et al. 2017), the selection of the reduced set of table-coordinates (Perry and Mueller 2018) and the closure of the scalar source terms (Kleinheinz et al. 2017). All these assumptions restrict the evolution of the flame trajectories and can lead to import discrepancies, especially for intermediate species prediction (for example CO) (Wu and Ihme 2016). In the literature, the application of transported finite rate chemistry models in Sydney burner simulation remains restricted as well as the demonstration of the related advantages in CO prediction. These reasons motivates the scope of this work.

6.3 Combustion modeling

6.3.1 Chemistry modeling

Two reduced order models are used in the current chapter, to model combustion chemistry in the Sydney inhomogeneous burner simulations:

- FPI-tabulated chemistry approach (Gicquel et al. 2000): flame trajectories are mapped from premixed flamelets using mixture fraction and progress variable.
- virtual chemistry model (Cailler et al. 2017): the main 2-step mechanism and the CO dedicated sub-mechanism are used, as described in Chap. 3.

6.3.1.1 FPI tabulated chemistry

The FPI (Flame Prolongation of ILDM) (Gicquel et al. 2000) or equivalentely FGM (Flamelet-Generated Manifolds) (Oijen and Goey 2000) combustion chemistry models rely on the pre-tabulation of flame trajectories using premixed flamelet archetypes.

A one to one relation ensures that each thermochemical quantity ψ^*, computed from a collection of 1-D premixed flamelets, is only function of the two chemtable coordinates Z and Y_c, which map the fresh gases equivalence ration and the coordinate normal to the flame front, respectively. Then, each flame thermochemical quantity ψ is tabulated in a lookup-table according to the relation $\psi = \psi^*[Y_c, Z]$

In this work, a flamelet database made of 1-D premixed freely propagating flames is computed, with the REGATH (Darabiha 1992) thermochemistry package, using the detailed chemistry GRI.3.0 (Smith et al. 2011) mechanism, involving 53 species and 325 reactions. Differential diffusion effects are accounted using the Hirschfelder and Curtiss approximation (Hirschfelder et al. 1954) detailed in Sec. 1.3.4.

To make the tabulation suitable for partially-premixed combustion, the fresh gas equivalence ratio is varied within the whole flammability limits (i.e $0.5 < \phi < 2.0$).

Z and Y_c are defined as follows:

- The mixture fraction Z is used to identify the fresh gas equivalence ratio, varying from 0 in pure air and 1 in pure fuel.
- The progress variable Y_c is used to map the rate of progress. It is bounded between 0 in fresh gases and Y_c^{eq} in fully burnt gases. Y_c is defined as a linear combination of species mass fractions, describing the reaction progress. In the present work Y_c is chooses equel to $Y_{CO} + Y_{CO_2}$ as supported by Fiorina et al. (2003). The normalized progress variable $C = Y_c/Y_c^{eq}$, bounded between 0 and 1, is also defined. It's use is equivalent to Y_c

The FPI chemtable, obtained from the collection of the 1-D premixed flames, is discretized in 200 points in C uniformly spaced and in 520 points in Z non uniformly spaced. Outside the flammability limit, where no flamelet informations are available, the thermochemical quantities are extrapolated.

Figure 6.1 shows the tabulated temperature and progress variable source term, as function of Z and C, extracted from the built lookup table.

The FPI-FGM tabulated chemistry method has been used in the LES framework in combination with several approaches for turbulence-chemistry interaction modeling: presumed PDF (Domingo et al. 2008) and transported PDF (Rieth et al. 2019), explicit flame filtering approach (Fiorina et al. 2010) and by using artificially thickened of the flame front (TFLES) (Auzillon et al. 2011), (Kuenne et al. 2011), (Proch and Kempf 2014), (Proch et al. 2017). Among the various strategies, in the present work, the artificially thickened model (TFLES) is used. This choice facilitates the comparison with virtual chemistry.

6.3.1.2 Virtual chemistry

Virtual chemistry, differently from FPI tabulation, is a transported chemistry reduced model. Few species, compared to detailed chemistry, are directly transported in the flow solver and the chemical species source term is directly computed at each time step.

In the LES computation of the Sydney inhomogeneous burner, virtual chemistry is employed using the formulation proposed and validated by Cailler (2018) and already described in Chap. 3.

The main virtual mechanism and the CO dedicated sub-mechanism are used to compute temperature, flame global quantities (flame speed and heat release) and CO formation.

The CO virtual sub-mechanism, as done by Cailler (2018), is optimized over a learning database made of combined premixed and non premixed flames to recover the CO flame regime affinity.

Virtual chemistry equivalence ratio dependent parameters are expressed, in this chapter, as function of a mixture fraction Z, normalized between 0 and 1, in pure air and fuel, respectively. This definition is consistent with the one used for tabulated chemistry. The same mixture fraction is also compared to experimental data, to evaluate the local mixing between fuel and air.

6.3.2 Coupling with LES

The two combustion chemistry models, detailed in the previous section, are coupled with the TFLES (Thickened Flame model for LES) turbulent combustion model (Colin et al. 2000b), using a tabulated and a transported chemistry formalism, respectively. SGS flame wrinkling is closed with the same model, as proposed by Charlette et al. (2002a). The use of the same modeling approach strengthens the value of the comparison. The details about the coupling of the two chemistry approaches with TFLES are given in the following sections.

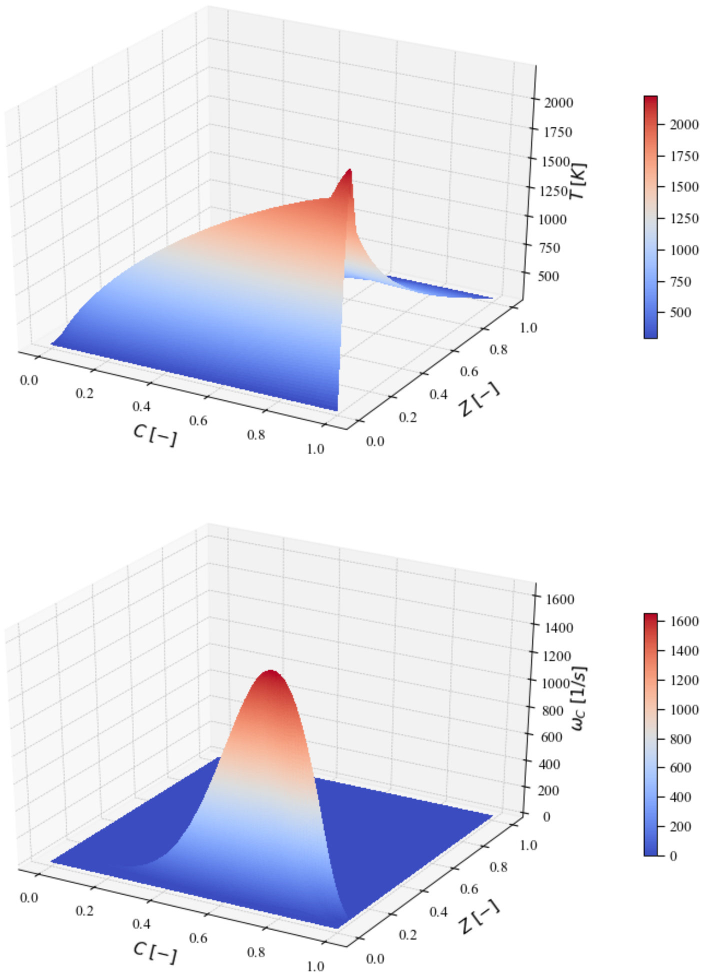

Figure 6.1: *2D look-up table. Temperature (T) and the normalized progress variable source term ω_C are shown as function of the mixture fraction Z and the normalized progress variable C.*

6.3.2.1 TFLES-FPI tabulated chemistry

In premixed tabulated chemistry the dynamic TFLES model (Legier et al. 2000) is applied to the filtered progress variable $\widetilde{Y_c}$ balance equation:

$$\frac{\partial \bar{\rho}\widetilde{Y_c}}{\partial t}+\frac{\partial}{\partial x_i}\left(\bar{\rho}\widetilde{u_i}\widetilde{Y_c}\right)=\frac{\partial}{\partial x_i}\left(\left[\alpha_{Yc}F_{Y_c}\Xi_\Delta\frac{\bar{\mu}}{Sc}+(1-\Gamma)\frac{\mu_t}{Sc_t}\right]\frac{\partial\widetilde{Y_c}}{\partial x_i}\right)+\frac{\Xi_\Delta\widetilde{\dot{\omega}_{Y_c}}}{F_{Y_c}} \tag{6.1}$$

The same operation was used in the FGM formalism (Kuenne et al. 2011; Hernández-Pérez et al. 2011) and in the FPI one (Auzillon et al. 2011). As detailed in Poinsot and Veynante (2005), the unresolved sub-grid convective fluxes are closed using a gradient assumption introducing a turbulent Schmidt number Sc_t and a turbulent viscosity μ_t. Hence, μ and μ_t are the laminar and the turbulent viscosity, respectively; instead, Sc and Sc_t are the laminar and the turbulent Schmidt numbers, respectively. A thickening factor F_{Y_c} is applied to both diffusion and the source term of the filtered progress variable balance equation. Ξ_Δ is the subgrid wrinkling flame surface and Γ the flame sensor. In TFLES-FPI formalism (Auzillon et al. 2011) the filtered progress variable source term $\widetilde{\dot{\omega}_{Y_c}}$ is directly extracted from the chemtable as a function of Z and Y_c:

$$\widetilde{\dot{\omega}}_{Y_c}=\dot{\omega}^*_{Y_c}[Y_c,Z] \tag{6.2}$$

The superscript * denotes quantities that are extracted from the flamelet database. The same operation is here performed for the dynamic viscosity ($\mu=\mu^*[Y_c,Z]$) and for the correction parameter α_{Yc} ($\alpha_{Yc}=\alpha^*_{Yc}[Y_c,Z]$). The correction parameter α_{Yc}, proposed by (Mercier et al. 2014), allows to account for differential diffusion effects in the direction normal to a premixed flame front, retrieving the correct flame propagation speed. Originally introduced for the F-TACLES formalism (Mercier et al. 2014), it is here adapted to TFLES-FPI model. α_{Yc} is tabulated from the premixed flamelet database, comparing the diffusive fluxes evaluated with mixture-averaged approximation (Hirschfelder et al. 1954) and the simplified transport model used in Eq. 6.1, as follows:

$$\alpha^*_{Y_c}[\widetilde{Yc},\tilde{z}]=-\frac{\sum_{k=1}^{N_{sp}}n_k\rho^*Y^*_kV^*_k}{\frac{\mu}{Sc}\frac{\partial\widetilde{Y^*_c}}{\partial x^*_i}} \tag{6.3}$$

In partially premixed combustion environment, to map the mixture stratification, a balance equation for the filtered mixture fraction $\widetilde{Z}$ is also introduced in the flow solver (Auzillon et al. 2011; Proch et al. 2017):

$$\frac{\partial \overline{\rho}\widetilde{Z}}{\partial t} + \frac{\partial}{\partial x_i}\left(\overline{\rho}\widetilde{u}_i\widetilde{Z}\right) = \frac{\partial}{\partial x_i}\left(\left[\frac{\overline{\mu}}{Sc} + \frac{\mu_t}{Sc_t}\right]\frac{\partial \widetilde{Z}}{\partial x_i}\right) \tag{6.4}$$

$\widetilde{Z}$ is transported as a non-reactive scalar and the unresolved sub-grid convective fluxes are closed with the same gradient assumption used in Eq. 6.1 (Poinsot and Veynante 2005).

Dynamic thickening A grid adaptive thickening factor is defined as follows (Franzelli 2011):

$$F_{Y_c} = \max(1 + (F_{max} - 1)\,\Gamma, 1) \tag{6.5}$$

where F_{max} reads:

$$F_{max} = n\frac{\Delta_x}{\delta_l[Z]} \tag{6.6}$$

Δ_x is the local cell size and $\delta_l[Z]$ is the laminar flame thermal thickness which is tabulated as function of local mixture fraction. n is the minimum number of mesh points required across the flame front to correctly resolve the flame structure. Here, it is chosen equal to 6. By introducing the flame sensor Γ the thickening is locally applied only where the flame is detected. Γ is here based on the progress variable source term (Franzelli 2011; Jaravel 2016) and defined as follows:

$$\begin{cases} \Gamma = 1 & \text{if} \quad \omega_{Y_c} > \omega^0_{Y_c} \\ \Gamma = 0 & otherwise \end{cases} \tag{6.7}$$

where $\omega^0_{Y_c}$ is a threshold value defined as:

$$\omega^0_{Y_c} = \max(\omega_{Y_c}[Z]) * Tr \tag{6.8}$$

$Max(\omega_{Y_c}[Z])$ is the maximum value of the progress variable source term which is tabulated in the computation as function of the local mixture fraction. While Tr is a threshold value chosen equal to 0.05.
As discussed by Franzelli (2011), the flame sensor is then filtered with a Gaussian function to avoid numerical problems.

6.3.2.2 TFLES-virtual chemistry

TFLES is coupled with virtual chemistry using a transported chemistry formalism, as in its original formulation (Colin et al. 2000b). The virtual main mechanism and pollutant CO sub-mechanism are coupled with the TFLES using a thickening factor F and a flame sensor gamma Γ that are properly defined for transported chemistry. Differently from the FPI tabulation method, where only a reduced set of scalars are transported in the flow solver, here each species that is involved in the mechanisms is transported. The TFLES balance equation for each filtered species mass fraction $\widetilde{Y_k}$ is formulated as follows:

$$\frac{\partial \overline{\rho}\widetilde{Y_k}}{\partial t}+\frac{\partial}{\partial x_i}\left(\overline{\rho}\widetilde{u_i}\widetilde{Y_k}\right)=\frac{\partial}{\partial x_i}\left(\left[F\Xi_{\Delta}\frac{\overline{\mu}}{Sc}+(1-\Gamma)\frac{\mu_t}{Sc_t}\right]\frac{\partial\widetilde{Y_k}}{\partial x_i}\right)+\frac{\Xi_{\Delta}\overline{\dot{\omega}_{Y_k}}}{F} \tag{6.9}$$

Ξ_Δ is the subgrid wrinkling flame surface. $\overline{\dot{\omega}_{Y_k}}$ is the thickened reaction rate which is closed with the Arrhenius formulations presented in Chap. 3.

Dynamic thickening The flame sensor Γ and a thickening factor F are defined according to the work of Mercier et al. (2017a). Dedicated species thickening factors F_{Y_k} and flame sensors Γ_{Y_k} are before introduced:

$$F_{Y_k}=\max(1+(F_{max}-1)\,\Gamma,1)\quad with\quad F_{max}=n_k\frac{\Delta_x}{\delta_{l_k}[Z]} \tag{6.10}$$

$$\begin{cases}\Gamma_{Y_k}=1 & \text{if} \qquad \omega_{Y_k}>\omega^0_{Y_k}\\ \Gamma_{Y_k}=0 & otherwise\end{cases} \tag{6.11}$$

where $\omega^0_{Y_k}$ is a threshold value defined as:

$$\omega^0_{Y_k}=\max(\omega_{Y_k}[Z])*Tr_k \tag{6.12}$$

$\delta_{l_k}[Z]$ is the reaction thickness of the species k (width at half maximum of the species source term) while n_k the minimum number of mesh points required across δ_{l_k} to ensure its proper resolution. Tr_k is a species source term threshold value while $Max(\omega_{Y_k}[Z])$ is the maximum value of the species source term that is function of the local mixture fraction. $Max(\omega_{Y_k}[Z])$ and $\delta_{l_k}[Z]$ are tabulated as function of a passive scalar Z, from a collection of 1-D premixed laminar flames, varying the fresh gases equivalence ratio in the whole flammability limit. This species flame sensor definition, based on species source term, and the dynamic thickening definition are close to the one used for FPI-tabulated chemistry in Sec. 6.3.2.1.

The global flame sensor Γ and the global thickening factor F applied in Eq. 6.9 are written as a boolean union of the Γ_{Y_k} and F_{Y_k} defined in Eq. 6.11 and in Eq. 6.10, respectively. In practice, Γ and F are expressed as follows:

Table 6.2: *Dynamic TFLES parameters for computing Γ_{Y_k} and F_{Y_k}.*

	F	P$_2$	CO	V$_2$
n_k	3.0	2.0	3.0	2.0
Tr_k	0.1	0.1	0.05	0.05

$$\Gamma = max\left(0, \Gamma_{Y_k}\right) \quad for \quad k \in [1, N_s] \tag{6.13}$$

$$F = max\left(0, F_{Y_k}\right) \quad for \quad k \in [1, N_s] \tag{6.14}$$

Where N_s is the number of selected species to build-up Γ and F. For Sydney inhomogeneous burner 4 species are selected: Fuel (F) and the virtual product P$_2$ from the main mechanism, CO and V$_2$ from the CO virtual sub-mechanism. With this species combination, Γ allows to properly encompass the flame reactive zone and F to properly solve the whole reactive layer and consequently the heat release rate. n_k and Tr_k are species depended parameters and they are chosen to retrieve a proper reproduction of the species reactive layer. Typical values of n_k are bounded between 2 and 5 while typical values of Tr_k are bounded between 0.05 and 0.2

For Sydney Inhomogeneous burner, the n_k and Tr_k employed parameters are summarized in Tab. 6.2. The same TFLES virtual chemistry strategy has been also successfully applied in recent previous works: the computations of the Cambridge stratified swirl burner (Mercier et al. 2017a) and Preccinsta burner in adiabatic (Cailler 2018) and non adiabatic (Maio et al. 2019) conditions.

6.3.2.3 Validation test case

1-D stoichiometric flames are computed using both FPI tabulated chemistry and virtual chemistry combined with the TFLES model employing the parameters detailed in the previous section. For the thickened flame simulations a mesh size of 0.2 mm is considered. It is a representative mesh size in the flame region in the 3-D LES of the Sydney inhomogeneous burner. Both thickened flame computations are compared with fully resolved unthickened ones employing a mesh size of 0.02 mm. All 1-D flames are computed with YALES2 solver (Moureau et al. 2011a).

Figure 6.2 shows, on the left, the flame sensor and the dimensionless TFLES heat release rate and, on the right, the TFLES temperature profiles compared to the fully resolved unthickened ones. The upper figures refers to the FPI-tabulated chemistry computations while the bottom ones to the virtual chemistry computations. Indeed, with the employed dynamic TFLES parameters, described above, heat release rate and as well as temperature profile are well described after the thickening operation. This ensure that the laminar flame speed in conserved with an error of 2.5% for FPI tabulated chemistry and 4%

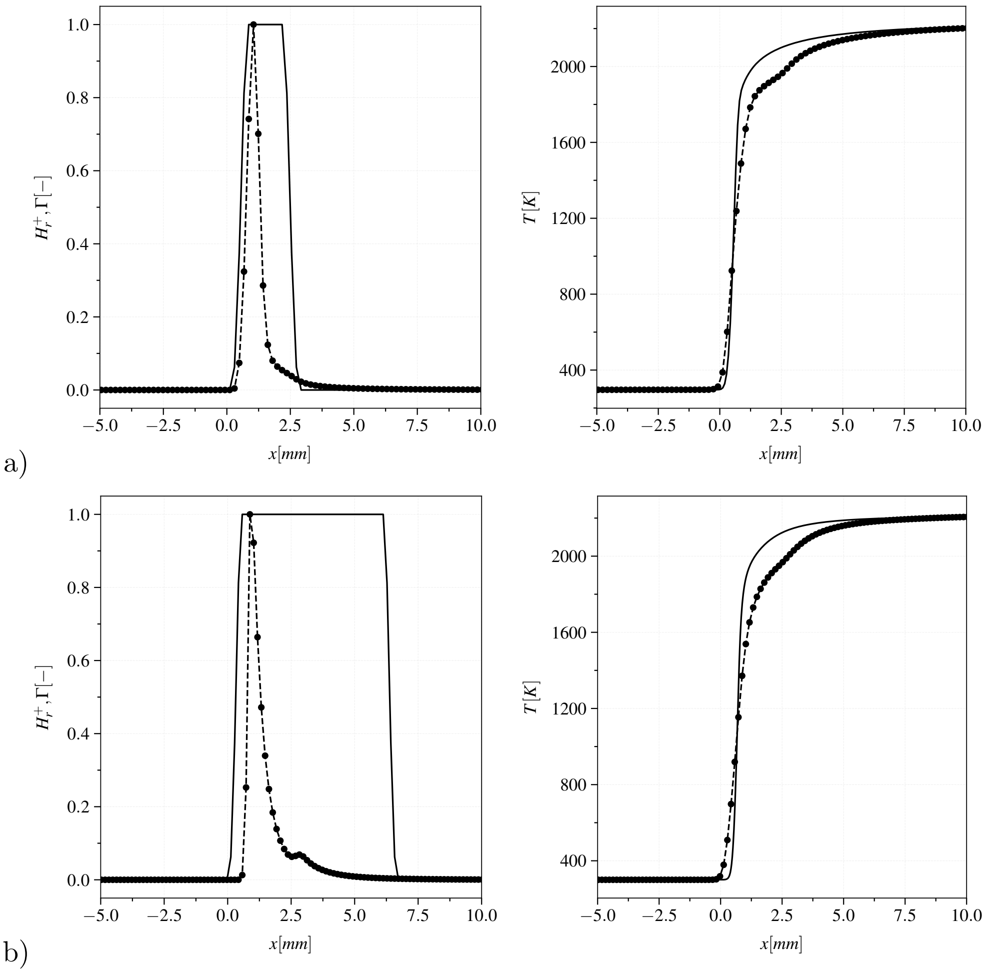

Figure 6.2: *TFLES stoichiometric 1-D flames with FPI tabulated chemistry and virtual chemistry. On the left: the flame sensor* Γ *(solid line) and the dimensionless heat release rate (dashed line). On the right: temperature profile of the TFLES computation (dashed line) compared to the temperature profile of the fully resolved, unthickened flame (solid line). The dots represents the mesh points of the thickened flame simulation. a) FPI tabulated chemistry. b) virtual chemistry*

for virtual chemistry. The virtual chemistry flame sensor, evaluated considering multiple chemical time scale (4 species), is visibly wider than the FPI tabulated chemistry one. This is due to the inclusion of product species in the flame sensor computation (P_2 and V_2). Howhever, this choice ensure a correct resolution of the product species but does not affect the laminar flame consumption speed prediction.

6.3.2.4 Wrinkling model

The analytic formulation proposed by Charlette et al. (2002a) and successively improved by Wang et al. (2011) is retained to model the SGS flame wrinkling:

$$\Xi_\Delta = \left(1 + min\left[\frac{\Delta}{\delta_L} - 1, f_\Delta \frac{u'_\Delta}{S_L}\right]\right)^\beta \tag{6.15}$$

where δ_L, S_L and Δ are the laminar flame thickness, laminar flame speed and the flame test filter size, respectively. u'_Δ is the sub-grid scale velocity fluctuation and f_Δ a parameter for including flame strain effect in the model. β is the fractal dimension of the flame and it is the controlling parameter for Ξ_Δ. More details about the theoretical formulation and derivation of Ξ_Δ are given in Charlette et al. (2002a), Charlette et al. (2002b) and Wang et al. (2011). In the present work S_L and δ_L are computed from 1-D premixed flames and tabulated as function of the local mixture fraction Z. β is chosen equal to 0.5.

6.4 Burner overview

6.4.1 Experimental set-up

The burner assembly shown in Fig 6.3 (Barlow et al. 2015) consists of two concentric tubes surrounded by a pilot annulus. It is centered in a wind tunnel supplying a co-flowing air stream at fixed velocity (the nominal co-flow velocity is equal to 15m/s). The particularity of the burner consists in the possibility to investigate different inhomogeneous flame configurations, simply by changing the geometry. The inner tube can be recessed in the outer one at different distances Lr from the burner exit plane, from 0 mm to 300 mm. When $Lr = 0$, fuel and air are injected separately in the chamber, promoting a diffusion flame. When $Lr = 300$, an homogeneous mixing between fuel and air is observed in the mixing tube, before the injection in the combustion chamber. For $0 < Lr < 300$, inhomogeneous mixing occurs and the partially premixed fuel-air mixture is injected in the chamber. It is also possible to feed alternatively air in the outer tube and fuel in the inner tube (FJ configuration) or fuel through the outer tube and air within the central tube (FA configuration). The way of feeding the tubes (FJ or FA) and the recession distance are the controlling

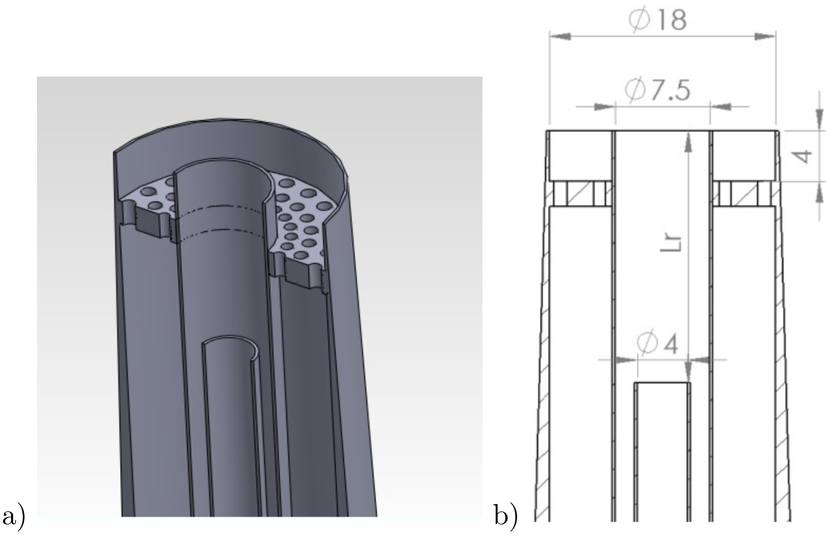

Figure 6.3: *The figure shows: a) a schematic 3D cut of the burner. b) a 2D section with the main burner lengths expressed in mm. The two figures are reproduced from Meares and Masri (2014)*

parameters to manage the degree of mixing between the streams. Different flame configurations may be stabilized at the burner exit, including cases in which stratified premixed and non-premixed flame structures co-exist.

At the beginning, the burner was designed to investigate the influence of mixture inhomogeneities on stabilization proces of partially premixed flames (Meares and Masri 2014). Then, different studies were conducted on a selected number of burner configurations with the scope to investigate the flame structure (Meares et al. 2015), (Barlow et al. 2015), issuing the partially premixed burner. The experimental databases (Masri 2016) (`http://web.aeromech.usyd.edu.au/thermofluids/database.php`) provides measurements for several burner configurations, obtained in different experimental campaigns, changing the fuel (compressed natural gas or methane) and the pilot composition (3-gas pilot or 5-gas pilot). Sydney University have provided velocity measurements by laser Doppler anemometry and high-speed OH PLIF imaging, while Sandia National Laboratory have provided measurements of temperature and major species mass fractions, using line-imaged Raman/Rayleigh scattering and laser-induced fluorescence (LIF) of CO.

6.4.2 Target case

The FJ case is preferred to the FA case for stability reasons. Volumetric air to fuel ratio VA/VF is fixed to 2. Employing methane as fuel, the prescribed air/fuel volumetric ratio corresponds to bulk equivalence ratio of 4.76.

The recession distance Lr is set to 75mm because it allows to reach the maximum blow-off velocity (114.3 m/s) for CH_4-air flames series. The pilot stream

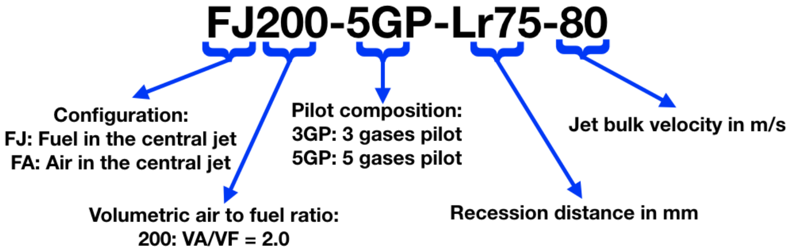

Figure 6.4: *Nomenclature used by experimental research groups to uniquely identify a flame configuration for Sydney inhomogensous burner.*

Table 6.3: *Main characteristics of the target flame configurations investigated in the thesis and in the 14th TNF workshop edition. Lr is the recession distance of the inner pipe. U_b is the mean bulk flow velocity of the main jet. Ubo is the blow off velocity. U_F and U_A are the bulk velocity at the fuel and air tube inlets respectively.*

Flame configuration	$Lr[mm]$	$U_b[m/s]$	Ub/Ubo	$U_A[m/s]$	$U_F[m/s]$	Re	$Hr(kW)$
FJ200-5GP-Lr75-80	75	80	0.7	83.4	93.8	37500	38.6

is feed with 5 gases mixture whose composition is defined to recover the equilibrium adiabatic flame temperature and composition of a stoichiometric methane-air flame (Barlow et al. 2015).

The chosen configuration, according to the nomenclature used by experimental groups to identify uniquely each burner configuration is explained in Fig. 6.4, is the FJ200-5GP-Lr75-80. In Table 6.3, the main operating parameters of the selected configuration are summarized including the bulk Reynolds number Re and the thermal power released by the flame Hr.

The bulk velocity of the investigated case corresponds to 70% of the blow-off limit. This operating point is shown in the blow-off plot in Fig. 6.5. It shows the experimental blow-off limit as function of the recession distance (Barlow et al. 2015). The enhancement in flame stabilization for the Lr75 case is experimentally attributed to the development of a premixed stratified flame structure close to the burner exit (Barlow et al. 2015). Then, within the first ten main tube diameters downstream, the flame relaxes toward a non-premixed combustion mode (Barlow et al. 2015).

The FJ200-5GP-Lr75-80 have been judged the most interesting cases for the numerical study for two main reasons: i) it exhibits the presence of multi-mode flame regimes (Barlow et al. 2015) ii) the widest experimental database exists for this configurations, including cold and hot inert data (Masri 2016).

For clarity and shortness reasons, the selected configuration is referred with the name Lr75Ub80 in the following part of the chapter.

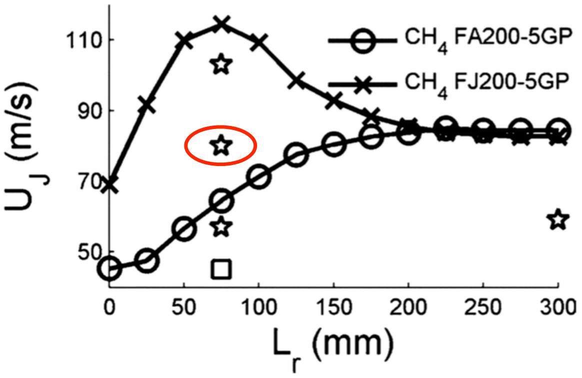

Figure 6.5: *Bulk jet velocity of the simulated flame (stars circled by red bound). It is placed in the graph that plots the measured blow off velocity U_{bo} versus recession distance Lr for the FJ and FA cases. The figure is reproduced from Barlow et al. (2015).*

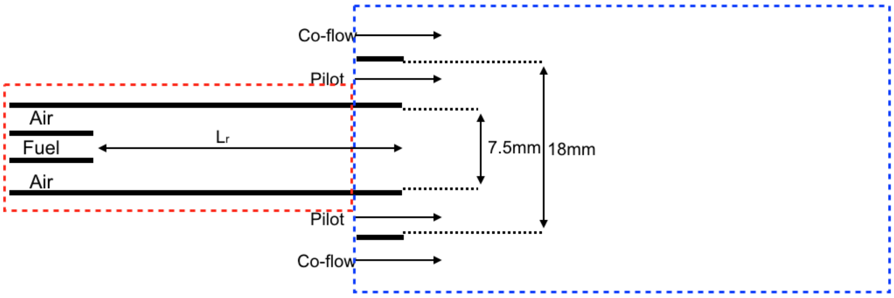

Figure 6.6: *Schematic view of the two computational domains. The non-reacting fluel/air mixing computational domain, simulated by Perry et al. (2017), is bounded in red. The reacting computational domain, simulated in the present work, is bounded in blue.*

6.5 Numerical set-up

6.5.1 Computational domain

The whole inhomogeneous flame geometry includes the burner assembly (pipe/annulus region and mixing tube) and the combustion chamber. The computation of the whole configuration is too CPU expensive, because an highly resolved LES is required to capture the mixing process between fuel and air.

Therefore, as shown in Fig. 6.6, two separate computational domains are retained: one for the mixing tube and the other for the combustion chamber.

For the combustion chamber domain, the boundary condition in correspondence of the main inlet must be provided as the output of the mixing tube region computation.

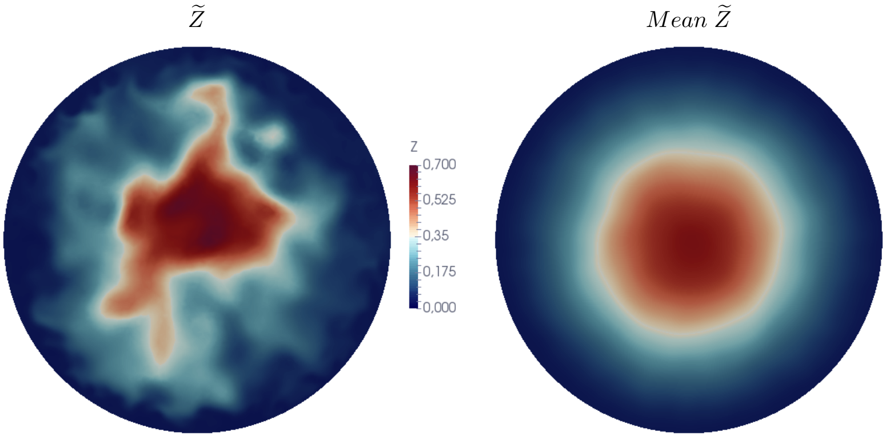

Figure 6.7: *2D colormap of instantaneous and mean mixture fraction profiles at main jet inlet. The instantaneous profiles are interpolated from the Princeton boundary conditions database and the temporal mean in done over 2.5 ms of physical time.*

The non-reacting simulations of the flow within the mixing tube is not performed here. The results provided by the Princeton group (Perry et al. 2017; Perry and Mueller 2018) and shared in the context of the TNF workshop, are retained.

Perry et al. (2017) conducted the non-reacting LES of the flow upstream of the main jet exit plane, splitting the domain domain into two regions that are separately computed. Firstly, the fully developed flow in the pipe/annulus region is simulated, secondly the turbulent mixing tube region is computed.

Perry et al. (2017) stored the output of the mixing tube computation over a plane, placed 1D (D is the main jet diameter) upstream the burner exit plane. 2-dimensional velocity and mixture fraction data are given in the database as function of the simulation time and the spatial coordinates. Mixture fraction and velocity profiles are time varying as the flow is turbulent and a non stationary LES is performed.

6.5.2 Inlet boundary conditions

6.5.2.1 Main tube

The Princeton database (Perry et al. 2017) is employed in this work to prescribe, as function of the simulation time, the 3 velocity components and the inhomogeneous mixture 1D upstream the main jet flame inlet. Each instantaneous solution is spatially interpolated from the Princeton mesh to the employed one.

Figure 6.7 shows 2-D instantaneous mixture fraction profiles prescribed at the main jet inlet. The figure shows an instantaneous snapshot and the mean profile

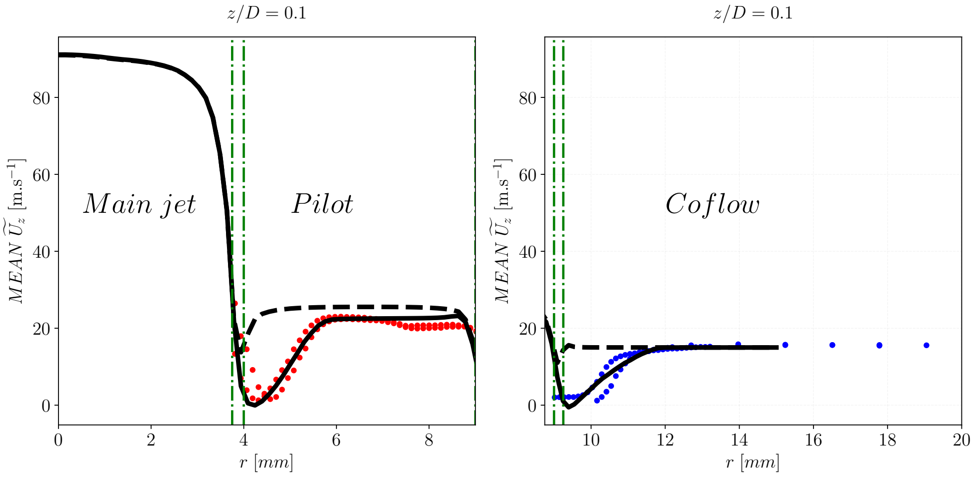

Figure 6.8: *Axial velocity mean profile at 0.1D downstream the burner exit plane. The red dots and the blue dots refer to two different experimental campaign aimed at measuring the pilot and the coflow velocity, respectively. The experimental velocity data (red and blue dots) are compared versus two different simulations. Dashed line: simulation conducted imposing, at the burner exit plane ($z/D = 0$), a flat axial velocity profile, equal to the experimental nominal one. Solid line: simulation conducted prescribing velocity boundary layers, fitted to retrieve the experimental mean velocity data available at $z/D = 0.1$. The vertical green lines indicate the thickness of the burner lips between the main jet and the pilot tube and between the pilot tube and the coflow stream, respectively.*

computed over 2.5ms of physical time.

6.5.2.2 Pilot and Coflow

6.5.2.2.1 Velocity Laminar velocity profiles are prescribed at pilot and at the coflow inlets because the two streams exhibit laminar bulk flow Reynolds numbers.

The experimental database (Masri 2016) provides mean axial velocity measurements at $0.1D$ downstream the burner exit plane, in reactive conditions, in correspondence of the pilot and coflow streams. These measurements are plotted in Fig. 6.8.

The experimental measurements have been performed along the burner diameter and are plotted as function of the radial distance r. It can be observed, that the experimental data are not exactly symmetric with respect to the center of the burner because of the presence of small asymmetry in the experimental set-up (Meares et al. 2015; Cutcher et al. 2017).

Two shear layers are observed at $z/D = 0.1$ downstream (z is the axial distance): at the interface between the the pilot and the main jet and at the interface between the coflow stream and the pilot tube, respectively.

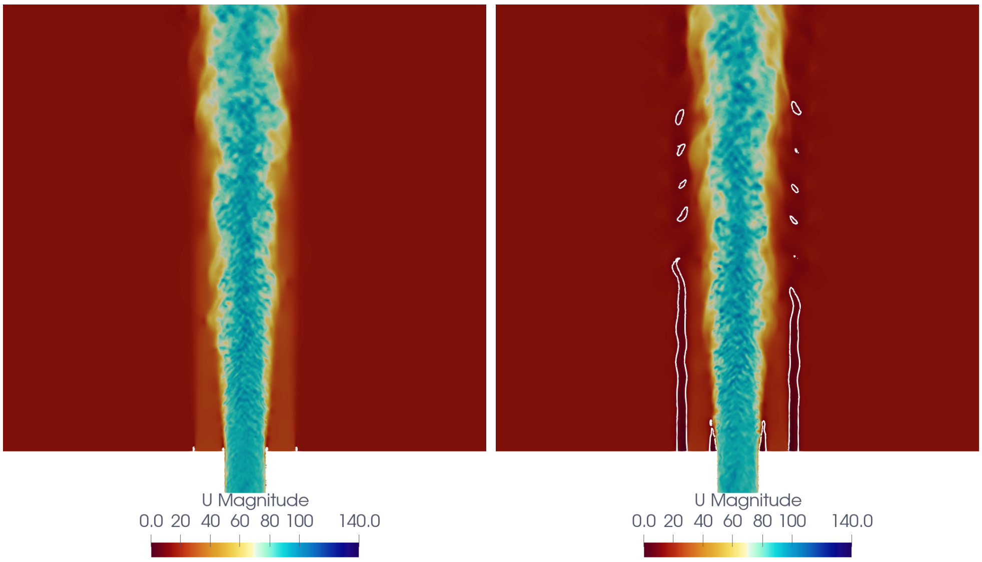

Figure 6.9: *2D instantaneous velocity magnitude field on the chamber mid-plane with 10 m/s iso-line in white. Two different velocity profiles are prescribed in pilot and coflow jets. On the left: the experimental nominal bulk velocity is imposed. On the right: a non uniform axial velocity profile is polynomially fitted to match the velocity measurements at* $z/D = 0.1$. *In both cases the simulation are conducted using the TFLES-FPI tabulated chemistry model, described in Sec. 6.3.2.1.*

To find the best velocity profile to prescribe at the pilot and coflow inlet tubes, two different simulations have been performed, imposing the pilot and coflow inlet velocity according to the two different criteria:

1. Flat velocity profile, using the bulk nominal value given by the experimental database.
2. A numerical polynomial axial velocity profile fitted to match the experimental data available at $z/D = 0.1$.

Figure 6.8 shows the radial numerical mean velocity profiles from the two simulations, compared aposteriori to experimental data at 0.1D downstream.

Indeed, the prescription of a numerical fitted velocity profile, for the pilot and coflow inlets, allows to better retrieve the shear layer that develops at the interface between the jets.

Figure 6.9 compares, over a 2-D cut-plane, the instantaneous velocity magnitude field for the two cases. When the tube boundary layers are reconstructed (right figure), the shear layers between the jets are more intense. The isocontour at $10 m/s$ (white line) confirms the velocity drops at the shear layers. This drop is not present when the flat velocity profile is imposed (left figure).

It can be observed that, when a fitted profile is imposed, the shear layers become unstable and some velocity instabilities are convected downstream.

It is also shown in Fig. 6.9, that the shear layer between the pilot and the coflow is more sensitive to the boundary conditions modification than the shear

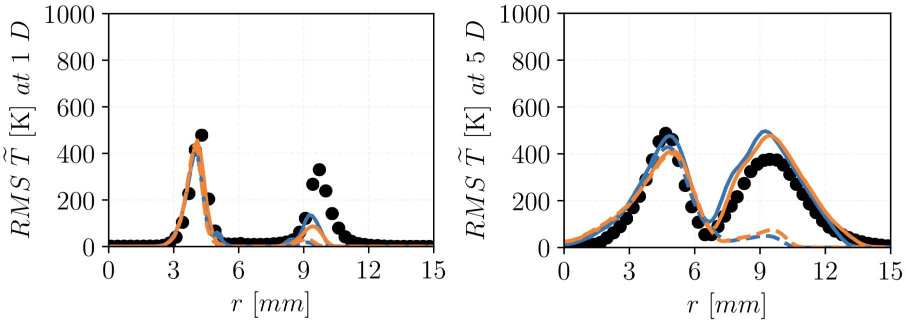

Figure 6.10: *1-dimensional radial rms temperature profile at $z/D = 1$ and $z/D = 5$. LES results are compared to experimental data. Dots: Experimental data. Solid lines: computation that consider numerically fitted profiles at the pilot and coflow inlets. Dashed line: nominal bulk velocity is considered at the pilot and coflow inlets. Blue: FPI tabulated chemistry. Orange: Virtual chemistry.*

layer between the main jet and the pilot. Indeed the velocity drop affects a longer distance in the outer shear layer; it is confirmed by the velocity $10m/s$ isocontour which is shorter for the inner shear layer.

The instability originated at the pilot-coflow shear layer affect the scalars computed fluctuations.

Figure 6.10 shows temperature rms profiles over 1-D radial probes at 1D and 5D downstream the burner exit. Experiments are compared to LES results. The two shear layers (main/pilot and pilot/coflow) induce two rms temperature peaks. When flat velocity injection is imposed at the pilot and coflow inlets the second rms peak is completely missed. Contrarily, prescribing numerical injection profiles, pilot-coflow shear layer fluctuations are enhanced at 1D and 5D downstream. However, at 1D, the magnitude of the fluctuations is improved but still underestimated.

From the analysis conducted in Fig. 6.8, Fig. 6.9 and Fig. 6.10, the numerically fitted polynomial profile is preferred and imposed as velocity boundary condition for the pilot and coflow inlets for the reactive simulations.

6.5.2.2.2 Scalars In addition to velocity profiles, the scalars values must be prescribed for the pilot and coflow inlets. The coflow tube is fed with pure air at 295 K both in cold and in reactive conditions. Instead, the pilot tube is fed differently in cold and reactive conditions. In cold conditions, ambient air is injected at 295 K.

While, in reactive conditions, the pilot tube is fed with a mixture of 5 gases (H_2, C_2H_2, O_2, N_2, CO_2), designed in the experimental study.

The fresh gases composition injected upstream of the pilot flame is reported in Tab. 6.4

The mixture is defined to recover the adiabatic equilibrium temperature and C/H composition of a stoichiometric CH_4/air flame (Barlow et al. 2015).

Table 6.4: *Measured pilot gases composition. Fresh inlet row: reactants measured upstream of the pilot flames holder. $z/D = 1$ row: pilot products composition measured at $z/D = 1D$. The corresponding temperature is also given.*

Pilot composition	C_2H_2	H_2	N_2	CO_2	O_2	H_2O	CO
Fresh inlet (295 K)	2.80E-02	1.16E-02	7.24E-01	5.66E-02	1.78E-01	-	-
$z/D = 1$ (2094 K)	-	1.30E-03	7.07E-01	1.18E-01	2.47E-02	1.17E-01	3.01E-02

Indeed, the pilot flame temperature estimated from an equilibrium computation performed at constant pressure and constant enthalpy, is equal to 2221K. This value is very close to the equilibrium adiabatic temperature of a stoichiometric CH_4/Air mixture (2223K), in the same conditions.

Pilot products and temperature near the burner exit plane ($z/D = 1$) are also measured (Barlow et al. 2015) and reported in Tab. 6.4. It can be observed that this mixture does not match adiabatic equilibrium conditions. Temperature is equal to 2094 K, which is lower than its adiabatic equilibrium value (2221K). Two possible reasons can cause this mismatch:

1. Heat losses: pilot products lower their enthalpy because of heat looses in the tubes.
2. Partial mixture oxidation: pilot gases do not have enough time to reach adiabatic equilibrium conditions and they remain partially oxidized at $z/D = 1$.

By conducting an equilibrium computation, at constant pressure and enthalpy, using the measured temperature and composition at $z/D = 1$, the equilibrium temperature (2240K) and composition are very close to the adiabatic one.

Consequently, it is possible to concluded that heat losses is not the leading phenomena, but the pilot mixture is only partially oxidized at $z/D = 1$.

In order to make the simulation injection close to the experimental one, a normalized progress variable $C = T/T^{eq}$ is defined for a 1-D premixed stoichiometric flamelet. The condition at the pilot inlet are tuned moving the injection conditions along the flamelet trajectory. The injection point is found when the LES computation is able to match the mean experimental bulk temperature in correspondence of the pilot stream, at 1D downstream, accepting an error of 1%.

In practice, the inlet pilot conditions are defined for the two combustion chemistry models as follows:

- In the FPI tabulated chemistry simulation: the pilot composition is specified using the mixture fraction Z and the progress variable C. The flamelet values are given in Tab. 6.5.
- In the virtual chemistry simulation: the inlet temperature and virtual species composition are specified. The flamelet values are given in Tab. 6.6.

Figure 6.11 compares the FPI-tabulated chemistry and the virtual chemistry mean temperature from LES with experiments, at 1D downstream. Indeed,

Table 6.5: *Inlet pilot gases scalars for FPI tabulated chemistry computation*

Z	C
0.055	0.941

Table 6.6: *Inlet pilot gases scalars for virtual chemistry computation: mass fractions of the species in Main and CO mechanisms.*

Temp	F	Ox	I	P_1	P_2
1950 K	0.22E-02	0.829E-02	0.206E+00	0.1909E-02	0.2056E-01
P_3	P_4	N_2	CO	V_1	V_2
0.6431E-02	0.2909E-01	7.2466E-01	0.198E-01	0.0	2.44E-01

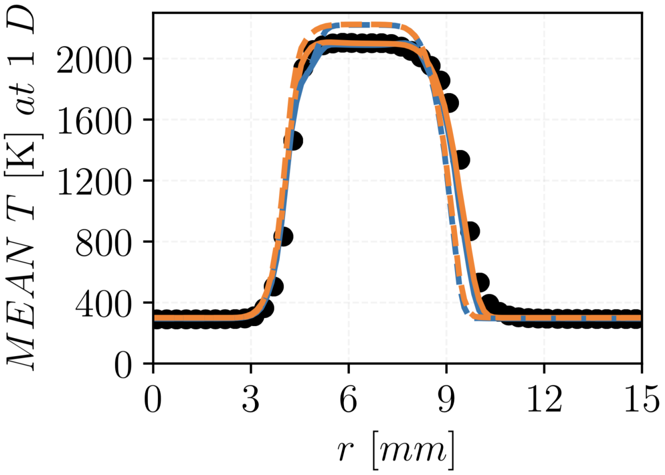

Figure 6.11: *1 dimensional radial mean temperature profile at $z/D = 1$. LES results are compared to experimental data. Dots: Experimental data. Dashed lines: equilibrium pilot scalars are imposed at the inlet. Continuous line: non-equilibrium pilot scalars are imposed at the inlet. Blue: FPI tabulated chemistry. Orange: Virtual chemistry.*

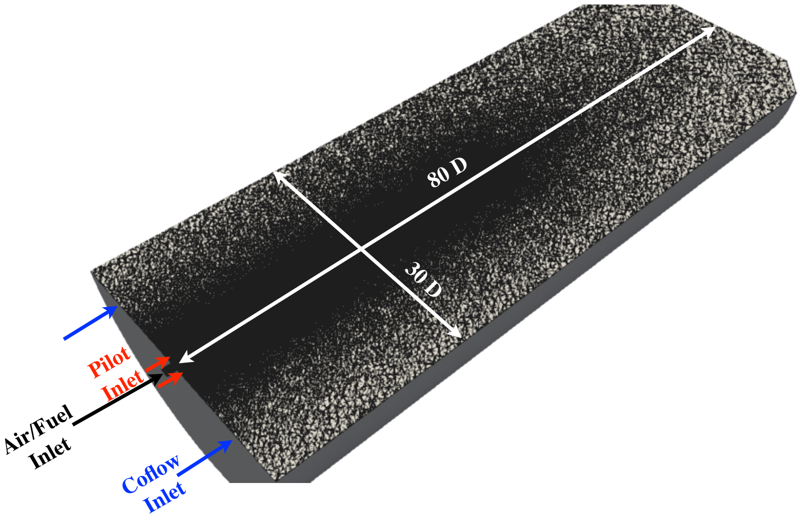

Figure 6.12: *3D view of the Inhomogeneous piloted burner reactive geometry. Half-portion of the whole geometry. On the 3-D cut the cell edges along with the geometry lengths and injections are reported.*

by adjusting the pilot inlet conditions to match the mean bulk temperature, the whole mean temperature profile at 1D is correctly reproduced with both chemistry models. Instead, when equilibrium conditions are prescribed, at pilot inlet (i.e. $C = 1$), temperature, at 1D downstream, is overestimated of the same amount with both combustion chemistry models.

6.5.3 Mesh and numerical parameters

Figure 6.12 shows a 3-D-cut of the computational domain employed in the numerical simulation of the Sydney Inhomogeneous burner. The length and the width of the domain are 80D and 30D, respectively. The computational domain is larger than the flame zone of interest to avoid outlet and wall effects on the flame. However, the computational cost it is not affected by this choice, because employing a tetrahedral unstructured mesh, the cell size is largely increased far from the zone of interest, as shown in Fig. 6.13.

The tetrahedral mesh features 10.1M nodes and the mesh size varies from 0.015mm in correspondence of the burner lips, to 5mm far from the flame zone. In the flame region of interest (up to 15D downstream) the mean cell size in around 0.2mm.

The maximum Mach number Ma encountered, in correspondence of the main jet exit, is ≈ 0.3. This value is low enough to retain the low Mach number hypothesis, valid for flow with $Ma \leq 0.3$ (Kraushaar 2011).

The calculations are performed with the unstructured finite-volume low Mach number code YALES2 Moureau et al. (2011a). A centered fourth-order scheme

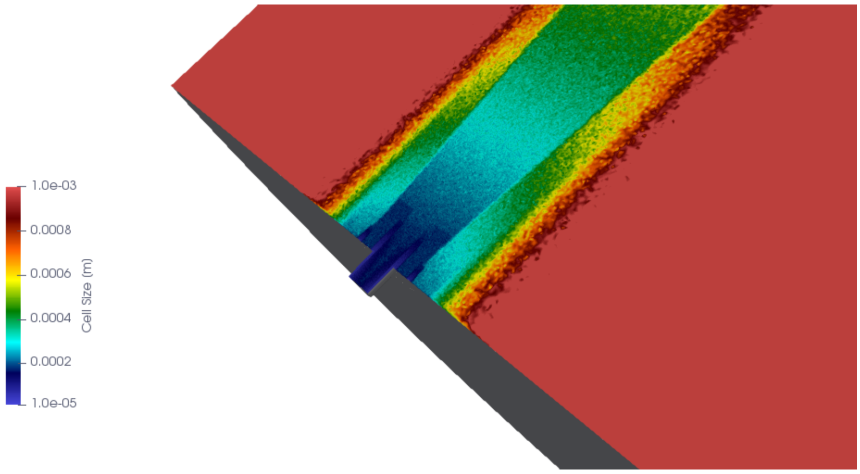

Figure 6.13: *Zoom of the above 3-D cut close to the injection tubes. The cut surface is coloured by the tetrahedral cell characteristic size clipped at 1mm maximum and 0.01mm minimum.*

Table 6.7: *Boundary conditions for the three injections in the different computations.*

Lr75Ub80	Main-jet	Pilot	Coflow
Cold	Air/Fuel mixture	Cold air	Cold air
Hot non-reactive	Cold air	Hot gases (Sec. 6.5.2.2.2)	Cold air
Reactive (FPI/Virtual)	Air/Fuel mixture	Hot gases (Sec. 6.5.2.2.2)	Cold air

in space and time is used for the numerical integration of the convective terms. The sub-grid Reynolds stresses tensor is closed with the WALE model (Nicoud and Ducros 1999).

Cold flow, hot non reactive and reactive simulations results are presented in the following sections.

The injection characteristics of the simulations, conducted in this chapter, are summarized in the Tab. 6.7.

Favre averaged LES statistics are computed and compared to experimental data in the following sections.

The hot non-reactive flow simulation is added as an intermediate numerical step, to analyse the impact of the pilot gases on the shear layers and on the mixing process. The details of this particular computation are given below.

6.6 Cold and non-reactive flow simulations

The validation of the numerical set-up for prediction of the aerodynamic field and of the non-reactive mixing is conducted through two intermediate steps:

1. Cold simulation: pilot is switched off and the partial premixed air-fuel mixture, as in Sec. 6.5.2.1, is injected through the central main jet.
2. Hot non-reactive simulation(inert): the pilot is switched on, as detailed in Sec. 6.5.2.2.2 but only air flows through the central pipe, to prevent chemical reaction. A mixture fraction is numerically defined to quantify the mixing between the pilot and the main jet steams.

The hot non-reactive simulation is an additional validation step, established in agreement with the TNF community, to further asses the robustness of the numerical set-up in the Sydney inhomogeneous burner simulation. This validation step is possible since Masri (2016) has provided, for the Lr75Ub80 case, velocity measurements in the same operating condition defined in the simulations.

The inert simulations (cold and hot non-reactive), in addition to validate the numerical set-up, allow to analyse and quantify the effect of the pilot stream in the mixing and flow processes.

6.6.1 Results

Mean and rms axial velocity profiles are shown in Figs. 6.14 and 6.15 for cold and hot non-reactive simulations, respectively. Results refer to the Lr75Ub80 case and they are shown at four different axial locations from the burner exit. In the cold flow simulation, the mean and rms profiles compare fairly well with the experimental data. At z/D=1 (z is the axial coordinate) the mean parabolic shape, issuing the main jet, observed in the experiments, is however not perfectly retrieved in the simulation. This discrepancy is observed also in the simulations conducted by the others TNF numerical groups (Barlow 2018). We have concluded, after discussing with the other TNF members, that it can be attributed to the boundary conditions database that does not perfectly characterize the penetration of the fuel jet in the air one, inside the mixing tube. The bulk rms in slightly underpredicted in the core of the jet even if its global shape is retrieved. The magnitude of the shear layer rms peak is correctly reproduced. Downstream, from z=5D, mean and rms solutions show that the jet velocity dissipation is very well reproduced.

The hot non-reactive simulation (Fig.6.15) velocity statistics compare also fairly well versus experiments. From 1D to 10D, the mean axial velocity shows a bulk profile, which is in accordance with experiments. Downstream, at z=20D, the simulation predicts a faster velocity decrease than experiments.

Figure 6.16 presents a comparison of the mixing process between the cold case and the hot non reactive case.

As anticipated above, in the hot non-reactive case, it is still possible to numerically define a mixture fraction to quantify the mixing between the pilot and

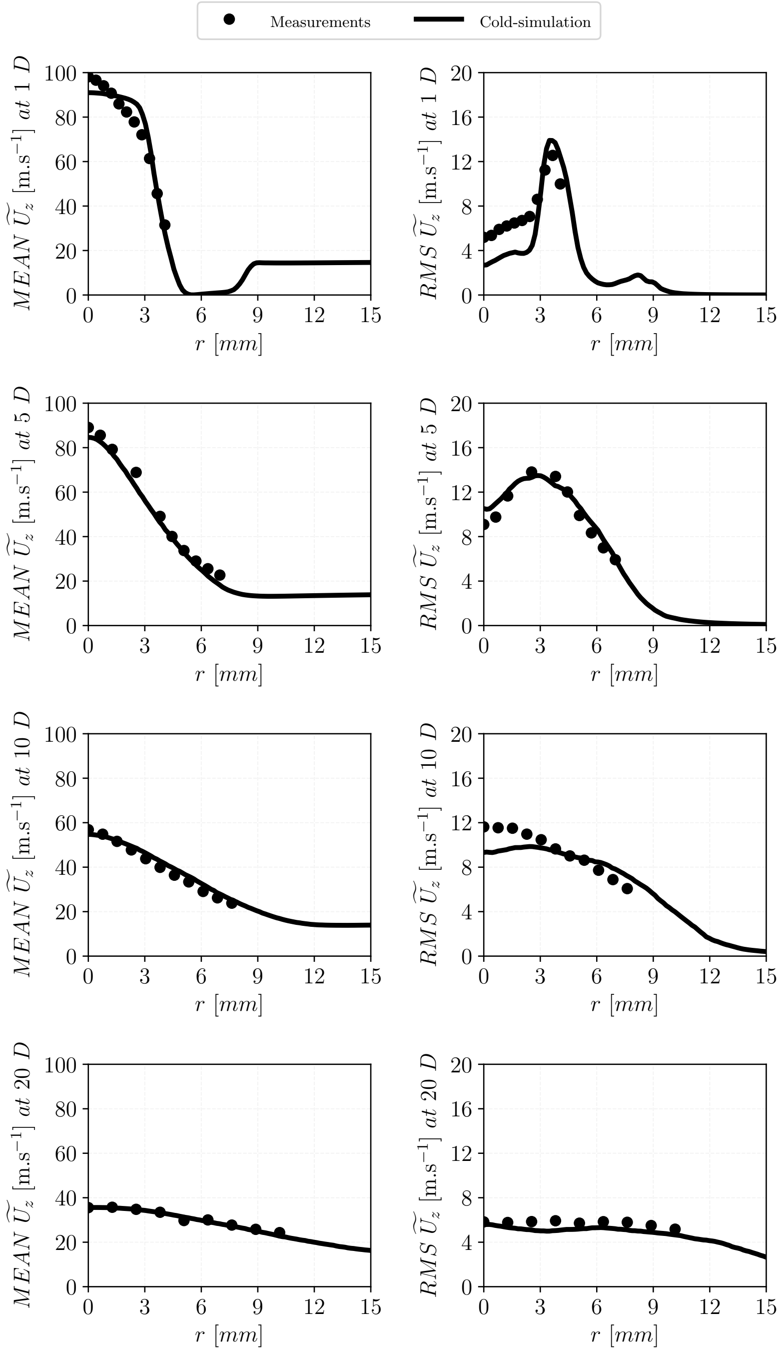

Figure 6.14: *Cold flow simulation. Axial velocity statistics (mean and rms) compared versus experimental data.*

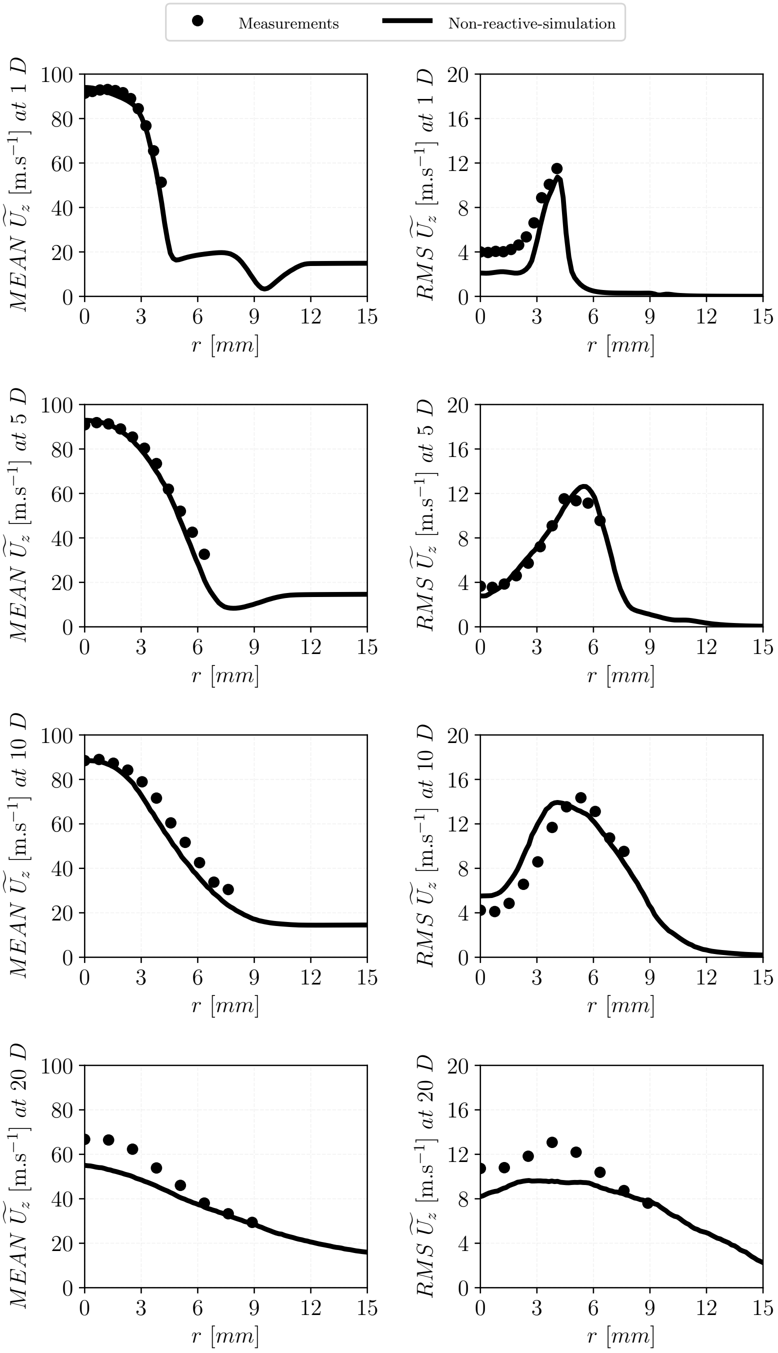

Figure 6.15: *Non reactive simulation. Axial velocity statistics (mean and rms) compared versus experimental data.*

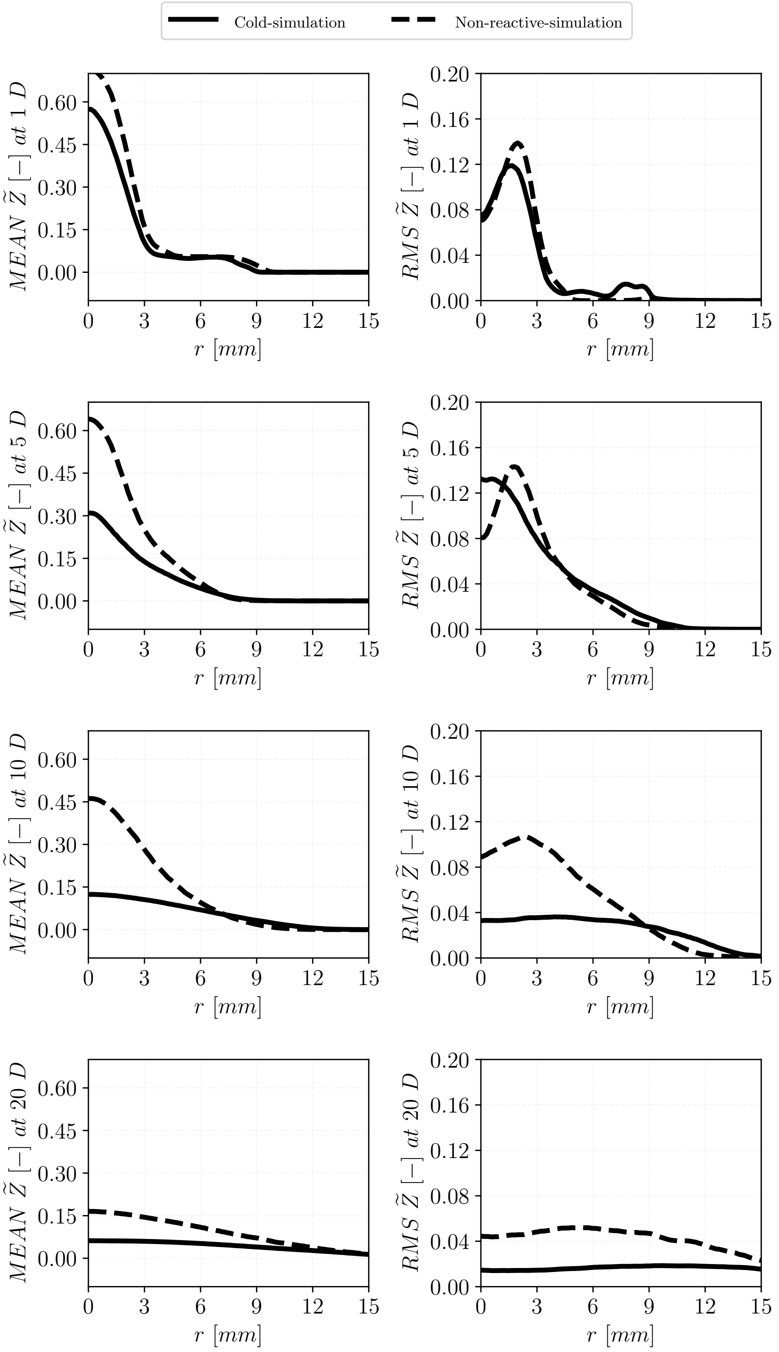

Figure 6.16: *Comparison of the mixture fraction statistics in cold and non reactive simulation. In non reactive simulation mixture fraction demarcate the air coming from the fuel jet.*

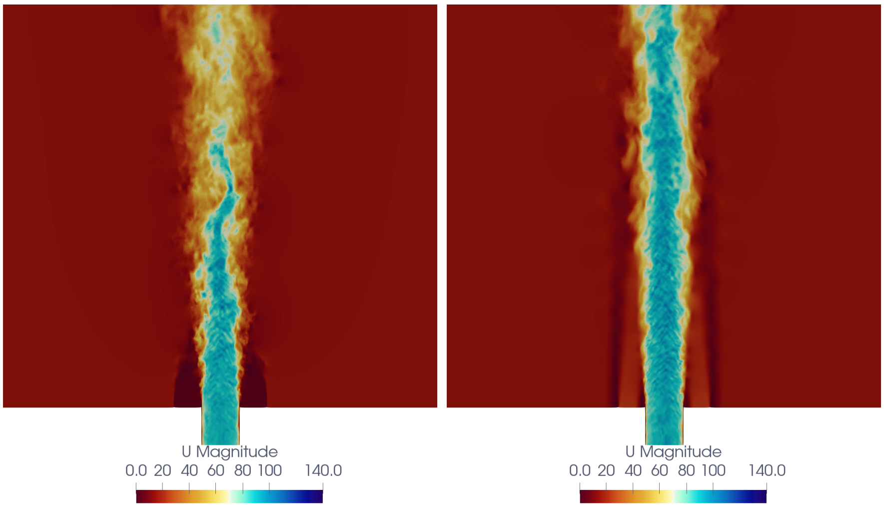

Figure 6.17: *2D instantaneous velocity magnitude field on the chamber mid-plane. On the left: cold simulation results are shown. On the right: hot non-reactive simulation results are shown.*

the main inflow steam.

Pilot hot gases prevent the mixing between the two streams: the main jet gases mix less with the coflow ones when the pilot is switched-on

Figure 6.17 compares the velocity 2-D instantaneous field for the cold and the hot non reactive simulations. In cold condition the low velocity pilot stream is not able to stabilize a long shear layer between the jets. The fast breakdown of the pilot-coflow shear layer, makes the coflow rapidly mixes with the main jet gases. On the contrary, in hot non-reactive conditions, the hot gases issuing the pilot tube, at higher velocity (bulk velocity around 25 m/s), create a layer which prevents the mixing between the main and coflow jets.

The mixing process in hot non-reactive conditions is closer to the reactive case one, presented in Fig. 6.19.

6.7 Reactive simulations

In reactive simulations, the mesh and numerical set-up applied in cold and hot non-reactive conditions are conserved. Velocity and scalars boundary conditions in the main jet and in the pilot are prescribed, in accordance with the analysis conducted in Sec. 6.5.2.

FPI-tabulated chemistry simulation and a virtual chemistry one are conducted in combination with TFLES turbulent combustion model, using the formalism presented in Sec. 6.3

LES results are presented for the Lr75Ub80 configuration, as for the cold and hot non-reactive case.

The analysis of the flame focuses mainly from the region close to the jet exit

(z=1D) to 15D downstream. This region has been identified, from the experimental studies, as crucial for flame stability behaviour (Barlow et al. 2015; Cutcher et al. 2017). The stability enhancement is experimentally attributed to the stratified premixed combustion regime close to the burner exit (Barlow et al. 2015). The flame regime relaxes to a non-premixed combustion one after 5D.
LES temporal statistics and instantaneous data (scatter plots) are compared to the experiments at different axial locations from the burner exit plane. Eventually, the scatter data are post-processed to compute the Wasserstein metric, as proposed by Johnson et al. (2017). This methodology helps to quantitatively quantify the discrepancy between the two combustion chemistry models (FPI and virtual chemistry) and experiments (Barlow 2018).

6.7.1 Radial statistics

Mean and rms 1-D LES radial profiles are presented and compared to the experiments, for axial velocity and scalars (mixture fraction, temperature and CO mass fraction). In the simulations, data are Favre-averaged in time, according to the definition given in Sec. 1.4.2.2. Then, LES statistics are spatial-azimuthally averaged to accelerate the statistical convergence. Results for both TFLES-FPI and TFLES-virtual chemistry are shown and compared.

6.7.1.1 Velocity

Figure 6.18 compares the axial velocity numerical statistics versus the experimental ones. At 1D downstream, a good agreement between experiments and numerical results is observed, in line with the profile shown in cold and hot non-reactive conditions (in Sec. 6.6.1). Further downstream, at 5D and 20D, in numerical simulations, despite the correct mean velocity shape is reproduced, the jet expansion is overestimated. RMS shape and peak are overall well reproduced at the different axial locations. The comparison between FPI-tabulated chemistry simulations and virtual chemistry results highlights no remarkable differences. Hence, the aerodynamic field is here weakly dependent on the combustion chemistry model. Instead, it is more sensitive to the inflow conditions injected in the 3 streams as supported by the TNF joint numerical study (Barlow 2018).

6.7.1.2 Mixture fraction

In the experimental database, Bilger's formulation (Bilger et al. 1990) is used for mixture fraction definition. In the simulations, the mixture fraction is defined as a conservative passive scalar both for FPI-tabulated and for virtual chemistry models. The numerical mixture fraction definition is consistent with experiments: it is defined to be normalized between 0 and 1 in pure air and in pure fuel, respectively.

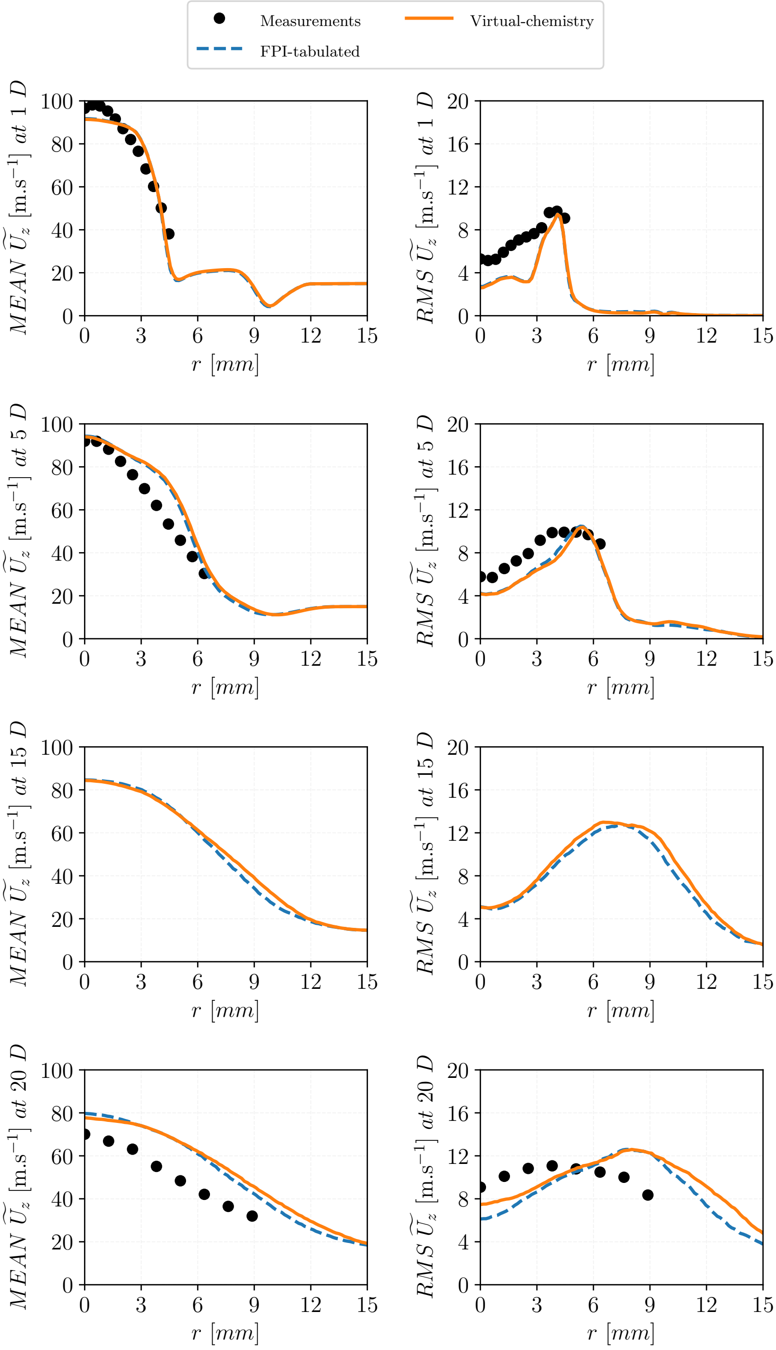

Figure 6.18: *Axial velocity statistics. Comparison of the FPI-tabulated and virtual chemistry results versus experimental data. At 15D experimental measurements are not available*

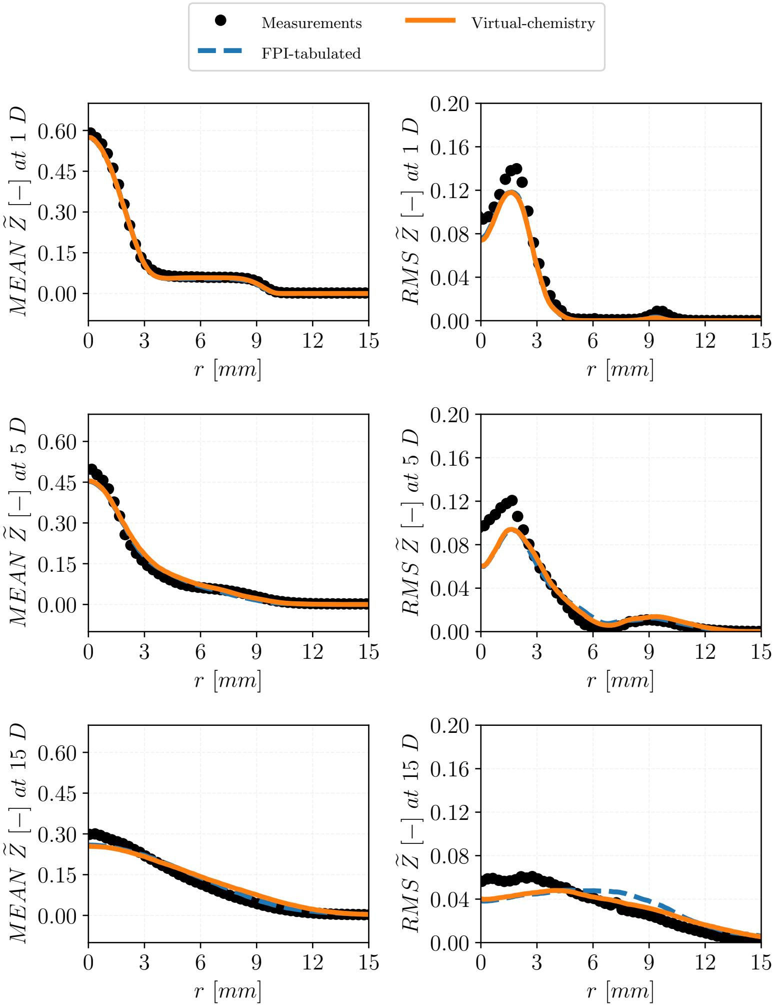

Figure 6.19: *Mixture fraction statistics. Comparison of the FPI-tabulated and virtual chemistry results versus experimental data.*

Figure 6.19 shows the mixture fraction numerical radial profiles compared versus experiments. An overall good agreement is observed for mean and rms values. At 1D and 5D downstream, the mean and rms mixture fraction profiles compare well to experiments. A slight underestimation of the rms peak, in correspondence of the shear layer, established between the main jet and the pilot, is observed. The small rms peak, in correspondence of the pilot-coflow shear layer is underestimated at 1D but it is well reproduced at 5D. At 15D downstream, the mean profiles show that simulations over-predict the mixing with respect to experiments, with both chemistry models. The rms are also slightly underestimated in the core of the jet.

The FPI-tabulated results and virtual chemistry ones do not show a remarkable difference in mixture fraction statistics. As for velocity, also the mixing shows a weak dependence from the combustion chemistry model but it is more sensitive to the inflow (Barlow 2018).

6.7.1.3 Temperature

Figure 6.20 compares the temperature numerical statistics versus the experimental ones. As pointed out in 6.5.2.2, the pilot inlet scalars are adjusted, over a flamelet trajectory, to reproduce the correct experimental mean pilot bulk temperature at 1D. The rms peak at the main jet-pilot shear layer is correctly reproduced but rms peak underestimation is observed in correspondence of the pilot-coflow shear layer.

At 5D, the mean temperature is correctly reproduced, especially in the virtual chemistry simulation. The temperature rms peaks at the shear layers are very well reproduced both with the FPI-tabulated model and virtual chemistry.

At 15D, some discrepancies exist, in mean temperature prediction with both combustion chemistry models. The temperature discrepancies affect the centerline region ($r < 5mm$) and the flame front region ($5mm < r < 12mm$). In the flame front region, temperature discrepancies are directly related to the mixing overprediction, observed in the previous section.

A further investigation of temperature statistics is conducted through the analysis of conditional means: the mean temperature is plotted in the mean mixture fraction space for the same axial location of the radial profiles (Fig. 6.21). Conditional mean data are useful to isolate temperature misprediction related to mixing misprediction.

In Fig. 6.21 experimental conditional mean data are reported for the positive and the negative radius, confirming a slight asymmetry in the burner set-up (Barlow et al. 2015). The effect of the asymmetry is mostly visible at 1D and 5D and it vanishes at 15D.

Conditional mean data confirm the transition from a stratified premixed flame structure, close to the burner nozzle, toward a non premixed like combustion mode starting from 5D.

At 1D, the experimental dip, in correspondence of the stoichiometric line, is

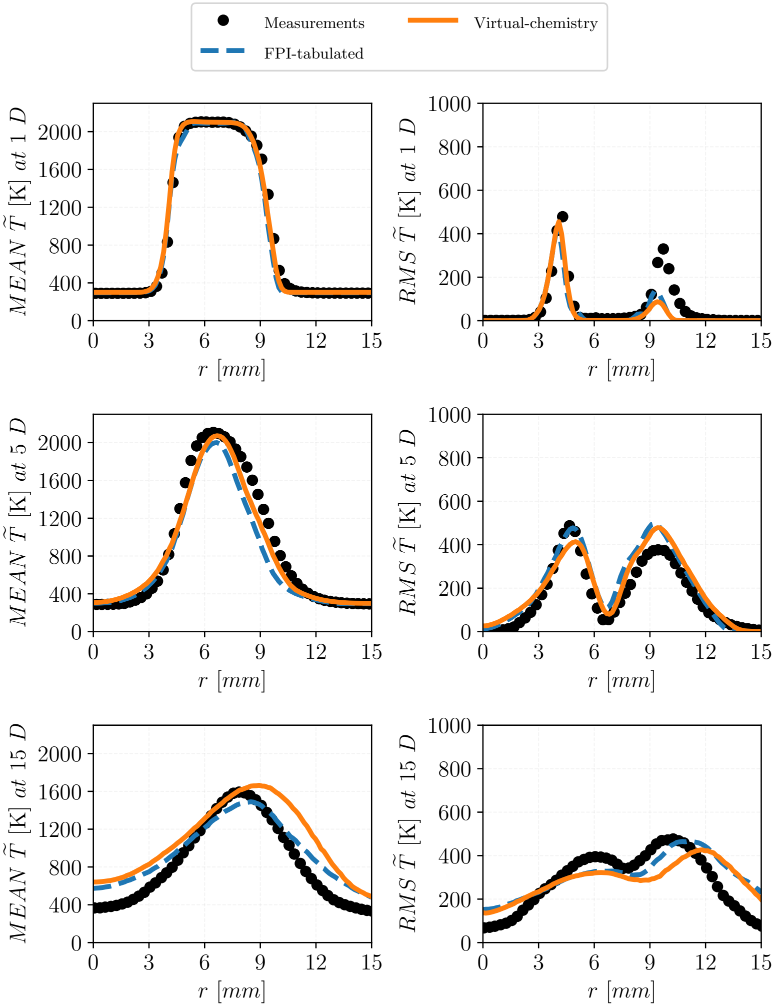

Figure 6.20: *Temperature statistics. Comparison of the FPI-tabulated and virtual chemistry results versus experimental data.*

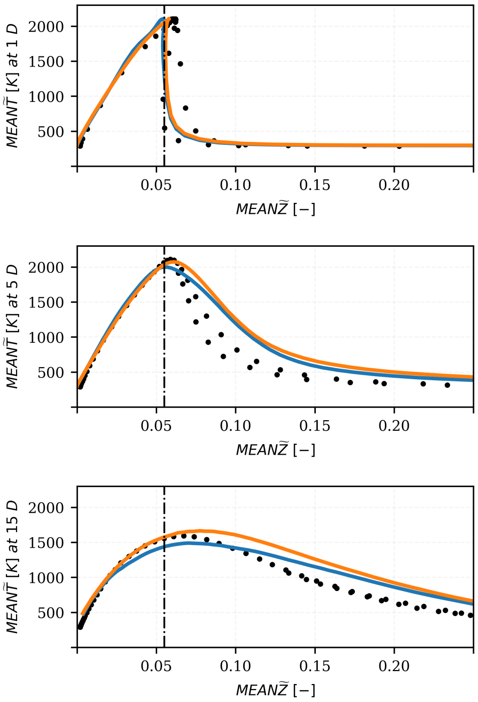

Figure 6.21: *Conditional mean temperature in mean mixture fraction space. Experimental data are plotted on the positive and negative radial side and compared to FPI-tabulated and virtual chemistry statistics. Dots: experiments. blue line: TFLES-FPI computation. Orange line: TFLES-virtual chemistry computation. The vertical mixture fraction stoichiometric line is also reported.*

correctly reproduced by the simulation results with both models. At 5D small discrepancy are only observed on the rich side. At z=15D, the lean, stoichiometric and moderately rich conditions are correctly retrieved by simulations especially with virtual chemistry. However, the mean temperature values on the rich side are slightly overestimated by both models.

This zone correspond, in the radial direction, to the centerline zone (core of the main jet).

Eventually, from the analysis of the conditional means, it is possible to conclude that: the radial mean temperature misprediction observed at 15D, in Fig. 6.20, are caused by mixing prediction errors in correspondence of the flame front, located in the peak temperature region, close to the stoichiometric mixture fraction ($r \sim 7mm$ in Fig. 6.20 at 15D).

Contrarily, the discrepancy observed in correspondence of the jet centerline zone ($r < 5mm$ in Fig. 6.20), are not entirely due to mixing problems as the conditional mean temperature overpredict the experimental values in the rich region.

This model discrepancy may be explained by multiple reasons: the uncorrect

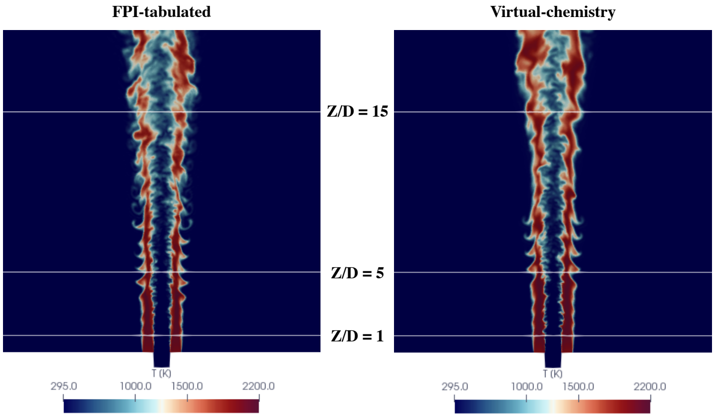

Figure 6.22: *Temperature 2D instantaneous snapshot on the chamber mid-plane. FPI-tabulated results are compared versus virtual-chemistry results. The different redial positions are also identified in the field.*

reproduction of the flame sensitivity to extinction and/or the uncorrect reproduction of heat release/aerodynamic field interaction.

Figure 6.22 shows temperature instantaneous snapshots from numerical simulation for both FPI-tabulated chemistry and for virtual chemistry computations. At 15D, some hot spots are convected toward the center of the jet. This phenomenon that causes the temperature increase in the centerline region (rich flame region) is not observed in the experiments.

6.7.1.4 CO mass fraction

1-D radial statistics of CO mass fraction, obtained from simulation, are compared versus experiments in Fig. 6.23. The agreement is very good up to 5D downstream, where temperature and mixing are also correctly predicted. Virtual chemistry results are better than FPI-tabulated chemistry ones. Indeed, when mixed combustion regimes are encountered (as at 5D), virtual chemistry is expected to perform better. It is optimized to predict CO in mixed combustion regime differently from FPI tabulated chemistry, which is based on flamelets trajectories accounting only for a premixed combustion regime.

At 1D, although, the mixing and temperature are well reproduced, numerical CO mean mass fraction underestimates experimental data both with virtual chemistry and with the FPI-tabulated chemistry models. A further investigation of the CO deviation at 1D, is proposed in the subsequent Section (Sec. 6.7.1.5).

RMS levels are well reproduced especially at 1D and 5D. Important discrepancies are observed at 15D downstream for mean and rms CO radial profiles, particularly when tabulated chemistry is used. This discrepancy is directly connected to temperature overestimation, at the same radial location, observed in

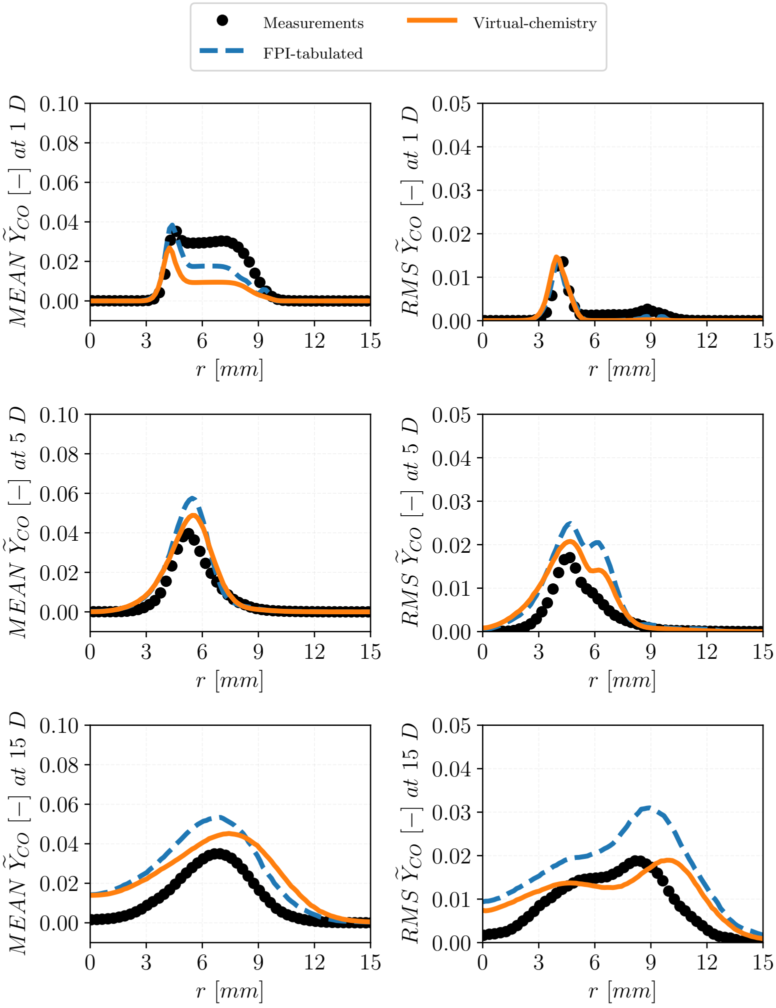

Figure 6.23: *CO mass fraction statistics. Comparison of the FPI-tabulated and virtual chemistry results versus experimental data.*

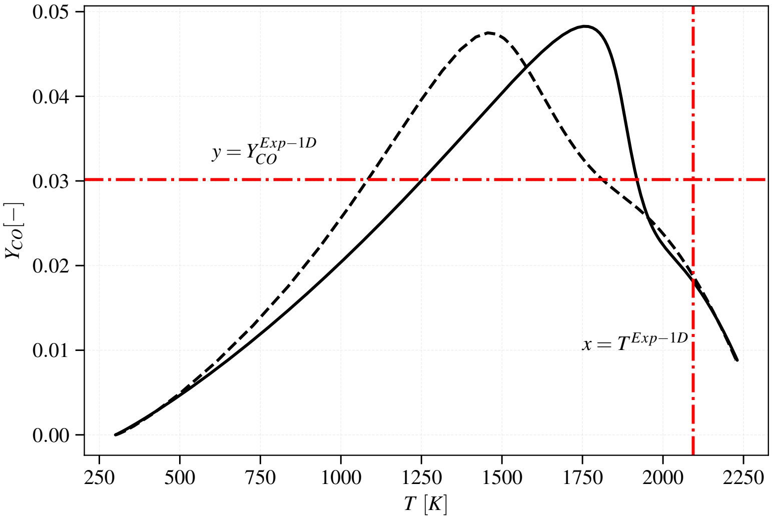

Figure 6.24: *Comparison of the flamelets trajectories in temperature/CO mass fraction phase space. The two flames are characterized by two different inlet conditions. Dashed line: 5-gases pilot inlet. Continuous line: CH_4 stoichiometric mixture. The vertical ($x = T^{Exp-1D}$) and the horizontal line ($y = Y_{CO}^{Exp-1D}$) show the measured mean temperature and CO mass fraction, respectively, at z=1D.*

the previous Section (Sec. 6.7.1.3).

6.7.1.5 5-gases pilot: flamelet analysis

A flamelet analysis is conducted to analyse the discrepancy observed in the mean CO prediction at 1D downstream,. Due to the experimental injection, the pilot bulk gases are supposed to evolve over a 1-D stoichiometric flamelet trajectory for the first simulation diameter.

Two unstretched laminar premixed flames are computed, with the code REGATH (Darabiha 1992), by changing the inlet composition:

- 1) Stoichiometric CH_4/Air mixture at 295K. This flamelet is supposed to represent the numerical simulation evolution.
- 2) 5-gases pilot composition (Tab. 6.4) at 295K. This flamelet is supposed to represent the experimental pilot gases evolution.

The two flamelets are plotted in the CO mass fraction/temperature space (Fig.6.24). The measured pilot bulk mean temperature T^{Exp-1D} and mean Y_{CO}^{Exp-1D} values are also reported in the plot. At the experimental temperature, the two flamelts values are both close to the mean numerical bulk CO value observed in the radial profiles at 1D, in Fig. 6.23 (Y_{CO} between 0.15 and 0.2). This means that the numerical LES scalar evolutions, in the pilot bulk region, for the first simulation diameter, is well approximated by a stoichiometric flamelet, as expected from the imposed injection. Instead, the experimental

Y_{CO}^{Exp-1D} exhibits an important departure from the premixed flame trajectory ($Y_{CO}^{Exp-1D} \sim 0.3$).

This analysis allows to conclude that, at 1D, a strong influence of the pilot boundary conditions persists for CO profiles. These boundary conditions need further insights in the future both from numerical and experimental studies.

6.7.2 Scatter plots

In order to analyse the flame trajectories, temperature and CO scatter instantaneous data are plotted in mixture fraction space in Fig. 6.25 and Fig. 6.26, respectively.

Numerical scatter data are collected, using annular radial probes, in accordance to experimental ones: several time shots are included considering a radial space between the centerline and 2D. 150000 samples are gathered and plotted for both simulations and experiments. As for radial statistics, results are shown for 3 axial positions , z =1D, 5D and 15D, where z is the axial coordinate.

6.7.2.1 Temperature

Barlow et al. (2015) and Cutcher et al. (2017) observed experimentally that the inhomogeneous Lr75Ub80 flame configuration exhibits stratified premixed combustion mode close to the injection and non premixed combustion mode further downstream.

Figure 6.25 shows temperature instantaneous scatter data in mixture fraction space, at different axial location from the burner exit plane, for both FPI-tabulated and virtual chemistry simulations. The stoichiometric mixture fraction vertical line is also reported. To underline the importance of the most populated regions, the scatter plots are colored by the local density of points.

The numerical scatter plots are qualitatively in good agreement with the experimental ones. The overall flame trajectories described by numerical simulations and measurements are comparable and the higher population regions are correctly captured.

As pointed out in the experimental study (Barlow et al. 2015), for the Lr75Ub80 inhomogeneous case, various flame structures are encountered. Near the burner exit, at z/D=1, a stratified premixed combustion mode is observed from the steep temperature in correspondence to the stoichiometric mixture fraction region. Further downstream, at z/D=5, the flame evolves toward a diffusion non-premixed like structure and the signs of premixed-stratified combustion gradually diminish. The transition to a non-premixed flame structure is confirmed for z=15D.

At z/D=15, experimental data cover a broader temperature spatial range than simulations. Furthermore, in experiments, low temperature samples around the stoichiometry are present, differently from simulations. These low temperature points, are experimentally attributed to extinction events (Barlow et al. 2015),

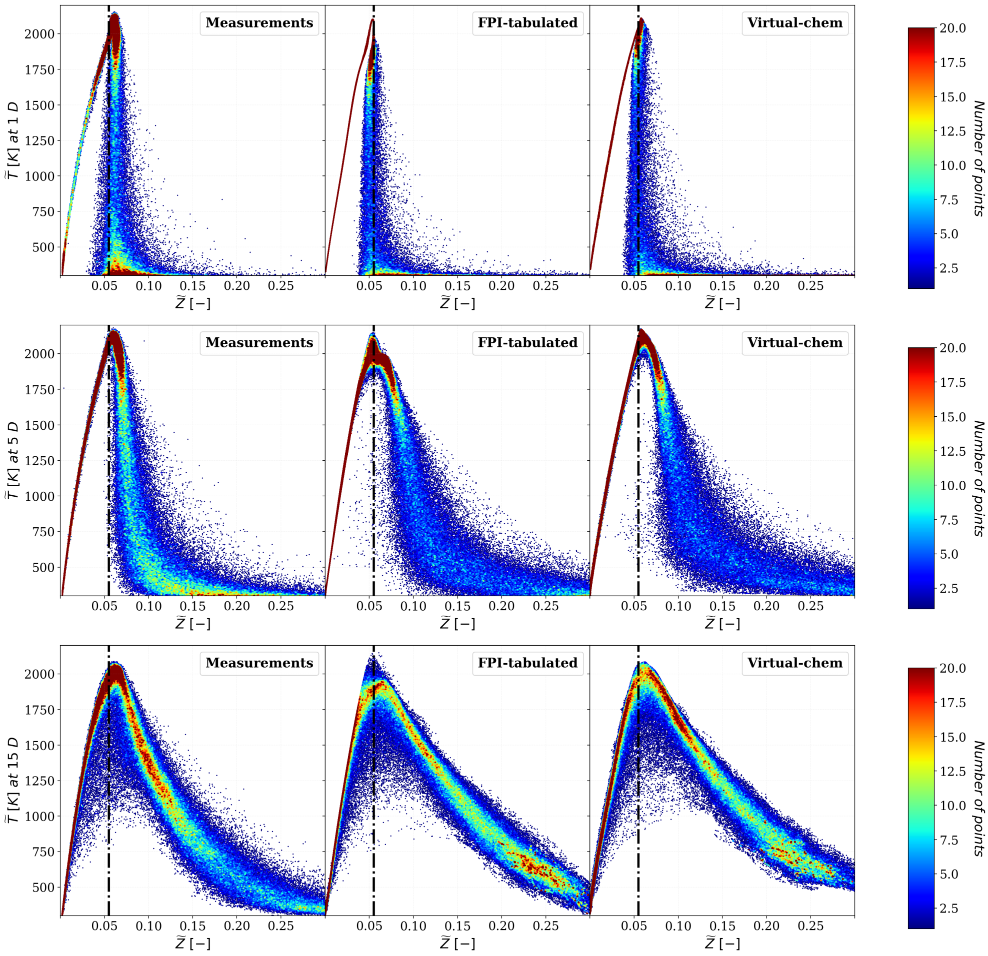

Figure 6.25: *Scatter instantaneous data in temperature-mixture fraction space at several axial planes from the burner exit (z/D = 1D, 5D, 15D). Experiments and simulations are compared. The local density of points is evaluated by uniformly dividing the domain in a grid of 500 points in both temperature and mixture fraction space and by clusterizing each scatter data in a cell of the mesh. Then, each scatter data is coloured by the local density of points. A vertical dashed dotted line is also drawn in correspondence of the stoichiometric mixture fraction value ($Z = 0.055$).*

as the flame configuration is close to the blow-off limit (70% of the blow-off velocity).

Hence, extinction phenomena are underestimated by numerical simulations both with FPI-tabulated chemistry and with virtual chemistry models. However, virtual chemistry results are closer to experiments in the high temperature region near the stoichiometric mixture fraction.

For the three axial locations (z/D=1,5,15), in the experiments, the peak temperature position is slightly shifted on the rich side and this phenomenon is better captured by virtual chemistry. The tabulated chemistry defects are here attributed to the unsuitability of the premixed flamelets trajectories to describe multiple flame structures. These phenomena are instead better retrieved using virtual transported chemistry.

6.7.2.2 CO mass fraction

CO mass fraction LES instantaneous data are scattered in mixture fraction space and conditioned by the respective temperature values (Fig. 6.26). The conditioning is performed to distinguish low temperature samples, representative of the cold mixing regions, from high temperature ones, encountered in the flame region.

The results are shown at the same axial positions of the temperature scatter plots (z= 1D, 5D, 15D). CO scatter data confirm the progressive evolution from a stratified premixed flame region at 1D toward a non-premixed flame region at 15D. This evolution, as for temperature, is well retrieved in both simulations.

At 1D diameter the high temperature CO band, retrieved from numerical simulations is thinner than the experimental one, with both combustion chemistry models. The CO peak position, close to the stoichiometric mixture fraction, at high temperature, is however well retrieved. In the FPI-tabulated chemistry data, non correct CO trajectories are observed for lean mixture fraction values.

At 5D, the high temperature CO scatter data are close to experiments with both models but the CO peak region is slightly overestimated especially in FPI-tabulated chemistry simulation.

The overestimation increases only for FPI-tabulated chemistry at 15D, while for virtual chemistry the flame trajectories are very close to experiments.

This confirms that CO is better predicted by virtual chemistry in multi-mode flames. Indeed, with virtual transported chemistry, including premixed and non-premixed flamelets in the model, CO is better predicted when multiple combustion regimes are encountered (Cailler 2018).

To confirm the differences observed in the CO scatter plots between the two combustion chemistry models, CO instantaneous 2-D fields are shown in Fig. 6.27. With FPI-tabulated chemistry the CO filtered mass fraction levels are higher than virtual chemistry ones. The overestimation is more pronounced starting from 5D downstream, when the non premixed combustion mode contribution becomes relevant.

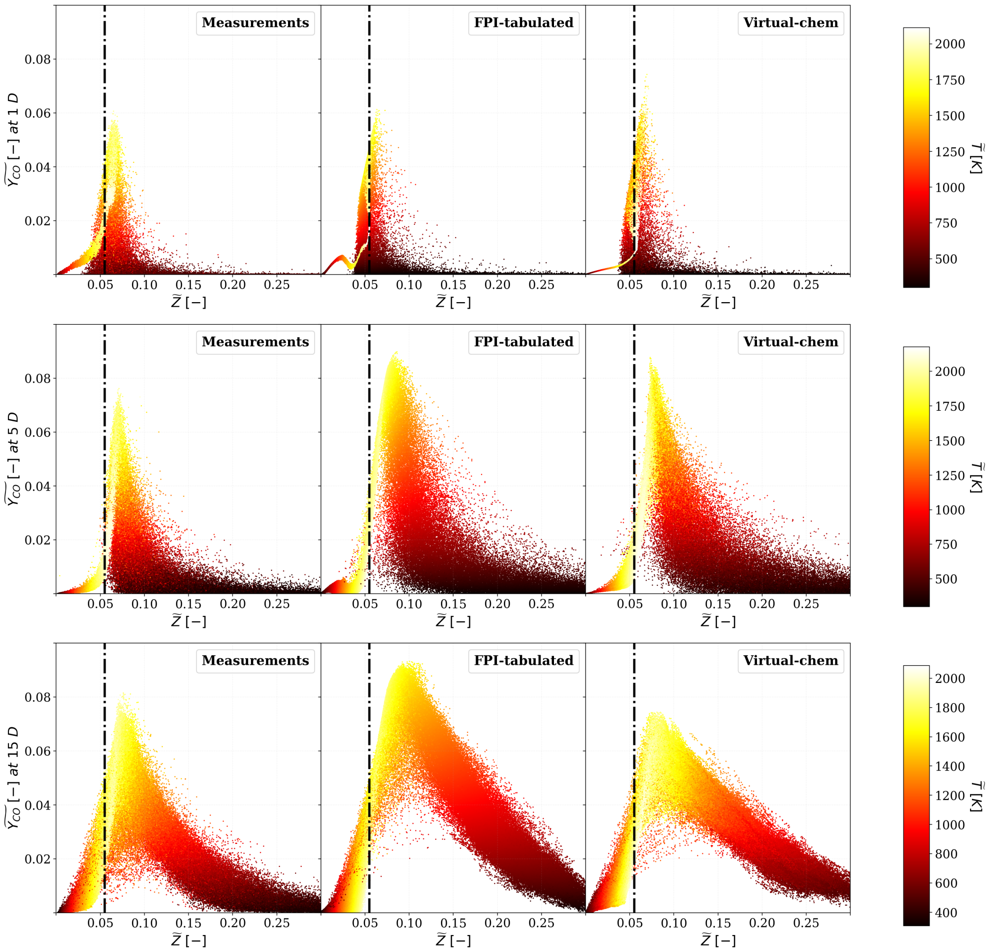

Figure 6.26: *Scatter instantaneous data in CO mass fraction-mixture fraction space coloured by local temperature. Data are shown over different axial planes from the burner exit (z/D = 1D, 5D, 15D). Experiments are compare to the simulations conducted with FPI-tabulated and with virtual chemistry. A vertical dashed dotted line is traced in correspondence of the stoichiometric mixture fraction value (Z = 0.055).*

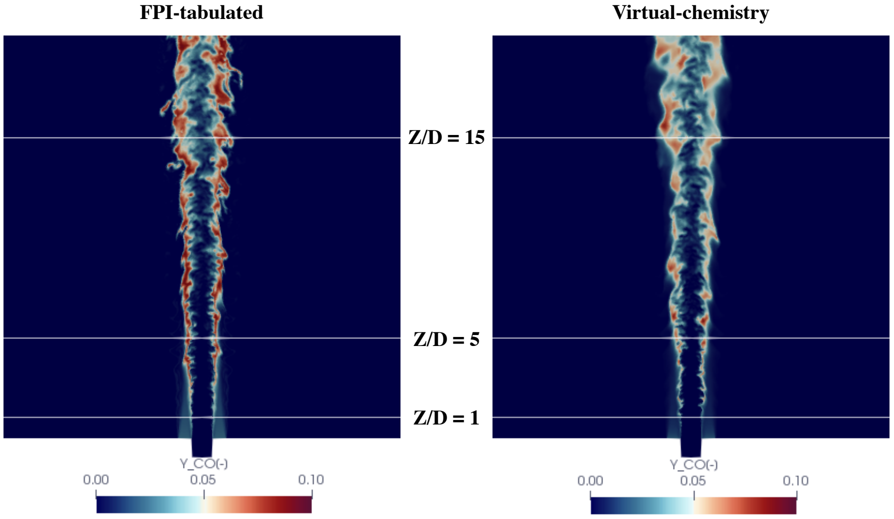

Figure 6.27: *CO mass fraction 2-D instantaneous snapshot on the chamber mid-plane. FPI-tabulated results are compared versus virtual-chemistry results.*

6.8 Wasserstein metric

The scatter data comparison, performed in the previous section, allows only a qualitative assessment of the two combustion chemistry models. To overcome this limitation, the Wasserstein metric (Dudley 1976; Pele and Werman 2009) is here used to post-process the scatter data.
Wasserstein metric was applied for the first time by Johnson et al. (2017), as a post processing tool for quantitative evaluation of combustion models versus experiments for Sydney Inhomogeneous burner.
In particular, the Wasserstein metric provides a single discrepancy measure that compares simulation scatter data with experimental ones combining multiple scalar quantities.
Here, the multi-scalar 2^{nd} Wasserstein metric (Su et al. 2015) is computed, using the code provided by Johnson et al. (2017). The metric is evaluated for both FPI-tabulated and virtual chemistry computations, retaining three scalars: Z, T and Y_{CO}.
Numerical scatter data and experimental ones constitute two empirical distributions N and E, respectively. Each element of the empirical distributions n_i and e_j contains information for the three considered scalars. As proposed by Johnson et al. (2017) data are normalized by the standard deviation of the experimental distribution to give appropriate importance to all retained scalars.
The 2^{nd} Wasserstein metric is computed as solution of the following minimiza-

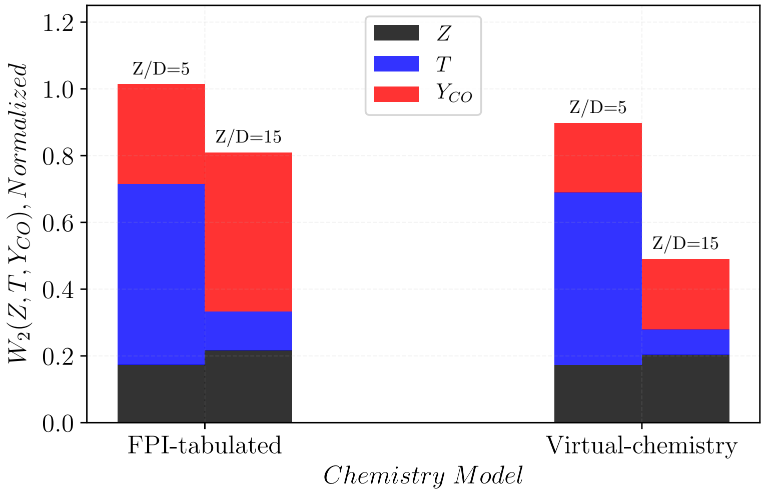

Figure 6.28: *Cumulative multi-scalar normalized 2^{nd} Wasserstein metric for two different awial locations $z/D = 5$, 15. $W_2(Z, T, Y_{CO})$ is compared for the two combustion chemistry models. The metric is decomposed in the single variable contributions to better analyse the results.*

tion problem:

$$W_2(Z, T, Y_{CO}) = \min_{\Gamma} \left(\sum_{i=1}^{n} \sum_{j=1}^{n'} \gamma_{ij} c_{ij} \right)^{1/2} \tag{6.16}$$

where Γ is the optimal transport matrix having elements γ_{ij} and dimension $n \times n'$. The unit transportation cost c_{ij} is defined as the 2^{nd} power of the pair-wise Euclidean distance:

$$c_{ij} = \sum_{v=1}^{N_v} (n_{k,i} - e_{k,j})^2 \tag{6.17}$$

where N_v is the number of scalar quantities that are considered that here is equal to 3 (Z, T and Y_{CO}).

To compute W_2, 1000 random samples are sorted both from the numerical and experimental database made of 50000 samples. 1000 were enough to ensure the convergence toward the same results.

Figure 6.28 shows the cumulative Wasserstein metric for z/D = 5,15 for both FPI-tabulated and virtual chemistry models. At z/D =1 data are not shown because a strong dependence from the pilot inlet boundary conditions has been observed (Sec. 6.7.1.5).

The cumulative W_2 decreases with the axial evolution with both combustion models. This trend is due to the decay of the turbulence and mixing intensity as explained by Johnson et al. (2017). The cumulative performance of the virtual chemistry model is better than tabulated chemistry one, in accordance with the scatter data qualitative results. Furthermore, the variable contribution separation helps to conclude that the better virtual chemistry performance is mainly due to a better Y_{CO} prediction.

6.9 Summary and discussion

It has been shown that the pilot-coflow velocity boundary conditions strongly impact the aerodynamic field established in the flame as well as the reactive scalars fluctuations in correspondence of the pilot-coflow shear layer. The prescription of a numerical velocity profile in the pilot and coflow tubes, fitting the closest experimental velocity measurements, allows to improve mean velocity and temperature fluctuation predictions.

By Prescribing Princeton boundary conditions at the main jet inlet, the performed LES is able to correctly reproduce the aerodynamic field in cold and hot non reactive conditions. However, it is observed a strong difference, in the mixing process, for cold and hot non-reactive conditions. In cold conditions the mixing process is faster because the two pilot shear layers break down earlier due to the pilot lower velocity.

In reactive conditions, the comparison between the virtual chemistry and FPI-tabulated combustion chemistry models have shown negligible impact on the velocity and mixing prediction but remarkable impact on temperature and CO statistics. In particular, when mixing is well predicted (at 5D downstream) virtual chemistry performs better than FPI-tabulated chemistry on temperature and CO mass fraction prediction. Indeed virtual transported chemistry is trained to recover flame trajectories in multi-mode flame conditions, differently from FPI tabulated chemistry where flame trajectories are tabulated from premixed flame archetypes. The scatter data post-processing, employing the Wasserstein metric, quantitatively confirms the better performance of the virtual chemistry model. The improving concerns mainly CO prediction.

Despite the numerous conclusions achieved in the present study, several open questions still remain unanswered for Sydney Inhomogeneous burner. They are mainly related to the correct characterization of the boundary conditions (velocity and scalars) imposed at the inlets and their impact on the shear layers and consequently on the mixing field. A deep joint experimental/numerical comparative study on Sydney Inhomogeneous burner was conducted during two last editions of the TNF14 (Barlow 2018) workshop. A summary of the workshops joint study conclusions are reported in the TNF14 Workshop Proceedings (Barlow 2018).

Chapter 7

LES of Preccinsta burner using non-adiabatic virtual chemistry

Contents

The non adiabatic virtual mechanism developed and validated in laminar flame conditions in Chap. 4 is used to carry-out the LES of a premixed turbulent combustion chamber exposed to wall heat losses. Comparison against experiment shows that non adiabatic simulation captures well the flame shape, the temperature and the CO prediction. The results are also compared to a recent analytic chemistry computation from literature to further demonstrate the validity of the virtual chemistry results.

7.1 Introduction

The main and CO non-adiabatic virtual schemes, developed in Chap 4, are used here to conduct an LES of the semi-industrial Preccinsta turbulent combustion chamber designed by Meier et al. (2007). Both adiabatic and non-adiabatic LES of the Preccinsta combustor are performed to investigate the capability

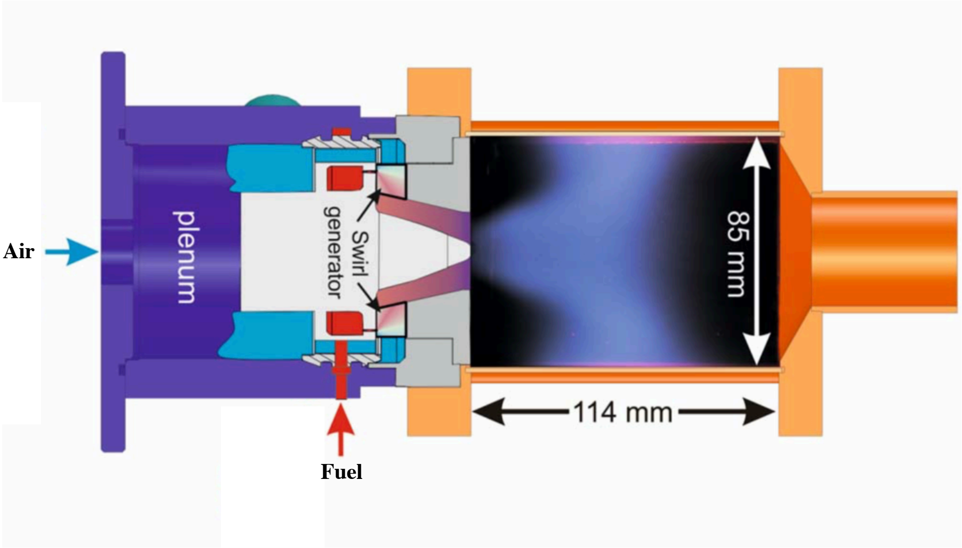

Figure 7.1: *Schematic drawing of the Preccinsta gas turbine model combustor and photo of a typical flame. Figure is adapted from Dem et al. (2015).*

of the virtual chemistry approach to capture the effect of heat losses on flame shape and CO formation. Finally a mesh refinement analysis is performed to investigate the impact of the turbulent combustion model on the numerical results.

7.2 Configuration and numerical set-up

7.2.1 Experimental configuration

The Preccinsta combustor is made of a plenum, a swirler and a combustion chamber (Meier et al. 2007).
Figure 7.1 shows a schematic drawing along with the main combustion chamber dimensions of the Preccinsta burner, as proposed by Dem et al. (2015).
In the experimental set up, dry air, at ambient temperature, is injected via the plenum (diameter = 78 mm) and fuel is fed through small holes (diameter = 1 mm), placed within the swirler. After mixing inside the swirler, the air/fuel mixture is injected in the combustion chamber in correspondence of the nozzle (diameter = 27.85 mm). Burnt gases are exhausted through a cone-shaped exhaust pipe (diameter = 40 mm).
The swirled injector promotes the development of a flame structure characterized by a Central Recirculation Zone (CRZ) and 2 Outer Recirculation Zones (ORZ).
Measurements are available for two different flame configurations: 1) An unsteady, thermoacoustic pulsating flame operated at 25 kW with a global equivalence ratio of $\phi = 0.70$, 2) a stable configuration, operating at 30 kW with a

global equivalence ratio of $\phi = 0.83$.

The "quiet", stable configuration is investigated in this work. LDV velocity measurements, OH* chemiluminescence detection and Laser Raman scattering measurements for temperature, major species and CO mass fraction are available (Meier et al. 2007).

7.2.2 Previous numerical studies

Many numerical simulations of the Preccinsta combustor have been conducted in the literature to validate several LES turbulent combustion models (Moureau et al. 2007; Galpin et al. 2008; Franzelli et al. 2012; Roux et al. 2005; Albouze et al. 2009; Fiorina et al. 2010; Moureau et al. 2011b; Wang et al. 2014; Mercier et al. 2015; Volpiani et al. 2017) .

All these simulations reproduce fairly well the flow dynamics as well as the mean flame front position, but fail to predict the flame temperature and CO production in the outer recirculation zone. These differences are attributed to the adiabatic wall assumption (Moureau et al. 2011b; Franzelli et al. 2012) not representative of the real experimental conditions where convective heat transfers occur through the injector system and quartz windows. A recent numerical study, conducted by Benard et al. (2018), demonstrates the value of retaining non adiabatic boundary conditions for the correct prediction of the external flame front lift-off.

7.2.3 Numerical set-up

Differently from the experiments, where fuel and air are injected separately, here the plenum is directly fed with a premixed mixture ($\phi = 0.83$) at a constant mass flow rate $\dot{m} = 12.9 \quad g.s^{-1}$.

Franzelli et al. (2012) has shown that the perfect premixed hypotheses weakly impacts on temperature and species statistics for the "quiet", stable configuration.

Figure 7.2 shows the computational domain retained in this work. The numerical geometry has been designed, in accordance with experimental lengths, and validated by Moureau et al. (2011b).

Two unstructured grids are used in the present simulations: a coarser grid made of 2.7 millions of nodes and a finer one composed of 20.9 millions of nodes. The characteristic mesh size in the flame region is equal to 0.6 mm and 0.3 mm in the coarser and finer mesh, respectively.

LES are conducted using the YALES2 low-Mach number, unstructured finite volume flow solver (Moureau et al. 2011a). A fourth-order temporal scheme is used to perform time integration of convective terms while a centered fourth-order scheme is used for spatial discretization. The sub-grid Reynolds stresses tensor is closed using the WALE model (Nicoud and Ducros 1999). Combustion chemistry is modeled using the non adiabatic virtual mechanism solving

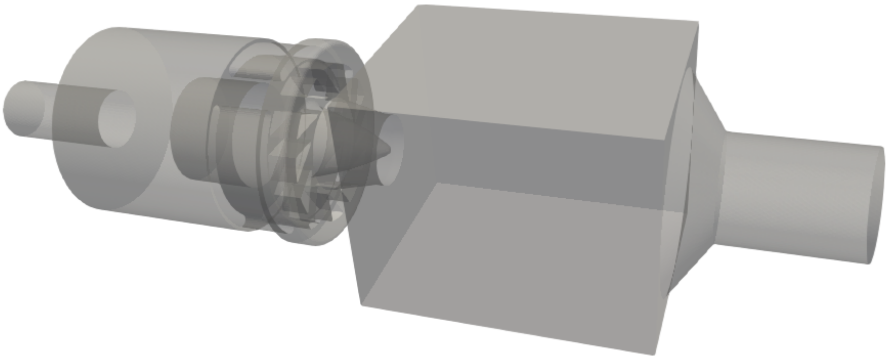

Figure 7.2: *Numerical computational domain used for the LES YALES2 simulations.*

both the two-step main mechanism and the CO dedicated sub-mechanism, as developed in the previous chapter.

7.2.3.1 Coupling Virtual chemistry with TFLES model

TFLES combustion model (Colin et al. 2000b) has been widly used in the simulation of the Preccinsta burner coupled with global (Franzelli et al. 2012; Volpiani et al. 2017; Albouze et al. 2009), analytic (Franzelli et al. 2013) and skeletal (Benard et al. 2018) reduced chemistry.

Here, virtual chemistry is coupled with turbulence using the Thickened Flame model for LES (TFLES) using the same approach employed for Sydney Inhomogeneous burner simulations.

Flame sensor and thickening are numerically computed using the same approach detailed in Sec. 6.3.2.2.

The modeling strategy has been before validated in a 1-D unstrained laminar flame at $\phi = 0.83$.

Figure 7.3 shows, on the left, the flame sensor and the TFLES dimensionless heat release rate and on the right the TFLES temperature profile compared to the fully resolved, unthickened one. The thickened flame is computed over a computational domain having a mesh size Δ_x =0.3 mm representative of the Preccinsta 3-D mesh.

Indeed, with the employed TFLES-Virtual chemistry numerical parameters, the heat release rate as well as temperature profile are well described. A slight distortion of the temperature profile, on the burned gases side, is observed. Such phenomenon is due to the dynamic thickening procedure. The laminar flame speed is conserved after the dynamic thickening procedure.

The Charlette model (Charlette et al. 2002a) is used to close the subgrid scale

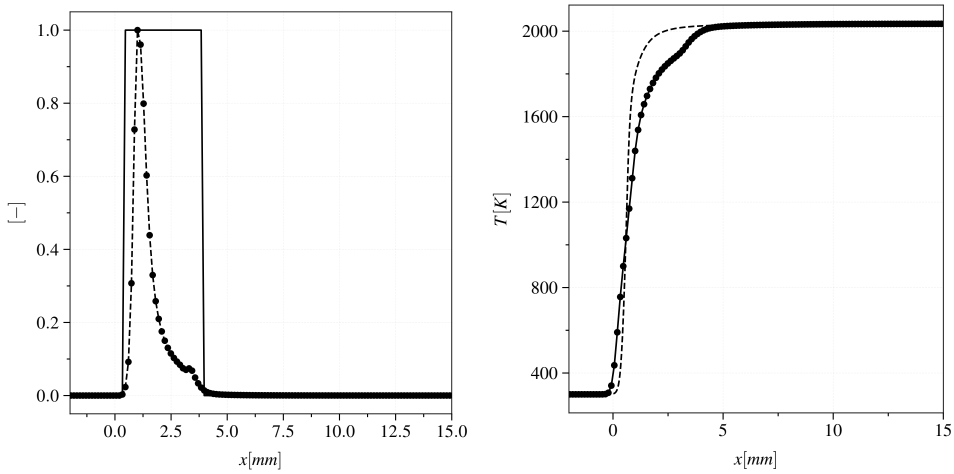

Figure 7.3: *1D flame at phi* = 0.83 *computed with virtual chemistry coupled with TFLES model using a local thickening formulation. On the left: the flame sensor* Γ *(continous line) and the dimensionless heat release rate (dashed line). On the right: temperature profile of the TFLES computation (dashed line) compared to the temperature profile of the fully resolved flame (continuous line). The dots represents the mesh points of the thickened flame simulation.*

flame wrinkling, setting the constant parameter $\beta = 0.5$.

7.2.3.2 Set wall heat losses

Adiabatic and non adiabatic simulations are performed.
As the wall temperature was not measured experimentally, a trial and error procedure based on non-adiabatic computation with the LU17 skeletal scheme (Sankaran et al. 2007) has been conducted by Benard et al. (2018). Wall temperature Dirichlet boundary conditions have been identified to match the experimental measurements of temperature and CO in the near wall region. The imposed wall temperature profile, along the chamber axial coordinate, is shown in Fig. 7.4. Adiabatic boundary conditions are retained over the injector nozzle. Instead heat transfer affects the external wall of the injector, the chamber base and the chamber lateral walls.
Figure 7.5 shows the 3D computational domain colored by the wall temperature imposed in the non adiabatic simulations.

7.2.3.3 Computations

Firstly, a cold flow simulation is performed to validate the LES aerodynamic predictions, comparing numerical results versus the LDV cold velocity measurements. Then, the three following reactive simulations are performed: adiabatic on the coarse grid (AC), non-adiabatic on the coarse grid (NAC) and non-

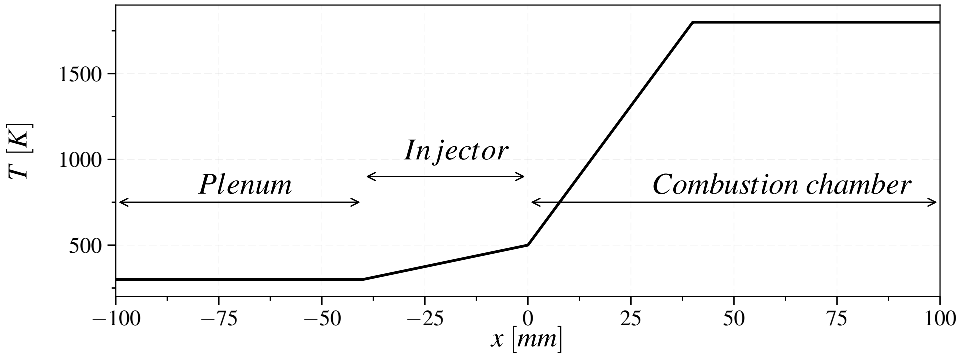

Figure 7.4: *Wall temperature profiles imposed along the flame side wall chamber.*

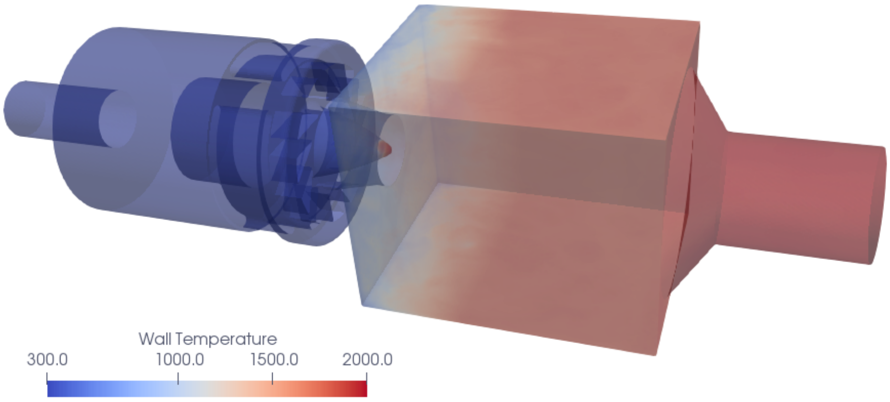

Figure 7.5: *3D computational domain colored by the wall temperature.*

Table 7.1: *Main characteristics of the three reactive LES conducted in this work.*

Flame configuration	AC	NAC	NAF
Boundary conditions	Adiab	N. Adiab	N. Adiab
Grid nodes	2.7M	2.7M	20.9M
Δ_x Flame region	0.6mm	0.6mm	0.3mm

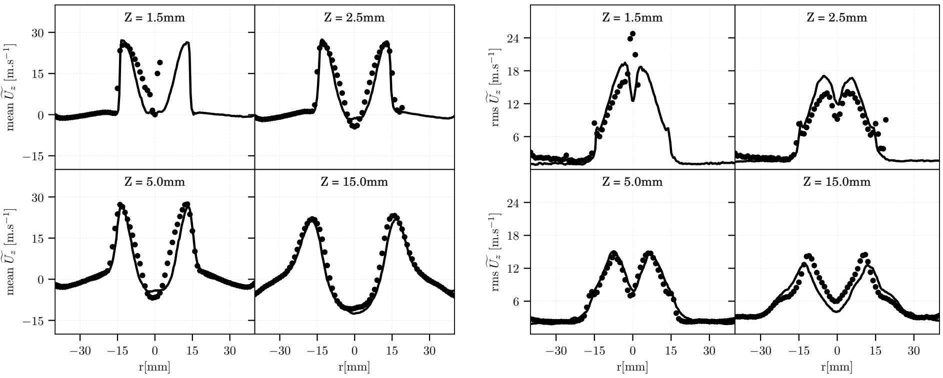

Figure 7.6: *Mean and rms axial velocity radial profiles at several axial locations from the injector. Circle: Experimental data. Continuous lines: LES cold flow simulation with employing the coarser mesh.*

adiabatic on the fine grid (NAF).
Table 7.1 summarizes the main characteristics of the three reactive LES.

7.3 Cold flow simulation

LES cold non reactive simulation results are here compared versus experimental data, over radial profiles, at various distances from the burner exit. Figures 7.6 and 7.7 compares the mean and rms statistical quantities for the axial and circumferential velocity components. A good agreement is observed for the various radial probes. Indeed, the aerodynamic field is correctly captured by the simulation. This allows to validate both the mesh and the sub-grid LES turbulence model.

7.4 Reactive simulation

The three reactive simulations (AC, NAC and NAF) are here compared. Temperature and CO mass fraction statistics are shown and compared to the experimental data. Mean heat release rate 2-D field is compared qualitatively to the experimental OH-chemiluminescence. Instantaneous 2-D heat release rate

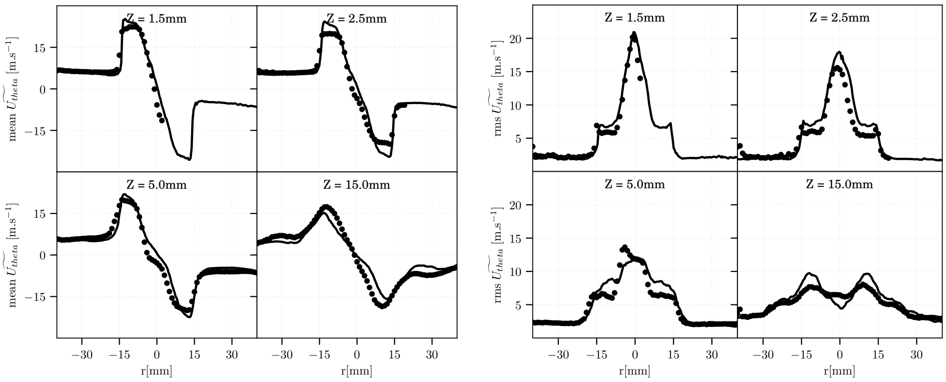

Figure 7.7: *Mean and rms circumferential velocity radial profiles at several axial locations from the injector. Circle: Experimental data. Continuous lines: LES cold flow simulation with employing the coarser mesh.*

and CO fields from numerical simulations are also analysed.

7.4.1 Temperature and heat release

Non-adiabatic virtual chemistry predicts very well the mean and RMS temperature profiles, as shown in Fig. 7.8. In particular, the comparison between AC and NAC demonstrates that accounting for heat losses clearly improves both mean and RMS temperature predictions in the near wall region, where the outer recirculation zone is located.

The mesh refinement (NAF results) does not reveal an important impact on temperature statistics, confirming the robustness of the TFLES model with respect to temperature profile and flame speed prediction.

Instantaneous heat release rate from the three numerical computations are compared on the chamber mid-plane in Fig.7.9. The adiabatic simulation shows a stable M-shape flame in accordance with the previous numerical works (Moureau et al. 2011b; Volpiani et al. 2017). The heat losses included in NAC induce a thinner outer branch of the flame and local flame extinctions in the outer recirculation zone. This observation is confirmed in NAF where the flame resolution is improved. A prevalent V-shape flame is retrieved in the non adiabatic simulations, accordingly to experimental observation. This observation agree with the recent numerical work of Benard et al. (2018) where exactly the same wall boundary conditions are prescribed.

Figure 7.10 qualitative compares OH experimental chemiluminescence with the mean computed heat release for AC and NAC computations. Unlike to experimental OH-LIF and OH-chemiluminescence measurements (Meier et al. 2007), AC predicts a M-shape flame. The experimental V-shape flame is better reproduced by NAC simulation.

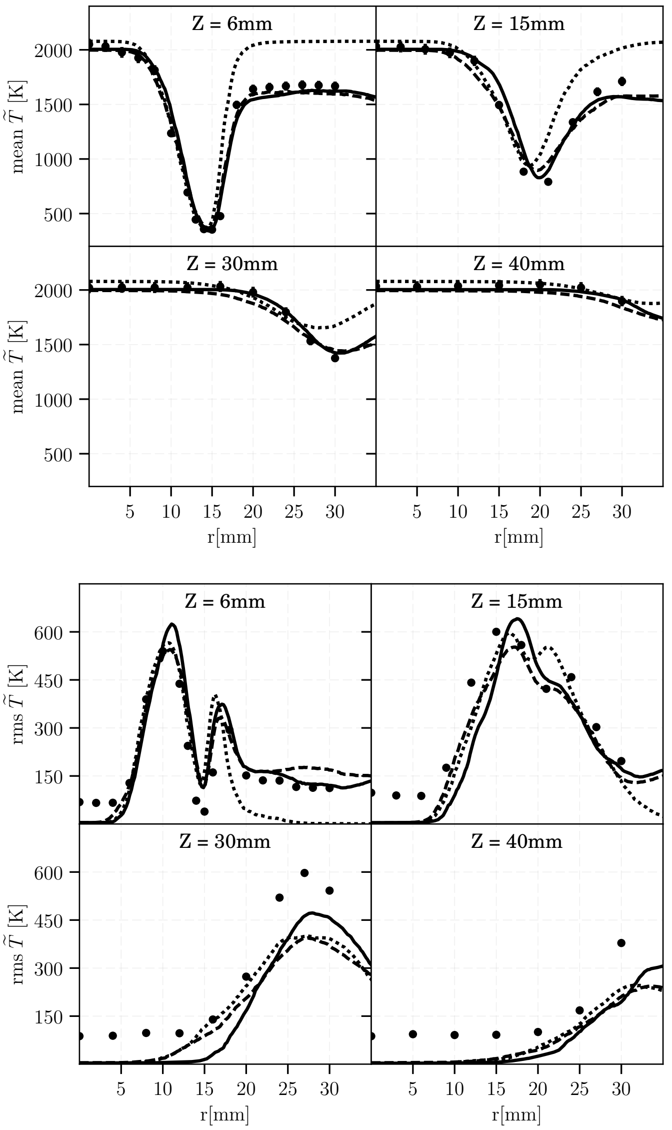

Figure 7.8: *Mean and rms temperature radial profiles at several axial locations from the injector. Circle: Experimental data. Squared dotted lines: AC results. Dashed lines: NAC results. Continuous lines: NAF results.*

Figure 7.9: *Instantaneous heat release rate from the three numerical simulations normalized between* 0 *and* 2.5×10^9 $W.m^{-3}$. *From left to right: AC, NAC and NAF computations.*

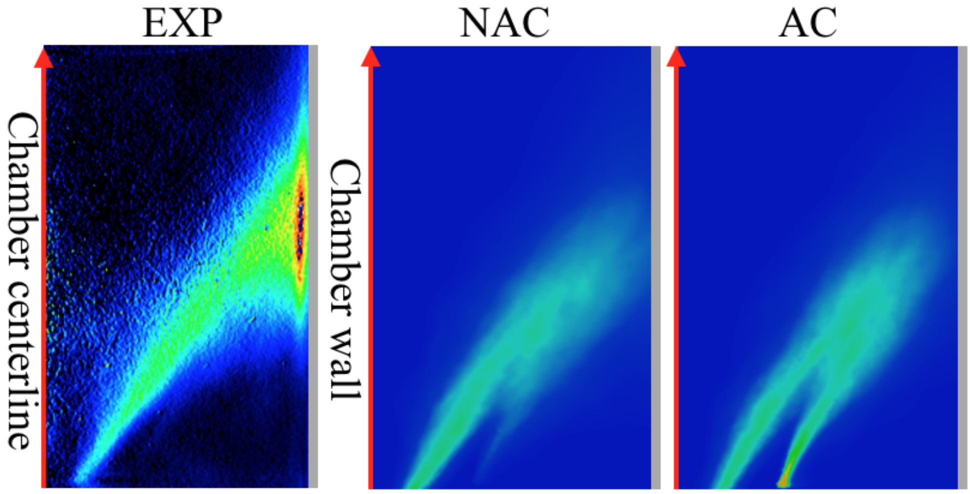

Figure 7.10: *Qualitative comparison between experimental OH chemiluminescence and computed mean heat release for NAC and AC simulations. The heat release rate is normalized between* 0 *and* 1×10^9 $W.m^{-3}$.

7.4.2 CO mass fraction

Figure 7.11 compares 2-D instantaneous CO snapshot on the chamber mid-plane for the three reactive computations.

The predicted chemical flame structure, identified here through an intermediate species concentration, differs significantly whether or not heat losses are considered. In accordance with the heat release rate analysis, CO snapshot confirms the transition from a n M-shape flame to a V-shape one if heat losses are considered. Furthermore, CO snapshots show an impact of the mesh refinement: in the NAF computation the CO layer is thinner than the NAC and the outer CO branch tends to vanish close to the burner exit.

Mean and RMS CO mass fraction are compared in Fig. 7.12. Adiabatic simulation overestimates the mean CO production in the outer recirculation zone. In particular, a peak of CO, not observed in the experiments, is predicted in AC at (r=17 mm; Z= 6 mm) and (r=22 mm; Z= 15 mm). The amplitude of this peak is drastically reduced by NAC which accounts for the impact of heat losses on the CO chemistry. Mesh refinement analysis, differently from mean temperature, shows an overall reduction of the CO mean profiles. Although mean CO prediction is improved in the NAF virtual chemistry computation, an overestimates of the CO peak, in the outer recirculation zone, still exists.

RMS CO profiles are well reproduced by the non adiabatic simulations with a weak impact of the mesh refinement.

7.5 TFLES impact on mean CO profiles

The mesh refinement analysis reveals an impact on the TFLES turbulent combustion model on CO mean profiles. The undesirable behavior is due to the artificial thickening of the flame front. This observation is in accordance with recent numerical studies that analyse the combined bad effect of the thickening factor (Mercier et al. 2017b; Benard et al. 2018) and the sub-grid efficiency function (Mercier et al. 2019; Mehl 2018) on CO prediction when the TFLES formalism is used.

To demonstrate the spurious effect observed in the mean CO profile in Fig. 7.12, the 1-D structure of a mean flame brush is manufactured from a random distribution of 100,000 1-D flamelet solutions, as proposed by Vervisch et al. (2010). The distribution of flamelet positions is adjusted to recover the PRECCINSTA mean flame brush thickness that is estimated to be about 5 mm at the first axial measurement (z=6 mm). The Reynolds averaging of this flamelets ensemble provides a reference mean CO mass fraction solution, shown in solid line in Fig. 7.13. The solution expected by the TFLES approach is also manufactured by randomly distributing a set of 1-D thickened flames. The Reynolds averaging of this ensemble of thickened flamelets is also performed. Results are plotted in Fig. 7.13 for the values F=4.5 and F= 2.25, which corresponds to the maximum values of flame thickening factors computed in coarse and fine

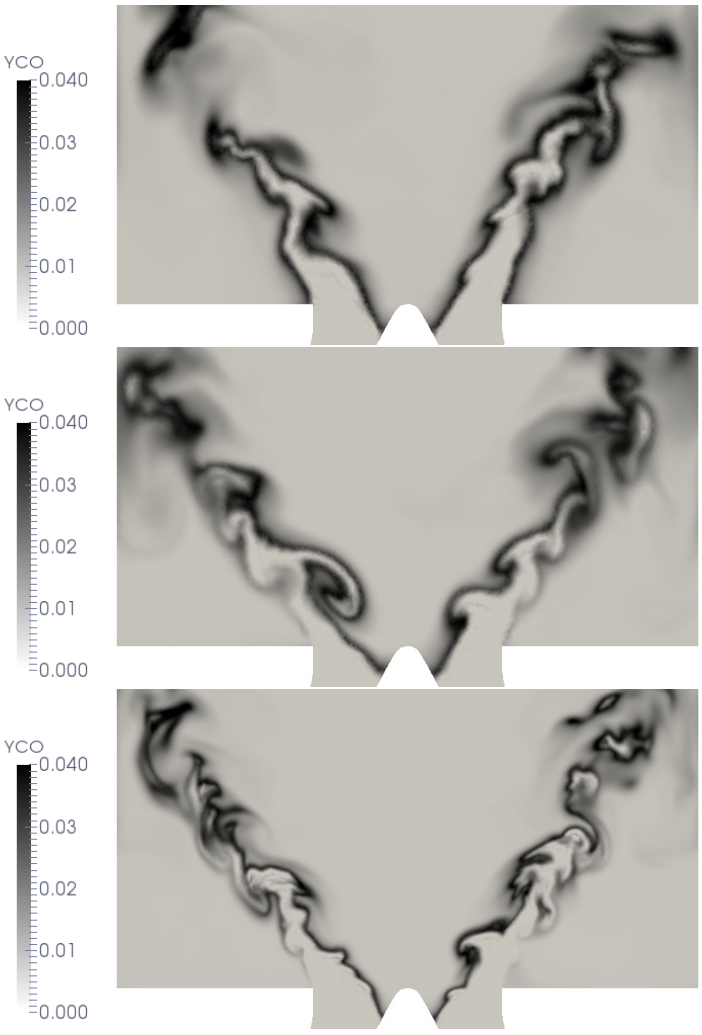

Figure 7.11: *Instantaneous CO filtered mass fraction snapshot on the middle-plane of the combustion chamber. From top to bottom: AC, NAC, NAF.*

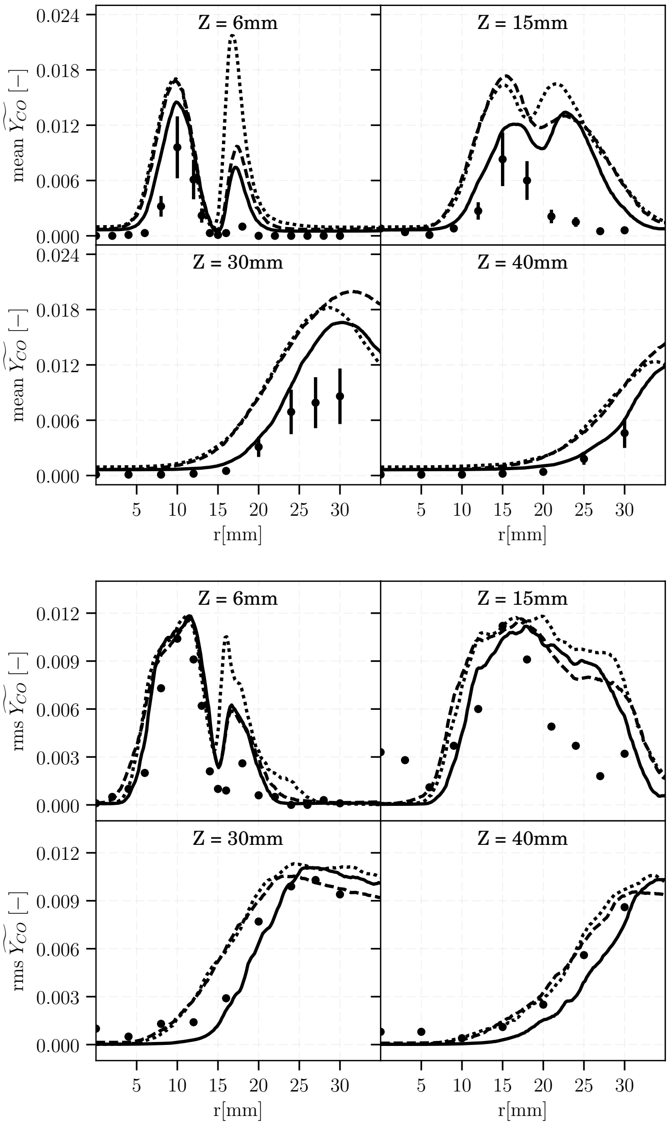

Figure 7.12: *Mean CO mass fraction radial profiles at several axial locations from the injector. Circle: Experimental data with the corresponding experimental errorbar. Squared dotted lines: AC results. Dashed lines: NAC results. Continuous lines: NAF results.*

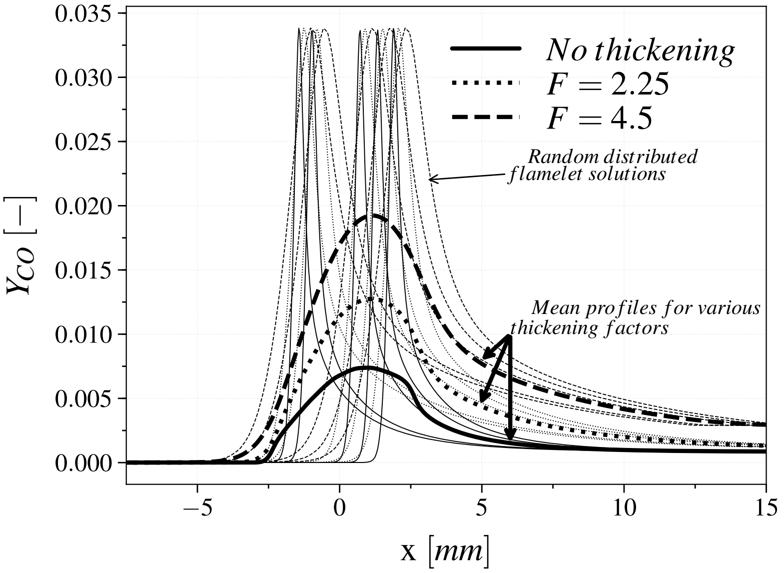

Figure 7.13: *Thin lines: Some of the random distributed flamelet solutions for the various thickening factors. Bold lines: Reynolds averaged mean profiles for the corresponding thickening factors.*

meshes at z= 6 mm, respectively. (dashed and dotted lines). The comparison between mean reference and thickened CO profiles shows that TFLES overestimates the peaks of mean intermediate species. The overestimation increases with F. As observed in Fig. 7.13, refining the mesh enable to decrease the thickening factor and limits its spurious influence on the species production.

7.6 Discussion

The virtual non adiabatic scheme is coupled with the TFLES turbulent combustion model to perform the LES of the Preccinsta chamber. The comparison between adiabatic and non adiabatic results shows a significant improvement in flame shape, temperature and CO mass fraction fields prediction. Non adiabatic simulations predicts a V shape like flame which is closer to the experimental observations.

Virtual chemistry LES results (temperature and CO mass fraction statistics) are also compared with the simultaneous computation conducted by Benard et al. (2018), who uses the LU17 skeletal scheme (Sankaran et al. 2007). The same boundary conditions and the same meshes are used for both virtual chemistry and skeletal chemistry computations.

The comparison (Fig. 7.14 and Fig. **??**) shows that virtual chemistry temperature and CO prediction are very close to reference skeletal chemistry, in adiabatic and non adiabatic cases.

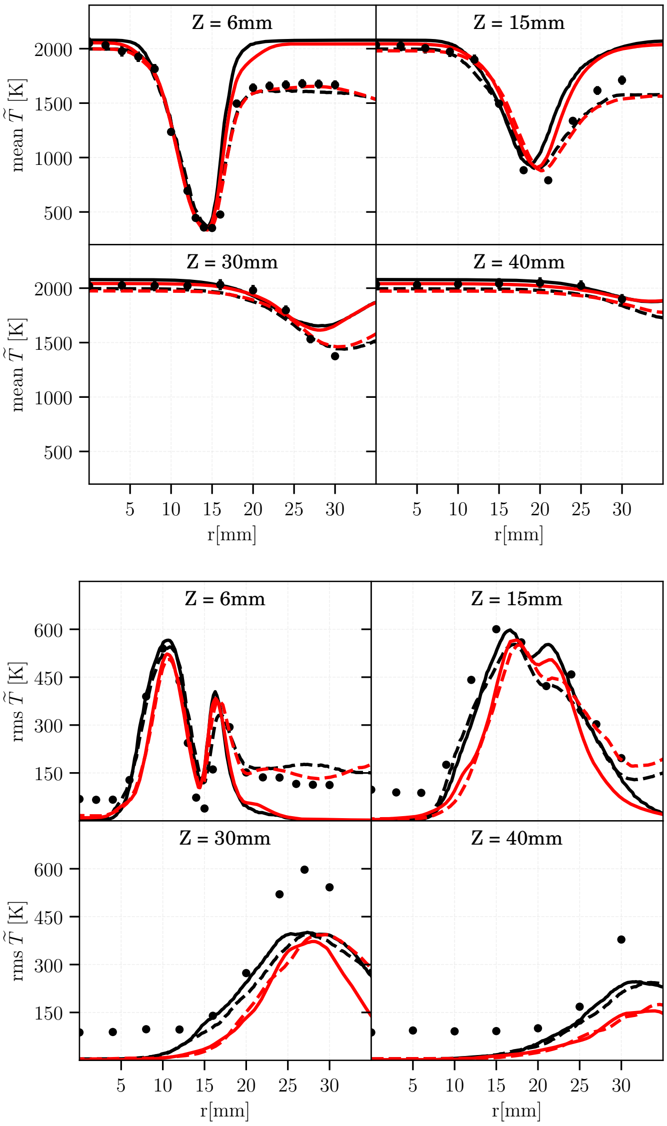

Figure 7.14: *Temperature mean and RMS comparison. Virtual chemistry results (black lines) are compared to the CORIA (Benard et al. 2018) one (red lines). Adiabatic (continuous line) and non adiabatic (dashed lines) results are shown for the same mesh.*

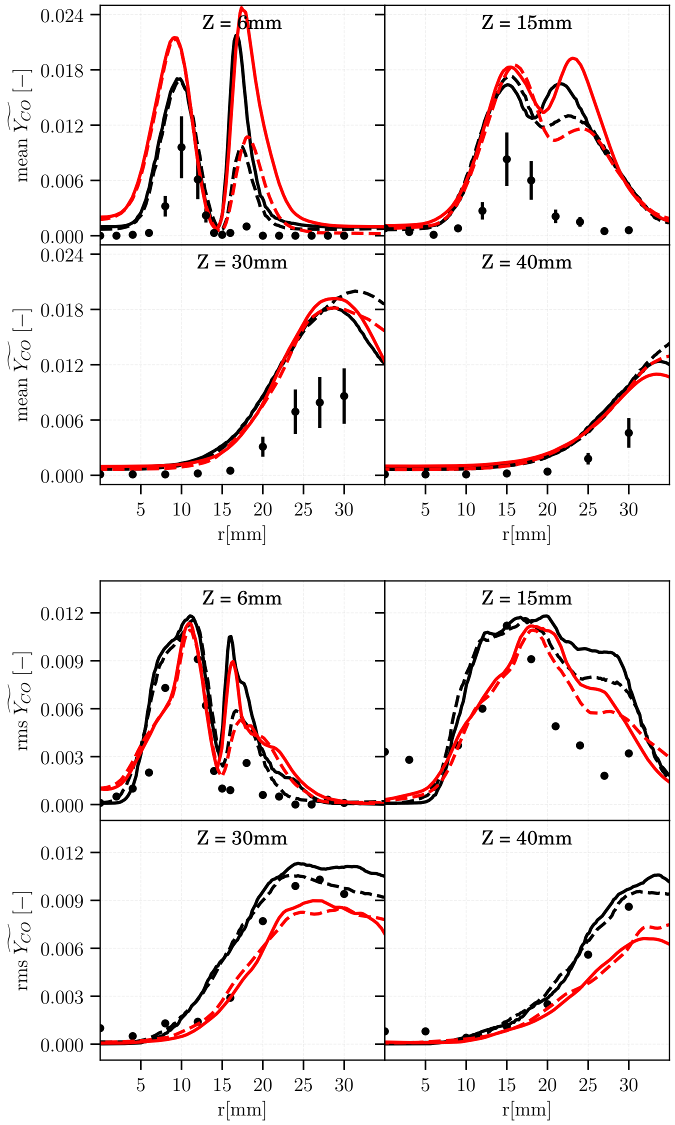

Figure 7.15: *CO mass fraction mean and RMS comparison. Virtual chemistry results (black lines) are compared to the CORIA (Benard et al. 2018) one (red lines). Adiabatic (continuous line) and non adiabatic (dashed lines) results are shown for the same mesh.*

Despite the improvements, discrepancies in CO mass fraction prediction still exist in the outer recirculation zone with respect to experiments. This misdirection is first attributed to the artificial thickening of the flame front and a numerical justification is found in accordance with recent numerical works. However the chemical flame structure and consequently CO are also sensitive to strain effects (Mercier et al. 2016) which are not considered in the non adiabatic virtual chemistry model. An improvement would be to enlarge the reference database used to train the virtual chemical scheme by adding for instance strained flamelets.

Conclusion

The main achievement of the present work has been the development and validation of reduced kinetic mechanisms able to combine accurate pollutants prediction (CO and NO) with low CPU cost. In particular, the research challenges associated with CO modeling in multi-modal and non adiabatic flame conditions and NO modeling in multi-modal flame conditions have been addressed. The recently developed virtual chemistry approach has been retained as modeling route to buid-up the reduced mechanisms. This work enlarges the virtual chemistry validity domain with respect to Cailler (2018) thesis work. In particular, a strategy to account for non-adiabatic flame conditions has been proposed and a new NO dedicated virtual sub-mechanism has been designed.

The developed NO virtual mechanism was tested in 2-D laminar premixed, non-premixed and partially premixed flame computations, proposing a direct comparison with detailed reference chemistry. This comparison showed a drastic CPU cost reduction in virtual chemistry computations with respect to detailed chemistry ones.

The applicability of virtual chemistry to model combustion chemistry in turbulent flame at low CPU cost has been also supported by two LES computations. Sydney Inhomogeneous burner LES has demonstrated that virtual chemistry is suitable to model multi-modal turbulent flame conditions predicting temperature and CO formation. It has been shown that virtual chemistry allows to achieve better results than premixed based tabulated chemistry, especially for CO prediction. Eventually, Preccinsta burner LES has shown that virtual chemistry is able to capture non-adiabatic turbulent flame conditions, giving comparable results to an analytically reduced chemistry literature computation.

Perspectives

Despite the promising results achieved, currently, the number of virtual species along with the virtual reactions network are empirically designed. The virtual chemistry architecture is based on the pure observation of the physical phenomenon to account for. Consequently, the number of degree of freedom (virtual species and reaction) may be not the optimal one and/or some important chemical pathways may be missed. To overcome this current limitation, new modeling strategies that provide an automatic build-up of the virtual chemistry network, from a time scale analysis of the reference chemical system, are in progress in the Phd thesis of Maldonado Colmán (2020).

In future works, it would be also challenging to employ the virtual NO scheme to compute a turbulent flame and to apply the same methodology to aeronautical fuels and bio-fuels: works are in progress in the Phd thesis of Nguyen Van (2020).

The application of virtual chemistry to soot prediction is also extremely challenging. For this purpose, a PAH dedicated sub-mechanism development is in progress in the the Phd thesis of Maldonado Colmán (2020).

List of publications

Peer-rewieved journal publications

- G. Maio, M. Cailler, R. Mercier and B. Fiorina, *Virtual chemistry for temperature and CO prediction in LES of non-adiabatic turbulent flames.* Proceedings of the Combustion Institute, 2019, vol. 37, no 2, p. 2591-2599.
- G. Maio, M. Cailler, A. Couci and B. Fiorina, *A virtual chemical mechanism for prediction of NO emissions from flames.* Combustion Theory and Modelling, 2019, Submitted.
- G. Maio, M. Cailler, N. Darabiha and B. Fiorina, *Capturing multi-regime combustion in turbulent flames with a virtual chemistry approach.* Proceedings of the Combustion Institute, 2020, Submitted.

Peer-rewieved conference publications

- G. Maio, M. Cailler, R. Mercier, V. Moureau and B. Fiorina, *LES modeling of piloted jet flames with inhomogeneous inlets using tabulated chemistry methods*, 55^{th} AIAA Aerospace Sciences Meeting, AIAA SciTech Forum.
- G. Maio, R. Mercier, M. Cailler, B. Fiorina, *Virtual chemistry for prediction of chemical flame structure in non adiabatic combustion*, 8^{th} European Combustion Meeting, 2017.

Appendix A

NO optimization criterion: zone separation and learning database definition

A.1 Introduction

The objective is to find a criterion to dissociate learning subspaces characteristic of fast (prompt) and slow (thermal and reburning) NO chemistry in both premixed and non-premixed flame archetypes. For premixed flames a spatial length scale δ_{FF} is defined to separate the computational domain in a *flame front* region and a *post-flame* one. A corresponding mixing time scale a_{FF} is identified for non-premixed flames.

A.1.1 Criterion definition

In the premixed flamelet database, for each fresh gases equivalence ratio ϕ^0, targeted thermo-chemical variables φ such as the temperature and the species mass fractions are expressed in terms of the spatial coordinate x, that correspond to the direction normal to the flame front. φ therefore reads:

$$\varphi = \varphi_p \left(\phi^0, x_p\right) \tag{A.1}$$

where p subscript denotes solutions of premixed flame configurations.
Examples of NO mass fractions profiles are plotted in Fig. A.1 for three different fresh gas equivalence ratio (the corresponding mixture fraction value is also indicated in the figure). The transition between fast NO (in the flame front) and slow NO (in the post-flame) kinetics affects the second order material derivative of NO mass fraction, related to the second order derivative of Y_{NO}

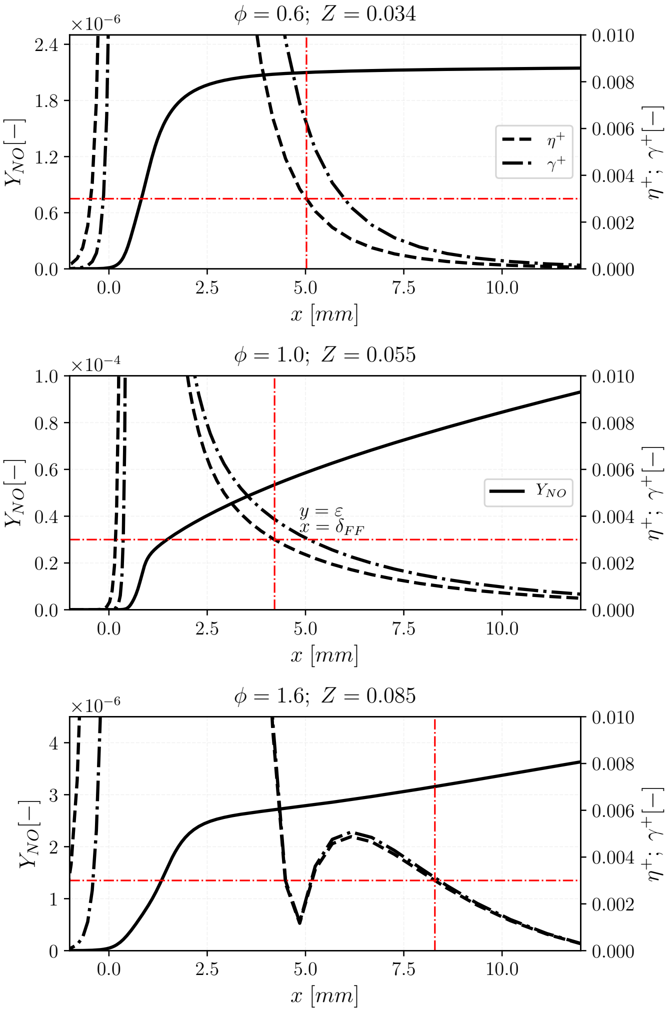

Figure A.1: *NO mass fraction and the dimensionless η^+ and γ^+ quantities from detailed chemistry computations for different equivalence ratio values. The corresponding mixture fraction Z is also indicated for each flame.*

in steady state, as follows:

$$\frac{D^2 Y_{NO}}{Dt^2} = u^2 \frac{d^2 Y_{NO}}{d{x_p}^2} = \gamma\left(x_p\right) \tag{A.2}$$

where u is the flow velocity. The dimensionless γ and the dimensionless Y_{NO} second derivative are defined as follows:

$$\gamma^+ = \frac{\left|\gamma\left(x_p\right)\right|}{\max\left|\gamma\left(x_p\right)\right|}; \qquad \eta^+ = \frac{\left|\frac{\mathrm{d}^2 Y_{NO}(x_p)}{\mathrm{d}{x_p}^2}\right|}{\max\left(\left|\frac{\mathrm{d}^2 Y_{NO}}{\mathrm{d}{x_p}^2}\right|\right)} \tag{A.3}$$

Figure A.1 also plots γ^+ and η^+ in the three premixed CH_4/air flames previously introduced. The transition between flame front and post-flame NO formation is identified using the dimensionless absolute value of the second derivative η^+.

When η^+ becomes lower than a certain threshold on the post-flame side the transition between fast and slow NO formation phenomena is defined at the spatial location x_p which satisfy the following condition:

$$\eta^+ = \varepsilon \tag{A.4}$$

where ε is a user-defined threshold value. Equation A.4 admits an ensemble of solutions $\{x_1^p, ..., x_n^p\}$. Among this ensemble of solutions, the flame front NO reaction layer δ_{FF} is defined so that fast NO chemistry is completed within the interval $[-\infty, \delta_{FF}]$:

$$\delta_{FF}(\phi^0) = \max\{x_{p1}, ..., x_{pn}\} \tag{A.5}$$

where $x_p = 0$ represents the beginning of the flame, defined here as the location where the flame temperature T rises $10K$ with respect to the fresh gas temperature T^{fg}. For premixed flame configurations, the *flame front* region and the *post-flame* one corresponds to the 1-D domains $\mathcal{A}^P = [-\infty, \delta_{FF}]$ and $\mathcal{A}^P = [\delta_{FF}, \infty,]$, respectively.

A cut-off time scale τ_{FF} between fast and slow NO chemistry is also introduced as the Lagrangian residence time taken by the fresh gases to reach δ_{FF} in premixed flames. τ_{FF} is defined as follows:

$$\tau_{FF}(\phi^0) = \int_0^{\delta_{FF}(\phi^0)} \frac{1}{u_p(\phi^0)} dx, \tag{A.6}$$

A mixture fraction Z is uniquely defined from the fresh gases equivalence ratio values ϕ^0 to reach 0 in pure air and 1 in pure fuel. τ_{FF} is plotted in Fig. A.2 as

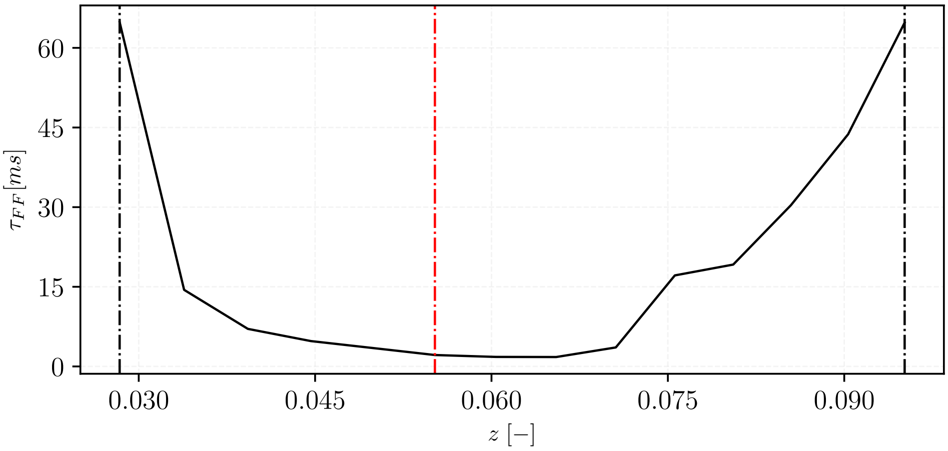

Figure A.2: *Flame front residence time as function of mixture fraction. The stoichiometric mixture fraction, lean and rich flammability limits are also shown through the three vertical lines.*

function of the mixture fraction Z in the whole flammability limit. The cut-off time scale averaged over the whole flammability domain reads:

$$\overline{\tau}_{FF} = \frac{1}{(Z^r - Z^l)} \int_{Z_l}^{Z_r} \tau_{FF}(Z) dZ, \tag{A.7}$$

where Z^l and Z^r are values of mixture fraction at the lean and rich flammability limits, respectively.

A.1.2 Extension to non-premixed counterflow flames

To identify the non-premixed flames that have to be included in the flame front optimization database, the averaged cut-off time scale $\overline{\tau}_{FF}$, previously defined, is used. It is assumed that the transition time scale between fast and slow NO chemistry is of the same order of magnitude for premixed and non-premixed flames. As consequence, $\overline{\tau}_{FF}$ is here employed to estimate the critical strain rate, characteristic of non-premixed counterflow flames using the following simplified relation:

$$a_{FF} = 1/\overline{\tau}_{FF}. \tag{A.8}$$

All flamelets computed with a strain rate higher than a_{FF} ($\mathcal{A}^{NP} = [a_{FF}, a_q]$) will serve as a target for optimizing the *flame front* chemistry block (reactions R_1^{NO}-R_3^{NO}).

Appendix B

Synthèse en français

Les deux principaux inconvénients des processus de combustion impliqués dans les dispositifs de conversion d'énergie sont: la contribution au réchauffement climatique et la pollution des zones industrielles et urbaines. Le secteur de l' énergie (production, transformation et utilisation) est largement basé sur les dispositifs de combustion et il est donc au cœur du probléme du changement climatique. Il contribue environ au deux tiers des émissions mondiales de gaz à effet serre et environ le 90% des émissions de dioxyde de carbone (CO2). Les émissions de CO2 sont directement liées à l'efficacité des systèmes de combustion et au type de combustible utilisé dans le processus. Par conséquent, l'amélioration de l'efficacité des appareils de combustion et la recherche de combustibles a plus faible contenu de carbone tels que le gaz naturel sont les principaux objectifs à poursuivre. En plus, pour améliorer la qualité de l'air local (en particulier dans les zones urbaines et industrielles), la réduction des émissions de polluants provenant des processus de combustion est d'une importance capitale.

Les ingénieurs utilisent la simulation numérique pour concevoir et optimiser les appareils de combustion afin d'améliorer leur efficacité et de réduire les émissions de polluants. La simulation CFD (Computational Fluid Dynamic), appliquée à la solution de processus de combustion complexes, a fait des efforts importants ces dernières années, permettant la simulation de chambres de combustion à échelle réelle. Toutefois, la reproduction précise de la formation de polluants (CO, NOx, hydrocarbures imbrûlés, etc...) et de la prévision de la structure de la flamme dans des simulations de flammes turbulentes, à un coût de calcul abordable, est toujours un sujet de recherche d'intérêt et qui doit être pleinement abordé et mieux compris. Pour faire face aux défis de modélisation de la combustion décrits ci-dessus, le présent travail de recherche se concentre sur la prédiction de la formation de CO et de NO dans des conditions de flamme complexes à un coût de calcul réduit. Les régimes de flammes multimodales et les pertes thermiques des flammes sont pris en compte. Ici, le mot multimodal signifie coexistence de structures de flamme prémélangées et non prémélangées. Dans cette thése, des modéles de chimie rèduite pour la prédiction du CO et du NO sont développés en utilisant le récente modèle de *chimie virtuelle*. La chimie virtuelle est un modèle d'ordre réduit qui vise à décrire les quantités globales de flammes, la température et la formation des polluants. La stratégie consiste à concevoir des mécanismes virtuels composés d'un ensemble réduit d'espèces virtuelles interagissant à travers un nombre réduit de réactions virtuelles. Les propriétés thermochimiques des espèces virtuelles et les constantes cinétiques des réactions virtuelles sont optimisées pour cibler les propriétés de flamme "réelles" d'intérêt telles que la température, le dégagement de chaleur et la concentration de polluants. Le mécanisme chimique virtuel est composé d'un mécanisme principal et de plusieurs sous-mécanismes virtuels satellites. Dans ce travail, des mécanismes virtuels sont développés et validés dans des archétypes de flamme laminaire 1-D. Ensuite, leur applicabilité aux calculs CFD laminaires et turbulents multidimensionnels est conduit, qui montrent la valeur de l'approche pour les applications industrielles. Les résultats multidimensionnels de de les simulations CFD sont soit validés par rapport aux données expérimentales pour les cas de tests turbulents, soit comparés à des calculs de chimie détaillés pour les configurations laminaires. Par rapport aux travaux de littérature précédents, le domaine de validité de l'approche de la chimie virtuelle est encore élargi. En plus, l'applicabilité de la chimie virtuelle aux calculs CFD multidimensionnels à un coût de calcul réduit, est démontrée. En particulier, la chimie virtuelle est mise à l'épreuve et validée dans le contexte LES (Large Eddy Simulation) dans deux configurations de flammes turbulentes pour prédire les émissions de CO: 1) "Sydney inhomogeneous piloted burner": représentatif des conditions de flammes turbulentes multimodales. Dans cette simulation le champ de CO prédit par le calcul numérique 3-D LES, en utilisant le nouveau modéle de chimie virtuelle optimisé, est en bon accord avec les expériences. 2) Brûleur "Preccinsta": une flamme confinée semi-industrielle impactée par les pertes de chaleur aux parois. Dans ce calcul, le champ 3-D prédit par la simulation numérique LES, en utilisant le nouveau modéle de chimie virtuelle, decrit bien les données expérimentales de température et de CO.

Un nouveau et original modéle cinétique d'ordre réduit pour la prédiction de NO (oxyde nitrique), basé sur la méthodologie de chimie virtuelle, est également développé dans cette thése. Pour prédire la formation de NO de la combustion multimode, des "flamelets" prémélangées et non prémélangées sont incluses dans la base de données d'apprentissage utilisée pour optimiser le mécanisme NO virtuel. Une procédure d'optimisation "multizone" est développée pour capturer avec précision à la fois la chimie du NO rapide (”prompt NO") et lente ("thermal NO" et "reburning"). Ensuite, le sous-mécanisme NO et la méthodologie d'optimisation proposés sont appliqués à la combustion méthane/air. Le modèle est d'abord testé dans des configurations de "flamelets" prémélangées et non prémélangées 1-D. L'approche est ensuite validé dans des simulations CFD de flamme laminaire 2-D, en fournissant une comparaison directe avec la chimie détaillée. Des configurations de flammes 2-D prémélangées, non prémélangées et partiellement prémélangées sont étudiées numériquement. Dans tous les cas, le mécanisme virtuel capture assez bien la température et la formation d' NO avec seulement 12 espèces virtuelles et 8 réactions virtuelles a la place de 53 espèces et 325 réactions de la chimie détaillée. Par conséquence, dans les calculs de chimie virtuelle une réduction drastique du temps de calcul est constaté (d'un facteur 40) par rapport à la chimie détaillée.

References

Aguilera-Iparraguirre, J., H. J. Curran, W. Klopper, and J. M. Simmie (2008). Accurate benchmark calculation of the reaction barrier height for hydrogen abstraction by the hydroperoxyl radical from methane. *The Journal of Physical Chemistry A 112*(30), 7047–7054. *(p. 33)*

Albouze, G., T. Poinsot, and L. Gicquel (2009). Chemical kinetics modeling and les combustion model effects on a perfectly premixed burner. *Comptes Rendus Mécanique 337*(6-7), 318–328. *(p. 167, 168)*

Auzillon, P., B. Fiorina, R. Vicquelin, N. Darabiha, O. Gicquel, and D. Veynante (2011). Modeling chemical flame structure and combustion dynamics in les. *Proceedings of the Combustion Institute 33*(1), 1331–1338. *(p. 124, 126, 127)*

Barlow, R. (2018). 14th international workshop on measurement and computation of turbulent nonpremixed flames (tnf). *https://tnfworkshop.org/workshop-proceedings/tnf14-workshop/*. *(p. 120, 143, 148, 151, 163)*

Barlow, R., S. Meares, G. Magnotti, H. Cutcher, and A. Masri (2015). Local extinction and near-field structure in piloted turbulent ch 4/air jet flames with inhomogeneous inlets. *Combustion and Flame 162*(10), 3516–3540. *(p. 7, 50, 67, 121, 131, 132, 133, 134, 138, 139, 148, 151, 157)*

Benard, P., G. Lartigue, V. Moureau, and R. Mercier (2018). Large-eddy simulation of the lean-premixed preccinsta burner with wall heat loss. *Proceedings of the Combustion Institute*. *(p. 28, 41, 45, 52, 67, 167, 168, 169, 172, 175, 178, 179, 180)*

Benard, P., G. Lartigue, V. Moureau, and R. Mercier (2019). Large-eddy simulation of the lean-premixed preccinsta burner with wall heat loss. *Proceedings of the Combustion Institute 37*(4), 5233–5243. *(p. 121)*

Berger, S., S. Richard, F. Duchaine, G. Staffelbach, and L. Gicquel (2016). On the sensitivity of a helicopter combustor wall temperature to convective and radiative thermal loads. *Applied Thermal Engineering 103*, 1450–1459. *(p. 73)*

Bilger, R., S. Stårner, and R. Kee (1990). On reduced mechanisms for methane air combustion in nonpremixed flames. *Combustion and Flame 80*(2), 135–149. *(p. 44, 148)*

Boileau, M., G. Staffelbach, B. Cuenot, T. Poinsot, and C. Bérat (2008).

Les of an ignition sequence in a gas turbine engine. *Combustion and Flame 154*(1-2), 2–22. *(p. 5)*

Burcat, A., B. Ruscic, et al. (2005). Third millenium ideal gas and condensed phase thermochemical database for combustion (with update from active thermochemical tables). Technical report, Argonne National Lab.(ANL), Argonne, IL (United States). *(p. 17)*

Bykov, V. and U. Maas (2007a, DEC). The extension of the ildm concept to reaction–diffusion manifolds. *Combust. Theor. Modell. 11*(6), 839–862. *(p. 73)*

Bykov, V. and U. Maas (2007b). The extension of the ildm concept to reaction–diffusion manifolds. *Combustion Theory and Modelling 11*(6), 839–862. *(p. 90)*

Bykov, V. and U. Maas (2009). Problem adapted reduced models based on reaction–diffusion manifolds (REDIMs). *Proceedings of the Combustion Institute 32*(1), 561–568. *(p. 50, 91)*

Cailler, M. (2018). *Virtual chemical mechanisms optimized to capture pollutant formation in turbulent flames.* Ph. D. thesis, Paris Saclay. *(p. 6, 7, 8, 50, 51, 52, 53, 54, 55, 56, 57, 60, 64, 66, 124, 129, 159, 183)*

Cailler, M., N. Darabiha, and B. Fiorina (2019). Development of a virtual optimized chemistry method. application to hydrocarbon/air combustion. *Submitted to Combustion and Flame*. *(p. 64, 73, 78, 81, 92, 93, 96, 98, 103, 120, 121)*

Cailler, M., N. Darabiha, D. Veynante, and B. Fiorina (2017). Building-up virtual optimized mechanism for flame modeling. *Proc. Combust. Inst.*. *(p. 35, 52, 53, 54, 56, 57, 60, 62, 73, 77, 79, 92, 94, 95, 97, 121, 123)*

Caudal, J., B. Fiorina, B. Labégorre, and O. Gicquel (2015). Modeling interactions between chemistry and turbulence for simulations of partial oxidation processes. *Fuel Processing Technology 134*, 231–242. *(p. 100)*

Cavallotti, C., R. Rota, T. Faravelli, and E. Ranzi (2007). Ab initio evaluation of primary cyclo-hexane oxidation reaction rates. *Proceedings of the Combustion Institute 31*(1), 201–209. *(p. 33)*

Charlette, F., C. Meneveau, and D. Veynante (2002a). A power-law flame wrinkling model for les of premixed turbulent combustion part i: non-dynamic formulation and initial tests. *Combust. Flame 131*(1), 159–180. *(p. 29, 124, 131, 168)*

Charlette, F., C. Meneveau, and D. Veynante (2002b). A power-law flame wrinkling model for les of premixed turbulent combustion part ii: dynamic formulation. *Combustion and Flame 131*(1-2), 181–197. *(p. 131)*

Chase, M. W., J. Curnutt, H. Prophet, R. McDonald, and A. Syverud (1975). Janaf thermochemical tables, 1975 supplement. *Journal of Physical and Chemical Reference Data 4*(1), 1–176. *(p. 76)*

Chatelier, A., T. Guiberti, R. Mercier, N. Bertier, B. Fiorina, and T. Schuller (2019). Experimental and numerical investigation of the response of a swirled flame to flow modulations in a non-adiabatic combustor. *Flow,* *Turbulence and Combustion*, 1–29. *(p. 45)*

Chomiak, J. (1990). Combustion a study in theory, fact and application. *Philadelphia, PA (USA); Abacus Press*. *(p. 27)*

Colin, O., F. Ducros, D. Veynante, and T. Poinsot (2000a). Thickened flame model for large eddy simulations of turbulent premixed combustion. *Physics of Fluids 12*(7), 1843–1862. *(p. 28, 29)*

Colin, O., F. Ducros, D. Veynante, and T. Poinsot (2000b). A thickened flame model for large eddy simulations of turbulent premixed combustion. *Physics of Fluids (1994-present) 12*(7), 1843–1863. *(p. 124, 128, 168)*

Cook, A. W. and J. J. Riley (1994). A subgrid model for equilibrium chemistry in turbulent flows. *Physics of fluids 6*(8), 2868–2870. *(p. 27)*

Cuoci, A., A. Frassoldati, T. Faravelli, and E. Ranzi (2013a). A computational tool for the detailed kinetic modeling of laminar flames: Application to C_2H_4/CH_4 coflow flames. *Combustion and Flame 160*(5), 870–886. *(p. 35, 92, 107, 111, 113, 116)*

Cuoci, A., A. Frassoldati, T. Faravelli, and E. Ranzi (2013b). Numerical modeling of laminar flames with detailed kinetics based on the operator-splitting method. *Energy & Fuels 27*(12), 7730–7753. *(p. 107, 111)*

Curran, H. J. (2018). Developing detailed chemical kinetic mechanisms for fuel combustion. *Proceedings of the Combustion Institute*. *(p. 15, 33, 34, 35)*

Curran, H. J., P. Gaffuri, W. J. Pitz, and C. K. Westbrook (1998). A comprehensive modeling study of n-heptane oxidation. *Combustion and flame 114*(1-2), 149–177. *(p. 33)*

Cutcher, H., R. Barlow, G. Magnotti, and A. Masri (2017). Turbulent flames with compositionally inhomogeneous inlets: Resolved measurements of scalar dissipation rates. *Proceedings of the Combustion Institute 36*(2), 1737–1745. *(p. 136, 148, 157)*

Dagaut, P., F. Karsenty, G. Dayma, P. Diévart, K. Hadj-Ali, A. Mzé-Ahmed, M. Braun-Unkhoff, J. Herzler, T. Kathrotia, T. Kick, et al. (2014). Experimental and detailed kinetic model for the oxidation of a gas to liquid (gtl) jet fuel. *Combustion and Flame 161*(3), 835–847. *(p. 34)*

Darabiha, N. (1992). Transient behaviour of laminar counterflow hydrogen-air diffusion flames with complex chemistry. *Combust. Sci. Technol. 86*(1-6), 163–181. *(p. 47, 49, 57, 72, 83, 88, 91, 123, 156)*

Day, M. S. and J. B. Bell (2000). Numerical simulation of laminar reacting flows with complex chemistry. *Combustion Theory and Modelling 4*(4), 535–556. *(p. 107)*

Dem, C., M. Stöhr, C. M. Arndt, A. M. Steinberg, and W. Meier (2015). Experimental study of turbulence-chemistry interactions in perfectly and partially premixed confined swirl flames. *Zeitschrift für Physikalische Chemie 229*(4), 569–595. *(p. 166)*

Domingo, P., L. Vervisch, and D. Veynante (2008). Large-eddy simulation of a lifted methane jet flame in a vitiated coflow. *Combustion and*

Flame 152(3), 415–432. *(p. 124)*

Dudley, R. M. (1976). *Probabilities and metrics: Convergence of laws on metric spaces, with a view to statistical testing*, Volume 45. Aarhus Universitet, Matematisk Institut. *(p. 161)*

Durand, L. and W. Polifke (2007). Implementation of the thickened flame model for large eddy simulation of turbulent premixed combustion in a commercial solver. In *ASME Turbo Expo 2007: Power for Land, Sea, and Air*, pp. 869–878. American Society of Mechanical Engineers. *(p. 29)*

Echekki, T. and J. H. Chen (2003). Direct numerical simulation of autoignition in non-homogeneous hydrogen-air mixtures. *Combustion and Flame 134*(3), 169–191. *(p. 33)*

Echekki, T. and E. Mastorakos (2010). *Turbulent combustion modeling: Advances, new trends and perspectives*, Volume 95. Springer Science & Business Media. *(p. 23)*

Egolfopoulos, F. N., N. Hansen, Y. Ju, K. Kohse-Höinghaus, C. K. Law, and F. Qi (2014). Advances and challenges in laminar flame experiments and implications for combustion chemistry. *Progress in Energy and Combustion Science 43*, 36–67. *(p. 33)*

Ern, A. and V. Giovangigli (1994). *Multicomponent transport algorithms*, Volume 24. Springer Science & Business Media. *(p. 22)*

Esclapez, L., P. C. Ma, E. Mayhew, R. Xu, S. Stouffer, T. Lee, H. Wang, and M. Ihme (2017). Fuel effects on lean blow-out in a realistic gas turbine combustor. *Combustion and Flame 181*, 82–99. *(p. 5)*

Faravelli, T., A. Frassoldati, and E. Ranzi (2003). Kinetic modeling of the interactions between NO and hydrocarbons in the oxidation of hydrocarbons at low temperatures. *Combustion and Flame 132*(1-2), 188–207. *(p. 89)*

Felden, A. (2016). *Development of Analytically Reduced Chemistries (ARC) and applications in Large Eddy Simulations (LES) of turbulent combustion*. Ph. D. thesis. *(p. 6, 52)*

Felden, A., E. Riber, and B. Cuenot (2018). Impact of direct integration of analytically reduced chemistry in les of a sooting swirled non-premixed combustor. *Combustion and Flame 191*, 270–286. *(p. 28, 41, 120, 121)*

Fenimore, C. (1971). Formation of nitric oxide in premixed hydrocarbon flames. In *Symposium (International) on Combustion*, Volume 13, pp. 373–380. Elsevier. *(p. 88)*

Fernandez-Tarrazo, E., A. L. Sánchez, A. Linan, and F. A. Williams (2006). A simple one-step chemistry model for partially premixed hydrocarbon combustion. *Combustion and Flame 147*(1-2), 32–38. *(p. 46, 90)*

Fiorina, B. (2019). Accounting for complex chemistry in the simulations of future turbulent combustion systems. In *AIAA Scitech 2019 Forum*, pp. 0995. *(p. 35, 36, 54, 90, 120)*

Fiorina, B., R. Baron, O. Gicquel, D. Thevenin, S. Carpentier, N. Darabiha, et al. (2003). Modelling non-adiabatic partially premixed flames using flame-prolongation of ILDM. *Combustion Theory and Modelling 7*(3), 449–470. *(p. 44, 73, 74, 79, 83, 120, 123)*

Fiorina, B., O. Gicquel, L. Vervisch, S. Carpentier, and N. Darabiha (2005). Approximating the chemical structure of partially premixed and diffusion counterflow flames using FPi flamelet tabulation. *Combustion and flame 140*(3), 147–160. *(p. 44, 73, 91, 120)*

Fiorina, B., R. Mercier, G. Kuenne, A. Ketelheun, A. Avdić, J. Janicka, D. Geyer, A. Dreizler, E. Alenius, C. Duwig, et al. (2015). Challenging modeling strategies for les of non-adiabatic turbulent stratified combustion. *Combust. Flame 162*(11), 4264–4282. *(p. 45, 71)*

Fiorina, B., D. Veynante, and S. Candel (2015). Modeling combustion chemistry in large eddy simulation of turbulent flames. *Flow, Turbulence and Combustion 94*(1), 3–42. *(p. 6, 27, 35, 42, 50, 72, 73, 89, 90)*

Fiorina, B., R. Vicquelin, P. Auzillon, N. Darabiha, O. Gicquel, and D. Veynante (2010). A filtered tabulated chemistry model for les of premixed combustion. *Combust. Flame 157*(3), 465–475. *(p. 28, 124, 167)*

Fournet, R., V. Warth, P. Glaude, F. Battin-Leclerc, G. Scacchi, and G. Come (2000). Automatic reduction of detailed mechanisms of combustion of alkanes by chemical lumping. *International Journal of Chemical Kinetics 32*(1), 36–51. *(p. 40)*

Franzelli, B. (2011). *Impact of the chemical description on direct numerical simulations and large eddy simulations of turbulent combustion in industrial aero-engines*. Ph. D. thesis, Université de Toulouse. *(p. 127)*

Franzelli, B., B. Fiorina, and N. Darabiha (2013). A tabulated chemistry method for spray combustion. *Proc. Combust. Inst. 34*(1), 1659–1666. *(p. 50, 73)*

Franzelli, B., E. Riber, and B. Cuenot (2013). Impact of the chemical description on a large eddy simulation of a lean partially premixed swirled flame. *Comptes Rendus Mécanique 341*(1-2), 247–256. *(p. 6, 29, 46, 168)*

Franzelli, B., E. Riber, L. Y. Gicquel, and T. Poinsot (2012). Large eddy simulation of combustion instabilities in a lean partially premixed swirled flame. *Combust. Flame 159*(2), 621–637. *(p. 46, 167, 168)*

Franzelli, B., E. Riber, M. Sanjosé, and T. Poinsot (2010). A two-step chemical scheme for kerosene–air premixed flames. *Combustion and Flame 157*(7), 1364–1373. *(p. 6, 14, 46, 51, 61, 73, 90, 120)*

Franzelli, B., A. Vié, M. Boileau, B. Fiorina, and N. Darabiha (2017). Large eddy simulation of swirled spray flame using detailed and tabulated chemical descriptions. *Flow, Turbulence and Combustion 98*(2), 633–661. *(p. 41)*

Frassoldati, A., T. Faravelli, and E. Ranzi (2003). Kinetic modeling of the interactions between NO and hydrocarbons at high temperature. *Combustion and Flame 135*(1-2), 97–112. *(p. 89, 95)*

Frenklach, M., H. Wang, and M. J. Rabinowitz (1992). Optimization and analysis of large chemical kinetic mechanisms using the solution mapping method in combustion of methane. *Progress in Energy and Combustion Science 18*(1), 47–73. *(p. 33)*

Galindo, S., F. Salehi, M. Cleary, and A. Masri (2017). Mmc-les simulations of turbulent piloted flames with varying levels of inlet inhomogeneity. *Proceedings of the Combustion Institute 36*(2), 1759–1766. *(p. 122)*

Galletti, C., G. Coraggio, and L. Tognotti (2013). Numerical investigation of oxy-natural-gas combustion in a semi-industrial furnace: validation of cfd sub-models. *Fuel 109*, 445–460. *(p. 5)*

Galpin, J., A. Naudin, L. Vervisch, C. Angelberger, O. Colin, and P. Domingo (2008). Large-eddy simulation of a fuel-lean premixed turbulent swirl-burner. *Combustion and Flame 155*(1-2), 247–266. *(p. 167)*

Germano, M., U. Piomelli, P. Moin, and W. H. Cabot (1991). A dynamic subgrid-scale eddy viscosity model. *Physics of Fluids A: Fluid Dynamics 3*(7), 1760–1765. *(p. 29)*

Gicquel, O., N. Darabiha, and D. Thévenin (2000). Laminar premixed hydrogen/air counterflow flame simulations using flame prolongation of ILDM with differential diffusion. *Proceedings of the Combustion Institute 28*(2), 1901–1908. *(p. 6, 42, 51, 90, 120, 121, 123)*

Glarborg, P., J. A. Miller, B. Ruscic, and S. J. Klippenstein (2018). Modeling nitrogen chemistry in combustion. *Progress in Energy and Combustion Science 67*, 31–68. *(p. 89)*

Godel, G., P. Domingo, and L. Vervisch (2009). Tabulation of NOx chemistry for large-eddy simulation of non-premixed turbulent flames. *Proceedings of the Combustion Institute 32*(1), 1555–1561. *(p. 6, 90, 91)*

Goussis, D. A. and U. Maas (2011). Model reduction for combustion chemistry. In *Turbulent Combustion Modeling*, pp. 193–220. Springer. *(p. 41)*

Guiberti, T. F., D. Durox, L. Zimmer, and T. Schuller (2015). Analysis of topology transitions of swirl flames interacting with the combustor side wall. *Combust. Flame 162*(11), 4342–4357. *(p. 71)*

Hasse, C. and N. Peters (2005). A two mixture fraction flamelet model applied to split injections in a di diesel engine. *Proceedings of the Combustion Institute 30*(2), 2755–2762. *(p. 50, 120)*

Hasse, C., V. Sohm, and B. Durst (2010). Numerical investigation of cyclic variations in gasoline engines using a hybrid urans/les modeling approach. *Computers & Fluids 39*(1), 25–48. *(p. 5)*

Haworth, D. (2010). Progress in probability density function methods for turbulent reacting flows. *Progress in Energy and combustion Science 36*(2), 168–259. *(p. 27)*

Hayhurst, A. and I. Vince (1980). Nitric oxide formation from N_2 in flames: the importance of prompt NO. *Progress in Energy and Combustion Science 6*(1), 35–51. *(p. 88)*

Herbinet, O., W. J. Pitz, and C. K. Westbrook (2008). Detailed chemical kinetic oxidation mechanism for a biodiesel surrogate. *Combustion and Flame 154*(3), 507–528. *(p. 39)*

Hermeth, S., G. Staffelbach, L. Y. Gicquel, V. Anisimov, C. Cirigliano, and T. Poinsot (2014). Bistable swirled flames and influence on flame transfer functions. *Combustion and Flame 161*(1), 184–196. *(p. 46)*

Hernández-Pérez, F., F. Yuen, C. Groth, and Ö. Gülder (2011). Les of a laboratory-scale turbulent premixed bunsen flame using fsd, pcm-fpi and thickened flame models. *Proceedings of the Combustion Institute 33*(1), 1365–1371. *(p. 126)*

Hirschfelder, J. O., C. F. Curtiss, R. B. Bird, and M. G. Mayer (1954). *Molecular theory of gases and liquids*, Volume 26. Wiley New York. *(p. 22, 123, 126)*

Huang, H., M. Fairweather, J. Griffiths, A. Tomlin, and R. Brad (2005). A systematic lumping approach for the reduction of comprehensive kinetic models. *Proceedings of the Combustion Institute 30*(1), 1309–1316. *(p. 40)*

Ihme, M., A. L. Marsen, and H. Pitsch (2007). Generation of optimal artificial neural networks using a pattern search algorithm: Application to approximation of chemical systems. *Journal of Neural Computation 20*, 1–29. *(p. 73)*

Ihme, M. and H. Pitsch (2008). Modeling of radiation and nitric oxide formation in turbulent nonpremixed flames using a flamelet/progress variable formulation. *Physics of Fluids 20*(5), 055110. *(p. 6, 27, 45, 73, 90)*

Ihme, M., L. Shunn, and J. Zhang (2012). Regularization of reaction progress variable for application to flamelet-based combustion models. *Journal of Computational Physics 231*(23), 7715–7721. *(p. 50)*

International Energy Agency, I. E. A. (2016). World energy outlook 2016. *https://webstore.iea.org/world-energy-outlook-2016*. *(p. 4, 88)*

International Energy Agency, I. E. A. (2017). World energy outlook 2017. *https://webstore.iea.org/world-energy-outlook-2017*. *(p. 2)*

International Energy Agency, I. E. A. (2018). World energy balances 2018: Overview. *https://webstore.iea.org/world-energy-balances-2018-overview*. *(p. 1)*

Jainski, C., M. Rißmann, B. Böhm, J. Janicka, and A. Dreizler (2017). Sidewall quenching of atmospheric laminar premixed flames studied by laser-based diagnostics. *Combust. Flame 183*, 271–282. *(p. 71)*

Jaouen, N., L. Vervisch, P. Domingo, and G. Ribert (2017). Automatic reduction and optimisation of chemistry for turbulent combustion modelling: Impact of the canonical problem. *Combustion and Flame 175*, 60–79. *(p. 35)*

Jaravel, T. (2016). *Prediction of pollutants in gas turbines using large eddy simulation*. Ph. D. thesis. *(p. 23, 52, 127)*

Jaravel, T., E. Riber, B. Cuenot, and G. Bulat (2017). Large eddy simulation of an industrial gas turbine combustor using reduced chemistry with accurate pollutant prediction. *Proceedings of the Combustion Institute 36*(3), 3817–3825. *(p. 6, 28, 39, 41, 72, 90, 121)*

Jaravel, T., E. Riber, B. Cuenot, and P. Pepiot (2018). Prediction of flame structure and pollutant formation of Sandia flame D using Large Eddy Simulation with direct integration of chemical kinetics. *Combustion and Flame 188*, 180–198. *(p. 6, 41, 90)*

Jin, H., A. Frassoldati, Y. Wang, X. Zhang, M. Zeng, Y. Li, F. Qi, A. Cuoci, and T. Faravelli (2015). Kinetic modeling study of benzene and pah formation in laminar methane flames. *Combustion and Flame 162*(5), 1692–1711. *(p. 35)*

Johnson, R., H. Wu, and M. Ihme (2017). A general probabilistic approach for the quantitative assessment of les combustion models. *Combustion and Flame 183*, 88–101. *(p. 122, 148, 161, 163)*

Jones, W. and R. Lindstedt (1988). Global reaction schemes for hydrocarbon combustion. *Combustion and flame 73*(3), 233–249. *(p. 6, 45, 46, 51, 73, 90, 120)*

Kärrholm, F. P. (2008). *Numerical modelling of diesel spray injection, turbulence interaction and combustion.* Chalmers University of Technology Gothenburg, Sweden. *(p. 27)*

Kee, R., J. Grcar, M. Smooke, and J. Miller (1985). A fortran program for modeling steady laminar one-dimensional premixed flames, report no. *SAND85-8240, Sandia National Laboratories*. *(p. 72, 73)*

Kee, R., F. Rupley, and J. Miller (1989). Chemkin-ii: A fortran package for the analysis of gas-phase chemical kinetics. 1989. *Sandia National Laboratory Report SAND89-8009B*. *(p. 19, 20)*

Kerstein, A. R., W. T. Ashurst, and F. A. Williams (1988). Field equation for interface propagation in an unsteady homogeneous flow field. *Physical Review A 37*(7), 2728. *(p. 27)*

Ketelheun, A., G. Kuenne, and J. Janicka (2013). Heat transfer modeling in the context of large eddy simulation of premixed combustion with tabulated chemistry. *Flow, turbulence and combustion 91*(4), 867–893. *(p. 28)*

Ketelheun, A., C. Olbricht, F. Hahn, and J. Janicka (2011). NO prediction in turbulent flames using LES/FGM with additional transport equations. *Proceedings of the Combustion Institute 33*(2), 2975–2982. *(p. 6, 90)*

Kleinheinz, K., T. Kubis, P. Trisjono, M. Bode, and H. Pitsch (2017). Computational study of flame characteristics of a turbulent piloted jet burner with inhomogeneous inlets. *Proceedings of the Combustion Institute 36*(2), 1747–1757. *(p. 122)*

Knudsen, E. and H. Pitsch (2009). A general flamelet transformation useful for distinguishing between premixed and non-premixed modes of combustion. *Combustion and flame 156*(3), 678–696. *(p. 50)*

Knudsen, E. and H. Pitsch (2012). Capabilities and limitations of multiregime flamelet combustion models. *Combustion and Flame 159*(1), 242–264. *(p. 50, 120)*

Kraushaar, M. (2011). *Application of the compressible and low-Mach num-*

ber approaches to Large-Eddy Simulation of turbulent flows in aero-engines. Ph. D. thesis, Institut National Polytechnique de Toulouse-INPT. *(p. 141)*

Kuenne, G., A. Ketelheun, and J. Janicka (2011). Les modeling of premixed combustion using a thickened flame approach coupled with fgm tabulated chemistry. *Combustion and Flame 158*(9), 1750–1767. *(p. 124, 126)*

Kuo, K. K. (2005). *Principles of combustion*. John Wiley 2005. *(p. 19, 89)*

Lam, S. H. (2013). Model reductions with special csp data. *Combustion and Flame 160*(12), 2707–2711. *(p. 40)*

Lamouroux, J., M. Ihme, B. Fiorina, and O. Gicquel (2014). Tabulated chemistry approach for diluted combustion regimes with internal recirculation and heat losses. *Combustion and flame 161*(8), 2120–2136. *(p. 45, 50)*

Lancien, T., K. Prieur, D. Durox, S. Candel, and R. Vicquelin (2018). Large eddy simulation of light-round in an annular combustor with liquid spray injection and comparison with experiments. *Journal of Engineering for Gas Turbines and Power 140*(2), 021504. *(p. 46)*

Lancien, T., K. Prieur, D. Durox, S. Candel, and R. Vicquelin (2019). Leading point behavior during the ignition of an annular combustor with liquid n-heptane injectors. *Proceedings of the Combustion Institute 37*(4), 5021–5029. *(p. 28)*

Launder, B. E. and D. B. Spalding (1983). The numerical computation of turbulent flows. In *Numerical Prediction of Flow, Heat Transfer, Turbulence and Combustion*, pp. 96–116. Elsevier. *(p. 23)*

Law, C. K. (2007). Combustion at a crossroads: Status and prospects. *Proceedings of the Combustion Institute 31*(1), 1–29. *(p. 116)*

Lefebvre, A. H. (1998). *Gas turbine combustion*. CRC press. *(p. 88)*

Legier, J.-P., T. Poinsot, and D. Veynante (2000). Dynamically thickened flame les model for premixed and non-premixed turbulent combustion. In *Proc. of the summer program*, pp. 157–168. Center for Turbulence Research, NASA Ames/Stanford Univ. *(p. 29, 126)*

Leonard, A. D. and J. C. Hill (1988). Direct numerical simulation of turbulent flows with chemical reaction. *Journal of scientific computing 3*(1), 25–43. *(p. 24)*

Li, Z., A. Cuoci, and A. Parente (2019). Large eddy simulation of mild combustion using finite rate chemistry: Effect of combustion sub-grid closure. *Proceedings of the Combustion Institute 37*(4), 4519–4529. *(p. 27)*

Lu, T., Y. Ju, and C. K. Law (2001). Complex csp for chemistry reduction and analysis. *Combustion and Flame 126*(1-2), 1445–1455. *(p. 41)*

Lu, T. and C. K. Law (2005). A directed relation graph method for mechanism reduction. *Proceedings of the Combustion Institute 30*(1), 1333–1341. *(p. 37)*

Lu, T. and C. K. Law (2006a). Linear time reduction of large kinetic mechanisms with directed relation graph: n-heptane and iso-octane. *Combustion and Flame 144*(1-2), 24–36. *(p. 39)*

Lu, T. and C. K. Law (2006b). Systematic approach to obtain analytic solutions of quasi steady state species in reduced mechanisms. *The Journal of Physical Chemistry A 110*(49), 13202–13208. *(p. 41)*

Lu, T. and C. K. Law (2007). An efficient reduced mechanism for methane oxidation with NO chemistry. In *5th US Combustion Meeting 2007*, pp. 1237–1251. Combustion Institute. *(p. 116)*

Lu, T. and C. K. Law (2008a). A criterion based on computational singular perturbation for the identification of quasi steady state species: A reduced mechanism for methane oxidation with NO chemistry. *Combustion and Flame 154*(4), 761–774. *(p. 6, 41, 51, 72, 90, 120)*

Lu, T. and C. K. Law (2008b). Strategies for mechanism reduction for large hydrocarbons: n-heptane. *Combustion and flame 154*(1-2), 153–163. *(p. 40)*

Lu, T. and C. K. Law (2009). Toward accommodating realistic fuel chemistry in large-scale computations. *Progress in Energy and Combustion Science 35*(2), 192–215. *(p. 5, 33, 37, 38, 40, 89, 90)*

Lu, T., C. K. Law, C. S. Yoo, and J. H. Chen (2009). Dynamic stiffness removal for direct numerical simulations. *Combustion and Flame 156*(8), 1542–1551. *(p. 5, 6, 34, 89)*

Maas, U. and S. B. Pope (1992a). Implementation of simplified chemical kinetics based on intrinsic low-dimensional manifolds. In *Symposium (International) on Combustion*, Volume 24, pp. 103–112. Elsevier. *(p. 42, 90, 100)*

Maas, U. and S. B. Pope (1992b). Simplifying chemical kinetics: intrinsic low-dimensional manifolds in composition space. *Combustion and flame 88*(3-4), 239–264. *(p. 42, 43, 120)*

Magnussen, B. (1981). On the structure of turbulence and a generalized eddy dissipation concept for chemical reaction in turbulent flow. In *19th aerospace sciences meeting*, pp. 42. *(p. 27)*

Magnussen, B. F. and B. H. Hjertager (1977). On mathematical modeling of turbulent combustion with special emphasis on soot formation and combustion. In *Symposium (international) on Combustion*, Volume 16, pp. 719–729. Elsevier. *(p. 27)*

Maio, G., M. Cailler, R. Mercier, and B. Fiorina (2019). Virtual chemistry for temperature and CO prediction in LES of non-adiabatic turbulent flames. *Proceedings of the Combustion Institute 37*(2), 2591–2599. *(p. 92, 121, 129)*

Maldonado Colmán, H. (2020). Ph. D. thesis, Paris Saclay. *(p. 184)*

Masri, A. (2015). Partial premixing and stratification in turbulent flames. *Proceedings of the Combustion institute 35*(2), 1115–1136. *(p. 49, 120)*

Masri, A. (2016). Experimental database for piloted flames with inhomogeneous inlets. *http://web.aeromech.usyd.edu.au/thermofluids/database.php*. *(p. 132, 133, 136, 143)*

McBride, B. J., S. Gordon, and M. A. Reno (1993). Coefficients for calculating thermodynamic and transport properties of individual species. *National Aeronautics and Space Administration, Office of Management.*. *(p. 17, 58)*

Meares, S. and A. R. Masri (2014). A modified piloted burner for stabilizing turbulent flames of inhomogeneous mixtures. *Combustion and Flame 161*(2), 484–495. *(p. 7, 8, 50, 67, 121, 132)*

Meares, S., V. Prasad, G. Magnotti, R. Barlow, and A. Masri (2015). Stabilization of piloted turbulent flames with inhomogeneous inlets. *Proceedings of the Combustion Institute 35*(2), 1477–1484. *(p. 121, 122, 132, 136)*

Mehl, C. (2018). *Large Eddy Simulation and complex chemistry for modeling the chemical structure of turbulent flames*. Ph. D. thesis. *(p. 175)*

Mehl, M., W. J. Pitz, C. K. Westbrook, and H. J. Curran (2011). Kinetic modeling of gasoline surrogate components and mixtures under engine conditions. *Proceedings of the Combustion Institute 33*(1), 193–200. *(p. 33)*

Meier, W., P. Weigand, X. R. Duan, and R. Giezendanner-Thoben (2007). Detailed characterization of the dynamics of thermoacoustic pulsations in a lean premixed swirl flame. *Combust. Flame 150*(1), 2–26. *(p. 7, 165, 166, 167, 172)*

Mercier, R. (2015). *Turbulent combustion modeling for Large Eddy Simulation of non-adiabatic stratified flames*. Ph. D. thesis, Ecole Centrale Paris. *(p. 24)*

Mercier, R., P. Auzillon, V. Moureau, N. Darabiha, O. Gicquel, D. Veynante, and B. Fiorina (2014). Les modeling of the impact of heat losses and differential diffusion on turbulent stratified flame propagation: application to the tu darmstadt stratified flame. *Flow, turbulence and combustion 93*(2), 349–381. *(p. 75, 79, 81, 126)*

Mercier, R., M. Cailler, and B. Fiorina (2017a). Les simulation of the cambridge stratified flame using optimized virtual mechanisms. In *55th AIAA Aerospace Sciences Meeting*, pp. 0606. *(p. 128, 129)*

Mercier, R., M. Cailler, and B. Fiorina (2017b). Les simulation of the cambridge stratified flame using optimized virtual mechanisms. In *55th AIAA Aerospace Sciences Meeting*, pp. 0606. *(p. 175)*

Mercier, R., T. Guiberti, A. Chatelier, D. Durox, O. Gicquel, N. Darabiha, T. Schuller, and B. Fiorina (2016). Experimental and numerical investigation of the influence of thermal boundary conditions on premixed swirling flame stabilization. *Combust. Flame 171*, 42–58. *(p. 71, 181)*

Mercier, R., C. Mehl, B. Fiorina, and V. Moureau (2019). Filtered wrinkled flamelets model for large-eddy simulation of turbulent premixed combustion. *Combustion and Flame 205*, 93–108. *(p. 175)*

Mercier, R., V. Moureau, D. Veynante, and B. Fiorina (2015). Les of turbulent combustion: on the consistency between flame and flow filter scales.

Proc. Combust. Inst. 35(2), 1359–1366. *(p. 167)*

Metcalfe, W. K., S. M. Burke, S. S. Ahmed, and H. J. Curran (2013). A hierarchical and comparative kinetic modeling study of c1- c2 hydrocarbon and oxygenated fuels. *International Journal of Chemical Kinetics 45*(10), 638–675. *(p. 35)*

Miller, J. A., R. J. Kee, and C. K. Westbrook (1990). Chemical kinetics and combustion modeling. *Annual Review of Physical Chemistry 41*(1), 345–387. *(p. 33)*

Moureau, V., P. Domingo, and L. Vervisch (2011a). Design of a massively parallel cfd code for complex geometries. *Comptes Rendus Mécanique 339*(2-3), 141–148. *(p. 121, 129, 141, 167)*

Moureau, V., P. Domingo, and L. Vervisch (2011b). From large-eddy simulation to direct numerical simulation of a lean premixed swirl flame: Filtered laminar flame-pdf modeling. *Combust. Flame 158*(7), 1340–1357. *(p. 167, 172)*

Moureau, V., P. Minot, H. Pitsch, and C. Bérat (2007). A ghost-fluid method for large-eddy simulations of premixed combustion in complex geometries. *Journal of Computational Physics 221*(2), 600–614. *(p. 167)*

Mukhopadhyay, S. and J. Abraham (2012). Influence of heat release and turbulence on scalar dissipation rate in autoigniting n-heptane/air mixtures. *Combustion and Flame 159*(9), 2883–2895. *(p. 37)*

Nafe, J. and U. Maas (2002). Modeling of NO formation based on ILDM reduced chemistry. *Proceedings of the Combustion Institute 29*(1), 1379–1385. *(p. 6, 90)*

Navarro-Martinez, S., A. Kronenburg, and F. Di Mare (2005). Conditional moment closure for large eddy simulations. *Flow, Turbulence and Combustion 75*(1-4), 245–274. *(p. 27)*

Nguyen, P., L. Vervisch, V. Subramanian, and P. Domingo (2010). Multidimensional flamelet-generated manifolds for partially premixed combustion. *Combust. Flame 157*(1), 43–61. *(p. 73)*

Nguyen, P.-D., L. Vervisch, V. Subramanian, and P. Domingo (2010). Multidimensional flamelet-generated manifolds for partially premixed combustion. *Combustion and Flame 157*(1), 43–61. *(p. 50, 91)*

Nguyen Van, C. (2020). Ph. D. thesis, Paris Saclay. *(p. 184)*

Nicoud, F. and F. Ducros (1999). Subgrid-scale stress modelling based on the square of the velocity gradient tensor. *Flow, turbulence and Combustion 62*(3), 183–200. *(p. 142, 167)*

Oijen, J. v. and L. D. Goey (2000). Modelling of premixed laminar flames using flamelet-generated manifolds. *Combustion Science and Technology 161*(1), 113–137. *(p. 123)*

OpenFOAM (2019). *www.openfoam.org*. *(p. 107, 111)*

Pecquery, F., V. Moureau, G. Lartigue, L. Vervisch, and A. Roux (2014). Modelling nitrogen oxide emissions in turbulent flames with air dilution: Application to LES of a non-premixed jet-flame. *Combustion and*

Flame 161(2), 496–509. *(p. 6, 45, 90)*

Pele, O. and M. Werman (2009). Fast and robust earth mover's distances. In *2009 IEEE 12th International Conference on Computer Vision*, pp. 460–467. IEEE. *(p. 161)*

Pepiot, P. (2008). *Automatic strategies to model transportation fuel surrogates*. Stanford University Stanford, CA, Ph.D thesis. *(p. 41, 116)*

Pepiot-Desjardins, P. and H. Pitsch (2008). An efficient error-propagation-based reduction method for large chemical kinetic mechanisms. *Combustion and Flame 154*(1-2), 67–81. *(p. 6, 38, 72, 90)*

Perry, B. A. and M. E. Mueller (2018). Effect of multiscalar subfilter pdf models in les of turbulent flames with inhomogeneous inlets. *Proceedings of the Combustion Institute*. *(p. 122, 135)*

Perry, B. A., M. E. Mueller, and A. R. Masri (2017). A two mixture fraction flamelet model for large eddy simulation of turbulent flames with inhomogeneous inlets. *Proceedings of the Combustion Institute 36*(2), 1767–1775. *(p. 45, 122, 134, 135)*

Peters, N. (1984). Laminar diffusion flamelet models in non-premixed turbulent combustion. *Progress in energy and combustion science 10*(3), 319–339. *(p. 6, 44, 90)*

Peters, N. (1985). Numerical and asymptotic analysis of systematically reduced reaction schemes for hydrocarbon flames. In *Numerical simulation of combustion phenomena*, pp. 90–109. Springer. *(p. 41)*

Peters, N. (1988). Laminar flamelet concepts in turbulent combustion. In *Symposium (International) on Combustion*, Volume 21, pp. 1231–1250. Elsevier. *(p. 120)*

Peters, N. (1993). Flame calculations with reduced mechanismsâFIXME"an outline. In *Reduced kinetic mechanisms for applications in combustion systems*, pp. 3–14. Springer. *(p. 41)*

Peters, N. (2000). *Turbulent combustion*. Cambridge university press. *(p. 49)*

Philip, M., M. Boileau, R. Vicquelin, E. Riber, T. Schmitt, B. Cuenot, D. Durox, and S. Candel (2015). Large eddy simulations of the ignition sequence of an annular multiple-injector combustor. *Proceedings of the Combustion Institute 35*(3), 3159–3166. *(p. 5, 46)*

Pierce, C. D. and P. Moin (2004). Progress-variable approach for large-eddy simulation of non-premixed turbulent combustion. *Journal of fluid Mechanics 504*, 73–97. *(p. 6, 45, 120)*

Pitsch, H. and L. D. De Lageneste (2002). Large-eddy simulation of premixed turbulent combustion using a level-set approach. *Proceedings of the Combustion Institute 29*(2), 2001–2008. *(p. 29)*

Poinsot, T. and D. Veynante (2005). *Theoretical and numerical combustion*. RT Edwards, Inc. *(p. 21, 22, 23, 25, 26, 48, 75, 126, 127)*

Poinsot, T. J. and D. P. Veynante (2018). Combustion. *Encyclopedia of Computational Mechanics Second Edition*, 1–30. *(p. 5, 24, 27)*

Polifke, W., W. Geng, and K. Döbbeling (1998). Optimization of rate coefficients for simplified reaction mechanisms with genetic algorithms. *Combustion and Flame 113*(1-2), 119–134. *(p. 46)*

Pope, S. B. (1985). Pdf methods for turbulent reactive flows. *Progress in Energy and Combustion Science 11*(2), 119–192. *(p. 27)*

Pope, S. B. (2000). *Turbulent flows.* Cambridge university press. *(p. 23, 24)*

Pope, S. B. (2004). Ten questions concerning the large-eddy simulation of turbulent flows. *New journal of Physics 6*(1), 35. *(p. 25)*

Proch, F., P. Domingo, L. Vervisch, and A. M. Kempf (2017). Flame resolved simulation of a turbulent premixed bluff-body burner experiment. part i: Analysis of the reaction zone dynamics with tabulated chemistry. *Combustion and Flame 180*, 321–339. *(p. 28, 124, 127)*

Proch, F. and A. Kempf (2015). Modeling heat loss effects in the large eddy simulation of a model gas turbine combustor with premixed flamelet generated manifolds. *Proc. Combust. Inst. 35*(3), 3337–3345. *(p. 28, 45, 71)*

Proch, F. and A. M. Kempf (2014). Numerical analysis of the cambridge stratified flame series using artificial thickened flame les with tabulated premixed flame chemistry. *Combustion and Flame 161*(10), 2627–2646. *(p. 29, 124)*

Raman, V., H. Pitsch, and R. O. Fox (2005). Hybrid large-eddy simulation/lagrangian filtered-density-function approach for simulating turbulent combustion. *Combustion and Flame 143*(1-2), 56–78. *(p. 27)*

Ranzi, E., M. Dente, A. Goldaniga, G. Bozzano, and T. Faravelli (2001). Lumping procedures in detailed kinetic modeling of gasification, pyrolysis, partial oxidation and combustion of hydrocarbon mixtures. *Progress in Energy and Combustion Science 27*(1), 99–139. *(p. 37, 40)*

Ranzi, E., A. Frassoldati, R. Grana, A. Cuoci, T. Faravelli, A. Kelley, and C. Law (2012). Hierarchical and comparative kinetic modeling of laminar flame speeds of hydrocarbon and oxygenated fuels. *Progress in Energy and Combustion Science 38*(4), 468–501. *(p. 35)*

Ranzi, E., A. Sogaro, P. Gaffuri, G. Pennati, and T. Faravelli (1994). A wide range modeling study of methane oxidation. *Combustion science and technology 96*(4-6), 279–325. *(p. 15)*

Ribert, G., O. Gicquel, N. Darabiha, and D. Veynante (2006). Tabulation of complex chemistry based on self-similar behavior of laminar premixed flames. *Combustion and Flame 146*(4), 649–664. *(p. 45, 50)*

Ribert, G., L. Vervisch, P. Domingo, and Y.-S. Niu (2014). Hybrid transported-tabulated strategy to downsize detailed chemistry for numerical simulation of premixed flames. *Flow, Turbulence and Combustion 92*(1-2), 175–200. *(p. 35, 50)*

Richard, S., O. Colin, O. Vermorel, A. Benkenida, C. Angelberger, and D. Veynante (2007). Towards large eddy simulation of combustion in spark ignition engines. *Proceedings of the Combustion Institute 31*(2), 3059–3066. *(p. 29)*

Rieth, M., J.-Y. Chen, S. Menon, and A. M. Kempf (2019). A hybrid flamelet finite-rate chemistry approach for efficient les with a transported fdf. *Combustion and Flame 199*, 183–193. *(p. 27, 122, 124)*

Roux, S., G. Lartigue, T. Poinsot, U. Meier, and C. Bérat (2005). Studies of mean and unsteady flow in a swirled combustor using experiments, acoustic analysis, and large eddy simulations. *Combust. Flame 141*(1), 40–54. *(p. 167)*

Sagaut, P. (2006). *Large eddy simulation for incompressible flows: an introduction.* Springer Science & Business Media. *(p. 23)*

Salehi, F., M. Cleary, A. Masri, Y. Ge, and A. Klimenko (2017). Sparse-lagrangian mmc simulations of an n-dodecane jet at engine-relevant conditions. *Proceedings of the Combustion Institute 36*(3), 3577–3585. *(p. 37)*

Sankaran, R., E. R. Hawkes, J. H. Chen, T. Lu, and C. K. Law (2007). Structure of a spatially developing turbulent lean methane–air bunsen flame. *Proc. Combust. Inst. 31*(1), 1291–1298. *(p. 169, 178)*

Smith, G. P., D. M. Golden, M. Frenklach, B. Eiteener, M. Goldenberg, C. T. Bowman, R. K. Hanson, W. C. Gardiner, V. V. Lissianski, and Z. W. Qin (2011). *http://www.me.berkeley.edu/gri_mech.* *(p. 14, 35, 72, 79, 88, 89, 91, 102, 115, 123)*

Stagni, A., A. Cuoci, A. Frassoldati, T. Faravelli, and E. Ranzi (2013). Lumping and reduction of detailed kinetic schemes: an effective coupling. *Industrial & Engineering Chemistry Research 53*(22), 9004–9016. *(p. 40, 107)*

Stagni, A., A. Frassoldati, A. Cuoci, T. Faravelli, and E. Ranzi (2016). Skeletal mechanism reduction through species-targeted sensitivity analysis. *Combustion and Flame 163*, 382–393. *(p. 39)*

Su, Z., Y. Wang, R. Shi, W. Zeng, J. Sun, F. Luo, and X. Gu (2015). Optimal mass transport for shape matching and comparison. *IEEE transactions on pattern analysis and machine intelligence 37*(11), 2246–2259. *(p. 161)*

Sutherland, J. C. and A. Parente (2009). Combustion modeling using principal component analysis. *Proceedings of the Combustion Institute 32*(1), 1563–1570. *(p. 40)*

Tian, L. and R. Lindstedt (2018). Evaluation of reaction progress variable-mixture fraction statistics in partially premixed flames. *Proceedings of the Combustion Institute*. *(p. 122)*

Tomlin, A. S., T. Turányi, and M. J. Pilling (1997). Mathematical tools for the construction, investigation and reduction of combustion mechanisms. In *Comprehensive chemical kinetics*, Volume 35, pp. 293–437. Elsevier. *(p. 37, 39)*

Turanyi, T. (1990). Reduction of large reaction mechanisms. *New Journal of Chemistry 14*(11), 795–803. *(p. 39)*

Turányi, T. and T. Bérces (1990). Kinetics of reactions occurring in the unpolluted troposphere, ii. sensitivity analysis. *Reaction Kinetics and Catalysis Letters 41*(1), 103–108. *(p. 40)*

Turányi, T. and A. S. Tomlin (2014). *Analysis of kinetic reaction mechanisms*. Springer. *(p. 40)*

Valorani, M., F. Creta, D. A. Goussis, J. C. Lee, and H. N. Najm (2006). An automatic procedure for the simplification of chemical kinetic mechanisms based on csp. *Combustion and Flame 146*(1-2), 29–51. *(p. 40)*

Van Oijen, J., A. Donini, R. Bastiaans, J. ten Thije Boonkkamp, and L. de Goey (2016). State-of-the-art in premixed combustion modeling using flamelet generated manifolds. *Progress in Energy and Combustion Science 57*, 30–74. *(p. 42, 73)*

Van Oijen, J., F. Lammers, and L. De Goey (2001). Modeling of complex premixed burner systems by using flamelet-generated manifolds. *Combustion and Flame 127*(3), 2124–2134. *(p. 6, 42, 73, 79, 90, 120, 121)*

Vascellari, M., S. Schulze, P. Nikrityuk, D. Safronov, and C. Hasse (2014). Numerical simulation of pulverized coal MILD combustion using a new heterogeneous combustion submodel. *Flow, Turbulence and Combustion 92*(1-2), 319–345. *(p. 5)*

Vermorel, O., S. Richard, O. Colin, C. Angelberger, A. Benkenida, and D. Veynante (2009). Towards the understanding of cyclic variability in a spark ignited engine using multi-cycle les. *Combustion and Flame 156*(8), 1525–1541. *(p. 5)*

Versteeg, H. K. and W. Malalasekera (2007). *An introduction to computational fluid dynamics: the finite volume method*. Pearson Education. *(p. 23)*

Vervisch, L., P. Domingo, G. Lodato, and D. Veynante (2010). Scalar energy fluctuations in large-eddy simulation of turbulent flames: Statistical budgets and mesh quality criterion. *Combustion and Flame 157*(4), 778–789. *(p. 25, 175)*

Vervisch, P. E., O. Colin, J.-B. Michel, and N. Darabiha (2011). NO relaxation approach (NORA) to predict thermal NO in combustion chambers. *Combustion and Flame 158*(8), 1480–1490. *(p. 91)*

Veynante, D., B. Fiorina, P. Domingo, and L. Vervisch (2008). Using self-similar properties of turbulent premixed flames to downsize chemical tables in high-performance numerical simulations. *Combustion Theory and Modelling 12*(6), 1055–1088. *(p. 73)*

Veynante, D. and R. Knikker (2006). Comparison between LES results and experimental data in reacting flows. *Journal of Turbulence* (7), N35. *(p. 24, 25)*

Veynante, D. and V. Moureau (2015). Analysis of dynamic models for large eddy simulations of turbulent premixed combustion. *Combustion and Flame 162*(12), 4622–4642. *(p. 29)*

Veynante, D. and L. Vervisch (2002). Turbulent combustion modeling. *Progress in Energy and Combustion Science 28*(3), 193–266. *(p. 27)*

Volpiani, P., T. Schmitt, and D. Veynante (2016). A posteriori tests of a dynamic thickened flame model for large eddy simulations of turbulent premixed combustion. *Combustion and Flame 174*, 166–178. *(p. 29)*

Volpiani, P. S., T. Schmitt, and D. Veynante (2017). Large eddy simulation of a turbulent swirling premixed flame coupling the tfles model with a dynamic wrinkling formulation. *Combust. Flame 180*, 124–135. *(p. 46, 167, 168, 172)*

Vreman, A., B. Albrecht, J. Van Oijen, L. De Goey, and R. Bastiaans (2008). Premixed and nonpremixed generated manifolds in large-eddy simulation of sandia flame D and F. *Combustion and Flame 153*(3), 394–416. *(p. 44, 90)*

Wang, G., M. Boileau, and D. Veynante (2011). Implementation of a dynamic thickened flame model for large eddy simulations of turbulent premixed combustion. *Combustion and Flame 158*(11), 2199–2213. *(p. 29, 131)*

Wang, G., M. Boileau, D. Veynante, and K. Truffin (2012). Large eddy simulation of a growing turbulent premixed flame kernel using a dynamic flame surface density model. *Combustion and Flame 159*(8), 2742–2754. *(p. 29)*

Wang, H. and M. Frenklach (1991). Detailed reduction of reaction mechanisms for flame modeling. *Combustion and Flame 87*(3-4), 365–370. *(p. 89)*

Wang, H. and S. B. Pope (2011). Large eddy simulation/probability density function modeling of a turbulent ch4/h2/n2 jet flame. *Proceedings of the Combustion Institute 33*(1), 1319–1330. *(p. 27)*

Wang, P., N. Platova, J. Fröhlich, and U. Maas (2014). Large eddy simulation of the preccinsta burner. *International Journal of Heat and Mass Transfer 70*, 486–495. *(p. 167)*

Westbrook, C. K. and F. L. Dryer (1981). Simplified reaction mechanisms for the oxidation of hydrocarbon fuels in flames. *Combustion science and technology 27*(1-2), 31–43. *(p. 6, 45, 73, 90, 120)*

Westbrook, C. K., C. V. Naik, O. Herbinet, W. J. Pitz, M. Mehl, S. M. Sarathy, and H. J. Curran (2011). Detailed chemical kinetic reaction mechanisms for soy and rapeseed biodiesel fuels. *Combustion and Flame 158*(4), 742–755. *(p. 33)*

Williams, F. (1985). Combustion theory-benjamin cummings publishing company (pearson). *San Francisco, USA*. *(p. 22)*

Wu, H. and M. Ihme (2016). Compliance of combustion models for turbulent reacting flow simulations. *Fuel 186*, 853–863. *(p. 122)*

Zeldovich, Y. B. (2014). *Selected Works of Yakov Borisovich Zeldovich, Volume I: Chemical Physics and Hydrodynamics*, Volume 140. Princeton University Press. *(p. 89)*

universite
PARIS-SACLAY

ÉCOLE DOCTORALE
Physique et ingénierie : électrons, photons, sciences du vivant (EOBE)

Titre: Prédiction des polluants dans les simulations numériques des flammes laminaires et turbulentes par méthode de chimie virtuelle

Mots clés: Modéle de combustion, Mècanisme réduit, Formation de polluants, Structures complexes de flamme, Stratification du mélange, Pertes thermique de la flamme

Résumé: La CFD est aujourd'hui utilisée par les ingénieurs de recherche comme un outil numérique pour concevoir et optimiser les dispositifs de combustion avancés qui sont utilisés dans les systèmes de conversion d'énergie. L'un des principaux objectifs de la recherche, dans le développement d'outils numériques avancés pour la CFD, est l'identification d'un modéle réduite de cinitique chimique de la combustion qui reproduit la structure de la flamme et la formation de polluants avec un coût de calcul abordable. En particulier, la prédiction de la formation de polluants est une tâche difficile lorsque des flammes complexes sont rencontrées: stratification du mélange, pertes de chaleur et recirculation des gaz brûlés. Le travail de recherche mené dans cette these se concentre sur la modélisation de la formation monoxyde de carbone (CO) et des oxydes d'azote (NOx) dans des conditions de flamme complexes en utilisant une methode récemment développée et appelée chimie virtuelle: celle-ci consiste à concevoir des mécanismes réduits constitués d'un réseau d'un nombre optimisé d'espèces virtuelles interagissant via des réactions virtuelles optimisées. Dans une première étape, les mécanismes virtuels sont développés et validés dans des configurations de flammes 1-D. Dans un deuxième temps, ceux-ci sont utilisés pour calculer plusieurs configurations de flammes 2-D laminaires et 3-D turbulentes sur une large gamme de régimes de combustion: prémélangé, non prémélangé, partiellement prémélangé et non adiabatique. Les résultats obtenus sont validés avec des données expérimentales et avec des calculs inclutant une cinetique chimique détaillée.

universite
PARIS-SACLAY

ÉCOLE DOCTORALE
Physique et ingénierie :
électrons, photons,
sciences du vivant (EOBE)

Title: Pollutant prediction in numerical simulations of laminar and turbulent flames using virtual chemistry

Keywords: Combustion model, Reduced mechanism, Pollutants formation, Complex flame structures, Mixture stratification, Flame heat loss

Abstract: CFD is nowadays used by research engineers as a numerical tool to design and optimize advanced combustion devices that are employed in energy conversion systems. In the development of advanced numerical CFD tools, one of the main research challenges is the identification of a reduced combustion chemistry model able to find a compromise between accurate reproduction of the flame structure and pollutants formation with an affordable CPU cost. In particular, pollutants formation prediction is a difficult task when complex flame environments are encountered: flame characterized by mixture stratification, heat loss and burnt gas recirculation. The present research work focuses on the modeling of CO and NOx formation in complex flame conditions using a reduced finite rate chemistry approach. CO and NOx reduced chemistry models are here developed using the recent virtual chemistry model; it consists in designing reduced mechanisms made of a network of an optimized number of virtual species interacting through virtual optimized reactions. In the first step, the virtual chemistry mechanisms are developed and validated in 1-D flames comparing the results with detailed chemistry. In a second step, they are employed to compute several 2-D laminar and 3-D turbulent flame configurations which include different combustion regimes: premixed, non-premixed, partially-premixed and non-adiabatic conditions. The obtained results are validated either with experimental data or with detailed chemistry computations.

Université Paris-Saclay
Espace Technologique / Immeuble Discovery
Route de l'Orme aux Merisiers RD 128 / 91190 Saint-Aubin, France